

UNIVERSITÄT
DES
SAARLANDES

Mechanochemical reduction reactions of transition metal oxides with solid hydrides and their elemental counterparts

Dissertation

zur Erlangung des Grades der

Doktorin der Naturwissenschaften

der Naturwissenschaftlich-Technischen Fakultät

der Universität des Saarlandes

vorgelegt von

Anna Michaely

Saarbrücken, 2025

Tag des Kolloquiums:	09.02.2026
Dekan:	Prof. Dr.-Ing. Dirk Bähre
Berichterstatter:	Prof. Dr. Guido Kickelbick
	Priv.-Doz. Dr.-Ing. habil. Guido Falk
Vorsitz:	Prof. Dr. Gregor Jung
Akad. Mitglied:	Dr. Andreas Rammo

Die nachfolgende Arbeit entstand im Zeitraum von Oktober 2021 bis September 2025 im Institut für Anorganische Festkörperchemie an der Universität des Saarlandes im Arbeitskreis von Herrn Prof. Dr. G. Kickelbick.

Danksagung

Zunächst möchte ich mich bei Herrn Prof. Dr. Guido Kickelbick für die Möglichkeit bedanken, die Promotion in seiner Arbeitsgruppe durchführen zu können, für die fachlichen Diskussionen und Anregungen, sowie für die Übernahme der Erstkorrektur meiner Arbeit. Weiterhin möchte ich PD Dr. Guido Falk für die wissenschaftliche Begleitung und die Übernahme der Zweitkorrektur danken.

Ein besonderer Dank geht an Dr. Robert Haberkorn und an PD Dr. Oliver Janka für eure Unterstützung bei Fragen zur Durchführung von Rietveld-Verfeinerungen und für die hilfreichen wissenschaftlichen Diskussionen. Außerdem möchte ich Tobias Straub vielmals für seine tatkräftige Unterstützung im Labor und die bereichernden Diskussionen über mechanochemische Fragestellungen danken.

Weiterhin möchte ich mich natürlich bei allen Kolleginnen und Kollegen bedanken, die mich die letzten Jahre begleitet haben. Vielen Dank für eure Unterstützung bei wissenschaftlichen Fragestellungen und für die freundliche und witzige Atmosphäre im Labor.

Ein weiterer Dank geht an Dr. Petra Herbeck Engel aus der Gruppe von Dr. Peter William de Oliveira vom Leibniz-Institut für Neue Materialien (INM) für die Aufnahme der Raman-Spektren und an die Arbeitsgruppe Kautenburger, insbesondere an Dr. Kristina Brix und Aaron Haben, für ICP-MS Messungen. Außerdem geht ein großer Dank an Prof. Dr. Christopher Kay für die Möglichkeit, EPR-Spektren aufzunehmen und an Haakon Wiedemann und Maxim Neuberger für die Unterstützung bei den Messungen und der anschließenden Interpretation. Vielen Dank auch an die Arbeitsgruppe von Prof. Dr. Oliver Clemens und insbesondere Hong Cheng für die Hilfe bei der Durchführung und Interpretation der Impedanzmessungen.

Kurzzusammenfassung

Übergangsmetalloxide sind meist nur bei hohen Temperaturen reduzierbar. Diese Arbeit untersucht das Potenzial der Mechanochemie, solche Reduktionen bei Raumtemperatur durchzuführen.

Zuerst wurde die mechanochemische Reduktion von TiO_2 und Nb_2O_5 mit LiH bzw. NaH untersucht, die laut EPR-Spektroskopie zu einer partiellen Reduktion führte. Aufgrund seiner geringen Ionengröße wurde ein Einbau von Li in das Oxid mittels Rietveldanalyse nachgewiesen. Die erfolgreiche Defektbildung, bestätigt durch NMR- und Raman-Spektroskopie, führte zu einer signifikanten Erhöhung der photokatalytischen Aktivität unter UV- und Vis-Licht.

Dagegen ergab die selbsterhaltende Reaktion zwischen V_2O_5 und NaH in der Mühle eine komplexe Mischung diverser kristalliner (Natrium-)Vanadiumoxide laut Rietveldanalyse. Höhere NaH-Konzentrationen führten zur Bildung von mehr Natriumvanadaten und niedrigeren Vanadium-Oxidationsstufen, was durch DFT-Rechnungen gestützt wurde. Die Reduktionsmittel Na, LiH und Li zeigten gleiche Trends wie NaH.

Im letzten Teil wurde die mechanochemische Synthese von MgV_2O_4 untersucht, die nur durch eine selbsterhaltende Reaktion von V_2O_5 und Mg gelang. Der Effekt der Mahlintensität auf Realbau und Leitfähigkeit wurde analysiert, wobei letztere bei starkem Mahlen aufgrund höherer Defektdichten sank.

Insgesamt erweisen sich (Erd-)Alkalimetall(-hydride) als effiziente Reduktionsmittel in der Mechanochemie, besonders bei exothermen Reaktionen und Einbau des Metalls in die Oxidstruktur.

.

Abstract

Transition metal oxides are usually reducible only at high temperatures. This work explores the potential of mechanochemistry to perform such reductions at room temperature.

First, the mechanochemical reduction of TiO_2 and Nb_2O_5 with LiH and NaH was studied, which led to a partial reduction according to EPR spectroscopy. Due to its small ionic radius, Li incorporation into the oxide was confirmed by Rietveld analysis. Successful defect formation, verified by NMR and Raman spectroscopy, resulted in a significant increase in photocatalytic activity under UV and visible light.

Contrary, the self-sustaining reaction of V_2O_5 and NaH in the ball mill yielded a complex mixture of various crystalline (sodium) vanadium oxides, as shown by Rietveld analysis. Higher NaH concentrations led to more sodium vanadates and lower vanadium oxidation states, as supported by DFT calculations. The reducing agents Na, LiH, and Li showed similar trends as NaH.

In the final part, the mechanochemical synthesis of MgV_2O_4 was investigated, which was only achieved by a self-sustaining reaction of V_2O_5 and Mg. The effect of the milling intensity on the microstructure and conductivity was analyzed, whereby the latter decreased after intense milling due to increased defect densities.

Overall, alkaline earth metals, alkali metals and their hydrides prove to be effective reducing agents in mechanochemistry, especially in exothermic reactions and when the metal is incorporated into the oxide structure.

Table of contents

1 Introduction 1

1.1 Mechanochemistry 1
1.1.1 Historical Development and Advantages of Mechanochemistry 1
1.1.2 Working Principle, Influential Parameters and Effects of Ball Mills 2
1.1.3 Current Advancements in Mechanochemistry 8

1.2 Transition Metal Oxides 10
1.2.1 Titanium Oxides 10
1.2.2 Niobium Oxides 14
1.2.3 Vanadium Oxides 17
1.2.4 Reduction of Transition Metal Oxides 21

1.3 Characterization of Ball Milled Samples by Powder X-Ray Diffraction and Rietveld refinement 27

2 Research goals 32

3 Results and Discussion 34

3.1 Black Titania and Niobia within Ten Minutes – Mechanochemical Reduction of Metal Oxides with Alkali Metal Hydrides 34

3.2 Highly exothermic and fast mechanochemical redox and intercalation reactions of V_2O_5 with sodium hydride 49

3.3 Mechanochemical reduction of V_2O_5: Alkali metals vs. Alkali Metal Hydrides – Which are the better Reducing Agents? 61
3.3.1 Introduction 61
3.3.2 Results and Discussion 61
3.3.3 Experimental section 70
3.3.4 Conclusion 72

3.4 Mechanochemical Synthesis of MgV_2O_4: Reactivity Pathways Driven by Milling Energy and Precursors 73

4 Conclusion and Outlook 87

5 References 90

6 Supplementary Information 110

6.1 Supporting Information – Black Titania and Niobia within Ten Minutes – Mechanochemical Reduction of Metal Oxides with Alkali Metal Hydrides 110

6.2 Supporting Information – Highly Exothermic and Fast Mechanochemical Redox and Intercalation Reactions of V_2O_5 with Sodium Hydride 129

6.3 Supporting Information – Mechanochemical reduction of V_2O_5: Alkali metals vs. Alkali Metal Hydrides – Which are the better Reducing Agents? 159

6.4 Supporting Information – Mechanochemical Synthesis of MgV_2O_4: Reactivity Pathways Driven by Milling Energy and Precursors 160

List of Abbreviations

a.u.	Arbitrary Unit
BPR	Ball-to-Powder Ratio
DFT	Density Functional Theory
DME	Dimethoxyethane
DRS-UV-Vis	Diffuse-Reflectance UV-Vis Spectroscopy
EIS	Electrochemical Impedance Spectroscopy
EPR	Electron Paramagnetic Resonance Spectroscopy
eq.	Molar Equivalent
FWHM	Full Width at half Maximum
GGA	General Gradient Approximation
GOF	Goodness of Fit
HR-TEM	High-Resolution Transmission Electron Microscopy
IB	Integral Breadth
IUPAC	International Union of Pure and Applied Chemistry
LO	Longitudinal Optic mode
MSR	Mechanically induced self-propagating Reaction
PAW	Projector-augmented Wave
PBEsol	Perdew-Burke-Ernzerhof optimized for bulk Solids
PXRD	Powder X-ray Diffraction
RAM	Resonant Acoustic Mixing
R_{exp}	Expected R-factor
rpm	Revolutions per Minute
R_{wp}	Weighted profile R-factor
SPE-MAS NMR	Single-Pulse Excitation Magic Angle Spinning Nuclear Magnetic Resonance Spectroscopy
TGA	Thermogravimetric Analysis
TMO	Transition Metal Oxide
TO	Transverse Optic Mode
TPR	Temperature Programmed Reduction
VASP	Vienna Ab initio Simulation Package

1 Introduction

1.1 Mechanochemistry

1.1.1 Historical Development and Advantages of Mechanochemistry

Historical Development of Mechanochemistry

Mechanochemistry, as elaborated in great detail by Lazlo Takacs,[1] has a long historical background that dates back to ancient times and will only be described briefly hereafter. The earliest known written documentation of a chemical reaction induced by grinding is found in the book *De Lapidibus* (*On stones*) from 315 B.C., authored by Theophrastus of Eresos, a student of Aristoteles. Therein, he describes the formation of elemental mercury through mechanical action after grinding the mineral cinnabar (HgS) in a copper mortar.[2]

Mathew Carey Lea, also known as the father of mechanochemistry, conducted pioneering systematic studies in the late 19th century, showing that only grinding decomposes silver chloride into elemental silver and chlorine gas, whereas thermal heating leads to melting without decomposition.[3]

The term "mechanochemistry" was first introduced in 1919 by Wilhelm Ostwald and later defined by Gerhard Heinicke in 1984 as *"a branch of chemistry dealing with the chemical and physicochemical changes of substances in all states of aggregation due to the influence of mechanical energy"*.[4] Around two decades later, the International Union of Pure and Applied Chemistry (IUPAC) also included a definition of a mechanochemical reaction in their *Compendium of Chemical Terminology* and defines it as a "*chemical reaction that is induced by the direct absorption of mechanical energy"*.[5]

Since then, the field of mechanochemistry has experienced significant growth as an environmentally benign branch of chemistry with increasing publication numbers and the identification by IUPAC as one of the top ten most emerging sustainable techniques in 2019.[6]

Advantages of Mechanochemistry

Mechanochemical reactions are typically performed with little (liquid-assisted grinding) or no solvents (neat grinding), making them an environmentally friendly synthetic approach that aligns with the 12 principles of green chemistry.[7] Since solvents can often be omitted, differences in the solubility of reactants don't cause problems. However, the aggregation state of the reactants is generally not limited to solids. Even gaseous compounds can successfully be

transformed, for example in the mechanochemical ammonia synthesis starting from N_2 and H_2 with iron[8] or iron-potassium[9] catalysts.

In addition to the advantage of omitting solvents, mechanochemical reactions are often faster and give higher yields compared to more traditional methods, making them applicable in various fields, including organic chemistry,[10] inorganic chemistry,[11] polymers,[12] metal oxides,[13] metal organic frameworks,[14] and mechanical alloying[15] as summarized in numerous review articles.

Although the temperature inside the milling jar can rise well above room temperature under extremely harsh milling conditions due to collisions of the milling balls, no additional heating of the mill is necessary, meaning that mechanochemical reactions generally proceed at room temperature. This is especially beneficial in comparison with the energy consuming high temperatures that are often required for more traditional solid-state reactions.

1.1.2 Working Principle, Influential Parameters and Effects of Ball Mills

1.1.2.1 Working Principles of Ball Mills

While the first mechanochemical reactions were carried out in a simple mortar and pestle, research has since then evolved to advanced high energy ball mills to transfer more impact, shear and friction forces onto the reaction mixture to induce the reaction. The combination and magnitude of these predominant forces vary between the ball mill types and directly influence the energy transfer efficiency and the reaction outcome.[16]

The two main types of ball mills employed for today's research activities are mixer mills and planetary ball mills. As shown in Figure 1a, milling jars of mixer mills undergo horizontal oscillations with radial movements, thereby subjecting milling balls to a figure-eight trajectory within the jar. In contrast, planetary ball mills consist of milling jars rotating on a so-called sun wheel in counter-direction to the motion of the wheel. The resulting centrifugal force forces the balls on a rotational trajectory. After sliding along the wall, they eventually lift off before colliding with the opposite inner wall (Figure 1b).[15] During this motion, impact forces primarily act on the powder that is trapped between colliding milling balls or between the wall of the milling jar and a colliding ball (Figure 1b, A). When the balls slide against the wall, the powder adhering to the wall predominantly experiences friction (Figure 1b, B), while shear forces occur between two sliding balls (Figure 1b, C).[16]

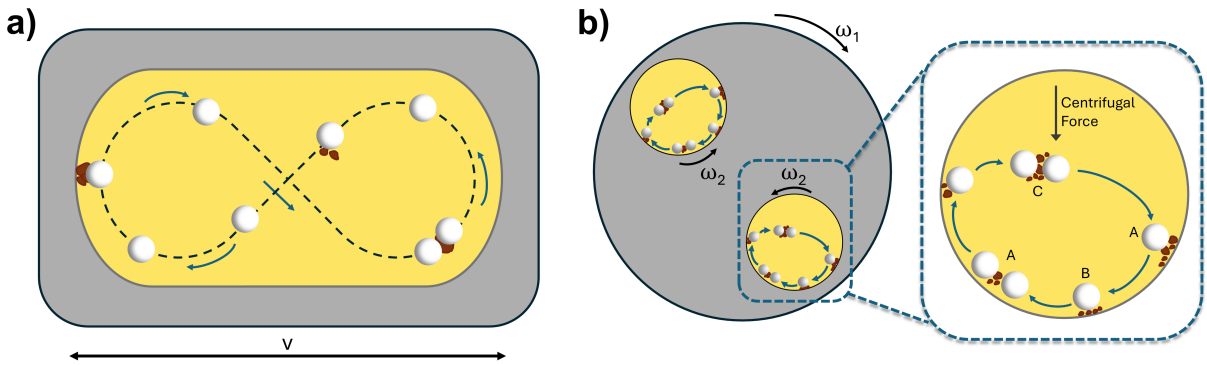

Figure 1: Schematic representation of the trajectory of the milling balls in the milling jar of (a) a mixer mill, which is shaken horizontally with a specific frequency ν and (b) a planetary ball mill with the rotational speed of the sun wheel ω_1 and the rotational speed of the milling jars ω_2. For the description of the processes A, B and C see text (*vide supra*). In both (a) and (b) the milling balls are shown in white, the reaction mixture in brown and the inside of the milling jar in yellow. The outer part of the milling jar is shown in gray in (a), while the gray color on (b) represents the sun wheel.

1.1.2.2 Influencing Parameters of Planetary Ball Mills

As can easily be imagined, the amount of energy transferred to the powder during milling depends on numerous parameters of the ball mill, such as milling speed and time, the number, density, and diameter of the milling balls as well as the ball-to-powder ratio. In the following, the influence of selected milling parameters on the reaction outcome of the ball milling process of inorganic solids is briefly discussed below.

Generally, the energy impact increases with increasing rotational speeds (Figure 2a), resulting in a more powerful energy transfer.[17, 18] However, excessive speeds cause a shift from a cataracting to a centrifugal milling regime (Figure 2b), where the milling balls become pinned to the wall of the milling jar due to the large centrifugal forces. This hinders an effective energy transfer and can result in larger crystallite sizes and decreased reactivity, as seen by higher ignition temperatures of the exothermic self-propagating reactions of Ni-Al, Ti-Si and Si-C powder mixtures.[19]

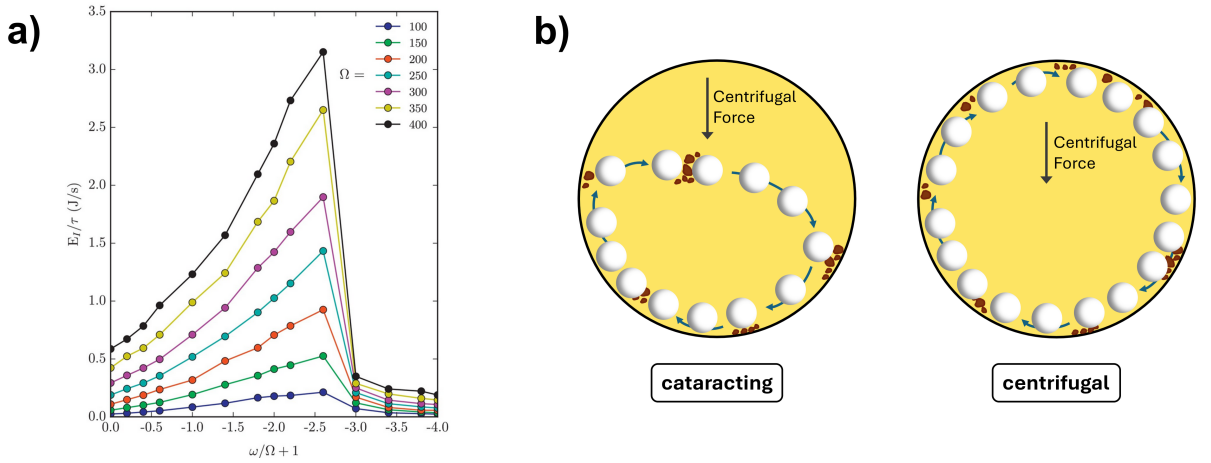

Figure 2: (a) Specific impact energy as a function of the rotational speed and the jar to plate angular velocities of a planetary ball mill for milling of CaF_2. Reproduced from M. Broseghini, L. Gelisio, M. D'Incau, C. L. Azanza Ricardo; N.M. Pugno, P. Scardi, "Modeling of the planetary ball-milling process: The case study of ceramic powders.", *J. Eur. Ceram. Soc.* **2016**, *36*, 2205-2212 with permission from Elsevier. (b) Schematic presentation of two different milling regimes: the cataracting one and the rolling one at high rotational speeds.

While long or harsh milling might seem beneficial at first, optimization of the milling time and speed is crucial as prolonged or intense milling can lead to amorphization[20, 21] and an increase of abrasion of the milling equipment, which causes contamination of the sample.[22] The extent of abrasion depends on the material of the milling equipment, with denser materials such as tungsten carbide (ρ = 14.3 g cm^{-3}) providing more energy impact but also increased abrasion compared to less dense ones such agate (density ρ = 2.65 g cm^{-3}).[15] Other typical materials include silicon nitride (ρ = 3.28 g cm^{-3}), corundum (ρ = 3.8 g cm^{-3}), zirconium oxide (ρ = 5.7 g cm^{-3}) and hardened stainless steel (ρ = 7.7 g cm^{-3}).[23] To overcome abrasion, the use of emerging milling media free resonant acoustic mixing (RAM) might offer a promising alternative, using high-frequency acoustic vibrations at the system's resonance frequency to rapidly accelerate and efficiently mix the reaction mixture.[24] For catalyzed reactions, performing a mechanocatalytic reaction by galvanostatic coating of the milling equipment is equally as promising. In addition to avoiding abrasion. the amount of required catalyst is minimized since the milling equipment itself acts as the catalyst.[25]

In addition to technical parameters of the ball mill, both the use of solvent and the milling temperature can also play an influencing role. Rather than omitting solvents entirely (neat grinding), adding small amounts of solvent (liquid-assisted grinding) can help to adjust the rheology of the reaction mixture and prevent cementation, which occurs when the powder accumulates in one spot inside the jar instead of mixing properly. Especially in molecular systems, the addition of solvent can significantly influence the reaction outcome. Depending

on the type and amount of solvent, Belenguer *et al.* were able to reversibly induce (new) polymorphic phase transitions of molecular disulfide systems,[26] while Krusenbaum *et al.* observed a significant enhancement of the generated surface area of a mechanochemically prepared porous polymer through liquid-assisted grinding.[27]

Regarding the influence of temperature, it can easily be imagined that an increase in milling temperature results in a change of reaction kinetics. By using a simple heat gun or more elaborated jar heaters to heat the milling jars, an increase in yield, rate and selectivity can be observed, especially in organic reactions.[28, 29] On the other hand, cryomilling with liquid nitrogen can facilitate the ball milling process with highly ductile or reactive reactants. For example, Kumar and Biswas prepared highly reactive free standing aluminum nanoparticles with sizes ranging from 5 to 15 nm in a top-down approach via cryomilling.[30]

Due to the many influencing parameters, a mathematical description of the amount of transferred energy during the milling process remains difficult. However, some models have been proposed over the years to provide insights into the milling process, especially in the field of mechanical alloying.[18, 31-33] The kinematic models by Abdellaoui and Gaffet estimate for example the shock power in planetary ball mills to range from 0.01 to 1.604 W g^{-1} $ball^{-1}$, making planetary ball mills significantly more energetic than attritor (<0.001 W g^{-1} $ball^{-1}$) or vibratory mills (0.005-0.24 W g^{-1} $ball^{-1}$).[31] Meanwhile, Burgio *et al.* proposed kinematic equations to estimate the total power P^* transferred to the system during milling as a function of the yield coefficient φ_b, the number of milling balls N_b, the milling time t, the mass of one ball m_b and the mass of the powder m_g, the rotational speed of the milling jars W_v and the sun wheel W_p, the inner diameter of the jar R_v and the distance of the center of the jar to the center of the plate R_p (Equation 1.1).[18]

$$P^* = \frac{-\varphi_b N_b m_b t (W_p - W_v)\left(\frac{W_v^3\left(\frac{R_v - d_b}{2}\right)}{W_p} + W_p W_v R_p\right)\left(R_v - \frac{d_b}{2}\right)}{2\pi m_g} \qquad (1.1)$$

Based on these kinematic equations, Rojac *et al.* were able to derive a milling map for the mechanochemical synthesis of $NaNbO_3$, which facilitates the comparison of the reaction outcomes obtained with different mills and different milling conditions. For their mechanochemical synthesis of $NaNbO_3$, they found that a minimum of 7 to 12 kJ g^{-1} of cumulative kinetic energy is required for a successful synthesis.[32] Recently, it was shown that

the Burgio-Rojac milling map can also be applied to other systems in the submicrometer range, when Kozma *et al.* determined a minimum single hit energy of 35 mJ hit^{-1} for the effective attrition of multiwall carbon nanotubes.[34] Furthermore, Jafter *et al.* have developed a tool to estimate the energy input as a function of the milling conditions and the geometry of the ball mill in order to easily reproduce mechanochemical reactions and transfer them to different types of mills.[35]

In addition to the difficult mathematical description of the milling process, the exact understanding of the initiation of mechanochemical reactions remains complex and rather unclear. Two of the most established models, the "Hot spot model" and the "Magma-Plasma model", postulate that the mechanochemical reaction is initiated by local rises in temperature after ball collisions. According to the controversial "Hot Spot model",[36] the temperature can locally attain several 1000 K in microseconds.[37-39] In contrast, the "Magma-Plasma model" suggests the formation of a plasmatic state during particle collisions, emitting excited fragments of solid matter, photons and electrons for a short time.[4, 40] In recent years, different kinetic,[41, 42] DFT-[43, 44] and molecular dynamics[45] simulation-based approaches can be found in literature to understand mechanochemical processes.

1.1.2.3 Effect of Ball Milling on Oxides

While the full conversion of the reactants into a new product is usually envisioned, ball milling can also have several other effects on inorganic solids such as metal oxides, which will be briefly elaborated hereafter.

Depending on the milling conditions, polymorphic phase transitions can be induced.[20-22, 46] For example, cubic Y_2O_3 continuously transforms into the metastable monoclinic polymorph (Figure 3a),[21] while anatase-type TiO_2 transforms into the high-pressure modification TiO_2-II after short milling times or into rutile-type TiO_2 after prolonged milling.[46] However, surface functionalization of anatase with phenyl phosphonic acid during reactive milling helps to stabilize the high-pressure modification and hinders the formation of rutile.[22]

Regarding the microstructure of oxides, ball milling leads to a reduction of the crystallite size down to the nanometer size (Figure 3b), while the strain often increases simultaneously (Figure 3c).[21, 47] It must also be noted that harsh milling can lead to amorphization of the sample and the introduction of structural disorder and defects.[21, 48, 49] In some materials, the formation of oxygen vacancies can also be observed.[50-52]

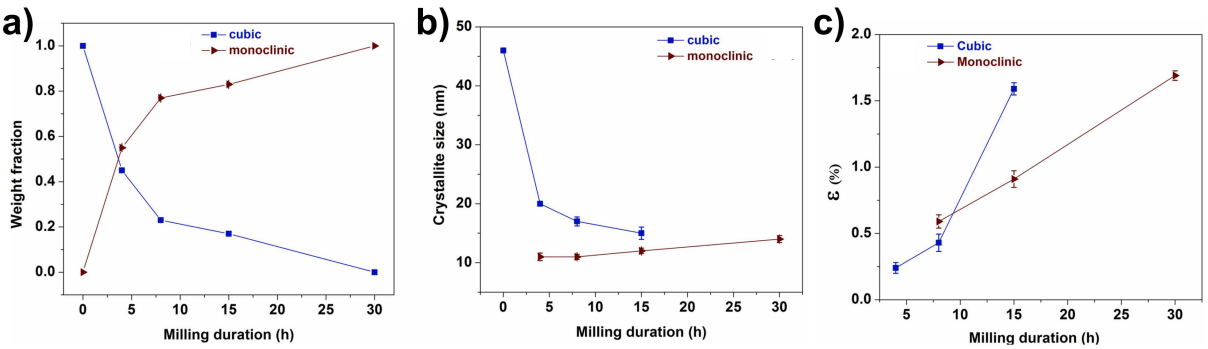

Figure 3: Evolution of the (a) phase percentage, (b) crystallite size and (c) strain during the polymorphic phase transition of cubic to monoclinic Y_2O_3, which is induced by ball milling. Reproduced from V. K. B.R; A; Dasgupta; C. Ghosh; S. K. Sinha. "Analysis of structural transformation in nanocrystalline Y_2O_3 during high energy ball milling." *J. Alloys Compd.* **2022**, *900*, 163550 with permission from Elsevier.

Under optimal ball milling conditions, these structural changes[53] or introduced defects[54] lead to an increased reactivity of the material, which is called mechanochemical activation. This mechanochemical activation often significantly reduces the temperature required for subsequent high temperature reactions. For example, Khalameida *et al.* reduced the reaction temperature for the lithium niobate synthesis from over 1000 °C to 450 °C under optimized milling conditions.[55]

In addition to a reduction of the reaction temperature, chemical properties such as the conductivity can also be altered, which are often analyzed by electrochemical impedance spectroscopy (EIS). By perturbating an equilibrated electrochemical system with an *ac* sinusoidal response and measuring their response over a wide frequency range, EIS allows the investigation of different electrical and physical processes occurring in the sample over different time scales. Based on the resistance R at the intercept of the x-axis in the low-frequency range and the dimensions of the pressed pellet with the thickness d and the cross-sectional area A, the total conductivity σ of the sample can be calculated according to the following equation.

$$\sigma = \frac{d}{R \times A} \tag{1.2}$$

The activation energy E_A of the conduction phenomenon can be determined by performing temperature-dependent measurements and using the Arrhenius relationship (Equation 1.3), with A being a pre-exponential factor, T the temperature, k the Boltzmann constant. Plotting the logarithm of the conductivity as a function of the reciprocal of the temperature yields a straight line, whose slope gives the value of E_A.

$$\sigma(T) = Aexp\left(-\frac{E_A}{kT}\right) \quad (1.3)$$

After mechanochemical activation, Straub *et al*. reported a two-order increase in conductivity and improved Li intercalation in mechanochemically activated Mn_3O_4,[47] while Becker *et al.* observed an increase in conductivity of up to three orders of magnitude after milling of Li_2TiO_3 and $Li_4Ti_5O_{12}$ for just 10 min.[56] Similarly, Iwaniak *et al*. reported a better conductivity of lithium titanates after activation, as well as a lower activation energy for conduction.[57]

1.1.3 Current Advancements in Mechanochemistry

Despite the many advantages of mechanochemistry and the steadily rising number of publications, ongoing research continues to expand its potential as a versatile tool in chemical synthesis. This is achieved by developing new types of mechanochemistry that combine the advantages of milling with those of other techniques. As already described in Chapter 1.1.2.2, using heat in thermo-mechanochemistry can strongly enhance the yield, rate and selectivity, particularly of organic reactions.[28, 29] Similarly, the use of galvanostatically coated milling balls as catalysts in mechanocatalysis enables a significant decrease of the catalyst load.[25] Other new developments include combining mechanochemistry with the advantages of electro-, sono- or photochemistry, giving rise to the new research fields electro-, sono-, and photo-mechanochemistry. As described in great detail by Martinez *et al.*, these approaches shorten reaction times and expand the range of accessible mechanochemical reaction pathways.[58]

In addition to combining mechanochemistry with other synthetic approaches, significant research progress is also being made in the in situ characterization of mechanochemical reactions in order to gain valuable insights into the complex processes involved and to better understand this type of reaction. Typical in situ characterization methods include the use of X-ray diffraction, as well as Raman, NMR and X-ray absorption spectroscopy, as summarized in numerous reviews.[59-62] For example, Julien *et al.* used in situ diffraction to study to formation of a microporous MOF-74 framework from ZnO, which not only helped to identify two new intermediates, but also revealed an unusual stepwise transformation of a close-packed intermediate into an open structure.[63] Despite the great advantage of such in situ characterization studies, more sophisticated milling equipment is needed. For example, the milling jars must be transparent, meaning that special jars must be made of PMMA or even quartz glass.

Less sophisticated and easy-to-use in situ characterization methods include the measurement of pressure and temperature, which can provide valuable insight into the reaction dynamics. Even a simple thermocouple attached to the external wall of the milling jar can deliver useful information on the temperature evolution during milling. As discussed in more detail in chapter 1.2.4.3, a sudden temperature increase can for example evidence the start of a mechanically induced self-propagating reaction.[64]

Two well-known ball mill manufacturers for academic research, Retsch GmbH and Fritsch GmbH, now offer commercial systems for continuous pressure and temperature monitoring during the milling process. These systems not only facilitate the detection of reaction onsets but enable differentiation between gradually proceeding reactions and sudden ones. While gradually proceeding reactions often show a steady rise in temperature and pressure, as observed during milling of Nb_2O_5 with LiH (Figure 4a), sudden ones can be evidenced by a sharp temperature and pressure increase, as seen during milling of V_2O_5 and LiH (Figure 4b). Moreover, for gas-evolving reactions, pressure monitoring allows evaluation of the extent of reactant conversion by comparing the measured final pressure with the theoretical value predicted from the ideal gas law (*vide infra*).

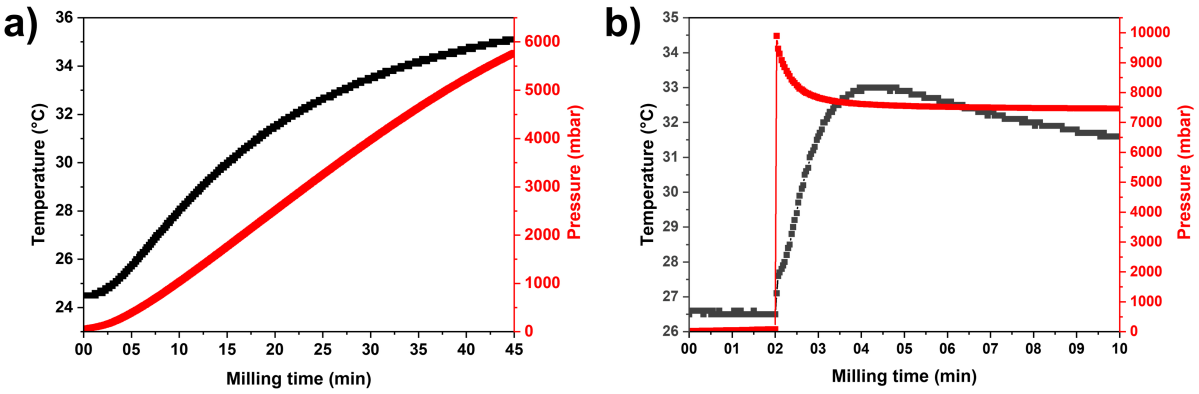

Figure 4: Pressure and temperature evolution during milling of 2 eq. LiH with (a) Nb_2O_5 (A. Michaely, unpublished results) and (b) V_2O_5.[65] Note the different scales.

1.2 Transition Metal Oxides

Transition metal oxides (TMOs) represent a diverse group of materials with versatile applications in (photo)catalysis, solid-state batteries, and other energy storage applications due to their wide range of different crystal structures and the many stable oxidation states of the respective transition metal. This work focuses on the mechanochemical reduction behavior of the group IV and V TMOs TiO_2, V_2O_5, and Nb_2O_5. In these oxides, the oxidation states of the transition metal ions range from +II to +IV for group IV metals and up to +V for group V metals. The three oxides TiO_2, V_2O_5, and Nb_2O_5 were selected for their distinct chemical properties and their anticipated differences in their mechanochemical reduction behavior. Among them, Nb_2O_5 is the most stable and least redox-active. Its surface is dominated by acidic sides and reductions in hydrogen temperature-programmed reduction (H_2-TPR) experiments require temperatures of ~800 to 1300 °C,[66] making reductions particularly challenging. Nb_2O_5 is also essentially insoluble in common acids, except in aqueous HF,[23] and has the lowest number of literature-known ternary oxides with Li and Na, with only ~15 different stoichiometric compounds.[67] In contrast, the mechanochemical reduction of V_2O_5 is expected to be easier as reductions in H_2-TPR set-ups already occur between ~600 and 780 °C. Furthermore, V_2O_5 has mainly surface redox sites,[66] is even soluble in diluted acids[23] and has a large number of ternary oxides (~35 distinct oxides),[67] suggesting that alkali metal ions are most likely involved during the reduction. Lastly, TiO_2 should display intermediate behavior. It possesses both surface redox and acidic sites,[68] is soluble in (hot) concentrated acids[23] such as H_2SO_4 and forms an intermediate set of ternary oxides (~20 different literature-known compounds).[67]

The following sections provide a brief overview of their crystal structures, syntheses, and applications of the investigated oxides.

1.2.1 Titanium Oxides

1.2.1.1 The Ti-O System

In addition to the three non-mixed-valent stoichiometric titanium oxides Ti(II)O, $Ti(III)_2O_3$ and $Ti(IV)O_2$ and the mixed-valent oxide Ti_3O_5 ($Ti_2O_3 \cdot TiO_2$), numerous suboxides, known as the Magnéli phases,[69] with a general sum formula of Ti_nO_{2n-1} (n = 4-10) are known to literature (Figure 5).[70] For commercial use and application, titanium dioxide has by far the highest importance among all titanium oxides.

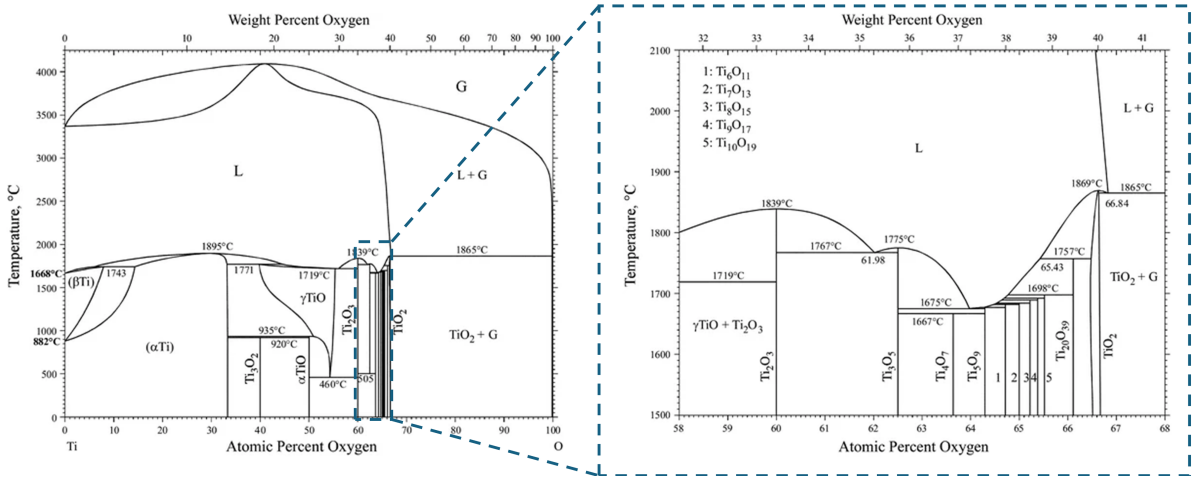

Figure 5: Phase diagram of the titanium oxygen system (left) with a zoom of the region from 58 to 68at% oxygen (right). Adapted and reprinted from H. Okamoto, "O-Ti (Oxygen-Titanium)", *J. Phase Equilib. Diffus.* **2011**, *32*, 473–474 with permission from Springer Nature.

1.2.1.2 The Polymorphic System of TiO_2

TiO_2 occurs in three natural polymorphs (rutile, anatase, and brookite) as well as several high-pressure modifications,[71-73] including TiO_2-II with an α-PbO_2 type-structure. TiO_2-II is the most studied high-pressure polymorph and has been explored for photochemical applications.[74] Depending on the temperature and pressure, metastable anatase can either be transformed in the low-pressure, high-temperature rutile phase or the high-pressure, high-temperature modification TiO_2-II (Figure 6).

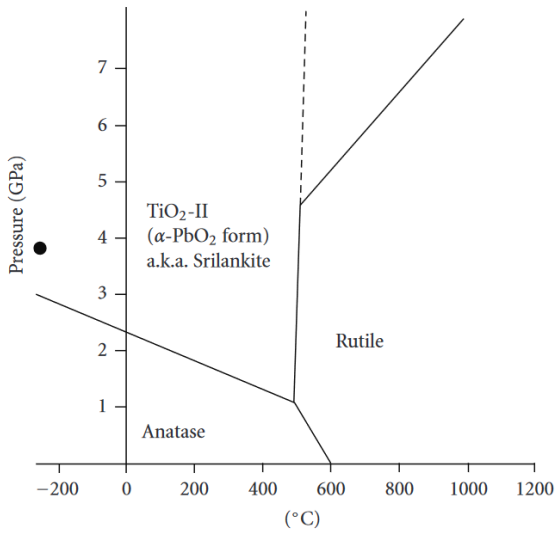

Figure 6: Phase diagram of the TiO_2 polymorphs rutile, anatase, and TiO_2-II. Reproduced from X. Nie, S. Zhou, G. Maeng, K. Sohlberg, "Doping of TiO_2 Polymorphs for Altered Optical and Photocatalytic Properties", *Internat. J. Photoenergy* **2009**, 294042 according to the Creative Commons Attribution License 3.0 (CC-BY) from Wiley.

Due to the complex synthesis of phase-pure orthorhombic brookite (*Pbca*),[75, 76] mainly rutile and anatase are of interest for commercial use and application. Both anatase and rutile crystallize in the tetragonal crystal system and consist of interconnected octahedral TiO_6 units. In rutile-type TiO_2 with space group $P4_2/mnm$ and lattice parameters $a = 458.0$ and $c = 297.0$ pm, the TiO_6 octahedra are connected to chains along [001] via cis-edge sharing, while the remaining two corners are linked to adjacent strands (Figure 7a).[77] Meanwhile, anatase-TiO_2 crystallizes with the space group $I4_1/amd$ with lattice parameters of $a = 378.5$ and $c = 951.4$ pm.[78] In contrast to rutile, the TiO_6 units share four edges with neighboring octahedra (Figure 7b).

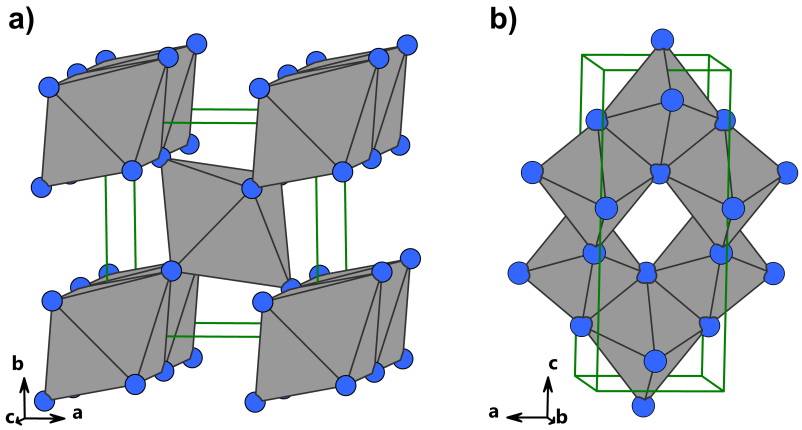

Figure 7: Crystal structure of (a) rutile-type TiO_2 with space group $P4_2/mnm$[77] and (b) anatase-type TiO_2 with space group $I4_1/amd$.[78] Oxygen atoms are shown in blue and the unit cell in green.

Synthesis and Mechanochemistry

Besides thermally induced polymorphic phase transitions, various synthesis methods have been explored over the years for the synthesis of either bulk or nanosized TiO_2 particles, rods and thin films to tailor the chemical properties, as described in detail in several review articles.[79-81] Typically, metastable anatase forms prior to rutile in the nanocrystalline size range of 14 nm due to a more desirable orientation of TiO_6 units[82] and a lower total free surface energy.[83] In addition to the mild sol-gel process with titanium alkoxides such as titanium tetraisopropoxide[84, 85] or halogenides such as $TiCl_4$[86, 87] as precursors, other synthetic approaches include hydro-[85, 88, 89] and solvothermal[90] treatment, flame pyrolysis,[91] but also gas phase synthesis such as chemical[92, 93] and physical[94] vapor deposition.

While ball milling can be used to induce polymorphic phase transitions of anatase TiO_2 into either TiO_2-II or rutile depending on the harshness of the milling conditions as described in Chapter 1.1.2.3, there are also some reports on the mechanochemical synthesis of TiO_2 from

different precursors. For example, Anuradha and Ranganathan obtained rutile-type TiO_2 with a crystallite size of 30 and 20 nm after 4 and 12 h of milling titanium and cupric oxide, CuO, respectively.[95] Other approaches use a combination of titanyl sulfate $TiO(SO_4)$ and NaCl[96] or Na_2CO_3[97] as well as $TiCl_4$ and $(NH_4)_2CO_3$ as precursors,[98] though some require additional thermal annealing to obtain (nano)crystalline TiO_2.

Properties and Applications

Due to different chemical and physical properties, anatase and rutile don't have the same main applications. Both polymorphs are wide band *n*-type semiconductors, yet their crystal structures and electronic band structures vary. Anatase exhibits an indirect optical band gap of 3.2 eV because the minimum of the conduction band and the maximum of the valence band occur at different points in the Brillouin zone. In contrast, rutile has a direct optical band gap of 3.0 eV, with both bands aligned at the same point.[99-102] Among the polymorphs, anatase nanoparticles exhibit the highest photocatalytic activity due to a longer lifetime of photogenerated electrons and holes with lower effective masses than rutile[103] and a high specific surface area.[104] These characteristics make anatase ideal for use in photocatalytic applications such as water purification,[105] self-cleaning surfaces,[106, 107] and dye-sensitized solar cells.[108]

Although the photocatalytic activity of rutile is lower than that of anatase, its high ordinary refractive index of 2.58 at 632.8 nm and 30 °C,[109] combined with its high stability and inertness, makes rutile-type TiO_2 suitable for use as a white pigment[110] in paper,[111] paint,[112] food,[113, 114] as well as cosmetics and hygiene products.[114, 115] However, recent concerns about the toxicity of especially nanosized TiO_2 might limit some of these applications in the future.[116, 117] Furthermore, rutile is also investigated as an anode material in lithium-ion batteries.[118, 119] At room temperature, Li occupies the octahedral sites in rutile-type TiO_2 during Li intercalation since the occupation of tetrahedral sites is only energetically favorable at low temperatures of around 10 K.[120] However, according to Borghols *et al.*, the rutile structure is only retained up to a maximum Li/Ti-ratio of approximately 0.07 and 0.15 for microsized and nanosized TiO_2, respectively.[120] At higher Li concentrations, cubic $Li_{0.5}Ti_{0.5}O$ with a rock salt-type structure forms.[121]

1.2.2 Niobium Oxides

1.2.2.1 The Nb-O-System

Nb(II)O, Nb(IV)O_2, and Nb(V)$_2O_5$ represent the three main stable oxides in the binary niobium-oxygen system, as shown in the phase diagram in Figure 8.[122] However, it must be noted that the existing phase diagrams do not fully capture the complexity of the niobium-oxygen system since the many stable and metastable sub-stoichiometric oxides NbO_x with $0 < x < 1$ and $2 < x < 2.5$ are not depicted. Among the three main oxides, Nb_2O_5 is the thermodynamically most stable one, and its properties and applications are discussed in the following.

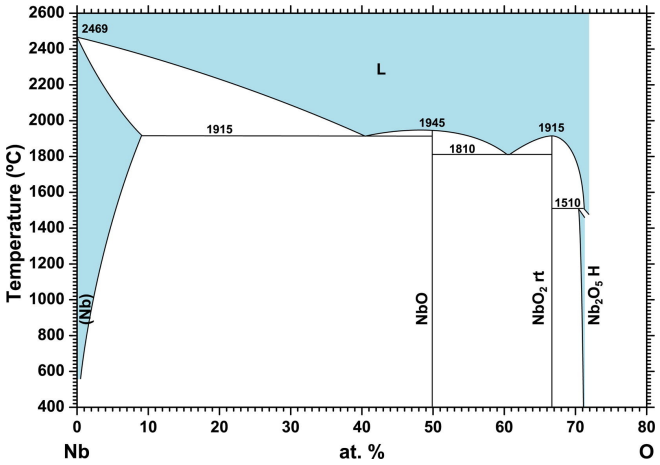

Figure 8: Phase diagram of the niobium oxygen system. Reprinted from C. Nico, T. Monteiro, M. P. F. Graça, "Niobium oxides and niobates physical properties: Review and prospects", *Prog. Mater. Sci.* **2016**, *80*, 1-37, with permission from Elsevier.

1.2.2.2 The polymorphic system of Nb_2O_5

Several stable and metastable polymorphs have been reported to literature, which are either named after their synthesis temperature or particle shape due to a lack of consistent nomenclature. Polymorphs that are named after their synthesis temperature include the low temperature modifications TT-Nb_2O_5 (TT for 'tief-tief' in German, 500-600 °C) and T-Nb_2O_5 (T for 'tief' in German, 600-800 °C), the medium temperature one M-Nb_2O_5 (M for 'mittel' in German, 850-900 °C) and the high temperature modification H-Nb_2O_5 (H for 'hoch' in German, >900 °C).[123, 124] In contrast, B-, N- and R-Nb_2O_5 are named after their shape. B is derived from the German word for 'Blätter' (leaves/sheets), N for 'Nadeln' (needles) and P for 'Prismen' (prisms).[124] While the previously described polymorphs can occur as a single phase, other polymorphs are only found in coexistence with other ones. For example, the high-pressure modification Z-Nb_2O_5 is only found alongside B-Nb_2O_5.[125]

Regarding their crystal structure, most Nb_2O_5 polymorphs consist of NbO_6 octahedra, which are connected in different ways depending on the polymorphs. For example, the monoclinic modification H-Nb_2O_5, which is thermodynamically stable under static conditions,[126] crystallizes in the space group *P2/m* with lattice parameters of $a = 1933.0$, $b = 382.3$, $c = 2032.2$ pm and $\beta = 115.8°$. H-Nb_2O_5 has a ReO_3 block-type structure of 3×5 and 3×4 blocks of corner sharing NbO_6 octahedra within the blocks and edge sharing between blocks (Figure 9).[127] Tetrahedral sites are partially occupied.

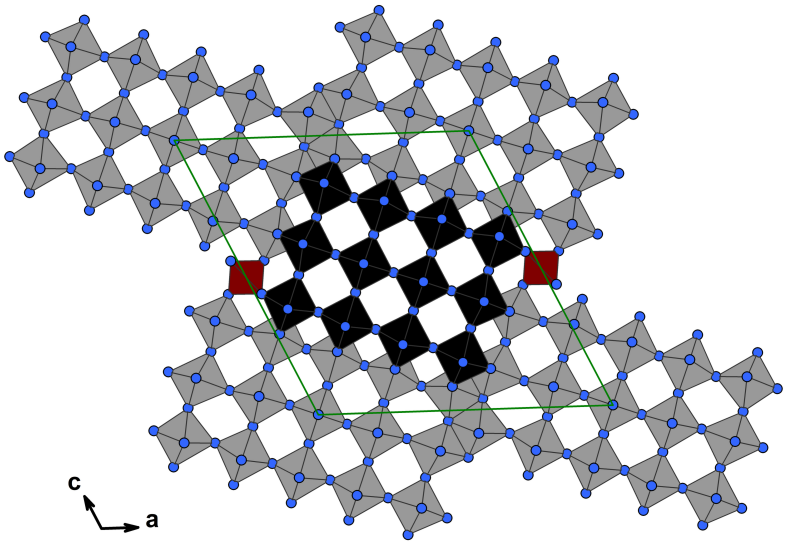

,

Figure 9: Crystal structure of monoclinic H-Nb_2O_5 with space group *P2/m*.[127] The 3×4 block of octahedrally coordinated Nb atoms is shown in black, the 3×5 block in light gray, while the tetrahedrally coordinated Nb atoms are drawn in red. Oxygen atoms are shown in blue and the unit cell in green.

Syntheses and Mechanochemistry

Typical precursors for the preparation of Nb_2O_5 are $NbCl_5$ or niobium alkoxides such as $Nb(OC_2H_5)_5$, which are then used for the preparation of Nb_2O_5 nanoparticles or thin films via a hydrothermal[128] or sol-gel[129-131] process or the Pecchini method, also known as the polymeric precursor method.[129, 132] In many cases, an annealing step is needed afterwards.

Mechanochemical approaches are rare in literature, but milling $NbCl_5$ and Na_2CO_3 for up to 6 h in a Spex Mixer mill yields Nb_2O_5 nanoparticles with an average size of 16 nm.[133]

In addition to solution-based approaches, some Nb_2O_5 polymorphs are easily prepared by thermal treatment of niobic acid or NbO_2 in air for several hours depending on the temperature (Figure 10).[124] Thermal oxidation of lower niobium oxides or even elemental niobium also results in the formation of Nb_2O_5.[134] In return, Nb_2O_5 can of course also be used as a starting material along with elemental niobium for the synthesis of reduced oxides NbO,[135, 136] NbO_2,[137]

and sub-stoichiometric ones such as $Nb_{12}O_{29}$[138, 139] using a high temperature reduction approach under hydrogen gas or vacuum.

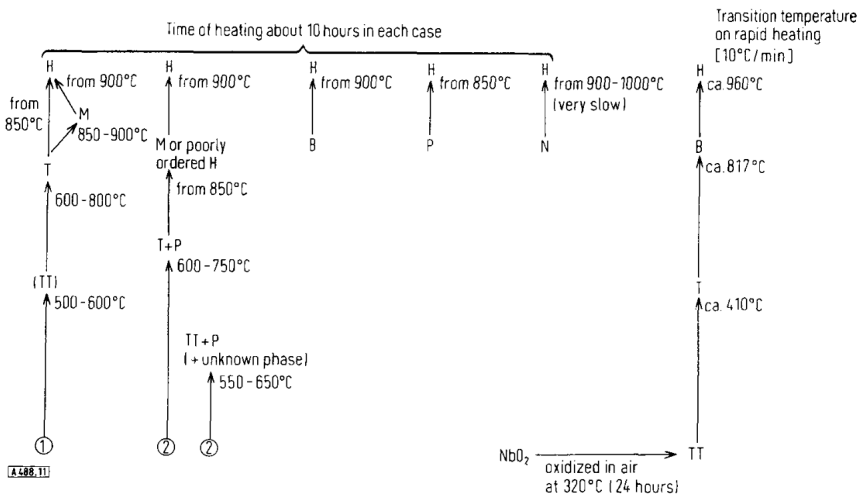

Figure 10: Thermal preparation of polymorphic phase transitions of Nb_2O_5. ① corresponds to washed amorphous niobic acid and ② corresponds to niobic acid with a high content of HCl remaining from the synthesis of niobic acid. H. Schäfer, R. Gruehn, F. Schulte, "The Modifications of Niobium Pentoxide", *Angew. Chem. Int. Ed.* **1966**, *1*, 40-52. Copyright Wiley-VCH Verlag GmbH.

In addition to the thermally induced polymorphic transformations of Nb_2O_5, they can also be triggered mechanochemically. Hibst and Gruehn first investigated the mechanochemical stability of several niobium oxides and observed that Nb_2O_5 polymorphs and sub-stoichiometric NbO_x phases ($2.4 < x < 2.5$) are not mechanochemically stable and transform into T-Nb_2O_5 at high milling intensities or TT-Nb_2O_5 under mild ones. In contrast, both NbO_2 and NbO do not transform during milling, but a partial oxidation to NbO_2 was detected for NbO after 8.5 h of milling.[140] In line with the results of Hibst and Gruehn, Ikeya and Senna obtained TT-Nb_2O_5 after milling amorphous Nb_2O_5 and H-Nb_2O_5 in a vibro-mill.[141, 142]

After performing a mechanochemical comproportionation reaction with Nb_2O_5 and Nb, Gaffet *et al.* reported the formation of NbO_2, but did not provide detailed information on the milling conditions.[143]

Properties and Applications

Due to its high stability, corrosion resistance and non-linear optical properties, Nb_2O_5 is used in many different applications such as humidity[144] and gas sensing[145, 146] or in optical switches.[147] However, the physical properties are strongly influenced by the polymorph and synthesis method. Therefore, the reported optical band gaps range from 3.1 eV and 3.9 eV,[148-150] while electrical conductivities and capacities range from 10^{-13} to 10^{-6} S cm^{-1},[149] and from

200 to 400 mA h g^{-1},[151-153] respectively. After intercalation of Li in H-Nb_2O_5 for example, Li^+ can be found in four-fold nonplanar, distorted tetrahedral and distorted square-pyramidal cavities.[127, 154] These properties make Nb_2O_5 also a suitable candidate as anode material in lithium-ion batteries,[151-153] and other electronic devices such as solid electrolytic capacitors,[155] memristors,[156] metal-insulator-metal tunnel diodes[157] and complementary metal-oxide-semiconductor devices[158]

1.2.3 Vanadium Oxides

1.2.3.1 The V-O System

Similar to niobium, the oxidation states of vanadium also ranges from +II to +V and many stable and metastable vanadium (sub)oxides are known (Figure 11).[159, 160] Notable thermodynamically stable compounds include vanadium dioxide (VO_2), divanadium trioxide (V_2O_3), divanadium pentoxide (V_2O_5), as well as the mixed valent Magnéli phase trivanadium pentoxide (V_3O_5), and the Wadsley phase trivanadium heptaoxide (V_3O_7).[161]

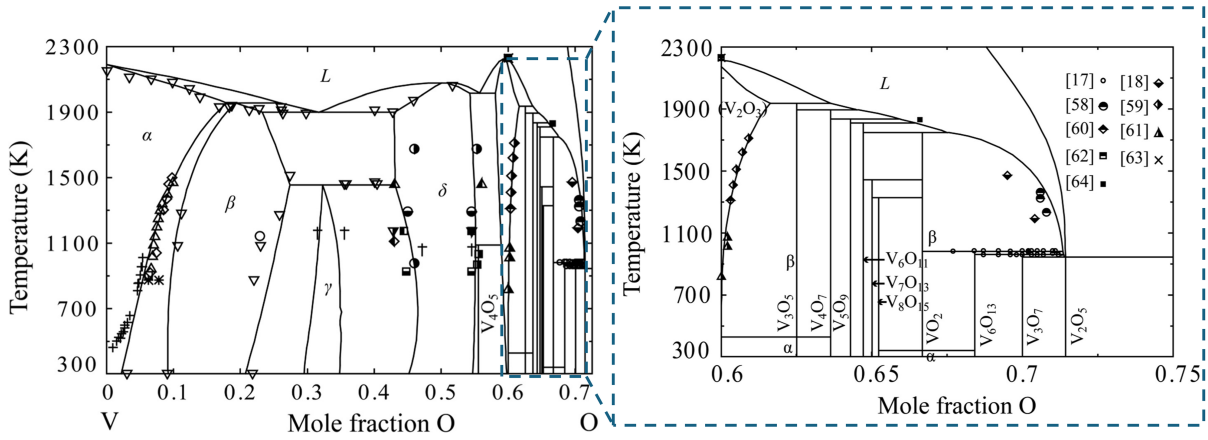

Figure 11: Phase diagram of the vanadium oxygen system (left) with a zoom of the region of the oxygen mole fraction from 0.6 to 0.75 (right). Adapted and reprinted from Z. Cao, S. Li, W. Xie, G. Du, Z. Qiao, "Critical evaluation and thermodynamic optimization of the V–O system", *Calphad* **2015**, *51*, 241-251 with permission from Elsevier.

1.2.3.2 The Polymorphic System of V_2O_5

Compared to Nb_2O_5, rather few polymorphic forms are known, including orthorhombic α-V_2O_5 (*Pmmn*), high-pressure phases β-V_2O_5 ($P2_1/m$) and δ-V_2O_5 ($C2/c$),[162] and metastable γ-V_2O_5 (*Pnma*), which can be obtained by (electro)chemical delithiation of γ-LiV_2O_5.[163] The most stable and widely used polymorph is α-V_2O_5 with lattice parameters of a = 357.1, b = 1154.4, and c = 438.3 pm.[164] It consists of layers of alternating VO_5 square pyramids stacked along

[001] (Figure 12a), with each square pyramid connected to a neighboring pyramid by corner sharing and to two pyramids by edge sharing within the layers (Figure 12b).

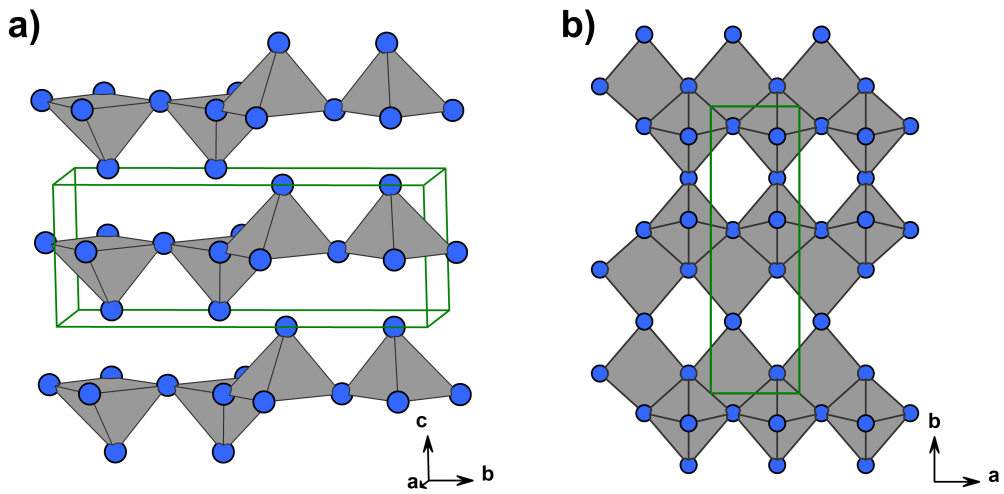

Figure 12: Crystal structure of α-V_2O_5 (*Pmmn*)[164] along (a) [100] and (b) [001]. Vanadium atoms are displayed in gray, oxygen atoms in blue and the unit cell in green.

Synthesis of V_2O_5 and Mechanochemistry

As with other transition metal oxides, V_2O_5 can be prepared via various well-established methods, including the sol-gel process,[165, 166] hydrothermal treatment,[167, 168] chemical and physical vapor deposition,[169-171] oxidation of elemental vanadium and lower vanadium oxides[172-174] or calcination of NH_4VO_3.[175] By tailoring the experimental conditions, different morphologies such as flowers,[167, 168] belts,[165, 170] wires[167, 169] and sheets[168] can be obtained, which in turn influence the materials properties and suitability for specific applications.

While there is no direct mechanochemical synthesis of V_2O_5 known to the best of my knowledge, Glushenkov *et al.* prepared V_2O_5 nanorods after milling commercial V_2O_5, followed by thermal annealing.[176] Similarly, Guimarães *et al.* claim the production of V_2O_5 nanoparticles by simply ball milling bulk V_2O_5.[177] In general, mechanochemical treatment of V_2O_5 does not lead to polymorphic phase transitions, but a decrease of the crystallite size down to ~10 nm accompanied by anisotropic strain broadening, typically described to occur along [001].[178-180] Extended milling has been demonstrated to also induce the partial formation of V^{3+} and V^{4+} due to oxygen loss,[181, 182] which, together with the anisotropy and higher surface area, results in enhanced catalytic activity for hydrocarbon oxidation.[183]

Even though the mechanochemical synthesis of V_2O_5 is rather unexplored, V_2O_5 has been used in numerous mechanochemical reactions for the preparation of lower vanadium oxides or even elemental vanadium, which is an important additive for high performance steels.[184] Takai *et al.*

were for example able to prepare VO_2 in only 3 h at room temperature by milling V_2O_5 with paraffin wax.[185] With carbon as a reducing agent, VO_2 is initially formed during milling, followed by a further reaction to V_2O_3. Due to the endothermic nature of a further reduction to VO or even elemental V, no reaction proceeds beyond V_2O_3 formation.[186] In contrast, Yang and McCormick successfully obtained elemental vanadium in a mechanically induced self-propagating reaction (see Chapter 1.2.4.3) using Mg, Al, and Ti as reducing agents.[187] Thus, by choosing the appropriate reducing agent, the formation of lower vanadium oxides can be effectively controlled.

Properties and Applications

Due to its versatile oxidation states, V_2O_5 is traditionally used as catalyst for the oxidation of numerous organic compounds,[188-190] but also on a large scale for the industrial production of sulfuric acid in the contact process.[191] While catalysis remains an important application of V_2O_5, many others have been explored. With its layered structure, a large interlayer spacing of ~4.4 Å, and a high theoretical capacity of 294 mA h g^{-1} for the insertion of two Li ions,[192] V_2O_5 is an excellent material for energy storage and conversion applications. These include lithium-[168, 193] and sodium-ion[192, 194] batteries, as described in a few reviews,[195, 196] as well as solid-state[195, 196] or redox flow batteries.[197] Furthermore, V_2O_5 exhibits electrochromic properties, meaning that the optical appearance changes as a response to an external stimulus, which was first discovered by Colton *et al.* in 1978.[198, 199] V_2O_5 can display both an anodic and cathodic electrochromic behavior with observable colors ranging from dark blue to yellow, making it a promising candidate for the fabrication of electrochromic devices.[200, 201] Moreover, as a semiconductor with a wide band gap of 2.3 eV and a good thermal stability, V_2O_5 is also suitable for use in solar cells,[202, 203] as well as gas sensing applications.[171, 204]

1.2.3.3 Alkali Metal and Alkaline Earth Metal Vanadates

Alkali Metal Vanadates

In addition to a rich vanadium-oxygen system, vanadium also forms a large variety of ternary vanadium oxides with alkali metals such as lithium and sodium. A total of around 20 and 15 different stoichiometric compounds are known to literature for Li and Na, respectively, with vanadium oxidation states ranging from +III to +V.[67] Due to the richness and complexity of these systems, only a brief overview of their general synthesis and application is given here. Detailed discussions of the crystal structures of relevant sodium vanadates can be found in Chapter 6.2. Despite the different ionic radii of lithium (76 pm) and sodium (102 pm),[205] the

crystal structures of Li and Na vanadates are closely related and many of the compounds with the same composition crystallize in the same crystal structure.

Alkali metal vanadates are typically prepared hydrothermally[206-208] or via solid state reactions of V_2O_5 or lower vanadium oxides such as VO_2 and V_2O_3 with the corresponding alkali metals, their oxides, or carbonates.[209-214] Due to the importance of the Na_2O-V_2O_5 sub-system in the roasting of vanadium slag,[215] the Na-V-O system has been more extensively studied than the Li-V-O one, particularly in the 1950s and 1970s. A strong exothermicity of the occurring reactions is frequently reported,[211, 216, 217] and mixtures of various vanadium oxides and sodium vanadates are commonly formed. A similar product mixture of different (lithium) vanadium oxides was also observed by Hagenmuller and Lesaicherre after investigating the reaction behavior of V_2O_5 with LiH at high temperatures.[218] Producing phase-pure alkali metal vanadates can therefore be challenging due to the complex nature of these systems.

In addition to the solution-based and high-temperature synthesis techniques mentioned earlier, some reports describe the formation of alkali metal vanadates via ball milling, but overall, literature remains limited. In 2011, Rojac *et al.* reported the mechanochemical formation of sodium metavanadate ($NaVO_3$), with vanadium in the oxidation state +V, through the reaction of V_2O_5 and Na_2CO_3 after 4 h of milling.[219] Meanwhile Haberkorn *et al.* showed that mechanochemical sodiation of V_2O_5 with Na_2S is possible, achieving a mean sodium content of $x = 0.3$ in $Na_xV_2O_5$.[220] However, in most ball milling studies, only a mechanochemical activation is performed or subsequent annealing is needed to obtain the desired product.[221-225] Most of the as-prepared vanadates are then further investigated for use as electrode material in lithium- and sodium-ion batteries and capacitors.[221-228] However, detailed application discussions are beyond the scope of this work.

Earth Alkaline Metal Vanadates

Regarding alkaline earth metal vanadates, fewer vanadates are known to literature compared to alkali metal vanadates. For example, in the Mg-V-O system, only around 10 different stoichiometric compounds can be found in the Pearson's Crystal Data database with vanadium oxidation states also ranging from +III to +V.[67] Given the particular significance of MgV_2O_4 in this work, other magnesium vanadates are not discussed.

MgV_2O_4 belongs to the spinel group and crystallizes in the cubic crystal system with space group $Fd\bar{3}m$ and a lattice parameter of 840.2 pm.[229] With the oxygen atoms forming a face-centered cubic structure, magnesium cations occupy 1/8 of the resulting tetrahedral sites, as

shown in purple in Figure 13, while half of the octahedral sites are filled by vanadium cations, as shown in gray in Figure 13.

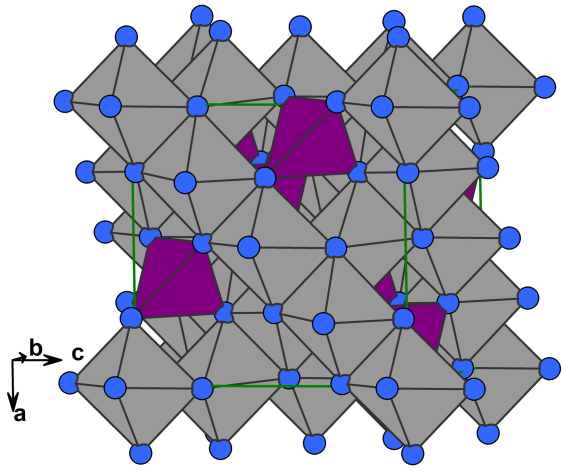

Figure 13: Crystal structure of spinel MgV_2O_4 with space group $Fd\bar{3}m$.[229] Polyhedra of octahedrally coordinated V atoms in MgV_2O_4 are shown in gray, ones of tetrahedrally coordinated Mg atoms are drawn in purple. Oxygen atoms are shown in blue and the unit cell in green.

Compared to other magnesium spinels such as $MgAl_2O_4$ and $MgFe_2O_4$, MgV_2O_4 has been studied less extensively and is typically prepared hydrothermally[230-232] or via solid-state reaction at high temperature.[233-236] To date, no study on the mechanochemical behavior or synthesis of MgV_2O_4 has been reported to the best of my knowledge.

MgV_2O_4 is an important intermediate in the reduction of V_2O_5 to elemental vanadium[230, 231, 236, 237] and is mainly investigated as a potential electrode material for magnesium-ion[230, 231, 236, 237] or zinc-ion batteries.[232] Studies have shown promising results for its use in magnesium-ion batteries, with capacities of 112 mA h g^{-1} for cactus-like MgV_2O_4[231] and 272 mA h g^{-1} at 0.2 A g^{-1} for urchin-like MgV_2O_4.[232]

1.2.4 Reduction of Transition Metal Oxides

1.2.4.1 Partial Reduction of Transition Metal Oxides and their Characterization

Partial Reduction of Transition Metal Oxides – Synthesis and Applications

In reduction reactions of transition metal oxides, the primary aim is usually to reduce all transition metal ions from their initial oxidation state to a specific lower oxidation state (e.g., from Ti^{4+} in TiO_2 to Ti^{3+} in Ti_2O_3). However, in some cases, performing a partial reduction, meaning that only a fraction of the metal ions are reduced (e.g., TiO_2 to TiO_{2-x}, with some Ti^{4+} reduced to Ti^{3+}) represents an intriguing pathway to alter the materials chemical and physical

properties through defect engineering.[238] To maintain charge neutrality of the solid, the partial reduction of the transition metal ion is accompanied by the introduction of defects such as oxygen vacancies.

A well-known example for successful defect engineering is the so-called black titania, which was first prepared by Chen *et al*. in 2011 after hydrogenation of commercially available white anatase-type TiO_2 for 5 days. In comparison to the pristine material, the obtained black oxide retained the same crystal structure, but exhibited a decreased optical band gap and a significantly enhanced photocatalytic activity for the degradation of methylene blue due the partial reduction of Ti^{4+} to Ti^{3+} and the presence of oxygen vacancies.[239] Because of this extraordinary enhancement of the photocatalytic performance, many synthesis routes and potential application areas have been explored since then, not only for TiO_2. Other synthesis approaches include annealing in oxygen-deficient environment[240, 241] or chemical reduction either at high temperatures or in solution-based processes. Hereby, metals such as magnesium[242, 243] or aluminum,[244, 245] but also the hydrides like $NaBH_4$,[246-250] CaH_2,[251, 252] and NaH[253] have been used as reducing agents. After the partial reduction, the as-prepared black oxides show an improved performance in photocatalytic dye degradation,[239, 244, 246, 247] hydrogen formation,[239, 242, 245, 250] and photoelectrochemical water splitting.[248, 251] In addition, they can also be used as high performance supercapacitors,[252] as electrode material for lithium-ion batteries[240] or as photoanodes for photocatalytic fuel cells.[249]

The alteration of physical and chemical properties after partial reduction are of course not native to TiO_2 and have also been applied to other transition metal oxides such as Nb_2O_5, which is also a wide-band gap semiconductor like TiO_2. Compared to the research field of black titania, the research area of black niobia is still rather unexplored. Typical reducing agents for high temperature synthesis of black niobia include Al[254, 255] and $NaBH_4$[256] to obtain high-performance materials for photoelectrochemical water-splitting and sodium-/potassium-ion batteries, respectively. Additionally, an annealing step at high temperatures, either under inert gas,[257] hydrogen,[258-260] or vacuum,[261] can also result in the partial reduction of Nb^{5+} to Nb^{4+} and the formation of oxygen-deficient Nb_2O_{5-x}.

Given the energy-consuming nature of the aforementioned approaches, the use of a more environmentally friendly method, such as ball milling, could prove advantageous. To date, the utilization of mechanochemistry for the synthesis of defective black transition metal oxides has not been explored extensively. While Zhou *et al.*[262] and Zhang *et al.*[263] enhanced the activity of TiO_2 for catalytic hydrogen evolution after milling with the non-conventional hydride TiH_2, the highly reactive alkali metals lithium and sodium have otherwise been explored as

mechanochemical reducing agents. In the latter experiments, TiO_2 was either ground in a simple pestle and mortar set-up with elemental lithium[264] or in a ball mill with a mixture of Na and NaCl[265] to avoid mixing issues due to the high ductility of sodium. Again, the black oxides demonstrated a better suitability for photocatalytic hydrogen evolution or as support for catalytic hydrogenation, compared to pristine TiO_2.

Characterization of partially reduced Transition Metal Oxides

To characterize optical and structural changes in these partially reduced oxides, a variety of characterization techniques can be employed, ranging from rather simple spectroscopic techniques such as UV-Vis spectroscopy to more sophisticated electron microscopy such as high-resolution transmission electron microscopy (HR-TEM), which are described in more detail for example in the review by Sarkar and Khan.[266] Of course, these characterization techniques can also be employed to analyze structural changes of other inorganic compounds after ball milling.

Defects disrupt the long-range ordering in the material, leading to structural disorder, which can be effectively investigated by Raman spectroscopy (Figure 14a). In materials with increased structural disorder and reduced crystallinity, Raman signals are significantly broadened compared to the pristine material. Some peaks might also be shifted, a phenomenon typically associated with local strain within the material.[267, 268] The presence of strain can be further confirmed through X-ray diffraction (XRD) and Rietveld refinement (see Chapter 1.3). Additionally, solid-state nuclear magnetic resonance (SS-NMR) spectroscopy can be employed to investigate the formation of structural disorder, as it probes the local environment of the investigated nucleus. Again, increasing structural disorder leads to a more inhomogeneous and disordered local environment, resulting in broader and less defined NMR signals.[269] While it is not necessarily possible to identify the origin of the signal, electron paramagnetic resonance (EPR) spectroscopy is also often applied for the characterization of black titania. In both NMR and EPR spectroscopy, the sample is subjected to a magnetic field and irradiated with radio frequency or microwave irradiation, respectively. While the spin of the nuclei is excited in NMR spectroscopy, EPR spectroscopy excites electronic spins. However, the sample must contain unpaired electrons to be EPR active. With fully oxidized transition metal oxides being typically diamagnetic and EPR-inactive, their partial reduction leads to the appearance of an EPR signal (Figure 14b) due to the formation of paramagnetic centers, which can for example be located on either single electron-trapped paramagnetic oxygen vacancies or reduced paramagnetic transition metal cations.[270] Their presence, as evidenced by the observed EPR

signal, clearly proves the successful partial reduction of the pristine oxide.[250, 252, 264] Thermogravimetric analysis (TGA) represents another method that can be used to detect oxygen vacancies. Although it has been used less frequently for characterizing black titania, several studies report successful application of TGA to analyze oxygen vacancies in oxidic compounds.[271-273] As shown for MoO_{3-x}, the defect concentration was determined by comparing the difference in mass changes upon heating the sample under inert gas and under air. A sample composition of $MoO_{2.87}$ was calculated.[271]

In addition to structural changes, partial reduction also alters the optical properties, resulting in an increased absorption of visible light (Figure 14c) and a decreased optical band gap.[244, 249, 264] Diffuse-reflectance UV-Vis spectroscopy (DRS UV-Vis) is a suitable method to study these changes in the solid powder. Using Kubelka-Munk function $F(R)$ and the Tauc relationship $(F(R)\ h\nu)^{\frac{1}{n}} = A(h\nu - E_g)$ with $h\nu$ being the photon energy, A is a proportionality constant, n a parameter indicating the type of band gap (n = 0.5 for direct and 2 for indirect allowed transitions),[274] the optical band gap E_g can be determined. For example, Ou *et al.* observed a decrease of the band gap from 3.2 to 3.0 eV for their synthesis of black titania.[264]

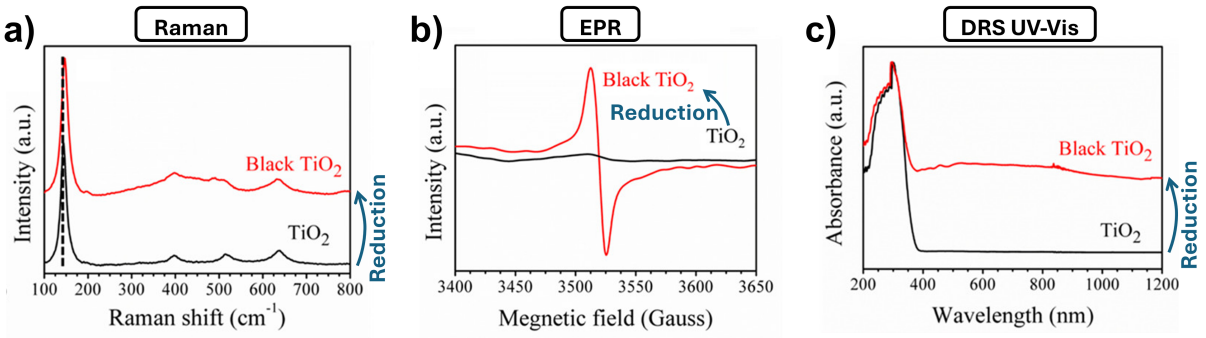

Figure 14: Change of the (a) Raman, (b) EPR and (c) DRS UV-Vis spectra after partial reduction, which leads to shifting of broadening of Raman signals, new EPR signals and an increased absorbance of visible light, respectively. The effects of a partial reduction are exemplary shown for the reduction of TiO_2 to black titania.[245] Adapted from H. Song, C. Li, Z. Lou, Z. Ye, L. Zu, "Effective Formation of Oxygen Vacancies in Black TiO_2 Nanostructures with Efficient Solar-Driven Water Splitting.", *ACS Sustainable Chem. Eng.* **2017**, *5*, 8982-8987 with permission from the American Chemical Society.

1.2.4.2 The use of Alkali and Alkaline Earth Metal Hydrides as Reducing Agents

While $NaBH_4$ has already been successfully used for the partial reduction of transition metal oxides such as TiO_2 and Nb_2O_5 (Chapter 1.2.4.1), binary alkali and alkaline earth metal hydrides represent another powerful class of reducing agents in inorganic chemistry with a standard potential of the redox pair H_2/H^- of –2.23 eV.[23] They have been utilized extensively in high

temperature reductions of numerous 3d transition metal oxides, particularly those with a perovskite or spinel structure.[275]

In 1999, Hayward *et al.* have shown the first topotactic reduction of $LaNiO_3$ to $LaNiO_2$ with NaH as reducing agent in an evacuated tube at 200 °C.[276] Since then, binary hydrides such as LiH, NaH, MgH_2, and CaH_2 have been employed as reducing agent in many topotactic reductions, typically conducted in ampules between 200 and 600 °C.[277-281] These studies have revealed that the relative reductive powers of different hydrides depend on the oxide. While NaH only shows a weak reactivity in the reduction of $BaTiO_3$ compared to CaH_2,[281] NaH demonstrates the highest reactivity for the reduction of Sr_2MnO_4.[279] Even if the reasons for the apparent different reactivities are complex and not fully understood, the desired reducing power for a specific oxide can be modulated by selecting the most suitable hydride.

Mechanistic pathways of the reduction with hydrides remain unresolved, with debates whether one ($H^- \rightarrow H^\bullet$) or two electrons ($H^- \rightarrow H^+$) are transferred from the hydride, and whether the reduction occurs via hydride ions or via hydrogen gas that is formed in situ during the thermal decomposition of the hydride.[278, 279, 281] In principle, an even more complex mechanism with a combination of both previously described effects appears possible. Interestingly, it seems that LiH often displays a more distinct and intricate reaction mechanism compared to other binary hydrides.[279, 281] Due to its small cationic radius, lithium can act as a second active species next to the hydride anion, as seen in the incorporation of Li during the reduction of $BaTiO_3$ with LiH,[282] an effect not observed with CaH_2, NaH, and MgH_2.[281]

In theory, instead of using alkali metal hydrides as reducing agents in high-temperature solid-state reactions, their elemental counterparts can alternatively be used as reducing agents. For example, depending on the transition metal oxide and the reaction conditions, Barker and Hooper *et al.* observed either the formation of reduced transition metal (oxides) along with alkali metal oxide as side product or different ternary alkali metal-containing oxides.[212, 283-286] Similarly, Qvick demonstrated the beneficial influence of sodium on the reduction of WO_3 due to the intermediate formation of tungsten bronzes.[287]

1.2.4.3 Mechanochemical reductions and mechanically induced self-propagating reactions

Mechanochemical reductions

The high stability of transition metal oxides typically requires the use of significant amounts of energy and elevated temperatures for their reduction. As previously stated, some studies report the preparation of their reduced counterparts in the ball mill, for example via mechanochemically induced comproportionation reactions as in the case of NbO_2[143] or by

choosing the appropriate reducing agent as for the formation of VO_2[185] or elemental vanadium starting from V_2O_5.[186, 187] Suitable reducing agents for mechanochemical reduction of oxides include group I and II metals[187, 288, 289] such as lithium and magnesium or main group elements[290-294] such as aluminum, silicon or carbon. In many cases, the transition metal is even obtained in its elemental form after milling. To the best of my knowledge, the use of alkali and alkaline earth metal hydrides as mechanochemical reducing agents for transition metal oxides has been studied even less. While several simple[295, 296] or complex[297] hydrides, boron hydrides,[298-300] or alanates[301-303] have already been prepared successfully via mechanochemical synthesis, some publications report also the use of alkali and alkaline earth metal hydrides for CO_2 conversion,[304] lithiation,[305] lithium-storage[306] or as a reducing agent for organic compounds.[307] Due to their high percentage of hydrogen, hydrides are mainly under investigation for improving their hydrogen storage properties.[308-311] In this context, Pukazhselvan *et al.* investigated the use of Nb doped MgO nanoparticles, obtained after milling Nb_2O_5 and MgH_2, for enhancing the hydrogen storage properties of MgH_2.[311] It is noteworthy that reduction reactions in ball mills are not confined to metal oxides. De Oliviera *et al.* prepared gold nanoparticles from AuCl with different (in)organic reducing agents, which exhibited divergent trends in terms of reductive strength compared to those observed in solution chemistry.[312] Meanwhile, Johnson Humphrey *et al.* prepared Ni(I) complexes from Ni(II) dichloride precursors after reaction with sodium,[313] while Gao *et al.* successfully reduced arenes with lithium in an air-tolerable milling process via a Birch reduction.[314]

Mechanically induced self-propagating reactions

Examination of the reaction energies of the above-described full reductions of transition metal oxides with Li, Mg, Al, and C reveal their highly exothermic nature, leading to the topic of mechanically induced self-propagating reactions (MSRs). MSRs are self-propagating reactions with an adiabatic temperature T_{ad} exceeding 1800 K that are induced during ball milling, as described in great detail by Lazlo Takacs.[315, 316] When the adiabatic temperature is unknown, T_{ad} can be estimated as the ratio of the reaction energy and the specific heat capacity of the reaction mixture.

Typically, mechanically induced self-propagating reactions can be divided into three phases. During the initial activation period, the reactants undergo mechanical activation and mixing during milling, which leads to a reduced particle size, increased surface area and defect formation. The duration of this phase varies significantly depending on the system and milling conditions and can range from a few minutes[65, 187, 317-319] to several hours.[64, 320] Once a critical

activation state is reached, instantaneous ignition occurs during which the reaction energy is suddenly released and the majority of the desired product forms. This combustion-like event is accompanied by sharp increases in temperature and pressure (Figure 15a), which can be detected using special milling equipment with build-in sensors (see Chapter 1.1.3). The final phase involves further milling to complete the reaction and produce a homogeneous product mixture.[315, 316]

In case of V_2O_5, MSRs have been observed for example during its reduction by Mg, Al and Ti to elemental vanadium[187] or during the formation of VC by ball milling V_2O_5, Mg and C.[318] During the mechanochemical co-reduction of V_2O_5 and TiO_2 with Al, which yielded a V-Ti alloy and intermetallic V_5Al_8, even the formation of thermites with milling balls trapped inside were observed (Figure 15b).[321] The occurrence of thermites, meaning large chunks of molten material despite the high melting points of inorganic materials, further underlines the harshness of such reactions.

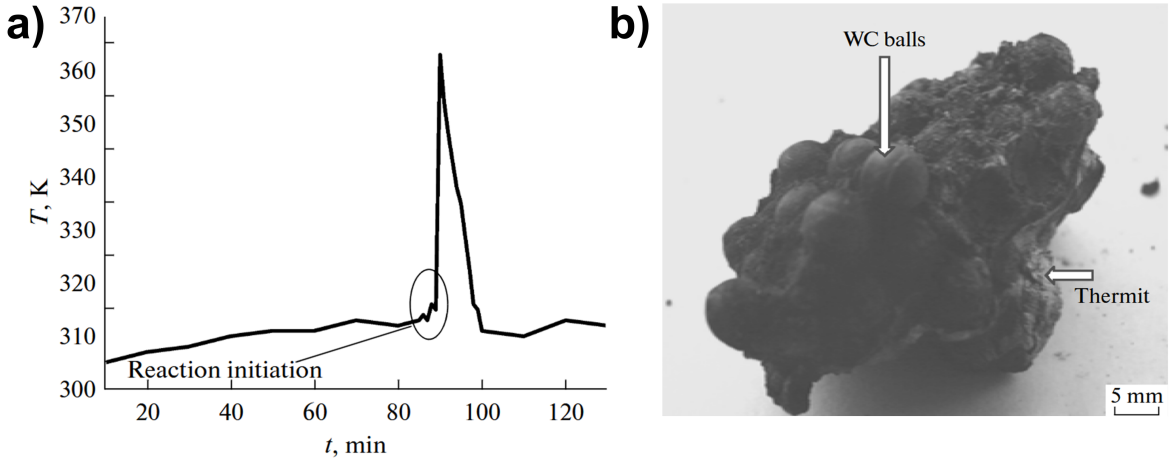

Figure 15: (a) Temperature evolution inside the milling jar during the coreduction of V_2O_5 and TiO_2 with Al and (b) WC milling balls embedded in a thermite after the reaction. Reprinted from Mukherjee, A., Krishnamurthy, N., „Phase evolution during mechanochemical coreduction of V_2O_5 and TiO_2 with Al“ *Int. J Self-Propag. High-Temp. Synth.* **2010**, *19*, 237-243 with permission from Springer Nature.

1.3 Characterization of Ball Milled Samples by Powder X-Ray Diffraction and Rietveld refinement

Since most inorganic solids are crystalline and their structures are well documented in databases such as the Pearson's Crystal Data database,[67] Powder X-ray Diffraction (PXRD) analysis combined with Rietveld refinement represents a powerful tool to quantify sample compositions and to assess microstructural changes. The following section provides a brief overview of the principles of PXRD and Rietveld refinement, along with the typical changes observed in

diffractograms after mechanochemical treatment, as these techniques serve as the primary characterization methods in this work.

PXRD analysis is based on the elastic scattering of (monochromatic) X-rays by the sample. A diffractogram is obtained after constructive interference between the irradiated X-rays and the periodic crystal according to the fundamental Bragg law (Equation 1.4), which was first introduced by Bragg and Bragg in 1913.[322] With n denoting the diffraction order, this law describes the relationship between the irradiated wavelength λ, the diffraction angle θ and the interplanar spacing d_{hkl}, which is directly linked to the dimension of the unit cell of the crystal structure.

$$n \cdot \lambda = 2 \cdot d_{hkl} \cdot \sin\theta \tag{1.4}$$

The position of each reflection is determined by the unit cell dimensions, while the observed intensities of each *hkl*-reflection I_{hkl} are proportional to the square of the absolute value of the structure factor F_{hkl} (Equation 1.5). With f_i being the atomic scattering factor (characteristic for each element), F_{hkl} is the sum over all amplitudes scattered by n atoms on a given lattice plane *hkl* (Equation 1.6). The observed relative intensities are thus directly related to the type and position of all atoms in the unit cell, resulting in a unique diffraction pattern for each distinct compound. This enables both phase identification and structural analysis.

$$I_{hkl} \sim |F_{hkl}|^2 \tag{1.5}$$

$$F_{hkl} = \sum_{i=1}^{n} f_i \cdot e^{2\pi i(hx_i + ky_i + lz_i)} \tag{1.6}$$

PXRD analysis does not only allow a qualitative assessment of the sample composition based on the positions and relative reflection intensities, but also enables quantitative analysis, including quantification of phases with weight percentages as low as 1-2%. The detected reflection profiles $Y(2\theta)$ are comprised of contributions from three distinct sources: the physical properties of the sample S, the emission profile of the X-ray source W and the geometrical constitution of the beam path G (Equation 1.7). To account for instrumental line broadening, the fundamental parameters approach can be used,[323, 324] which is implemented in powerful refinement programs such as Topas 5.0.[325]

$$Y(2\theta) = (W \otimes G) \otimes S \tag{1.7}$$

One of the most powerful techniques for such quantitative phase analysis is the so-called Rietveld refinement, developed by Hugo Rietveld in the 1960s.[326, 327] This method is a least-square mathematical approach based on minimizing the weighted squares of sums between the intensity of every point y_i(obs) in the experimental diffraction pattern and every corresponding calculated intensity y_i(calc) (Equation 1.8).[328] The weight w_i can be expressed as the inverse of the estimated standard deviation of the ith measurement point.[324]

$$S_y = \sum_i w_i \cdot \left(y_i(obs) - y_i(calc)\right)^2 = \sum_i \frac{1}{\sigma_i^2} \cdot \left(y_i(obs) - y_i(calc)\right)^2 \rightarrow Minimum \tag{1.8}$$

The quality of the performed Rietveld refinement can be evaluated using different figures of merit. One of the most important parameters is the R_{wp} value, which is defined as the square root of the minimized weighted squares of sums between y_i(obs) and y_i(calc) divided by the weighted sum of the squared observed intensities (Equation 1.9). In an ideal scenario, this value would be minimal, approaching the expected R-factor (R_{exp}), which represents the best achievable R_{wp} value for the specific refinement with a given number of used data points N and a number of refined parameters P (Equation 1.10). By calculating the ratio of the weighted profile R-factor R_{wp} and the expected R-factor R_{exp}, the goodness of fit (GOF) parameter is obtained, which is ideally close or equal to one for an excellent refinement (Equation 1.11).

$$R_{wp} = \sqrt{\frac{\sum_i w_i \cdot \left(y_i(obs) - y_i(calc)\right)^2}{\sum_i w_i \cdot \left(y_i(obs)\right)^2}} \tag{1.9}$$

$$R_{exp} = \sqrt{\frac{N - P}{\sum_i w_i \cdot \left(y_i(obs)\right)^2}} \tag{1.10}$$

$$GOF = \frac{R_{wp}}{R_{exp}} \tag{1.11}$$

In addition to determining the quantitative sample composition, Rietveld refinement also allows for microstructural analysis, namely the crystallite size and strain, which influence the width of

the observed reflections. Given that polycrystalline samples consist of numerous crystallites with finite sizes and often contain local imperfections such as point defects and dislocations, leading to increased strain, the theoretically expected infinitively sharp reflections are never observed in diffraction experiments. Instead, the measured reflections are more or less broadened depending on the size of the crystallites and the severity of the strain, which can cause asymmetric broadening.

In 1918, Scherrer first introduced a formula to calculate the crystallite size L as a function of the irradiated wavelength λ and the Bragg angle θ, the breadth of the reflection β_{size} and the Scherrer constant K under the assumption that broadening purely originates from crystallite sizes (Equation 1.12).[329] While the breadth of a reflection was initially taken at the full width at half maximum (FWHM), the integral breadth (IB), meaning the ratio of the peak area and the peak height, is often taken nowadays.[330]

$$L = \frac{K \cdot \lambda}{\beta_{size} \cdot \cos\theta} \tag{1.12}$$

It is important to note that sample broadening can also originate from the presence of strain ϵ, which exhibits a tangent dependence from the diffraction angle (Equation 1.13),[324] meaning that line broadening due to microstrain becomes especially dominant at high diffraction angles.

$$\epsilon = \frac{\beta_{strain}}{4 \cdot \tan\theta} \tag{1.13}$$

Due to a strong correlation of crystallite size and strain, it is challenging to clearly distinguish between the contribution of both effects towards line broadening. The first attempts to separate both phenomena were made by Williamson and Hall in 1953.[331] They assumed that the total line broadening β_{total} can be deconvoluted into the sum of the broadening originating from the crystallite size β_{size} and the strain β_{strain} (Equation 1.14). Together with equations 1.12 and 1.13, an equation of a straight line is obtained, which allows the derivation of β_{strain} from the slope and of β_{size} from the y-axis interception after plotting $\beta_{total} \cdot cos\,\theta$ against $sin\,\theta$ (Equation 1.15).

$$\beta_{total} = \beta_{size} + \beta_{strain} \tag{1.14}$$

$$\beta_{total} \cdot \cos\theta = \frac{K \cdot \lambda}{L} + 4 \cdot \epsilon \cdot \sin\theta \tag{1.15}$$

Based on the previously mentioned fundamental parameters approach to account for instrumental line broadening, Rietveld refinement represents an even more powerful method to describe the microstructure of a sample and to quantify the sample composition, provided that a valid refinement model is in place. Depending on the data quality, even phases with a weight percentage of 2% or less can be quantified. To overcome challenges with describing the form of the reflection with purely Lorentzian or Gaussian shape, Double-Voigt functions are nowadays used in Topas. In principle, crystallite sizes of asymmetric crystallites can also be determined for example with the Stephens model,[332] which will not further discussed hereafter as it was not necessary for the present work.

Typically, high energy ball milling leads to a decrease of the crystallite size down to the nanometer range and increasing strain due to the continuous impact of the milling balls,[21, 333, 334] resulting in significant broadening of the reflections. In addition, harsh or prolonged milling of oxides often produces strained, poorly crystalline or even amorphous samples with increased structural disorder and defects.[48, 49] Since structural disorder cause local lattice distortions, both the intensities and the shape of reflections can be affected. However, developing a refinement model that adequately accounts for these structural changes is very challenging, making the refinement of heavily milled samples extremely complex or even impossible.
Since amorphous phases cannot be directly characterized by PXRD analysis but are often present in samples after harsh milling, their quantification can be achieved using the well-established internal standard method. For this, a known weight percentage ($wt\%_{of\ spiked}$) of a well crystalline, fine-grained compound such as Si, SiO_2, Al_2O_3 and CaF_2 is homogeneously mixed with the sample. Using equation 1.16 and the refined amorphous phase percentage ($wt\%_{in\ spiked\ sample}$) determined in Topas in the subsequent Rietveld refinement, the real percentage of amorphous phase in the sample ($wt\%_{original\ sample}$) can be calculated.

$$\mathrm{wt\%_{original\ sample}} = \frac{\mathrm{wt\%}_{in\ spiked\ sample}}{1 - \mathrm{wt\%}_{of\ spiked}} \tag{1.16}$$

2 Research goals

The aim of this work is to explore the potential of mechanochemistry as a synthetic route for the reduction of transition metal oxides. In particular, alkali metals, binary alkali metal hydrides, and magnesium are investigated as reducing agents.

Transition metal oxides are a very promising class of materials for application in photocatalysis, sensors, and energy storage due to their versatile oxidation states, which directly influence the properties of the respective oxide. However, conventional reduction methods that lower the oxidation state of transition metal ions typically require high temperatures and are energy intensive. These methods also often yield products with relatively large crystallite sizes. In contrast, mechanochemistry offers an environmentally friendly approach at room temperature that aligns with the 12 Principles of Green Chemistry. Moreover, additional defect formation during milling can further enhance the chemical and physical properties of the final material.

The aim of this thesis is to explore the feasibility of facile and rapid reduction reactions in a ball mill and to advance mechanochemistry as a greener synthesis approach in inorganic chemistry. More specifically, this work shall systematically investigate the mechanochemical reduction of transition metal oxides at room temperature and the influence of different milling parameters on the final sample composition and material properties.

Synthesis of black TiO_2 and black Nb_2O_5 in the ball mill

Partial reduction and defect formation can significantly enhance the chemical and physical properties of transition metal oxides. The formation of partially reduced black titania and black niobia by mechanochemical reduction of TiO_2 and Nb_2O_5 with alkali metal hydrides LiH and NaH is therefore investigated. In addition to studying the influence of milling time and hydride concentration on the degree of reduction via EPR spectroscopy, structural and optical changes are evaluated by PXRD and TGA measurements, as well as ^{6}Li SPE-MAS NMR, Raman and UV-Vis spectroscopy. The effect of the mechanochemical treatment on the photocatalytic properties will be investigated (results published).

Mechanochemical reaction of V_2O_5 with alkali metal hydrides and their elemental counterparts

Given the wide range of literature known lower vanadium oxides and the richness of the ternary system Na-V-O, the reaction behavior of V_2O_5 with NaH as reducing agent under mechanochemical conditions is systematically studied, focusing on the influence of hydride concentration and milling time. Quantum mechanical DFT calculations using the VASP program package are performed to support and further understand the experimental results. Since elemental alkali metals are theoretically even stronger reducing agents than the respective hydrides, the mechanochemical reduction of V_2O_5 with NaH is expanded to the reducing agents Na, LiH, and Li and differences in the reaction behavior are elucidated (results with NaH published; results with Na, LiH and Li unpublished).

Mechanochemical synthesis of MgV_2O_4 from different reactant combinations

Lastly, the mechanochemical synthesis of spinel-type MgV_2O_4, a promising battery material, is investigated for the first time. Supported by quantum mechanical DFT calculations, the feasibility of MgV_2O_4 formation with different reactant combinations is explored. The effect of ball milling on the crystal structure is assessed by PXRD and EPR analysis, while the electrochemical properties are studied by electrochemical impedance spectroscopy (results published).

3 Results and Discussion

3.1 Black Titania and Niobia within Ten Minutes – Mechanochemical Reduction of Metal Oxides with Alkali Metal Hydrides

This study investigates the reduction of the transition metal oxides TiO_2 and Nb_2O_5 with the powerful and readily available reducing agents NaH and LiH in a straightforward and rapid high energy ball milling approach. Within 10 min of milling, both oxides are partially reduced to their black counterparts TiO_{2-x} and Nb_2O_{5-x}, while the crystal structures of the pristine oxide are retained. In literature, these partially reduced black transition metal oxides show extraordinary electronic and photocatalytic properties,[245, 247, 251] which are typically achieved through energy-intensive, high temperature treatment.[240-247] This study demonstrates that such materials can also be obtained via a rapid ball milling process at room temperature.

Both the milling time and hydride concentration strongly influence the outcome of the mechanochemical reduction. In general, longer milling times and higher amounts of the reducing agent resulted in a higher degree of reduction of the transition metal ions. Notably, LiH exhibits a higher reducing power than NaH, as evidenced by a higher degree of reduction of Ti^{4+}/Nb^{5+} to Ti^{3+}/Nb^{4+} and an increased formation of unpaired electrons, as confirmed by EPR spectroscopy.

While PXRD measurements and subsequent Rietveld refinements show that the crystal structures of the pristine oxides are retained, LiH reduction also leads to the formation of cubic $Li_{0.5}Ti_{0.5}O$ in the case of TiO_2 and Li intercalation in Nb_2O_5 due to the smaller ionic radius of Li^+ (76 pm) compared to Na^+ (102 pm). The incorporation of lithium is further confirmed by ICP-MS measurements and ^{6}Li solid-state NMR spectroscopy. The latter also indicates substantial structural disorder, as evidenced by featureless and broadened NMR signals. For TiO_2 reduced with LiH for 30 or 60 min, an additional interaction of the paramagnetic Ti^{3+} ions with the Li nucleus can be seen. The presence of structural disorder and defects is consistent with the results of Raman spectroscopy as well as with UV-Vis spectroscopy, which show a decrease of the band gap of up to 0.4 eV. Due to the presence of these defects, the synthesized materials exhibit a significantly better photocatalytic performance in the degradation of methylene blue compared to the pristine oxides under illumination under both UV and visible light illumination (Figure 16).

The results of this study were published:
A. Michaely, O. Janka, E. C. J. Gießelmann, R. Haberkorn, H. T. A. Wiedemann, C. W. M. Kay, G. Kickelbick, Black Titania and Niobia within Ten Minutes – Mechanochemical Reduction of Metal Oxides with Alkali Metal Hydrides. *Chem. Eur. J.* **2023**, 29, e202300223. DOI:10.1002/chem.202300223

The publication is reproduced with permission from Wiley-VCH.

Anna Michaely carried out the experimental work, the majority of sample characterization and data interpretation, as well as the preparation of the original draft of the publication. Elias Gießelmann performed the NMR measurements, their interpretation and assisted with editing the manuscript. Haakon Wiedemann conducted the EPR spectroscopy measurements and further contributed with their interpretation and editing of the manuscript along with Christopher Kay. Oliver Janka and Robert Haberkorn assisted with scientific ideas, interpretation, and discussions of the acquisitioned data, as well as editing of the manuscript. Guido Kickelbick has contributed with scientific ideas, supervision, discussions of the results, and improvements of the final manuscript.

This publication builds upon promising results obtained during the master thesis of Anna Michaely, which focused on the mechanochemical reduction of Nb_2O_5 with LiH and $NaBH_4$.[335] During the PhD thesis, these reduction studies were extended to TiO_2 as an additional transition metal and NaH as a further reducing agent. Moreover, due to a change in the washing procedure, all experiments reported in this publication were conducted during the PhD thesis (including the reduction of Nb_2O_5 with LiH). In addition, further characterization methods have been applied, and photocatalytic degradation studies were carried out.

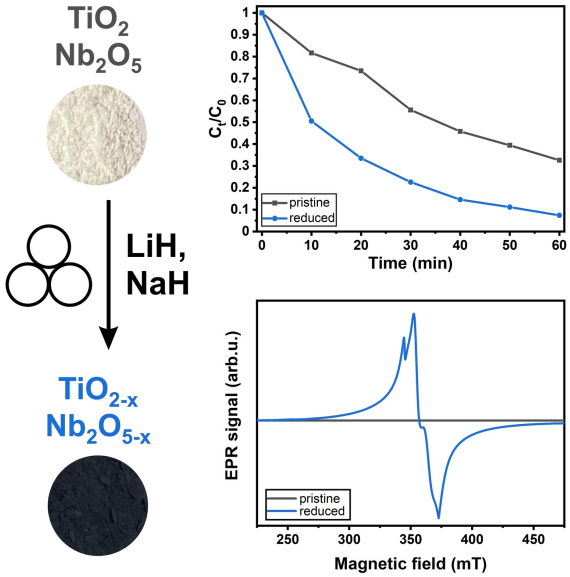

Figure 16: Table of contents graphic – Partial reduction of TiO_2 and Nb_2O_5 with LiH and NaH resulting in the formation of paramagnetic species due to the reduction of Ti^{4+} and Nb^{5+} and in an enhanced performance for the photocatalytic degradation of methylene blue.[336]

Chemistry–A European Journal
Research Article
doi.org/10.1002/chem.202300223
Chemistry Europe
European Chemical Societies Publishing
www.chemeurj.org

Black Titania and Niobia within Ten Minutes – Mechanochemical Reduction of Metal Oxides with Alkali Metal Hydrides

Anna Michaely,[a] Oliver Janka,[a] Elias C. J. Gießelmann,[a] Robert Haberkorn,[a] Haakon T. A. Wiedemann,[b] Christopher W. M. Kay,[b, c] and Guido Kickelbick*[a]

Abstract: Partially or fully reduced transition metal oxides show extraordinary electronic and catalytic properties but are usually prepared by high temperature reduction reactions. This study reports the systematic investigation of the fast mechanochemical reduction of rutile-type TiO_2 and H-Nb_2O_5 to their partially reduced black counterparts applying NaH and LiH as reducing agents. Milling time and oxide to reducing agent ratio show a large influence on the final amount of reduced metal ions in the materials. For both oxides LiH shows a higher reducing potential than NaH. An intercalation of Li^+ into the structure of the oxides was proven by PXRD and subsequent Rietveld refinements as well as ^{6}Li solid-state NMR spectroscopy. The products showed a decreased band gap and the presence of unpaired electrons as observed by EPR spectroscopy, proving the successful reduction of Ti^{4+} and Nb^{5+}. Furthermore, the developed material exhibits a significantly enhanced photocatalytic performance towards the degradation of methylene blue compared to the pristine oxides. The presented method is a general, time efficient and simple method to obtain reduced transition metal oxides.

Introduction

The partial reduction of transition metal oxides (TMO) results in an increase in oxygen vacancies and subsequently in materials with altered electronic properties compared to the original oxides, leading to extraordinary changes in their chemical and physical behavior.[1] A prominent example is the so-called black titania, which was first obtained by Chen et al. via hydrogenation of TiO_2 for 5 days.[2] Due to the introduction of defects and the partial reduction of the Ti^{4+} cations, the material exhibits enhanced photocatalytic activities compared to the pristine oxide. Since then, defect engineering by full or partial reduction of metal ions has become a growing field of research. Today black Nb_2O_{5-x},[3] ZrO_{2-x},[4] WO_{3-x},[5] V_2O_{5-x},[6] and MoO_{3-x}[7] are other prominent examples of this class of materials. Compared to the pristine oxides, the defect-rich counterparts usually exhibit enhanced light absorption[4] as well as improved photocatalytic[6,8] and photoelectrochemical (PEC)[3,9] performance. Besides gas phase hydrogenation,[2,8b] they can also be prepared by annealing at high temperatures in an oxygen-deficient atmosphere,[10] or via chemical reductions, for example, with Mg,[11] Al,[3] or $NaBH_4$.[8a,12] Mechanochemical reduction can lower the required temperatures and therefore the energy consumption in the preparation of such materials. Furthermore, mechanochemical reactions are often faster and additional defects are introduced solely by the impact of the ball milling process, which can also increase the chemical reactivity of the final material. To the best of our knowledge, few mechanochemical approaches for the partial reduction of transition metal oxides have been investigated. Often, the reduction is carried out using highly reactive alkali metals, such as Na[13] or Li[14] or non-conventional hydrides such as TiH_2.[15]

In our study, we used LiH and NaH as readily available alkali metal hydrides and powerful reducing agents in the fast solventless mechanochemical reduction of TiO_2 and Nb_2O_5 at room temperature. While Li^+ (76 pm) has a smaller cationic radius compared to Na^+ (102 pm),[16] NaH exhibits a lower enthalpy of formation and hence a lower stability and thus higher reactivity of NaH ($-56.3\ kJ\,mol^{-1}$) compared to LiH ($-90.5\ kJ\,mol^{-1}$).[17] It can therefore be expected that both hydrides have a different reactivity for the reduction of TMO or reaction behavior such as the involvement of the alkali metal ion during the reaction, which is systematically studied below.

[a] A. Michaely, Dr. O. Janka, E. C. J. Gießelmann, Dr. R. Haberkorn, Prof. Dr. G. Kickelbick
Inorganic Solid-State Chemistry
Saarland University
Campus, Building C4.1, 66123 Saarbrücken (Germany)
E-mail: guido.kickelbick@uni-saarland.de
[b] H. T. A. Wiedemann, Prof. Dr. C. W. M. Kay
Physical Chemistry and Didactics of Chemistry
Saarland University
Campus, Building B2.2, 66123 Saarbrücken (Germany)
[c] Prof. Dr. C. W. M. Kay
University College London
London Centre for Nanotechnology
17–19 Gordon Street, London WC1H 0AH (UK)

Supporting information for this article is available on the WWW under https://doi.org/10.1002/chem.202300223

© 2023 The Authors. Chemistry - A European Journal published by Wiley-VCH GmbH. This is an open access article under the terms of the Creative Commons Attribution Non-Commercial License, which permits use, distribution and reproduction in any medium, provided the original work is properly cited and is not used for commercial purposes.

© 2023 The Authors. Chemistry - A European Journal published by Wiley-VCH GmbH

Chemistry–A European Journal
Research Article
doi.org/10.1002/chem.202300223
Chemistry Europe
European Chemical Societies Publishing

TiO_2 was chosen for the experiments as it is the most studied oxide for photocatalysis and defect engineering. A lot of studies use anatase-type TiO_2 ($I4_1/amd$) or commercially available P25 due to their high photocatalytic activity. We chose the photocatalytically less active rutile[18] modification ($P4_2/mnm$) for our study because it has a higher mechanical stability than anatase.[19] Similar to TiO_2, H-Nb_2O_5 is also a stable wide-band gap *n*-type semiconductor with $E_g = 3.1$ eV. It is mainly investigated for use in sensors and numerous electronic devices, but there are also some reports on the application of Nb_2O_5 in dye-sensitized solar cells[20] and other photocatalytic applications.[21] Thus, it is worth to further investigate Nb_2O_5 as a potentially promising alternative for TiO_2 for photocatalytic applications. In the following, the influence of the type of reducing agent, milling time and composition on the photocatalytic activity of mechanochemically prepared TiO_2 and Nb_2O_5 is systematically investigated.

Results and Discussion

Crystal chemistry

It is known from the literature that the reduction of oxides with LiH at high temperatures can lead to the incorporation of Li into the oxides, for example, in the reaction of LiH with $BaTiO_3$[22] or Sr_2MnO_4.[23] Therefore, it seems possible that Li is also to some extend inserted into TiO_2 and Nb_2O_5 during the mechanochemical reduction. To facilitate the following discussion about the possible Li intercalation, the crystal chemistry of (lithiated) TiO_2 and Nb_2O_5 will be discussed briefly.

Rutile-type TiO_2 crystallizes in the tetragonal crystal system with space group $P4_2/mnm$ with lattice parameters of $a = 458.0$ pm and $c = 297.0$ pm.[24] In the crystal structure, each Ti^{4+} cation is octahedrally surrounded by oxide anions. These TiO_6 octahedra form chains along [001] via *cis*-edge sharing, the remaining two corners are linked to adjacent strands. Upon insertion of Li, either the tetra- or octahedral sites are occupied (Figure 1a). Using neutron diffraction measurements, Borghols et al. showed that the rutile structure is retained up to a maximum of $Li_{0.07}TiO_2$ ($a = 461.9$ pm, $c = 295.4$ pm).[25] It was shown that the occupation of the tetrahedral sites is energetically favored at low temperatures (10 K), while the occupation of the octahedral sites becomes more favorable at room temperature. For even higher Li contents, for example, $Li_{0.5}Ti_{0.5}O$ the cubic NaCl-type structure ($Fm\bar{3}m$, $a = 414.0$ pm)[26] is observed.[27] Both Li and Ti are octahedrally coordinated by the oxide anions and share the Wyckoff position *4a* (Figure 1b).

For Nb_2O_5 several polymorphs, depending on the synthesis temperature, have been reported. The monoclinic high temperature phase H-Nb_2O_5 crystallizes with space group $P2/m$ and lattice parameters of $a = 1933.0$ pm, $b = 382.3$ pm, $c = 2032.2$ pm and $\beta = 115.8°$.[28] The Wadsley-Roth phase consists of blocks formed by 3×5 and 3×4 [NbO_6] octahedra. These are connected by common corners within a block; however, edge sharing is observed between these entities. Finally, the tetrahedrally coordinated niobium site in H-Nb_2O_5 is only half-occupied.[29] Different lithiated Nb-oxides have been described for example, by Cava et al.[28] who identified five cavities in H-Nb_2O_5. Catti and Ghaani[30] characterized lithiated H-Nb_2O_5 ($Li_{1.714}Nb_2O_5$) via neutron diffraction experiments and localized the Li^+ cations in four-fold nonplanar, distorted tetrahedral and distorted square-pyramidal voids (Figure 1c), in line with the positions proposed by Cava et al. However, the localization of the Li atoms leads to a reduction in symmetry (*P2*, $a = 1913.2$ pm, $b = 413.5$, $c = 2014.2$ pm, $\beta = 119.57°$).[30]

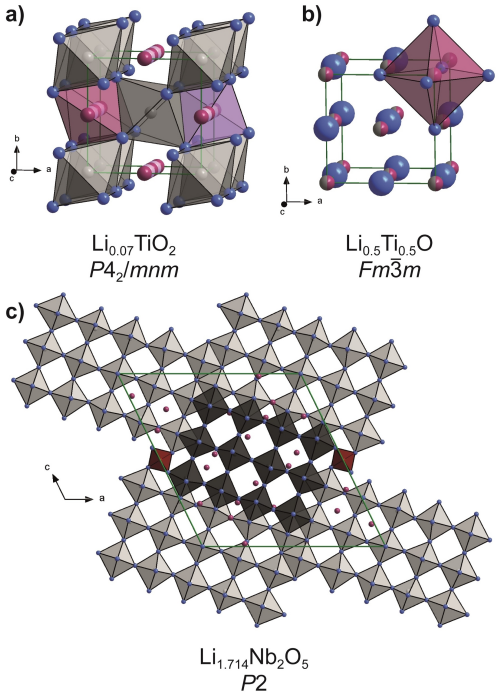

Figure 1. (a) Crystal structure of lithiated rutile-type $Li_{0.07}TiO_2$,[25] tetrahedrally coordinated Li atoms are shown in purple, octahedrally coordinated Li atoms are pink, Ti atoms are shown in gray and oxygen atoms in blue. (b) Crystal structure of NaCl-type $Li_{0.5}Ti_{0.5}O$,[26] Li atoms are purple, Ti atoms are shown in gray and oxygen atoms in blue. (c) Crystal structure of lithiated H-Nb_2O_5.[30] The 3×4 block of octahedrally coordinated Nb atoms in H-Nb_2O_5 is shown in dark gray, the 3×5 block in light gray, the tetrahedrally coordinated Nb atoms are drawn in red. The space groups are given.

Optical color change after ball milling

The partial reduction of TiO_2 and Nb_2O_5 by a mechanochemical route was performed by milling the TMO with *n* equivalents of LiH and NaH ($n = 0.5$, 1 and 2) for 10, 30, and 60 min at a fixed milling speed of 300 rpm. In the following, the samples are denoted as *NM_n:m_t*. The first letter being T for TiO_2 or N for Nb_2O_5, the second letter corresponds to the alkali metal hydride (N = NaH, L = LiH), while *n* and *m* represent the number of

© 2023 The Authors. Chemistry - A European Journal published by Wiley-VCH GmbH

Chemistry–A European Journal | Research Article
doi.org/10.1002/chem.202300223
Chemistry Europe
European Chemical Societies Publishing

equivalents of TiO_2/Nb_2O_5 and the hydride, respectively. Finally, *t* represents the milling time in minutes.

After only 10 minutes of ball milling at room temperature, a visually perceptible color change of the powders from white to light gray in the case of TiO_2 or brownish-gray to dark blue-black for Nb_2O_5 was observed. The obtained coloration is clearly depending on the amount of hydride added (Figure 2). The observed coloration of the samples after ball milling is most likely caused by the reduction of Ti^{4+} to Ti^{3+}[31] and of Nb^{5+} to Nb^{4+}.[32] However, for reasons of electroneutrality, the reduction must be either accompanied by the intercalation of alkali metal ions or the formation of oxygen vacancies, which also can give rise to color centers.[10b] Also a combination of both effects seems possible. Therefore, ball milling of the oxides in the presence of the reducing agents should produce various types of defects in the compounds. For both oxides, the milled powders have a darker color when LiH was used as the reducing agent compared to samples reduced under the same conditions applying NaH. Usually, NaH would be expected to have a higher reductive power and therefore we expected the darker color in the corresponding samples. This assumption is based on the size difference of the alkali metal ions (Li^+: 76 pm, Na^+: 102 pm)[16] and on the lower enthalpy of formation and thus also the lower stability and thus higher reactivity of NaH ($-56.3\ kJ\,mol^{-1}$) compared to LiH ($-90.5\ kJ\,mol^{-1}$).[17] It has already been reported that Li-containing reducing agents can behave differently due to the incorporation of Li into the oxide,[22] which could also be the reason for the apparent higher reactivity of LiH in our study.

With the EASY GTM system for the Fritsch Pulverisette 7 *premium line*, we can monitor the development of temperature and pressure in the grinding bowl. A continuous increase in pressure up to several bar can be observed, which is due to the development of hydrogen with increasing milling time. At the same time, the temperature also increases, but remains below 35 °C (Figure S1, Supporting Information).

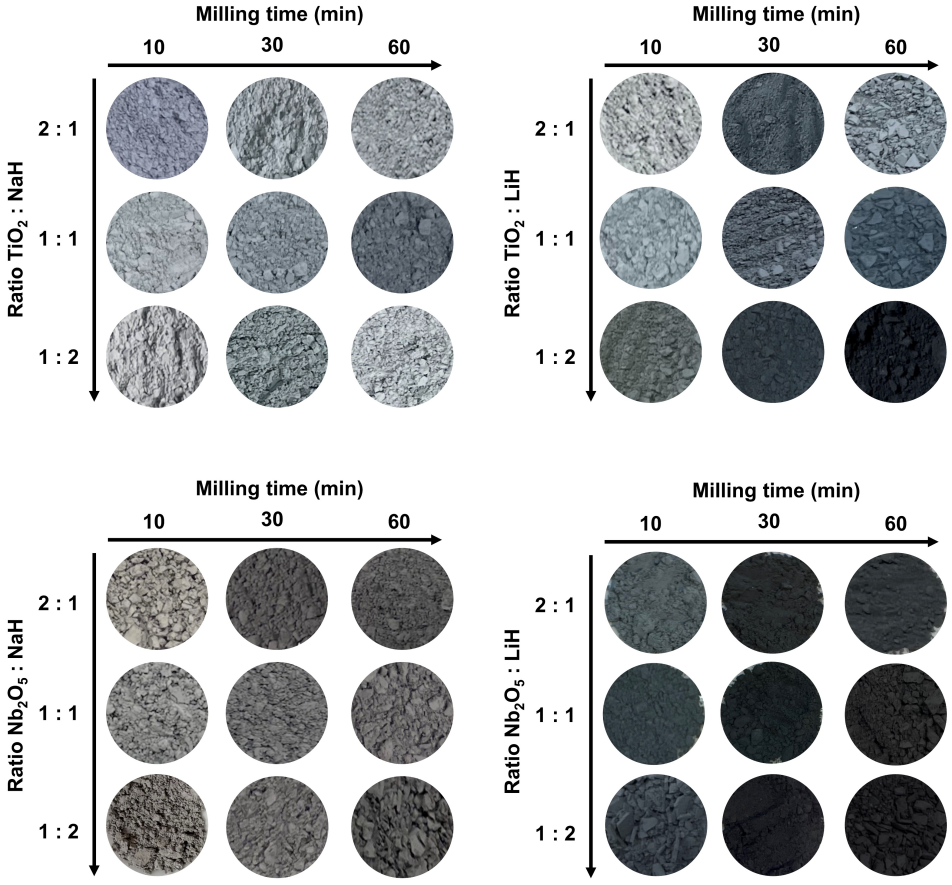

Figure 2. Photographs of reduced TiO_2 and Nb_2O_5 obtained after milling with NaH and LiH at various molar ratios between 10 and 60 min at a constant milling speed of 300 rpm.

© 2023 The Authors. Chemistry - A European Journal published by Wiley-VCH GmbH

Chemistry–A European Journal | Research Article
doi.org/10.1002/chem.202300223
Chemistry Europe
European Chemical Societies Publishing

Powder X-ray diffraction analysis

Powder X-ray diffraction (PXRD) patterns were recorded to gain a better understanding of the processes during ball milling and to analyze possible changes in the crystal structure due to the partial reduction. No significant changes in the PXRD patterns are observed after milling TiO_2 (rutile, $P4_2/mnm$) with NaH (NaCl-type, $Fm\bar{3}m$). The observed powder pattern still corresponds to rutile-type TiO_2. Contrary, the reflections at around 27.4° (110) and 54.0° 2θ (211) show a strong asymmetry after ball milling with LiH (NaCl-type, $Fm\bar{3}m$) caused by an increasing amount of disorder due to the reaction with LiH (Figure 3a). Both reflections are dominated by changes of the *a* lattice parameter of TiO_2, indicating that the structural changes such as the intercalation of Li^+[33] and the formation of oxygen vacancies mainly influence the *ab*-plane.[34] To accommodate for these structural changes in the Rietveld refinement, a multi-fraction model with different fractions of rutile-type TiO_2 was used (Figure S2-6, Supporting Information). Moreover, the reflections at ~44° (200) and ~63° 2θ (220) are significantly broadened due to an overlap with newly emerging reflections corresponding to the cubic $Li_{0.5}Ti_{0.5}O$ phase with a rock salt-type structure ($Fm\bar{3}m$) (Figure S6, Supporting Information) exhibiting titanium in the oxidation state +III. This observation is in line with the formation of $Li_{0.5}Ti_{0.5}O$ when rutile-type TiO_2 is lithiated via more conventional reagents such as *n*-BuLi[33b] or hydrothermally with LiOH,[35] but can also be achieved by grinding the oxide with Li.[33b]

The fraction of $Li_{0.5}Ti_{0.5}O$ increases with longer milling time and higher amounts of initial LiH (Figure 3b), for example from 9 to 44 wt% after milling with 2 equiv. LiH for 10 and 60 min, respectively. The increase of the Li-containing phase with increasing milling time was proven by the determination of the Li to Ti ratio by ICP-MS measurements. After milling TiO_2 for 10 and 60 min with 2 equiv. LiH, a molar Li:Ti ratio of 0.08:1 and 0.38:1 was determined. These results are in good agreement with the results of the Rietveld refinements, which gave an overall composition of $Li_{0.09(1)}TiO_2$ and $Li_{0.36(1)}TiO_2$ for the samples TL_1:2_10 and TL_1:2_60, respectively. The presence of Li inside the sample is further proven by ^{6}Li solid-state NMR (see below In contrast, no sodiation was observed in TiO_2 reduced with NaH after reduction, possibly due to the larger radius of Na^+ compared to Li^+. A similar change in color and lithiation was also observed after ball milling anatase-type TiO_2 ($I4_1/amd$) with LiH. In addition to the transformation of anatase into the orthorhombic high-pressure form (α-PbO_2-type, *Pbcn*), which is known to occur during milling,[36] orthorhombic $Li_{0.5}TiO_2$ (*Imma*) was also formed (Figure S12, Supporting Information).

For Nb_2O_5, no significant changes in the crystal structure are observed by PXRD measurements after milling with both hydrides. The observed diffraction patterns still correspond to monoclinic H-Nb_2O_5 ($P2/m$) regardless of the reducing agent and milling time (Figure S13a, Supporting Information). However, the unit cell volumes revealed an increase for Nb_2O_5 upon reduction with LiH, whereas no significant increase was observed for NaH (Figure S13b, Supporting Information). Only lithiated, but no sodiated Nb_2O_5 phases have been reported in the literature, where the crystal structure was maintained during the intercalation of the alkali metal ions,[30] which is again due to a smaller ionic radius of Li^+ compared to Na^+.[16] Hence, the increase of the unit cell volume of several Å^3 can be attributed to an intercalation of Li^+,[28,30] whose presence is also proven by ^{6}Li solid-state NMR (see below). Based on the increase of the unit cell volume of LiH reduced samples, a sample composition between $Li_{0.02(1)}Nb_2O_5$ and $Li_{0.25(1)}Nb_2O_5$ was calculated (Table S2, Supporting Information).

Elemental analysis (CHN) of sample TL_1:2_60 revealed that no significant amount of hydrogen is found, indicating that no hydrogen is introduced into the crystal structure. Therefore, no Ti–OH or Ti–H bonds are formed, as it is sometimes reported for black titania prepared by hydrogenation.[2,37] However, the formation of these bonds strongly depends on the synthesis conditions[1] and open questions about the actual structure remain.[38] Since no significant hydrogen concentration was detectable, the hydride ion will most likely transfer one or two electrons to the oxide[39] during the ball milling process, followed by the reduction of Ti^{4+}/Nb^{5+} to Ti^{3+}/Nb^{4+} along with the formation of oxygen vacancies or the insertion of Li^+ to respect charge neutrality. It is also possible that the mechanochemical reduction process follows an even more complicated

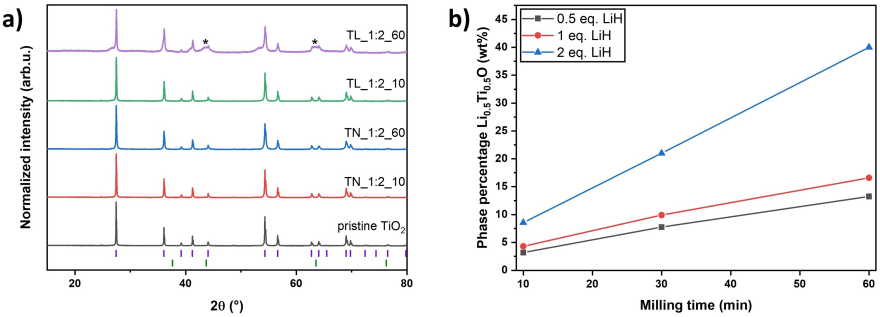

Figure 3. (a) PXRD patterns of pristine and reduced titania. Violet ticks indicate the Bragg positions of rutile-type TiO_2 ($P4_2/mnm$) and green ones of $Li_{0.5}Ti_{0.5}O$ ($Fm\bar{3}m$). The position of the most intense reflections of the latter are marked with asterisks. (b) Phase percentage of $Li_{0.5}Ti_{0.5}O$ versus milling time and LiH amount, obtained by Rietveld refinement.

© 2023 The Authors. Chemistry - A European Journal published by Wiley-VCH GmbH

Chemistry–A European Journal | Research Article doi.org/10.1002/chem.202300223 | Chemistry Europe European Chemical Societies Publishing

reaction mechanism,[23] but no experimentally proven mechanistic details can be given currently.

TGA measurements

In a next step, TGA measurements were performed to investigate the re-oxidizability of the samples by heating them under nitrogen to 600 °C followed by heating under synthetic air to 900 °C to see if a reoxidation, which is accompanied by a mass increase, takes place.[40] After the thermal treatment, all samples turned white again due to the reoxidation of Ti^{3+}/Nb^{4+} to Ti^{4+}/Nb^{5+} during the formation of alkali metal titanates or niobates and/or the refilling of oxygen vacancies.[7,41] In most samples, no significant mass gain was observed, most likely due to the low degree of reduction. Only for TL_1:2_60 and NL_1:2_60 a mass gain of 1.4 and 0.7% due to the uptake of oxygen was observed, respectively (Figure S14, Supporting Information). PXRD measurements confirmed that in all samples the reoxidation of Ti^{3+} and Nb^{4+} to Ti^{4+} and Nb^{5+} occurred. While samples with a lower degree of reduction or samples reduced via NaH were simply reoxidized to TiO_2 and Nb_2O_5, lithium titanates and niobates such as $Li_4Ti_5O_{12}$ ($Fm\bar{3}m$)[42] and $LiNb_3O_8$ ($P2_1/c$)[43] were formed from higher reduced samples (Figure S15, Supporting Information). The color change of TiO_2 if heated under air in absence of a sodiation reaction (Figure S16, Supporting Information) leads to the conclusion, that oxygen defects according to TiO_{2-x} can form in principle. However, since the formation of the before mentioned Li-titanates and Li-niobates can also only occur upon oxygen uptake, a differentiation between reduction via lithium intercalation and reduction due to oxygen vacancies is not possible.

^{6}Li solid-state NMR experiments

Solid-state MAS NMR investigations of ^{6}Li or ^{7}Li nuclei are a powerful technique to probe the local environment of the Li^+ ions in their respective host structures as for example shown for TiO_2.[44] And although the differences in the chemical shifts are small ($\delta = -1$ to 1 ppm), a site assignment was possible. Figure 4a shows a comparison of the ^{6}Li MAS NMR spectra of the LiH reduced TiO_2 samples after 10, 30 and 60 minutes of milling. The presence of a resonance near $\delta \sim 1$ ppm clearly proves the presence of Li in the solid. The increasing intensity of the NMR signal is proportional to the milling times suggesting that more Li is present in the samples since the measurement conditions for the NMR spectra (number of scans, acquisition time, pulse sequence, delay time) were kept the same for all samples. In addition, the full width at half maximum (FWHM) of the signal increases with prolonged milling times (Table S5, Supporting Information), indicating higher structural disorder. A deeper analysis of the individual spectra using the DMFit software program package showed that the line shape varies significantly. Gaussian-Lorentz fit functions were used for analysis of the asymmetry of the peaks (Figure 4b, d, f and Table S5, Supporting Information). All samples show a broad asymmetric signal over the range from −5 up to 9 ppm. The maximum of the resonance can be observed around $\delta \sim 1$ ppm, which is typical for ionic, diamagnetic Li species.[45] For the reduced samples with a milling time of 10 minutes, the line shape can be described well with a single line fit. In contrast, single line fits applied to the spectra obtained from the longer milled samples (30 and 60 min) show a rather bad agreement with the experimental data. The intensity profile, at higher and lower frequencies, cannot be described in a satisfactory way. Especially the intensity in the region between 5 to 8 ppm seems to be caused by a signal originating at least one other Li species. The addition of a second signal (Gaussian-Lorentz function) indicated that this resonance is centered around $\delta =$ 8.4 ppm, however, an extremely large FWHM is found (Figure 4c, e).

When comparing this data to the literature[44a–d] it becomes clear that the presented spectra are rather broad and featureless. Even in ball-milled samples of Li-titanates, synthesized by a high temperature solid-state approach, structural information about the location of the Li ions within the structures could be obtained due to sharp lines and the sensitivity of ^{6}Li to the structural and electronic environment.[44e] This is in total contrast to the measurements performed here because no detailed insight about the coordination of Li^+ in the structure could be obtained. Therefore, it can be concluded that these systems exhibit significant disorder resulting in many different crystallographic Li sites, which leads to a large variation of the Li–O bond lengths and in turn to the observed line broadening. The broad resonance with its large shift of $\delta \sim 8$ ppm, though disagrees with the previously mentioned NMR studies. However, NMR investigations on paramagnetic $LiCoO_2$ reported resonance shifts of up to 17 ppm.[45] The intermetallic compound Li_4Pt_3Si shows even resonance shifts of up to ~120 ppm.[46] Here the nuclear magnetic moment interacts with the magnetic moment of the Co atoms in the case of $LiCoO_2$ or the conduction electrons of Li_4Pt_3Si leading to these drastic shifts known as Knight shifts. Since the reduced TiO_2 shows a black color, but is not metallic in nature, the signal at $\delta \sim 8$ ppm could be explained from the interactions of the paramagnetic Ti^{3+} centers with the Li nuclei similar to $LiCoO_2$.[45] This hypothesis is further strengthened by the fact that the signal at $\delta \sim 8$ ppm increases in intensity with prolonged ball milling time and the recorded electron paramagnetic resonance (EPR) spectra (see below). Finally, the ^{6}Li NMR spectrum of LiH reduced Nb_2O_5 (1:2 ratio) after 60 min ball milling was exemplarily also fitted with a single Gaussian-Lorentz line (Figure S17, Supporting Information). The main resonance shows a chemical shift around $\delta \sim 1$ ppm with a comparable FWHM (Table S5, Supporting Information).

Electron paramagnetic resonance spectroscopy

EPR spectroscopy was used to detect and further investigate the presence of unpaired electrons at the Ti^{3+} and Nb^{4+} centers. According to Chester et al., the hyperfine structure of their niobium-doped rutile only showed hyperfine splitting at

© 2023 The Authors. Chemistry - A European Journal published by Wiley-VCH GmbH

Chemistry–A European Journal
Research Article
doi.org/10.1002/chem.202300223
Chemistry Europe
European Chemical Societies Publishing

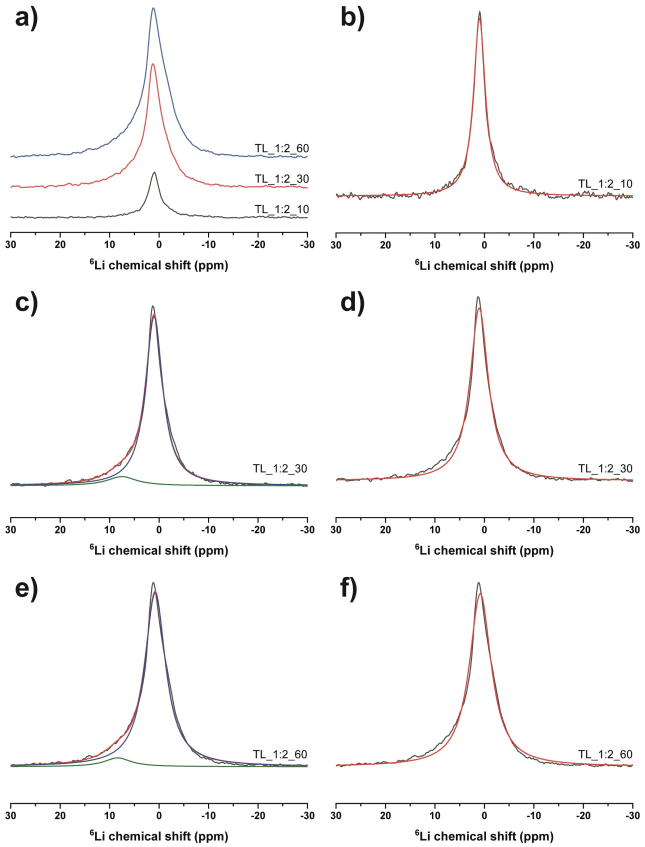

Figure 4. (a) ^{6}Li MAS NMR spectra of TiO_2 + LiH (1 : 2) after ball-milling of 10 (gray), 30 (red) and 60 (blue) minutes. (b, d, f) Individual ^{6}Li MAS spectra for the given ball milling times fitted with a single Gaussian-Lorentz line. ^{6}Li MAS spectra for TiO_2 + LiH after a milling time of (c) 30 and (e) 60 minutes fitted with two lines. Spectra are plotted in black; red lines are the fitting curves; the blue and green lines indicate the individual spectral components.

temperatures below 25 K.[47] Therefore, the EPR experiments were conducted at 10 K. EPR experiments above 10 K showed a broad signal without hyperfine lines, which was a first qualitative evidence for the presence of unpaired electrons in both reduced titania and niobia samples. The observed EPR signal (Figure 5) could be caused by paramagnetic oxygen vacancies V_0, as well as Ti^{3+} and other lower valence Ti species, as documented for many oxide materials.[48] The formation of

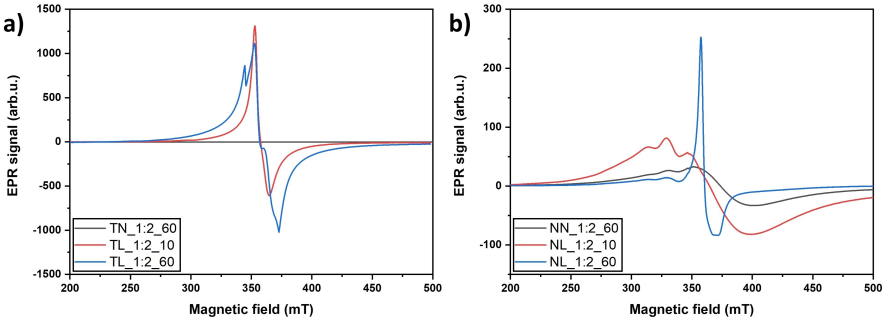

Figure 5. Continuous wave (CW) EPR spectra of NaH (black line) and LiH (blue and red lines) reduced (a) TiO_2 and (b) Nb_2O_5 samples.

© 2023 The Authors. Chemistry - A European Journal published by Wiley-VCH GmbH

Chemistry–A European Journal
Research Article
doi.org/10.1002/chem.202300223
Chemistry Europe
European Chemical Societies Publishing

unpaired electrons during the mechanochemical reduction of TiO_2 with LiH could be confirmed, while the NaH reduced TiO_2 only showed a weak intensity signal. To differentiate and compare the different ball milling times, the peak areas of the reduced oxides were compared. As expected, for samples obtained after prolonged milling, the peak area increases with milling time.[14] Thus, the longer the milling time, the more Ti^{4+} ions are reduced to Ti^{3+}, which is accompanied by the formation of oxygen vacancies or the intercalation of Li.

The formation of unpaired electrons during the mechanochemical reduction of Nb_2O_5 with LiH/NaH could be confirmed as well, but with lower intensities and peak areas and thus, fewer paramagnetic species. The Nb^{4+} concentration shows the same time dependency as in titania with a higher formation of oxygen vacancies and Li intercalation with prolonged milling duration. Theoretically, a total of ten instead of the three visible lines would be expected for $^{93}Nb^{4+}$ due to hyperfine coupling since niobium has a nuclear spin of 9/2 (100% natural abundance). Similarly, a total of six lines is expected for $^{47}Ti^{3+}$ ($I=5/2$, 7.4% natural abundance) and eight lines for $^{49}Ti^{3+}$ ($I=7/2$, 5.4% natural abundance) but ~87% of the Ti centers have no spin, and therefore no coupling. The total number of lines does not match the expectation, but hyperfine splitting constants could be derived from the visible peaks. For the TiO_2/LiH system, 7.9 mT and for the Nb_2O_5/LiH system, 17.8 mT, were extracted.

Raman spectroscopy

In order to further investigate the structural changes, Raman spectra were recorded. Both pristine and reduced titania show the typical Raman signals of rutile at 143, 240, 446 and 609 cm^{-1}, which can be assigned to the Raman modes B_{1g}, second-order scattering, E_g and A_{1g} (Figure 6a).[49] Similarly, the typical Raman bands of monoclinic H-Nb_2O_5, namely Nb–O–Nb angle-deformations between 160 to 300 cm^{-1}, transverse optic modes (TO) originating from symmetric stretching of NbO_6 octahedra between 600 and 700 cm^{-1} and the longitudinal optic mode (LO) of NbO_6 edge-shared octahedra at around 990 cm^{-1} were observed for all Nb_2O_5 samples (Figure 6b).[50] No major changes are observed for NaH reduced oxides in both cases, suggesting that only minor structural changes, for example introduction of oxygen defects, occurred during the mechanochemical reduction. In case of LiH reduced TiO_2 a redshift of up to 10 cm^{-1} of the multi-photon band at around 230 cm^{-1} and a blueshift of 15 cm^{-1} of E_g is observed, while a red shift of up to 8 cm^{-1} occurred of the LO mode of the symmetric Nb–O stretching of LiH reduced Nb_2O_5. Furthermore, the Raman bands become more broadened the more reduced the samples are due to the increase of structural disorder for example, due to Li intercalation[51] or formation of other defects during the ball milling process.[52]

Compared to the pristine oxides, all reduced samples exhibit a significantly stronger absorption in the visible region

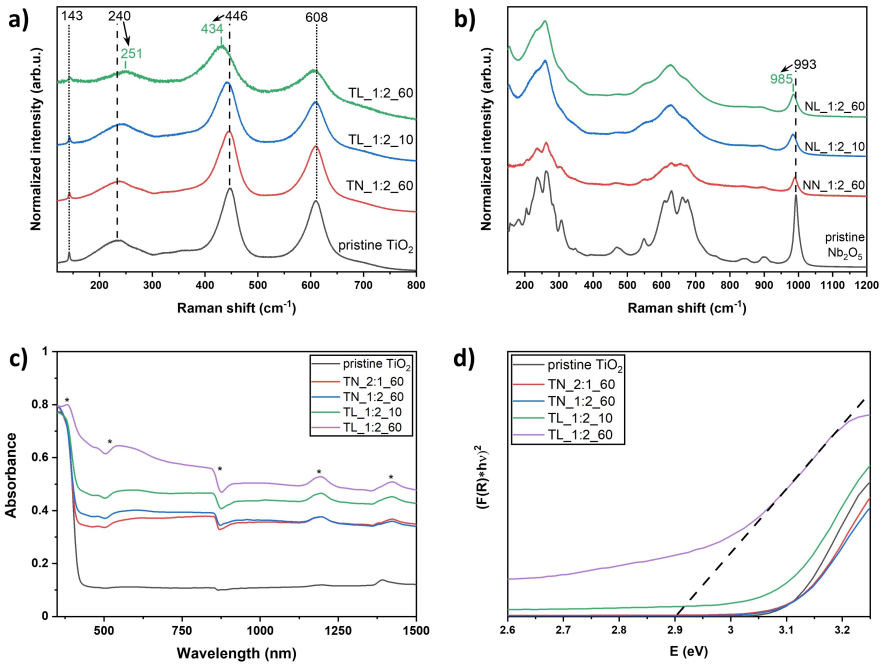

Figure 6. Raman spectra of pristine (black) and with 2 equiv. NaH (60 min, red) and LiH (10 min, blue; 60 min, green) reduced (a) TiO_2 and (b) Nb_2O_5, (c) DRS-UV-Vis absorbance spectra and (d) Kubelka-Munk plot of pristine and reduced TiO_2. Lamp, detector, and filter changes in c) are marked with an asterisk, the evaluation of the band gap is shown by the dashed line in d).

© 2023 The Authors. Chemistry - A European Journal published by Wiley-VCH GmbH

Chemistry–A European Journal | Research Article
doi.org/10.1002/chem.202300223
Chemistry Europe
European Chemical Societies Publishing

(Figure 6c) as shown via the UV-Vis diffuse reflectance spectra (DRS). A clear correlation between the color of the samples and the absorbance of visible light was observed. The values of the optical band gaps and their changes during the reduction were obtained based on the Kubelka-Munk function $F(R)$ and the Tauc relationship $(F(R)h\upsilon)^{\frac{1}{n}} = A(h\upsilon - E_g)$ with $h\nu$ being the photon energy, A is a proportionality constant, E_g the band gap energy and n a parameter depending on the type of band gap. For direct allowed electronic transitions n equals $\frac{1}{2}$ and for indirect allowed transitions n equals 2.[53] According to literature, rutile-type TiO_2 and monoclinic H-Nb_2O_5 both have a direct band gap.[54] In both cases, the optical band gap of the reduced oxides is significantly lowered (up to 0.4 eV compared to the pristine oxide) due to the partial reduction and introduction of defects (Figure 6d, Figure S18, Table S6, Supporting Information)).[14]

Photocatalytic degradation experiments

Often, a reduction in the band gap and absorption properties over a wider range of wavelengths leads to improved (photogenerated) charge carrier properties and higher photocatalytic activity.[14] To evaluate the photocatalytic activities of the reduced oxides compared to the pure oxides, the photochemical degradation of methylene blue (MB), commonly used in tests of the photocatalytic activity of heterogeneous catalysts and found as a pollutant in the wastewater of the textile industry, was studied.[55] For the experiments under UV irradiation, a light source emitting 365 nm was used, while the wavelengths emitted by the visible light source range from 400 to 700 nm with the strongest irradiance being at around 450 and 550 nm. Blank experiments show that without the addition of a catalyst, the photobleaching of MB is only minimal (Figure 7). Overall, no enhancement is observed for NaH reduced TiO_2 and Nb_2O_5 samples, possibly due to the small degree of reduction. In contrast, all LiH reduced samples exhibit an improved performance compared to the pristine oxides. When visible light was used for the degradation experiments, about 33% of the MB was degraded after 5 h using untreated rutile-type TiO_2 was used as catalyst. When a LiH reduced TiO_2 sample was used milled for 10 and 60 min, a significant increase to 45 and 70% of the degraded MB was observed in the same period (Figure 7a). Due to the successful introduction of defects and the partial reduction of Ti^{4+} to Ti^{3+}, the synthesized materials even show a higher photocatalytic activity under visible light compared to the commercially available and widely used photocatalyst Evonik P25 (Figure 7a), which consists of both anatase and rutile TiO_2. In the case of H-Nb_2O_5 only a slight enhancement of the photocatalytic performance of the LiH reduced sample obtained after 10 min of milling ($C_t/C_0 = 0.69$) was observed compared to pristine H-Nb_2O_5 ($C_t/C_0 = 0.72$). LiH treated Nb_2O_5 obtained after 60 min of ball milling in contrast shows a significant improvement since a MB conversion of 65%

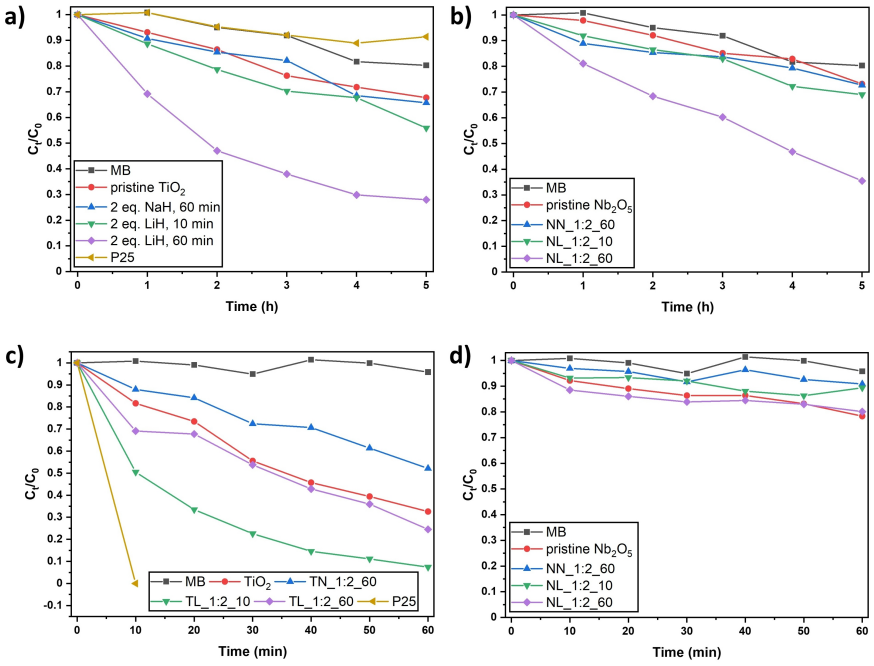

Figure 7. Photocatalytic degradation of methylene blue (MB) (a), (b) under visible light and (c), (d) under UV (365 nm) light without catalyst (black), with pristine titania and niobia (red) and with reduced titania and niobia (blue: NaH, 60 min; green: LiH, 10 min; purple: LiH, 60 min) and with commercially available P25 (yellow). Note the different time scales between (a, b) and (c, d).

© 2023 The Authors. Chemistry - A European Journal published by Wiley-VCH GmbH

Chemistry–A European Journal
Research Article
doi.org/10.1002/chem.202300223
Chemistry Europe
European Chemical Societies Publishing

was achieved after 5 h of irradiation (Figure 7b). It can therefore be concluded that longer milling times and thus a higher degree of reduction for the LiH reduced samples favor the degradation of MB using visible light. In contrast, under irradiation with UV light (365 nm) a complete discoloration of the MB solution was achieved after only 60 min using the LiH reduced titania sample obtained after 10 min of milling ($C_t/C_0 =$ 0.07). Interestingly, both pristine rutile TiO_2 and the LiH reduced sample (60 min) exhibit a lower photocatalytic activity in the UV range (Figure 7c). In comparison to the standard photocatalyst P25, our prepared materials show a somewhat lower photocatalytic activity since a complete discoloration of the MB solution can be achieved with these tailor-made materials after only 10 min with P25 under UV irradiation (Figure 7b). This is attributed to the fact that our sample still predominately composed of photocatalytically less active rutile. As for the niobia samples, both pristine and reduced niobia show almost no activity in the UV range (Figure 7d), which makes the reduced titania samples the more suitable for photocatalytic applications, especially in the UV range.

To exclude that the enhancement of the photocatalytic properties only originates from ball milling, TiO_2 was milled for 60 min and its photocatalytic activity was measured under both UV and visible light. In general, mechanochemistry is a suitable method for the preparation of catalysts.[56] While some publications report an enhancement of the photocatalytic activity of oxides,[57] sulfides[58] or composite materials[59] depending on the milling conditions, no enhancement was observed compared to pristine rutile-type TiO_2 in the present case (Figure S19, Supporting Information), in contrast to the already active anatase phase cited above. This shows that the mechanochemical reaction with the alkali metal hydrides is the main reason for the faster MB degradation. The higher activity of the synthesized materials can be ascribed to the presence of defects such as Ti^{3+}/Nb^{4+}, resulting in a smaller band gap and consequently a better absorption of light, as well as a probable reduction of the recombination rate of photogenerated electron-hole pairs.[11a,14]

In literature, there are some reports on the use of rock salt-type $Li_{0.5}Ti_{0.5}O$ as a catalyst for the photocatalytic dye degradation[35a] and hydrogen generation.[60] Since the compounds formed during ball milling of TiO_2 and LiH, $Li_{0.5}Ti_{0.5}O$ was prepared via a solid-state reaction under argon using TiO_2 and 2 equiv. LiH (Figure S20, Supporting Information). The reaction mixture was heated to 600 °C for 60 min. Afterwards, the obtained material was washed with NH_4Cl/MeOH and MeOH. As a proof of concept that not all measured effects of reduced titania samples are caused by $Li_{0.5}Ti_{0.5}O$, its photocatalytic activity was compared with the photocatalytic activity of TL_1:2_60 under visible light irradiation and with TL_1:2_10 under UV (365 nm) irradiation. As shown in Figure 8, $Li_{0.5}Ti_{0.5}O$ performs slightly better under visible irradiation than TL_1:2_60 but shows a poor performance under UV irradiation. This suggests that not all observed effects originate from the presence of $Li_{0.5}Ti_{0.5}O$ such as the good MB degradation ability under UV light of our synthesized material, but it seems that $Li_{0.5}Ti_{0.5}O$ might be especially beneficial for an effective MB degradation under visible light irradiation.

Conclusion

In summary, a simple and rapid room temperature mechanochemical process was developed for the reduction of rutile-type TiO_2 and H-Nb_2O_5 using alkali metal hydrides. Depending on the synthesis conditions (type and amount of reducing agent and milling duration), samples with a color ranging from light gray to blue to gray and black were obtained. In general, longer milling times and higher amounts of the reducing agent resulted in a higher degree of reduction of the transition metal ions. After reduction using NaH, no significant changes in the crystal structure were observed from PXRD measurements, but the formation of cubic $Li_{0.5}Ti_{0.5}O$ and the intercalation of Li was observed for TiO_2 and Nb_2O_5 when reduced with LiH. The intercalation may occur due to the smaller radius of Li^+ compared to Na^+. The band gap of the ball milled transition metal oxides decreased by up to 0.4 eV, while more paramagnetic centers were formed with longer milling time, as shown by EPR spectroscopy. ^{6}Li NMR spectroscopic investigations clearly demonstrate that the samples contain significant

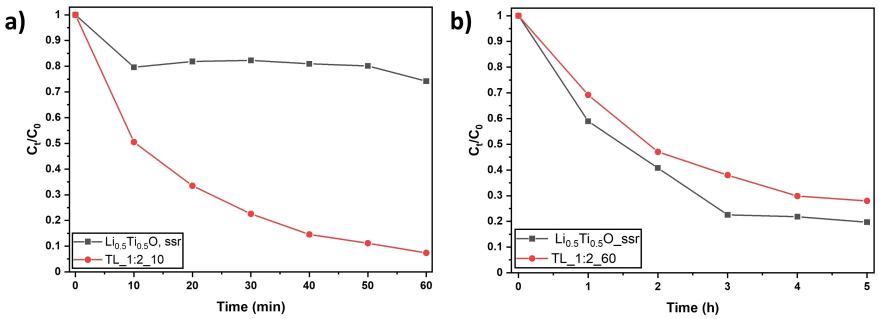

Figure 8. Photocatalytic degradation of MB with $Li_{0.5}Ti_{0.5}O$ prepared by solid state reaction and LiH reduced titania (60 min and 10 min) under (a) visible and (b) UV (365 nm) light.

© 2023 The Authors. Chemistry - A European Journal published by Wiley-VCH GmbH

Chemistry–A European Journal | Research Article doi.org/10.1002/chem.202300223 | Chemistry Europe European Chemical Societies Publishing

amounts of disorder since the signals are featureless. In the case of LiH reduced TiO_2 milled for 30 or 60 min, a second signal arises that could be attributed to the interaction of the paramagnetic Ti^{3+} ions with the Li nucleus. Raman spectroscopy revealed an increase in structural disorder due to the formation of defects. These are more pronounced when LiH is used, as indicated by the darker color of the reduced oxides. Due to these defects, a significantly better photocatalytic performance of the synthesized materials compared to the pristine oxides was achieved under illumination with both UV and visible light.

Experimental Section

Materials: Nb_2O_5 (ChemPur, Karlsruhe, Germany, 99.98 %), TiO_2 (Alfa Aesar GmBH, Karlsruhe, Germany, 99.5 %), LiH (Alfa Aesar GmBH, Karlsruhe, Germany, 99.4 %), and NaH (Merck, Darmstadt, Germany, $>$98 %) were used without further purification and stored in a glovebox under argon atmosphere. All solids have been characterized by powder X-ray diffraction before use.

Synthetic procedures: The syntheses were performed in a planetary ball mill Pulverisette 7 *premium line* (Fritsch, Idar-Oberstein, Germany) using ZrO_2 grinding jars with a volume of 45 mL and 180 Y-stabilized ZrO_2 milling balls with a diameter of 5 mm. All syntheses were performed under inert gas by filling and closing the milling jars in an argon filled glovebox. For the ball milling experiments 3.00 g of Nb_2O_5 (11.29 mmol, 1 equiv.) or TiO_2 (37.6 mmol, 1 equiv.) were milled with n equiv. of LiH or NaH (n = 0.5, 1 and 2). The milling speed was set to 300 rpm, and the milling time was varied from 10 to 30 to 60 min.

Afterwards, the samples were washed with 0.1 M NH_4Cl/MeOH and MeOH under argon several times to remove unreacted alkali metal hydrides as well as side products. Both solvents were degassed with argon for 1 h beforehand. After centrifugation, samples were dried in a vacuum oven at 80 °C and stored in an argon-filled glovebox.

Testing of the photocatalytic activity: The photocatalytic experiments were performed in an EvoluChem™ PhotoRedOx Box (HepatoChem, Beverly, USA) equipped with 2×20 ml sample holder, an EvoluChem 365PF lamp (365 nm) for testing the photocatalytic activity in the UV region and an Evoluchem 6200PF lamp (cold white) for the Vis region.

In a typical methylene blue (MB) degradation experiment, 15 mg of catalyst (1 mg/ml) were added to 15 mL of an aqueous MB solution (20 ppm). After stirring for 30 min in the dark, the suspensions were irradiated. After certain time intervals, 0.4 ml of suspension were periodically sampled and centrifuged to separate the photocatalyst from the solution. The MB solution was then diluted by a factor of 2 before the concentration of MB was measured by UV-Vis spectroscopy (PerkinElmer Inc., Shelton, USA).

Characterization: Powder X-ray diffraction (PXRD) patterns were recorded on a D8-A25-Advance diffractometer (Bruker AXS, Karlsruhe, Germany) under ambient conditions in Bragg-Brentano θ-θ-geometry (goniometer radius 280 mm) with Cu K_α-radiation (λ = 154.0596 pm). A 12 µm Ni foil served as a K_β filter at the primary beam side. At the primary beam side, a variable divergence slit was mounted and a LYNXEYE detector with 192 channels at the secondary beam side. Experiments were carried out in a 2θ range of 7 to 120° with a step size of 0.013° and a total scan time of 2 h. Rietveld refinements of the recorded diffraction patterns was performed using TOPAS 5.0 (Bruker AXS, Karlsruhe, Germany) software.[61] Crystallographic structure and microstructure were refined, while instrumental line broadening was included in a fundamental parameters approach.[62] The mean crystallite size $<$L$>$ was calculated as the mean volume weighted column height derived from the integral breadth. Crystal structure data were obtained from the Pearson's Crystal database.[63]

Electron paramagnetic resonance (EPR) spectra were recorded using a Bruker Elexsys E580 X-band spectrometer with a Bruker ER 4118X-MD5 resonator. All shown EPR spectra were recorded at 10 K using a closed cycle cryostat (Cryogenic CF VTC).

For the acquisition of the Raman spectra, a Raman microscope LabRAM HR Evolution HORIBA Jobin Yvon A (Longmujeau, France) with a 633 nm He-Ne Laser (Melles Griot, IDEX Optics and Photonics, Albuquerque, USA) and an 1800 lines/mm grating was used.

UV-Vis diffuse reflectance spectra were recorded on a Perkin Elmer Lambda 750 spectrometer (PerkinElmer Inc., Shelton, USA) equipped with a 100 mm integration sphere from 290 to 1500 nm with a 2 nm increment and an integration time of 0.2 s. $BaSO_4$ was used as the white reference.

Thermogravimetric analyses (TGA) were performed on a TG F1 Iris (Netzsch Gerätebau GmbH, Selb, Germany). The samples were first heated from room temperature to 600 °C under nitrogen flow (40 mL min^{-1}) followed by heating to 900 °C under synthetic air (40 mL min^{-1}, N_2/O_2 4 : 1). The heating rate was set to 20 K min^{-1}.

^{6}Li single-pulse excitation magic angle spinning (SPE MAS) NMR spectra were recorded at 58.91 MHz on a Bruker AV400WB spectrometer (Bruker, Karlsruhe, Germany) at 298 K in standard ZrO_2 rotors with a diameter of 4 mm. A spinning rate of 13 kHz and a relaxation delay of 3 s were applied. Solid LiCl was used as an external reference with a chemical shift of 0 ppm. Spectra were recorded using the TopSpin software.[64] Fitting of the spectra was performed using the DMFit software program package.[65]

The elemental quantification was conducted via inductively coupled plasma mass spectrometry (ICP-MS) with a commercial ICP-MS system (8900 Triple Quad and SPS4 autosampler, Agilent, Santa Clara, USA). Stock solutions of single element ICP-MS standards of Li^+ (Merck Millipore, Darmstadt, Germany), Ti^{4+} (VWR, Radnor, USA) and Sc^{3+} (Merck Millipore, Darmstadt, Germany) were used. The detector dwell time was 100 µs, the repetition was 3 times, and the measured isotopes were ^{7}Li in no-gas mode and ^{47}Ti using He as collision gas as well as ^{45}Sc (all used modes) as internal standard. For the ICP-MS measurements, the washed samples were dissolved in H_2SO_4 (Fisher Chemical, Loughborough, United Kingdom, $\geq$95 %).

Elemental analysis was performed using a Vario Micro Cube CHN analyzer (Elementar, Langenselbold, Germany).

Acknowledgements

We thank Dr. Kristina Brix for the ICP-MS, Dr. Petra Herbeck-Engel for Raman, Dr. Clemens Matt for EPR and Dr. Michael Zimmer for NMR measurements. Instrumentation and technical support for this work were provided by the Service Center NMR at UdS, with financial support from Saarland University and German Science Foundation DFG. Additionally, instrumentation and technical assistance were provided by the Service Center X-ray Diffraction, with financial support from Saarland University

© 2023 The Authors. Chemistry - A European Journal published by Wiley-VCH GmbH

Chemistry–A European Journal | Research Article doi.org/10.1002/chem.202300223 | Chemistry Europe European Chemical Societies Publishing

and German Science Foundation (project number INST 256/349-1). Open Access funding enabled and organized by Projekt DEAL.

Conflict of Interest

The authors declare no conflict of interests.

Data Availability Statement

The data that support the findings of this study are available in the supplementary material of this article.

Keywords: black niobia · black titania · hydrides · mechanochemistry · solid-state reactions

[1] X. Chen, L. Liu, F. Huang, *Chem. Soc. Rev.* **2015**, *44*, 1861–1885.
[2] X. Chen, L. Liu, P. Y. Yu, S. S. Mao, *Science* **2011**, *331*, 746–750.
[3] a) H. Cui, G. Zhu, Y. Xie, W. Zhao, C. Yang, T. Lin, H. Gu, F. Huang, *J. Mater. Chem. A* **2015**, *3*, 11830–11837; b) W. Zhao, W. Zhao, G. Zhu, T. Lin, F. Xu, F. Huang, *Dalton Trans.* **2016**, *45*, 3888–3894.
[4] A. Sinhamahapatra, J.-P. Jeon, J. Kang, B. Han, J.-S. Yu, *Sci. Rep.* **2016**, *6*, 27218.
[5] T. Matsukawa, T. Ishigaki, *Dalton Trans.* **2021**, *50*, 7590–7596.
[6] A. Badreldin, M. D. Imam, Y. Wubulikasimu, K. Elsaid, A. E. Abusrafa, P. B. Balbuena, A. Abdel-Wahab, *J. Alloys Compd.* **2021**, *871*, 159615.
[7] H.-S. Kim, J. B. Cook, H. Lin, J. S. Ko, S. H. Tolbert, V. Ozolins, B. Dunn, *Nat. Mater.* **2017**, *16*, 454–462.
[8] a) H. Tan, Z. Zhao, M. Niu, C. Mao, D. Cao, D. Cheng, P. Feng, Z. Sun, *Nanoscale* **2014**, *6*, 10216–10223; b) L. Han, Z. Ma, Z. Luo, G. Liu, J. Ma, X. An, *RSC Adv.* **2016**, *6*, 6643–6650.
[9] Z. Wang, C. Yang, T. Lin, H. Yin, P. Chen, D. Wan, F. Xu, F. Huang, J. Lin, X. Xie, M. Jiang, *Energy Environ. Sci.* **2013**, *6*, 3007–3014.
[10] a) S.-T. Myung, M. Kikuchi, C. S. Yoon, H. Yashiro, S.-J. Kim, Y.-K. Sun, B. Scrosati, *Energy Environ. Sci.* **2013**, *6*, 2609–2614; b) B. Santara, P. K. Giri, K. Imakita, M. Fujii, *Nanoscale* **2013**, *5*, 5476–5488.
[11] a) A. Sinhamahapatra, J.-P. Jeon, J.-S. Yu, *Energy Environ. Sci.* **2015**, *8*, 3539–3544; b) M. Ye, J. Jia, Z. Wu, C. Qian, R. Chen, P. G. O'Brien, W. Sun, Y. Dong, G. A. Ozin, *Adv. Energy Mater.* **2017**, *7*, 1601811.
[12] W. Fang, M. Xing, J. Zhang, *Appl. Catal. B* **2014**, *160–161*, 240–246.
[13] M. Zhang, Q. Pei, W. Chen, L. Liu, T. He, P. Chen, *RSC Adv.* **2017**, *7*, 4306–4311.
[14] G. Ou, Y. Xu, B. Wen, R. Lin, B. Ge, Y. Tang, Y. Liang, C. Yang, K. Huang, D. Zu, R. Yu, W. Chen, J. Li, H. Wu, L.-M. Liu, Y. Li, *Nat. Commun.* **2018**, *9*, 1302.
[15] X. Zhou, N. Liu, J. Schmidt, A. Kahnt, A. Osvet, S. Romeis, E. M. Zolnhofer, V. R. R. Marthala, D. M. Guldi, W. Peukert, M. Hartmann, K. Meyer, P. Schmuki, *Adv. Mater.* **2017**, *29*, 1604747.
[16] R. D. Shannon, *Acta Crystallogr. Sect. A* **1976**, *32*, 751–767.
[17] C. E. Housecroft, A. G. Sharpe, *Inorganic Chemistry*, Pearson Education Limited, **2008**, p. 279.
[18] J. Zhang, P. Zhou, J. Liu, J. Yu, *Phys. Chem. Chem. Phys.* **2014**, *16*, 20382–20386.
[19] R. Ren, Z. Yang, L. L. Shaw, *J. Mater. Sci.* **2000**, *35*, 6015–6026.
[20] A. Le Viet, R. Jose, M. V. Reddy, B. V. R. Chowdari, S. Ramakrishna, *J. Phys. Chem. C* **2010**, *114*, 21795–21800.
[21] K. Su, H. Liu, Z. Gao, P. Fornasiero, F. Wang, *Adv. Sci.* **2021**, *8*, 2003156.
[22] H. Guo, A. Jaworski, Z. Ma, A. Slabon, Z. Bacsik, R. Nedumkandathil, U. Häussermann, *RSC Adv.* **2020**, *10*, 35356–35365.
[23] B. C. Hernden, J. A. Lussier, M. Bieringer, *Inorg. Chem.* **2015**, *54*, 4249–4256.
[24] G. Greenwood, *Phil. Mag.* **1924**, *48*, 654–663.
[25] W. J. H. Borghols, M. Wagemaker, U. Lafont, E. M. Kelder, F. M. Mulder, *Chem. Mater.* **2008**, *20*, 2949–2955.
[26] D. W. Murphy, R. J. Cava, S. M. Zahurak, A. Santoro, *Solid State Ionics* **1983**, *9–10*, 413–417.
[27] M. Vijayakumar, S. Kerisit, C. Wang, Z. Nie, K. M. Rosso, Z. Yang, G. Graff, J. Liu, J. Hu, *J. Phys. Chem. C* **2009**, *113*, 14567–14574.
[28] R. J. Cava, D. W. Murphy, S. M. Zahurak, *J. Electrochem. Soc.* **1983**, *130*, 2345–2351.
[29] C. Valencia-Balvín, S. Pérez-Walton, G. M. Dalpian, J. M. Osorio-Guillén, *Comput. Mater. Sci.* **2014**, *81*, 133–140.
[30] M. Catti, M. R. Ghaani, *Phys. Chem. Chem. Phys.* **2014**, *16*, 1385–1392.
[31] C. Dwivedi, T. Mohammad, V. Kumar, V. Dutta, *Vacuum* **2020**, *182*, 109612.
[32] H. Schäfer, R. Gruehn, F. Schulte, *Angew. Chem. Int. Ed.* **1966**, *5*, 40–52; *Angew. Chem.* **1966**, *78*, 28–41.
[33] a) M. V. Koudriachova, N. M. Harrison, S. W. de Leeuw, *Phys. Rev. B* **2002**, *65*, 235423; b) E. Baudrin, S. Cassaignon, M. Koelsch, J.-P. Jolivet, L. Dupont, J.-M. Tarascon, *Electrochem. Commun.* **2007**, *9*, 337–342.
[34] H. Li, Y. Guo, J. Robertson, *J. Phys. Chem. C* **2015**, *119*, 18160–18166.
[35] a) H.-D. Yang, Y.-Y. Kang, P.-P. Zhu, Q.-W. Chen, L. Yang, J.-P. Zhou, *J. Alloys Compd.* **2021**, *872*, 159759; b) D. R. Zhang, H. L. Liu, R. H. Jin, N. Z. Zhang, Y. X. Liu, Y. S. Kang, *J. Ind. Eng. Chem.* **2007**, *13*, 92–96.
[36] J. Chaudhuri, M. L. Ram, B. K. Sarkar, *J. Mater. Sci.* **1994**, *29*, 3484–3488.
[37] a) X. Chen, L. Liu, Z. Liu, M. A. Marcus, W.-C. Wang, N. A. Oyler, M. E. Grass, B. Mao, P.-A. Glans, P. Y. Yu, J. Guo, S. S. Mao, *Sci. Rep.* **2013**, *3*, 1510; b) Z. Wang, C. Yang, T. Lin, H. Yin, P. Chen, D. Wan, F. Xu, F. Huang, J. Lin, X. Xie, M. Jiang, *Adv. Funct. Mater.* **2013**, *23*, 5444–5450; c) Z. Zheng, B. Huang, J. Lu, Z. Wang, X. Qin, X. Zhang, Y. Dai, M.-H. Whangbo, *Chem. Commun.* **2012**, *48*, 5733–5735.
[38] X. Liu, G. Zhu, X. Wang, X. Yuan, T. Lin, F. Huang, *Adv. Energy Mater.* **2016**, *6*, 1600452.
[39] a) R. Nedumkandathil, A. Jaworski, J. Grins, D. Bernin, M. Karlsson, C. Eklöf-Österberg, A. Neagu, C.-W. Tai, A. J. Pell, U. Häussermann, *ACS Omega* **2018**, *3*, 11426–11438; b) Y. Kobayashi, Z. Li, K. Hirai, C. Tassel, F. Loyer, N. Ichikawa, N. Abe, T. Yamamoto, Y. Shimakawa, K. Yoshimura, M. Takano, O. J. Hernandez, H. Kageyama, *J. Solid State Chem.* **2013**, *207*, 190–193.
[40] B. Oberhausen, G. Kickelbick, *Nanoscale Adv.* **2021**, *3*, 5589–5604.
[41] S. Zhang, G. Liu, W. Qiao, J. Wang, L. Ling, *J. Colloid Interface Sci.* **2020**, *562*, 193–203.
[42] A. Deschanvres, B. Raveau, Z. Sekkal, *Mater. Res. Bull.* **1971**, *6*, 699–704.
[43] B. M. Gatehouse, P. Leverett, *Acta Crystallogr. Sect. C* **1972**, *1*, 83–86.
[44] a) S. Britto, M. Leskes, X. Hua, C.-A. Hébert, H. S. Shin, S. Clarke, O. Borkiewicz, K. W. Chapman, R. Seshadri, J. Cho, C. P. Grey, *J. Am. Chem. Soc.* **2015**, *137*, 8499–8508; b) M. Wagemaker, R. van de Krol, A. P. M. Kentgens, A. A. van Well, F. M. Mulder, *J. Am. Chem. Soc.* **2001**, *123*, 11454–11461; c) K. Hoshina, Y. Harada, H. Inagaki, N. Takami, *J. Electrochem. Soc.* **2014**, *161*, A348-A354; d) M. Vijayakumar, S. Kerisit, K. M. Rosso, S. D. Burton, J. A. Sears, Z. Yang, G. L. Graff, J. Liu, J. Hu, *J. Power Sources* **2011**, *196*, 2211–2220; e) D. Becker, R. Haberkorn, G. Kickelbick, *Inorganics* **2018**, *6*, 117.
[45] C. Pan, Y. J. Lee, B. Ammundsen, C. P. Grey, *Chem. Mater.* **2002**, *14*, 2289–2299.
[46] a) R. Pöttgen, T. Dinges, H. Eckert, P. Sreeraj, H.-D. Wiemhöfer, *Z. Phys. Chem.* **2010**, *224*, 1475–1504; b) T. Dinges, R.-D. Hoffmann, L. van Wüllen, P. Henry, H. Eckert, R. Pöttgen, *J. Solid State Electrochem.* **2011**, *15*, 237–243.
[47] P. F. Chester, *J. Appl. Phys.* **1961**, *32*, 866–868.
[48] Y. Su, J. Lang, L. Li, K. Guan, C. Du, L. Peng, D. Han, X. Wang, *J. Am. Chem. Soc.* **2013**, *135*, 11433–11436.
[49] S. P. S. Porto, P. A. Fleury, T. C. Damen, *Phys. Rev.* **1967**, *154*, 522–526.
[50] A. A. McConnell, J. S. Aderson, C. N. R. Rao, *Spectrochim. Acta Part A* **1976**, *32*, 1067–1076.
[51] V. V. Strelchuk, S. I. Budzulyak, I. M. Budzulyak, R. V. Ilnytsyy, V. O. Kotsyubynskyy, M. Y. Segin, L. S. Yablon, *Semicond. Phys. Quantum Electron. Optoelectron.* **2010**, *13*, 309–313.
[52] S. K. Gautam, F. Singh, I. Sulania, R. G. Singh, P. K. Kulriya, E. Pippel, *J. Appl. Phys.* **2014**, *115*, 143504.
[53] S. Landi Jr., I. R. Segundo, E. Freitas, M. Vasilevskiy, J. Carneiro, C. J. Tavares, *Solid State Commun.* **2022**, *341*, 114573.
[54] a) Y. Jia, M. Zhong, F. Yang, C. Liang, H. Ren, B. Hu, Q. Liu, H. Zhao, Y. Zhang, Y. Zhao, *J. Phys. Chem. C* **2020**, *124*, 15066–15075; b) S. Sathasivam, B. A. D. Williamson, S. A. Althabaiti, A. Y. Obaid, S. N. Basahel, M. Mokhtar, D. O. Scanlon, C. J. Carmalt, I. P. Parkin, *ACS Appl. Mater. Interfaces* **2017**, *9*, 18031–18038; c) I. Erdem, H. H. Kart, *Mater. Sci. Semicond. Process.* **2014**, *28*, 59–65; d) M. Landmann, E. Rauls, W. G. Schmidt, *J. Phys. Condens. Matter.* **2012**, *24*, 195503.
[55] P. O. Oladoye, T. O. Ajiboye, E. O. Omotola, O. J. Oyewola, *Results Eng.* **2022**, *16*, 100678.

© 2023 The Authors. Chemistry - A European Journal published by Wiley-VCH GmbH

Chemistry–A European Journal
Research Article
doi.org/10.1002/chem.202300223
Chemistry Europe
European Chemical Societies Publishing

[56] A. P. Amrute, J. De Bellis, M. Felderhoff, F. Schüth, *Chem. Eur. J.* **2021**, *27*, 6819–6847.
[57] K. Saitow, T. Wakamiya, *Appl. Phys. Lett.* **2013**, *103*, 031916.
[58] W. Ashraf, A. Khan, S. Bansal, M. Khanuja, *Physica E Low Dimens. Syst. Nanostruct.* **2022**, *140*, 115152.
[59] a) M. Ye, J. Pan, Z. Guo, X. Liu, Y. Chen, *Nanotechnol. Rev.* **2020**, *9*, 558–567; b) J. Zhou, M. Zhang, Y. Zhu, *Phys. Chem. Chem. Phys.* **2015**, *17*, 3647–3652.
[60] M. K. Kim, W. H. Sim, M. Choi, H. Lim, Y. Kwon, H. M. Jeong, *Catal. Today* **2021**, *359*, 23–27.
[61] Bruker AXS, *Topas 5*, Karlsruhe, Germany, **2014**.
[62] R. W. Cheary, A. A. Coelho, J. P. Cline, *J. Res. Natl. Inst. Stand. Technol.* **2004**, *109*, 1–25.
[63] P. Villars, K. Cenzual, Pearson's Crystal Data: Crystal Structure Database for Inorganic Compounds (on DVD), Release 2022/23, ASM International®, Materials Park, Ohio, USA
[64] Bruker Corp., *Topspin 2.1*, Karlsruhe, Germany, **2008**.
[65] D. Massiot, F. Fayon, M. Capron, I. King, S. Le Calvé, B. Alonso, J.-O. Durand, B. Bujoli, Z. Gan, G. Hoatson, *Magn. Reson. Chem.* **2002**, *40*, 70–76.

Manuscript received: January 23, 2023
Accepted manuscript online: February 10, 2023
Version of record online: April 5, 2023

© 2023 The Authors. Chemistry - A European Journal published by Wiley-VCH GmbH

3.2 Highly exothermic and fast mechanochemical redox and intercalation reactions of V_2O_5 with sodium hydride

This study extends the aforementioned mechanochemical reduction methods to the V_2O_5-NaH system. While vanadium oxides are traditionally used as catalysts, they are also interesting materials for electrochemical energy storage applications due to the accessibility of different oxidation states of vanadium. Additionally, they exhibit a rich and interesting ternary system with sodium, including sodium vanadates that are for example also promising for battery and energy storage applications.

The study aims to systematically investigate the influence of milling time and sodium hydride concentration on the final reaction outcome. While the initial sodium hydride concentration was identified as the more influential parameter on the product composition than the milling time, a mixture of different crystalline (sodium) vanadium oxides with vanadium oxidation states ranging from +V to +III was obtained under the formation of hydrogen gas under all tested milling conditions. Three main trends were identified with increasing NaH concentration on the final product. Firstly, higher percentages of sodium vanadates are formed as more sodium is present in the reaction mixture. For example, while V_2O_3 is one of the main products with 2 eq. NaH, the use of 4 eq. NaH only leads to the formation of sodium vanadates Na_3VO_4 and $NaVO_2$. Secondly, lower oxidation states of vanadium are accessible. With 1 eq. NaH, the lowest observed oxidation state of vanadium is +IV, while vanadium in the oxidation state +III in the form of $NaVO_2$ is only formed with 2.5 or more equivalents of NaH. A further increase of the NaH concentration does not result in a further reduction since the same products, Na_3VO_4 and $NaVO_2$, are formed as with 4 eq. sodium hydride. Lastly, sodium vanadates that are richer in sodium are preferably formed the more NaH was used for the mechanochemical reduction. Among the three vanadates $NaVO_3$, $Na_4V_2O_7$ and Na_3VO_4 with vanadium in the oxidation state +V, $NaVO_3$ is only present with 1 and 1.5 eq. NaH, while $Na_4V_2O_7$ is formed with 2 and 2.5 eq. NaH and Na_3VO_4 especially with 3 and 4 eq. of sodium hydride.

For all tested reactions, the start of the reaction is indicated by a sudden steep increase in pressure inside the milling jar after just a few minutes of milling, indicating that all reactions occur in a highly exothermic self-propagating manner. A similar large exothermicity and product formation was even observed when performing the reaction in a simple pistil-mortar setup (Figure 17). Subsequent quantum mechanical calculations suggest that the formation of sodium vanadates, especially with vanadium in the oxidation stare +V, are energetically most favored. Consequently, their formation can be regarded as the driving force. The experimentally

observed exothermic and self-propagating character of these reactions is further supported by these theoretical calculations.

The results of this study were published:
A. Michaely, C. Luckas, R. Haberkorn, G. Kickelbick, Highly Exothermic and Fast Mechanochemical Redox and Intercalation Reactions of V_2O_5 with Sodium Hydride. *Inorg. Chem.* **2024**, 63, 18, 8099-8108, DOI:10.1021/acs.inorgchem.4c00200.

The publication is reproduced with permission from the American Chemical Society. Copyright 2024.

Anna Michaely performed most of the experimental work, data interpretation and the theoretical calculations, along with writing the original draft. Christopher Luckas carried out preliminary experiments with V_2O_5 and NaH, as well as data interpretation during his bachelor thesis under the supervision of Anna Michaely and Guido Kickelbick.[337] He also provided assistance with improving the final manuscript. Robert Haberkorn contributed scientific ideas, interpretation, and discussions of the acquisitioned data, as well as editing of the manuscript. Guido Kickelbick was involved with scientific ideas, supervision, discussions of the results, and editing of the manuscript.

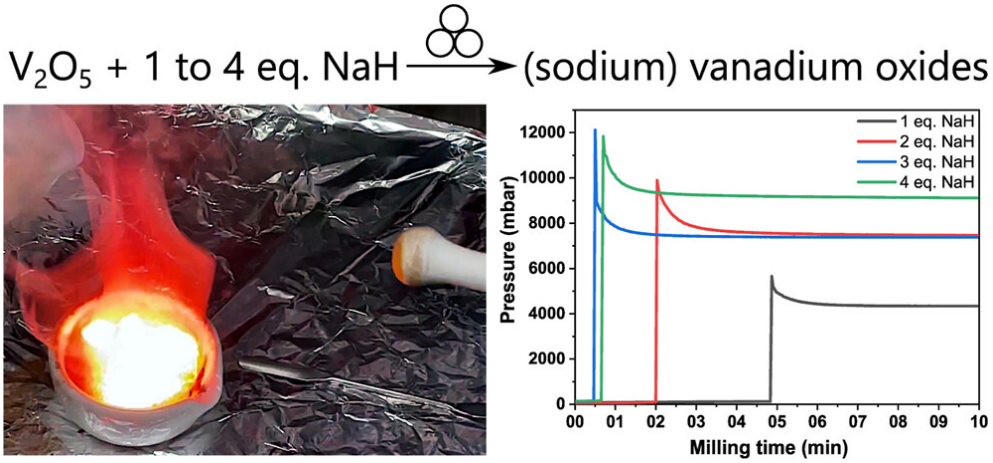

Figure 17: Table of contents graphic – Highly exothermic and rapid mechanochemical reaction of V_2O_5 with NaH, as seen by the sudden increase in pressure, and resulting in the formation of several (sodium) vanadium oxides with different oxidation states and sodium to vanadium ratios depending on the synthesis conditions.[65]

Inorganic Chemistry

pubs.acs.org/IC Article

Highly Exothermic and Fast Mechanochemical Redox and Intercalation Reactions of V_2O_5 with Sodium Hydride

Anna Michaely, Christopher Luckas, Robert Haberkorn, and Guido Kickelbick*

Cite This: *Inorg. Chem.* 2024, 63, 8099−8108 Read Online

ACCESS | Metrics & More | Article Recommendations | Supporting Information

ABSTRACT: Vanadium oxides exhibit promising characteristics for electrochemical energy storage, owing to their capability to switch between different oxidation states, in combination with the incorporation of alkali metals. Here, we report on a systematic investigation of the mechanochemical reduction of V_2O_5 with NaH. In contrast to conventional high-temperature synthesis methods, the mechanochemical reaction occurs already after a few minutes. We observed a mixture of different (sodium) vanadium oxides with vanadium oxidation states ranging from +III to +V. Remarkably, these highly exothermic self-propagating reactions occur even within a rudimentary pistil-mortar setup. Hereby, the hydride concentration has a greater effect on the final sample composition than the milling time. In general, higher percentages of sodium vanadates are formed instead of vanadium oxides, and the lower oxidation states of vanadium are accessible with increasing amounts of NaH. Theoretical calculations confirm these experimental observations and emphasize the central role of sodium vanadates, especially with vanadium in the +V oxidation state, in carrying out the observed exothermic reactions. This comprehensive study sheds light on the mechanochemical reduction of vanadium oxides and underlines their potential for further development of electrochemical energy storage systems.

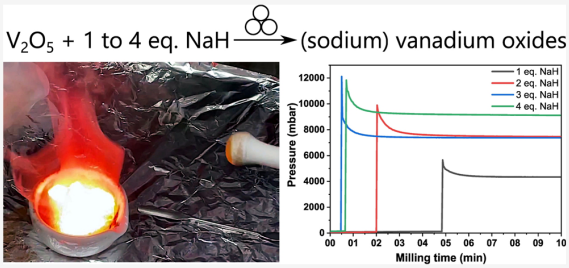

INTRODUCTION

Besides their traditional use as catalysts,[1] vanadium oxides are highly interesting energy storage and conversion materials[2,3] due to their many addressable oxidation states. An attractive application is, for example, the redox flow battery[4] but also their application as electrode materials in lithium[5] or sodium-ion batteries.[6] Even new concepts of energy storage are possible with vanadates such as photochargeable lithium-ion batteries.[7]

In the vanadium−oxygen system, many stable and metastable vanadium (sub)oxides with an oxidation state of vanadium ranging from +II to +V are known in the literature.[8] Thermodynamically stable phases include, for instance, vanadium dioxide (VO_2), divanadium trioxide (V_2O_3), vanadium pentoxide (V_2O_5), the Magnéli phase trivanadium pentoxide (V_3O_5), and Wadsley phase trivanadium heptaoxide (V_3O_7).[3] While vanadium has a single oxidation state in the first three oxides, the latter two represent compounds with mixed vanadium oxidation states. Additionally, several mixed-valent metastable vanadium oxides of both the Magnéli[9] and the Wadsley series are known.[10]

In addition to the wide range of literature-known vanadium oxides, vanadium also forms many ternary oxidic compounds with several alkali and alkaline earth metals such as lithium, sodium, potassium, and calcium.[11] These alkali metal vanadates differ in the amount of alkali metal ions and the oxidation state of vanadium. Here, the sodium vanadates, with over 10 different literature-known compounds[11] represent an interesting ternary system. While the $Na_2O−V_2O_5$ system is the most important subsystem in the roasting process of vanadium slag[12] for the preparation of vanadium metal, which is widely used in the production of steel and alloys,[13] the sodium vanadates themselves are also promising materials for numerous applications. Most sodium vanadates, such as $NaVO_3$,[14] $Na_4V_2O_7$,[15] and Na_xVO_2,[16] are hereby primarily investigated as potential cathode materials for sodium-ion batteries (SIBs). While there are also some investigations into the use of Na_3VO_4[17] in SIBs, it is also investigated in the medical field as an inhibitor of phosphatases and in the treatment of diabetes.[18]

The Na−V−O system has been studied in detail between the 1950s and 1970s. Here, the reaction outcome of V_2O_5 with Na_2CO_3,[19] and liquid sodium[20] at elevated temperatures was investigated. Similarly, the solid−state reaction of lower vanadium oxides such as VO_2[20,21] and V_2O_3[20−22] with Na_2O or liquid sodium results in the formation of numerous sodium vanadates with the oxidation state of vanadium ranging from +III to +V, and sometimes lower vanadium oxides such as VO as

Received: January 16, 2024
Revised: March 19, 2024
Accepted: April 9, 2024
Published: April 24, 2024

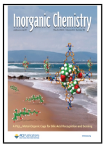

ACS Publications

© 2024 The Authors. Published by American Chemical Society

https://doi.org/10.1021/acs.inorgchem.4c00200
Inorg. Chem. 2024, 63, 8099−8108

a side phase. Contrary to the energy-intensive high-temperature solid-state reactions described above, mechanochemistry represents a promising sustainable and energy-efficient synthesis method in which the reaction is induced only by the absorption of mechanical energy. In general, mechanochemical reactions are performed without or with only small amounts of solvent at room temperature, making them a greener and more energy-efficient synthesis technique. In addition, the reactions work often faster than conventional synthesis methods, and new or more reactive products can be obtained.[23]

To our knowledge, the behavior of the Na−V−O system in the ball mill has been largely unexplored, and very few examples of the mechanochemical preparation of sodium vanadates can be found in the literature. Rojac et al. reported on the formation of sodium metavanadate $NaVO_3$, with vanadium in the +V oxidation state, by the mechanochemically induced reaction of V_2O_5 and Na_2CO_3.[24] Haberkorn et al. have shown that the mechanochemical sodiation of V_2O_5 with Na_2S makes it possible that an average sodium content of $x = 0.3$ can be achieved in $Na_xV_2O_5$.[25] The number of publications on the mechanochemical reduction of V_2O_5 has also been very low so far. For example, Takai et al. reported on the formation of VO_2 after ball milling V_2O_5 with paraffin wax for 3 h.[26] Alternatively, Mg, Al, or Ti can be applied as reducing agents to obtain elemental vanadium.[27] The latter reactions are highly exothermic, and a combustion event was detected.[27] A similar high exothermicity was observed for the coreduction of V_2O_5 and TiO_2 with aluminum in an attritor mill, resulting in the formation of V−Ti alloy and V_5Al_8.[28]

We have recently shown that alkali metal hydrides are readily available and powerful reducing agents for the partial reduction of rutile-type TiO_2 and monoclinic H−Nb_2O_5 in a fast and energy efficient ball milling process.[29] Thus, the question arises whether alkali metal hydrides can also be applied as reducing agents for the mechanochemical reduction of V_2O_5 or if a simultaneous formation of alkali metal vanadates takes place. As for the reaction of V_2O_5 with alkali metal hydrides, no excessive studies have been reported yet. To the best of our knowledge, only one report exists from 1963 on the reaction of V_2O_5 with LiH at high temperatures, but only a qualitative sample composition was given.[30]

In this study, we therefore systematically investigate the mechanochemical reaction of V_2O_5 with NaH in a high-energy planetary ball mill as well as the influence of the milling time and hydride concentration on the reaction outcome. The experimental findings are further supported by mechanochemical calculations using the Vienna ab initio simulation package (VASP).

EXPERIMENTAL SECTION

Materials. V_2O_5 (abcr, Karlsruhe, Germany, 99.9%) and NaH (Merck, Darmstadt, Germany, >98) were used without further purification and stored in a glovebox under an argon atmosphere. All solids have been characterized by X-ray diffraction before use.

Synthetic Procedures. *Mechanochemical Syntheses.* All syntheses were performed under an argon atmosphere using the glovebox technique. The syntheses were performed in a planetary ball mill Pulverisette 7 Premium line (Fritsch, Idar-Oberstein, Germany) using ZrO_2 grinding jars with a volume of 45 mL. The batch size was set to 3 g, and V_2O_5 was milled with n eq NaH (n = 1, 1.5, 2, 2.5, 3, and 4). After the powders were lightly mixed with a spatula and added into the milling jar, they were milled at 300 rpm for 10 min using 90 ZrO_2 milling balls with a diameter of 5 mm. The evolution of pressure and temperature during ball milling was studied for selected samples using the EASY GTM system (Fritsch, Idar-Oberstein, Germany). In contrast to normal milling jars, the lid of the EASY GTM milling jar has a built-in pressure and temperature sensor that enables continuous monitoring of both parameters. To avoid damage of the milling jar, the mass of NaH was set to 0.60 and 0.80 g for 3 and 4 equiv NaH, respectively.

Characterization. Powder X-ray diffraction (PXRD) patterns of the pulverized samples were recorded at room temperature on a X'Pert MPD diffractometer (PANalytical, Almelo, Netherlands) in the Bragg−Brentano θ−θ-geometry (goniometer radius 280 mm) with Cu K_α-radiation (λ = 154.0596 pm). A 12 μm Ni foil working as a K_β filter and a variable divergence slit were mounted at the primary beam side. A PIXcel^{1D} detector was used at the secondary beam side. Experiments were carried out in a 2θ range of 7−120° with a step size of 0.013° and a total scan time of 2 h. Rietveld refinements of the recorded diffraction patterns were performed using TOPAS 5.0 (Bruker AXS, Karlsruhe, Germany) software.[31] Crystallographic structure and microstructure were refined, while instrumental line broadening was included in a fundamental parameter approach.[32] The mean crystallite size $\langle L \rangle$ was calculated as the mean volume-weighted column height derived from the integral breadth. Crystal structure data were obtained from Pearson's Crystal database.[11]

Reoxidation of selected samples was carried out in a simultaneous thermogravimetric analysis system (TGA/DSC 1 Star HT/1600 system, Mettler Toledo, Columbus, OH, USA) under a flow rate of 40 mL min^{-1} and a heating rate of 10 K min^{-1}. The samples were first heated from room temperature to 350 °C under argon, followed by heating to 550 °C with an Ar/O_2 mixture in a ratio of 1:4.

Quantum Mechanical Calculations. Calculation of the free energy of the (sodium) vanadium oxides was carried out using the projector-augmented wave (PAW) method by Blöchl[33] implemented in the VASP.[34] Exchange and correlation effects were accommodated using the General Gradient Approximation functional by Perdew−Burke−Ernzerhof optimized for bulk solids (PBEsol).[35] POT-PAW_PBE_54 potentials were used for all calculations, more specifically, Na_sv, V_sv, O_h, and H−h. The convergence criteria for electronic and ionic relaxation were set to 10^{-4} and 10^{-5} eV, respectively, while the cutoff energy was set to 800 eV. The Brillouin zone was sampled by automatically generating a Γ-centered k-point mesh with a resolution of minimum 0.035 Å^{-1} per cell. All calculations were carried out without spin polarization.

RESULTS AND DISCUSSION

Mechanochemical Reactions with Sodium Hydride. V_2O_5 was ball milled with n equivalents of NaH (n = 1, 1.5, 2, 2.5, 3, and 4) for 10, 30, 60, and 120 min at 300 rpm in the Fritsch Pulverisette 7 Premium line planetary ball mill under argon using ZrO_2 milling equipment to study the influence of milling time and hydride concentration on the product composition during the mechanochemical reaction of V_2O_5 and NaH. We were particularly interested in determining whether solid-state reduction is also possible at room temperature and which mixtures of (sodium) vanadium oxides are formed depending on the milling conditions. A visually perceivable color change of the powders was observed after only 10 min of milling, which strongly depends on the initial hydride concentration. While the reaction mixture turned from ochre to dark green with a lower hydride concentration (1−1.5 equiv), a darker black powder was obtained with increasing concentrations of NaH, suggesting that some reaction occurred even after very short milling times. Ball milling of pure V_2O_5 only led to a decrease of crystallite size, and no polymorphic phase transformations were observed (Supporting Information, Figure S11).

Additionally, the evolution of temperature and pressure inside the grinding jar during milling was recorded by using the EASY GTM system by Fritsch. Irrespective of the hydride concentration, a combustion event is observed by a steep, sudden increase in pressure, for example, up to 9.9 bar with 2 equiv NaH,

https://doi.org/10.1021/acs.inorgchem.4c00200
Inorg. Chem. 2024, 63, 8099−8108

Inorganic Chemistry pubs.acs.org/IC Article

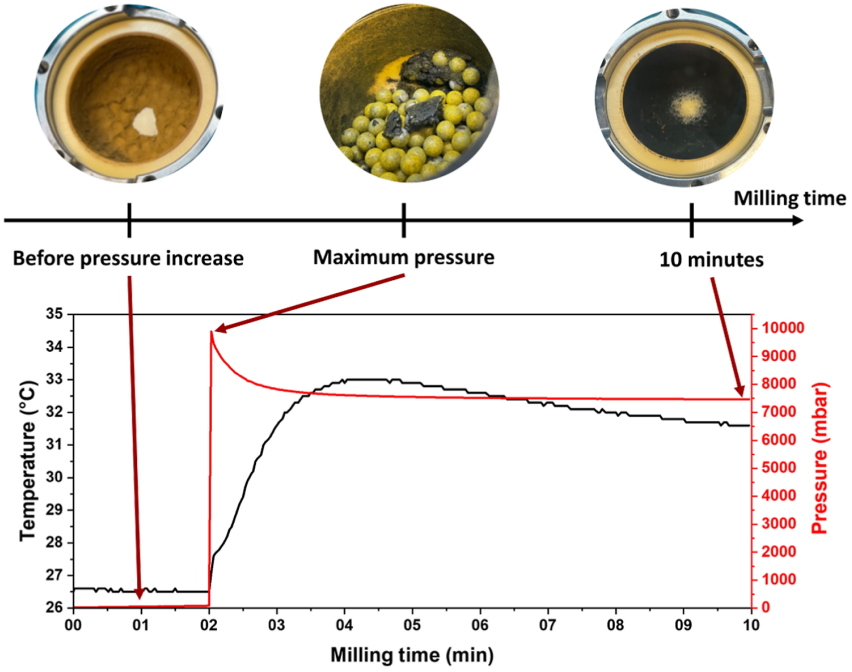

Figure 1. Appearance of the milling mixture as well as the pressure−temperature curves shortly before and at the maximum pressure increase as well as after a milling time of 10 min for the reaction of V_2O_5 with 2 equiv of sodium hydride.

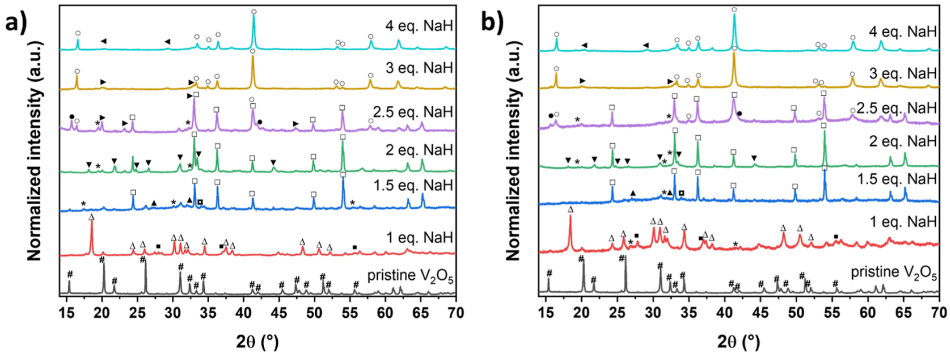

Figure 2. PXRD patterns of pristine V_2O_5 (black) and of the samples obtained after milling V_2O_5 with 1 (red), 1.5 (blue), 2 (green), 2.5 (purple), 3 (yellow), and 4 equiv (light blue) of NaH for (a) 10 min and (b) 120 min. Unidentified reflections are marked with asterisks. Characteristic reflections corresponding to V_2O_5 (*Pmmn*) are marked with #, those corresponding to VO_2 ($P4_2/mnm$) are marked with (black solid square) ■, those corresponding to V_3O_5 ($C2/c$) are marked with (solid square open circle) ◘, those corresponding to V_2O_3 ($R\bar{3}c$) are marked with (open square) □, those corresponding to $NaVO_3$ ($C2/c$) are marked with (triangle up solid) ▲, those corresponding to $Na_4V_2O_7$ ($C2/c$) are marked with (triangle down solid) ▼, those corresponding to Na_3VO_4 ($P2_13$) are marked with (triangle right-pointing solid) ▶, those corresponding to Na_3VO_4 ($Pmn2_1$) are marked with (triangle left-pointing solid) ◀, those corresponding to NaV_2O_5 (*Pmmn*) are marked with (triangle up open) Δ, those corresponding to NaV_2O_4 ($C2/c$) are marked with (circle solid) ●, and those corresponding to $NaVO_2$ ($R\bar{3}m$) are marked with (circle open) ○. If a phase occurs as the main phase in different diffractograms, its main reflections are marked in all of the corresponding diffractograms. To facilitate comparison, XRD data have been normalized between zero and one.

which was detected after only a few minutes of milling (Figure 1; Supporting Information, Figure S12). This steep pressure increase marks the beginning of the exothermic self-propagating reaction between V_2O_5 and NaH and is caused by the sudden release of reaction heat, which heats the gaseous atmosphere in the closed milling jar. A similar combustion event and pressure increase were detected in the mechanochemical synthesis of the three transition metal carbides VC, NbC, and TaC.[36] In contrast to the carbide synthesis, where the initial pressure is almost instantly regained after the combustion event, we observe a pressure drop of 20−25% to a constant pressure with the V_2O_5−NaH system. With 2 equiv NaH, the final pressure inside the milling jar remained at ∼8 bar, for example. The elevated pressure inside the jar indicates the formation of hydrogen gas due to the decomposition and reaction of NaH. A positive oxy-hydrogen sample confirms the presence of hydrogen gas after milling. Overall, the more sodium hydride is used initially, the higher the pressure inside the milling jar, and the more hydrogen

https://doi.org/10.1021/acs.inorgchem.4c00200
Inorg. Chem. 2024, 63, 8099−8108

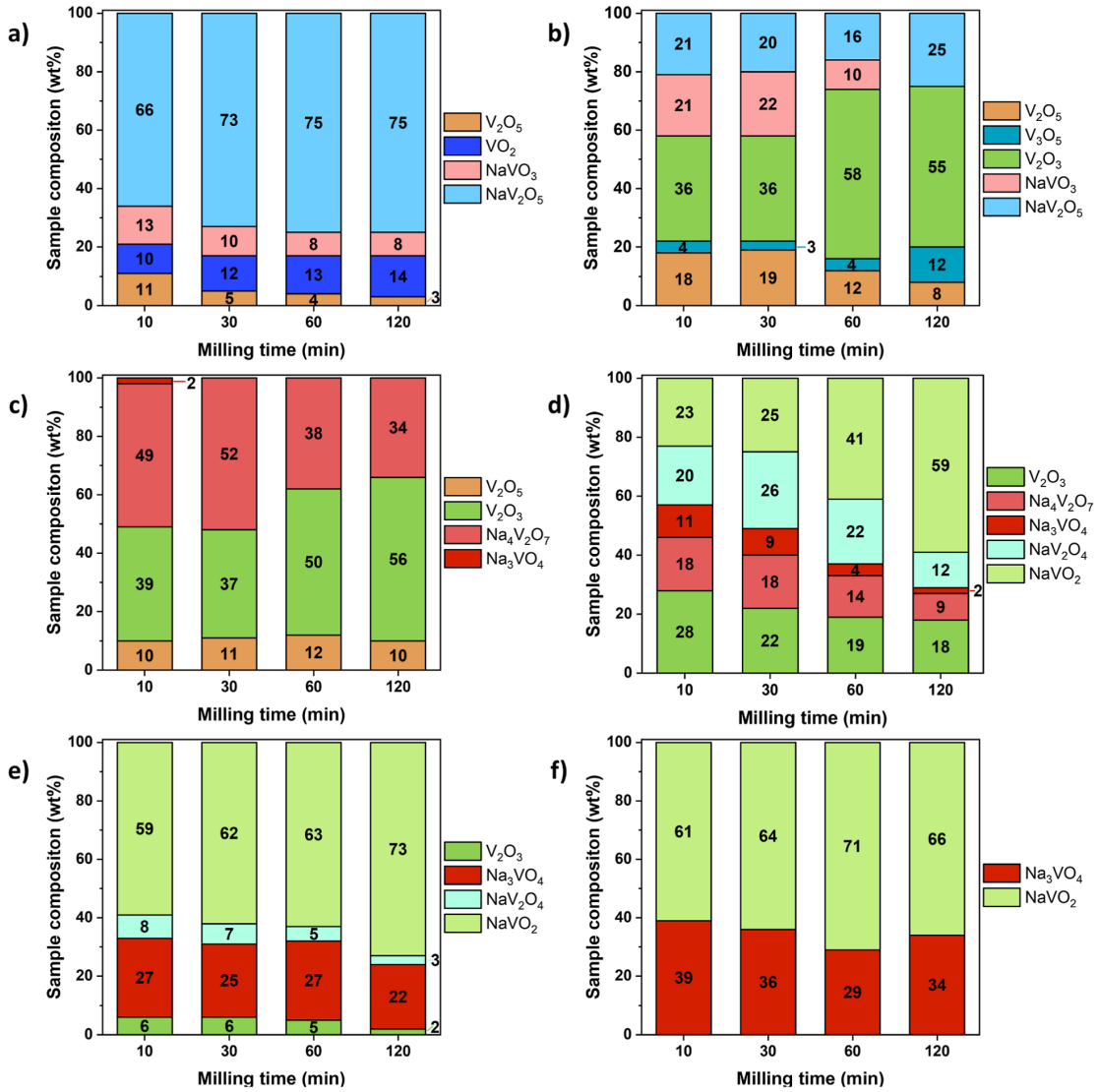

Figure 3. Sample composition in weight percent as obtained by Rietveld refinement for V_2O_5 milled with (a) 1, (b) 1.5, (c) 2, (d) 2.5, (e) 3, and (f) 4 equiv NaH for different milling times. For simplicity, if different polymorphs of an oxide were found in a sample, they were added together in this figure but are detailed in the Supporting Information.

is released. In contrast to the sudden rise in pressure, the increase in temperature to about 35 °C is slightly delayed. Since a certain percentage of the heat is absorbed by the milling jar and since the entire atmosphere inside the jar also must first warm up, the detection of a temperature increase takes longer.

Stopping the reaction manually at the maximum pressure showed that the reaction first occurs at the steep increase in pressure, while only V_2O_5 and NaH are present in the reaction mixture beforehand (Figure 1). Overall, the samples are rather inhomogeneous at the maximum pressure, as both darker platelets and chunks are found next to finer ochre-colored (1.5 and 2 equiv NaH) or black powders (3 and 4 equiv NaH) (Supporting Information, Figure S13). However, subsequent PXRD measurements and Rietveld refinement (Supporting Information, Figure S14) showed that the same product phases are present at the highest pressure and after 10 min of milling (vide infra). The presence of grains of molten product after milling indicates that temperatures of several hundred degrees are temporarily reached, causing local melts. These sudden and exothermic reactions between V_2O_5 and NaH could also be induced in a porcelain mortar inside an argon-filled glovebox (see additional movie), showing that very little activation energy is needed to induce these self-propagating reactions. Previous studies of reactions of the Na−V−O system report a high exothermicity in solid-state reactions of vanadium oxides with Na_2CO_3[37] or Na_2O[21] at elevated temperatures, as well as spontaneous reactions of V_2O_5 with Na_2O after ignition with electrical heating.[38] According to Rietveld refinement, the same products, namely, Na_3VO_4 and $NaVO_2$, were formed as in the ball mill (vide infra), but the conversion was much lower since significant amounts of unreacted V_2O_5 and NaH are still present (Supporting Information, Figure S15). Due to the sudden

https://doi.org/10.1021/acs.inorgchem.4c00200
Inorg. Chem. 2024, 63, 8099−8108

Inorganic Chemistry pubs.acs.org/IC Article

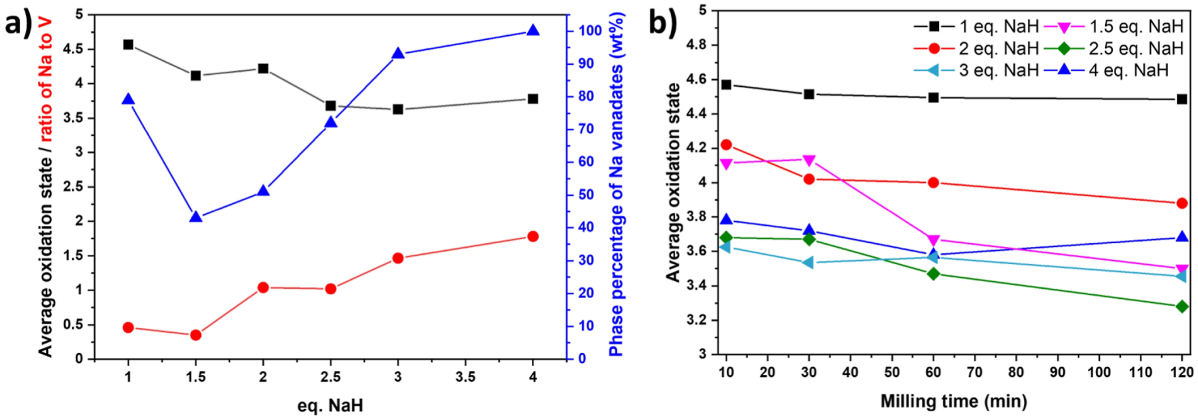

Figure 4. (a) Influence of the hydride concentration on the average oxidation state and the average sodium/vanadium ratio in each oxide in the final sample prepared in 10 min of milling. Additionally, the evolution of the total phase percentage of sodium vanadates in each sample is shown. (b) Influence of the milling time on the average oxidation state in the final product for different NaH concentrations. The lines in both graphs connecting the measured points serve as orientation aids for the eye.

ignition and high exothermicity of the reactions, great care must be taken when carrying out the reactions in a mortar to avoid damage to the glovebox or gloves. In comparison, carrying out the reactions in the milling jars is preferable and rather safe, as they are robust and can withstand a pressure of up to 20 bar. However, it is advisable to estimate the potential pressures inside the milling jars before starting any reactions to avoid damage.

To study the influence of hydride concentration and milling time on the reaction outcome, PXRD measurements and Rietveld refinement were performed to analyze the sample composition of V_2O_5 milled with 1−4 equiv NaH between 10 and 120 min. As shown in Figure 2, all diffraction patterns differ significantly from the diffraction pattern of pristine V_2O_5, indicating that a reaction has taken place even after short milling times. Furthermore, the NaH concentration strongly influences the final sample composition, as the diffraction patterns vary significantly in the number and positions of reflections depending on the ratio of V_2O_5 to NaH. Because the diffractograms change little with longer milling (Figure 2b), it can be expected that the sample composition does not change as much with the milling time, making the hydride concentration the more influential parameter for the final sample composition. Generally, it can be stated that the reaction of V_2O_5 with NaH can lead to a reduction of the vanadium species as well as the intercalation of Na^+ ions. Both reaction types can occur simultaneously, which generates Na vanadates with V in an oxidation number $<V^+$, or a reduced Na-free vanadate is formed.

Subsequent Rietveld refinement (Supporting Information, Figures S16−S21, Tables S2−S7) confirms the above postulated hypothesis that, especially, the sodium hydride concentration influences the reaction outcome (Figure 3; Supporting Information, Figure S22). Depending on the number of initial equivalents of NaH (sodium) vanadium oxides with vanadium in various oxidation states are formed with good reproducibility (Supporting Information, Figure S23, Tables S8−S11), namely $NaVO_3$ ($C2/c$), $Na_4V_2O_7$ ($C2/c$), and Na_3VO_4 ($P2_13$ and $Pmn2_1$), +IV/V in NaV_2O_5 ($Pmmn$), +IV in VO_2 ($P4_2/mnm$), +III/IV in V_3O_5 ($C2/c$) and NaV_2O_4 ($C2/c$), and +III in V_2O_3 ($R\bar{3}c$) and $NaVO_2$ ($R\bar{3}m$). Hereby, a wide range of crystal structures can be observed. Among the observed oxides, V_2O_5 is the only compound consisting of VO_5 square pyramids, together with the intercalate NaV_2O_5, which has the same host structure but with additional sodium atoms between the layers of edge and corner-sharing square pyramids. All other experimentally detected vanadium oxides consist of interconnected VO_6 octahedra, which are described in more detail in the Supporting Information, and form either different types of strands, as in the case of VO_2 and V_3O_5, or layers of edge-sharing octahedra, as in the case of V_2O_3. In the ternary system Na−V−O, the crystal structures of the sodium vanadates NaV_2O_4 and $NaVO_2$ show a close resemblance to the one of V_2O_3. While edge-sharing octahedra form layers of hexagonal six-membered rings in V_2O_3, NaV_2O_4, and $NaVO_2$ consist of $(VO_2)_n$ layers of edge-sharing octahedra with sodium atoms between the layers. In contrast, all sodium vanadates with V^{5+} are built of VO_4 tetrahedra, which either form corner-sharing chains along the c axis as in $NaVO_3$, $V_2O_7^{4-}$ anions as in $Na_4V_2O_7$ or are isolated tetrahedra as in Na_3VO_4. Among the different literature-known sodium vanadates, Na_3VO_4 and $NaVO_2$ represent the sodium vanadates, which have the highest ratio of sodium to vanadium and the lowest oxidation number of vanadium, respectively.[11]

Interestingly, after performing the reactions with 1, 2, and 4 equiv NaH in a furnace at 400 °C for 60 min under argon, the formation of the same products was observed. However, more additional unidentified reflections are present than in the ball-milled samples. Thus, the performance of these reactions in the ball mill at room temperature is not only faster but also leads to less unidentifiable products.

Some general trends can be deduced by comparing the sample compositions as obtained by Rietveld refinement for varying hydride concentrations.

1 With increasing NaH amounts, higher percentages of sodium vanadates are formed instead of vanadium oxides (Figure 4a). For example, V_2O_3 is the major phase with 1.5 and 2 equiv NaH, while (almost) no V_2O_3 or other vanadium oxides are present with 3 and 4 equiv sodium hydride. The samples prepared with 1 equiv NaH might be viewed as the exception since NaV_2O_5 (V in the oxidation state +IV/V) is the major phase independent of milling time. However, NaV_2O_5 is also an intercalate of V_2O_5 with a very similar crystal structure since sodium

https://doi.org/10.1021/acs.inorgchem.4c00200
Inorg. Chem. 2024, 63, 8099−8108

ions only intercalate between V_2O_5 layers (Supporting Information, Figures S1 and S8).

2 Lower oxidation states of vanadium are accessible with increasing hydride concentrations. For example, with 1 equiv NaH, the lowest observed oxidation state of vanadium is +IV. In contrast, $NaVO_2$ with vanadium in the oxidation state +III is only formed with 2.5 or more equivalents of NaH. Also, by going from 2.5 to 4 equiv NaH, the phase percentage of $NaVO_2$ steadily increases (Figure 3d–f). Furthermore, the average oxidation state of the final sample decreases with increasing hydride concentrations, as shown in Figure 4a, meaning that higher degrees of reduction are achieved.

3 The use of more NaH leads to the formation of sodium vanadates that are richer in sodium, as can be observed, for example, in the phase percentages of the three vanadates $NaVO_3$, $Na_4V_2O_7$, and Na_3VO_4 with vanadium in the oxidation state +V. While $NaVO_3$ is only present with 1 and 1.5 equiv NaH, $Na_4V_2O_7$ is formed in the case of 2 and 2.5 equiv NaH and Na_3VO_4, especially with 3 and 4 equiv of sodium hydride. Based on Pauling's rules on crystal structures, Na_3VO_4 consisting of isolated VO_4 tetrahedra is expected to be energetically more stable than $Na_4V_2O_7$ (isolated $V_2O_7^{4-}$ anions formed by two corner-sharing tetrahedra) and $NaVO_3$ (chains of corner-sharing VO_4 tetrahedra or even edge-sharing units depending on the polymorph) (Supporting Information, Figure S5–S7). Thus, the more Na_3VO_4 is formed with a higher hydride concentration, the more energy should be released during the reaction. This agrees well with the higher exothermicity observed for increasing NaH amounts. Subsequent theoretical calculations confirm the lower formation energy of Na_3VO_4 compared to the other two vanadates (vide infra).

As for longer milling times, the formation of oxides with vanadium in the oxidation state + III in the form of V_2O_3 and $NaVO_2$ augments, meaning that a slightly higher degree of reduction is achievable with longer milling times (Figure 4b). However, compared with varying sodium hydride concentrations, the sample composition changes only very little with milling time.

When the overall sample composition calculated from Rietveld refinement is compared to the expected one based on the initial ratio of the reagents (Supporting Information, Table S2–S7), the experimental sodium-to-vanadium ratio is too low, meaning that some sodium is missing in the final sample, especially with increasing milling times. This could originate from an amorphous phase, an amorphous side product such as Na_2O, and/or the presence of additional unidentified/literature-unknown sodium-rich vanadates. Therefore, the presence of amorphous phases was exemplarily checked for the samples obtained after 10 and 120 min of milling with 1.5 and 2 equiv NaH by adding 35 wt % silicon powder as an internal standard. Subsequent Rietveld refinement showed that the samples with 1.5 equiv NaH contained 11 and 19 wt % and with 2 equiv NaH 8 and 15 wt % of an amorphous phase after 10 and 120 min, respectively. Thus, it is very likely that the deviation between the experimental and theoretical sodium-to-vanadium ratios in the final sample can be explained by the presence of the amorphous phases. For example, in the case of V_2O_5 milled with 1.5 equiv NaH for 10 min, an overall sample composition formula of $Na_{1.5}V_2O_5$ is expected for the final product based on the initial ratio of the reactants. However, after performing the reaction in the mill, only a composition of $Na_{0.5}V_2O_{4.21}$ was found based on Rietveld refinement, meaning that the overall sodium-to-vanadium ratio is too low. After the PXRD measurement with silicon powder as an internal standard, the sample composition formula of the crystalline products was refined to $Na_{0.86}V_2O_{4.49}$. Assuming a composition of $Na_{2.0}V_{0.11}O_{4.05}$ ($Na_2O{\cdot}0.055\ V_2O_5$) for the amorphous phase, a composition formula of $Na_{1.5}V_2O_{4.83}$ can subsequently be deduced for the whole sample, which agrees very well with the expected theoretical composition within the evaluation accuracy of Rietveld refinement. Based on the derived composition of the amorphous phase, it can then be concluded that, along with smaller amounts of V^{5+}, the amorphous phase mainly consists of Na_2O, which explains the previously discussed deviation due to its abundance of sodium. To further investigate the deviation of the theoretical and experimental sample composition, the sample prepared with 1.5 equiv NaH and 10 min of milling was reoxidized by heating the sample in a platinum crucible to 350 °C under argon, followed by heating to 550 °C under a mixture of argon and oxygen. XRD analysis and Rietveld refinement showed that the sample consists of 5 wt % NaV_2O_5 (*Pmmn*), 64 wt % $NaVO_3$ (*C*2/*c*), and 31 wt % $Na_{1.2}V_3O_8$ ($P2_1/m1$) (Supporting Information, Figure S28), which corresponds to an overall sample composition of $Na_{1.52}V_2O_{5.71}$. This is in excellent agreement with the theoretical sodium/vanadium ratio of 1.5 and further supports the earlier hypothesis of sodium-containing amorphous phases. Moreover, the increase of the amorphous phase with increasing milling times is not surprising because of the continuous impact of the milling balls and is in line with a stronger deviation of the experimental and theoretical sodium-to-vanadium ratio for longer milling times.

To the best of our knowledge, the reactions of V_2O_5 and NaH have not been described in the literature yet. Nevertheless, the deduced general trends described above can still be compared with similar investigated systems, such as the solid-state reaction of V_2O_5 with LiH at 600 °C[30] or the reaction of V_2O_5 with different sodium-containing reaction partners, such as Na_2CO_3[37] or elemental sodium.[20] By studying the reaction behavior of V_2O_5 with LiH, Hagenmüller and Lesaicherre also observed the same trend that V_2O_3 is mainly formed with intermediate hydride concentrations, while the use of higher concentrations lead to only the formation of reduced lithium vanadates, which have lower oxidation states the more LiH is used. In contrast, low hydride concentrations favor the formation of $Li_xV_2O_5$ bronzes, which is in very good agreement with NaV_2O_5 bronze being the main phase with 1 equiv NaH in our case. Furthermore, in the high temperature reaction of V_2O_5 with Na_2CO_3, Barker observed a similar reaction trend regarding the sodium-to-vanadium ratio in sodium vanadates with V^{5+} as we did. As expected, higher Na_2CO_3 concentrations, meaning that more sodium is present in the reaction mixture, led to the formation of sodium vanadates that became increasingly richer in sodium. Thus, the observed trends for the product composition of our room-temperature mechanochemical approach are in overall good agreement with the results of high temperature approaches for similar systems reported in the literature. Due to the high exothermicity of the reactions, which have also been observed by other authors,[21,37] the same underlying processes seem to be present and are less dependent on the synthesis methods in terms of qualitative product composition.

https://doi.org/10.1021/acs.inorgchem.4c00200
Inorg. Chem. 2024, 63, 8099–8108

Table 1. Reaction Enthalpies (ΔH_r) and Reaction Enthalpies per Atomic Mass Unit of the Reactants ($\Delta H_{r,\ reactant}$) of the Possible Partial Reaction Equations for the Reduction of V_2O_5 with NaH to Reduced Vanadium Oxides and the Formation of Sodium Vanadates from Vanadium Oxides and Na_2O

Nr.	reaction	ΔH_r (eV)	$\Delta H_{r,\ reactant}$ (meV u^{-1})
1	$V_2O_5 + 2NaH \rightarrow 2VO_2 + Na_2O + H_2$ (1)	−1.16	−5.05
2	$3V_2O_5 + 10NaH \rightarrow 2V_3O_5 + 5Na_2O + 5H_2$ (2)	−3.66	−4.65
3	$V_2O_5 + 4NaH \rightarrow V_2O_3 + 2Na_2O + 2H_2$ (3)	−1.15	−4.14
4	$V_2O_5 + NaH \rightarrow NaV_2O_5 + 0.5H_2$ (4)	−2.39	−11.61
5	$V_2O_5 + Na_2O \rightarrow 2NaVO_3$ (5)	−3.43	−14.07
6	$V_2O_5 + 2Na_2O \rightarrow Na_4V_2O_7$ (6)	−5.62	−18.36
7	$V_2O_5 + 3Na_2O \rightarrow 2Na_3VO_4$ (7)	−7.63	−20.75
8	$V_2O_5 + 2VO_2 + Na_2O \rightarrow 2NaV_2O_5$ (8)	−3.51	−8.61
9	$V_2O_3 + 2VO_2 + Na_2O \rightarrow 2NaV_2O_4$ (9)	−2.55	−6.75
10	$V_2O_3 + Na_2O \rightarrow 2NaVO_2$ (10)	−1.42	−6.72

Table 2. Reaction Enthalpies (ΔH_r) and Reaction Enthalpies per Atomic Mass Unit of the Reactants ($\Delta H_{r,\ reactant}$) of the Overall Reaction Equations for the Reactions between V_2O_5 and NaH

Nr.	equiv NaH	reaction	ΔH_r (eV)	$\Delta H_{r,\ reactant}$ (meV u^{-1})
11	1	$V_2O_5 + NaH \rightarrow VO_2 + NaVO_3 + 0.5H_2$ (11)	−2.30	−11.15
12	1.33	$3V_2O_5 + 4NaH \rightarrow V_2O_3 + 4NaVO_3 + 2H_2$ (12)	−8.01	−12.49
13	2	$2V_2O_5 + 4NaH \rightarrow V_2O_3 + Na_4V_2O_7 + 2H_2$ (13)	−6.77	−14.72
14	2.4	$5V_2O_5 + 12NaH \rightarrow 3V_2O_3 + 4Na_3VO_4 + 6H_2$ (14)	−18.72	−15.64
15	3	$2V_2O_5 + 6NaH \rightarrow Na_3VO_4 + 3NaVO_2 + 3H_2$ (15)	−7.68	−15.13

As previously shown in Figure 3e,f, the sample composition of the samples prepared with 3 and 4 equiv NaH is quite similar, with $NaVO_2$ and Na_3VO_4 being the main two phases present in the reaction mixture. For both hydride concentrations, the molar ratio is approximately 3:1 after 10 min of milling. According to Pearson's Crystal Database, Na_3VO_4 has the highest sodium-to-vanadium ratio of the literature-known sodium vanadates, while the oxidation state of vanadium in $NaVO_2$ is the lowest experimentally observed oxidation state of vanadium in sodium vanadates.[11] The question thus arises whether the use of even more equivalents of sodium hydride leads to even lower oxidation states of the vanadium or to higher sodium contents in possibly literature-unknown sodium vanadates. In the next step, V_2O_5 was therefore ball milled with 6 equiv NaH for 10 min, resulting in the formation of a fine black powder. Rietveld refinement showed that next to unreacted NaH (3 wt %) and elemental sodium (6 wt %), the sample only consists of $NaVO_2$ (63 wt %) and Na_3VO_4 ($P2_13$:17 wt %,*Pnma*: 11 wt %) in a molar ratio of around 4:1 (Supporting Information, Figure S29). This shows that even with higher concentrations of sodium hydride, no lower oxidation states of the vanadium or higher sodium contents in possibly literature-unknown sodium vanadates can be achieved. The formation of only $NaVO_2$ and Na_3VO_4 with an excess of the sodium-containing reducing agent is in very good agreement with the results of Barker and Hooper. After adding V_2O_5 to an excess of liquid sodium at 150−600 °C, they also only observed the formation of $NaVO_2$ and Na_3VO_4, along with sometimes VO depending on the purification process.

Evaluation of Possible Reaction Pathways and Driving Forces Using Quantum Mechanical Calculations. To further understand these exothermic mechanochemical reactions between V_2O_5 and NaH and to evaluate which conceivable reaction pathways are energetically most favorable, quantum mechanical calculations using the Vienna ab initio package (VASP) were performed. In a first step, the formation enthalpies of the reactants and all experimentally observed products were calculated (Supporting Information, Table S12). Since the formation energies of different polymorphs are very similar to each other for all oxides, the lowest formation energy of the polymorphs was used in each case to calculate and compare the reaction energies.

Partial reaction equations were first formulated for the reduction of V_2O_5 with NaH to the reduced oxides VO_2, V_3O_5, and V_2O_3 (Table 1, eqs 1−3) as well as for the formation of sodium vanadates from vanadium oxides with sodium oxide (Table 1, eqs 4−10) to facilitate further discussion. These partial reaction equations can then be combined into overall reaction eqs (Table 2, eqs 11−15) to explain the experimental findings. For easy comparison, all reaction energies are also normalized to the atomic mass unit (u) of the reactants.

In comparison with literature data, our calculated potential of gaseous hydrogen (−6.41 eV) is slightly lower than that calculated by Cheng et al. (−6.677 eV)[39] and Kresse (−6.8 eV).[40] This discrepancy can be explained by the use of different computational methods and calculation parameters. As for the formation energies of the sodium vanadates $NaVO_3$, $Na_4V_2O_7$, and Na_3VO_4, it can be stated that our calculated formation energies for these oxides are in excellent agreement with the values tabulated by Vdovin et al. (Supporting Information, Table S13).[41]

As shown in Table 2, the reaction enthalpies per atomic mass unit of the reactants $\Delta H_{r,\ reactant}$ range roughly between −11 and −16 meV u^{-1}, showing that all reactions are highly exothermic. A general criterion of self-propagating reactions is an adiabatic temperature greater than 1800 K.[42] Hereby, the adiabatic

https://doi.org/10.1021/acs.inorgchem.4c00200
Inorg. Chem. 2024, 63, 8099−8108

temperature can be approximated by dividing the reaction enthalpy by the heat capacity of the product,[43] which are both ideally known for the same temperature. In the literature, only the specific heat capacities of V_2O_5, V_2O_3, $NaVO_3$, $Na_4V_2O_7$, and Na_3VO_4 can be found for temperatures above room temperature. Since they all lie in the range of 0.7 to 0.9 J g^{-1} K^{-1} (Supporting Information, Table S14), 0.8 J g^{-1} K^{-1} can be estimated as a base to get an approximate idea of the possible temperature increases for the reactions described in Table 2. Thus, with the reaction enthalpies of eqs 11 (−11 meV u^{-1}) and 14 (−16 meV u^{-1}) and a heat capacity of 0.8 J g^{-1} K^{-1}, temperature variations of 1327 and 1930 K are calculated, respectively. Since both obtained temperatures are either close to or above the temperature criterion of 1800 K, this approximation supports that the occurring reactions take place in a self-sustaining manner.

As expected, reactions with a low ratio of NaH to V_2O_5 dominate at low hydride concentrations. For example, only VO_2 is formed with 1 equiv NaH instead of other reduced vanadium oxides such as V_3O_5 or V_2O_3 because this reaction is energetically more favorable (eqs 1−3). However, since the formation of NaV_2O_5 (ratio of NaH to V_2O_5 is 1:1) has a lower formation energy of ΔH_r = −2.39 eV than the formation of VO_2 and $NaVO_3$ (ΔH_r = −2.30 eV), NaV_2O_5 will be formed predominantly, as observed experimentally. Thus, the theoretical equations can be used to model and explain the experimental findings.

Even though the formation of VO_2 remains energetically favored with 1.5 and 2 equiv NaH (Supporting Information, Tables S11−S12), V_2O_3 with V^{3+} is mainly (1.5 equiv of NaH) or exclusively (2 equiv of NaH) formed with increasing hydride concentrations. For example, in the case of 2 equiv NaH, no unreacted V_2O_5 would be left according to eq 1 if V_2O_5 was only reduced to VO_2. Consequently, no further reaction would be possible (Supporting Information, Table S16). In contrast, only 50% of the initial V_2O_5 is consumed during the reduction to V_2O_3, meaning that the remaining 50% V_2O_5 can further react with Na_2O to form $Na_4V_2O_7$. Similarly, 20% more $NaVO_3$ can be formed in the case of 1.5 equiv NaH if the reduction proceeds until V_2O_3 (Supporting Information, Table S15). Compared to the reductions to vanadium oxides or other sodium vanadates, the energies of formation of sodium vanadates with V^{5+} ($NaVO_3$, $Na_4V_2O_7$, and Na_3VO_4) are significantly lower (Table 1). As a result, the reduction to V_2O_3 with the formation of $NaVO_3$, $Na_4V_2O_7$, or Na_3VO_4 is ultimately more energetically favorable than the reduction to VO_2, which also explains why VO_2 is observed experimentally only with the use of 1 equiv of sodium hydride. The formation of these sodium vanadates with V^{5+} can therefore be viewed as a driving force for the reaction between V_2O_5 and NaH.

Even though the formation of Na_3VO_4 is thermodynamically most favored, it is only formed in significant amounts with more than 2.5 equiv NaH. With the use of less sodium hydride, $NaVO_3$ and $Na_4V_2O_7$ are favored since mechanochemical reactions are usually kinetically controlled, and less sodium must diffuse in these cases. The more NaH is present during the reaction, sodium-richer vanadates are formed. Experimentally, it was further observed that sodium vanadates with V^{3+} are only formed if more than 2.5 equiv NaH are used for the reaction. Looking at reactions 29 and 35 (Supporting Information), more V_2O_3 is formed during the reduction of V_2O_5, which can then react in an exothermic reaction to reduced sodium vanadates NaV_2O_4 and $NaVO_2$ (Supporting Information Tables S13−S14). As described before, the use of more than 3 equiv NaH always leads to the same main phases, Na_3VO_4 and $NaVO_2$, according to the reactions presented in Table S17 (Supporting Information).

While most of the experimental sample compositions can be described well with a combination of the reaction equations shown in Table 1, they do not represent the high percentage of V_2O_3 formed with 1.5 and 2 equiv NaH after longer milling times. In the literature, V_2O_3 is often prepared via solid-state reduction of V_2O_5 with hydrogen gas at high temperatures.[44] In theory, it is therefore also conceivable that large amounts of V_2O_3 are formed with prolonged ball milling due to the reduction of unreacted V_2O_5 with freshly formed hydrogen gas originating from the decomposition of NaH, the presence of which was detected by the positive oxyhydrogen sample. Since no significant pressure decrease is observed after the initial pressure drop, this scenario seems unlikely. On the other hand, the presence of smaller, unknown reflections renders the identification and explanation of all occurring processes difficult. Furthermore, all VASP calculations are performed at 0 K, meaning that no entropic effects are considered, which will still be present during our ball milling reactions. Nonetheless, the performed VASP calculations give a better insight into the occurring reactions and help with the understanding of the observed sample compositions.

CONCLUSIONS

In conclusion, the simple and rapid room-temperature mechanochemical reaction between V_2O_5 and sodium hydride was systematically investigated. After only a few minutes of milling, a large increase in pressure inside the milling jar was observed due to the exothermicity of the reaction and the formation of hydrogen gas, as evidenced by a positive oxyhydrogen test. Depending on the synthesis conditions, a mixture of different vanadium oxides and sodium vanadates with vanadium oxidation states ranging from +V to +III was identified by Rietveld refinement. Hereby, the hydride concentration has a greater influence on the final sample composition than on the milling time. In general, with increasing amounts of NaH, higher percentages of sodium vanadates are formed instead of vanadium oxides; sodium vanadates with V^{5+} become richer in sodium and lower oxidation states of vanadium are accessible. Subsequent VASP calculations showed that the formulated total reaction equations become more exothermic as more hydride is used for the ball mill process, which agrees nicely with the experimental observations. Furthermore, the formation of sodium vanadates with V^{5+} is energetically most favored, causing the reduction of V_2O_5 to V_2O_3 to be overall more favorable than the reduction to VO_2. The formation of these sodium vanadates with V^{5+} is therefore the driving force for the observed strongly exothermic reactions between V_2O_5 and NaH.

ASSOCIATED CONTENT

Supporting Information

The Supporting Information is available free of charge at https://pubs.acs.org/doi/10.1021/acs.inorgchem.4c00200.

Additional powder X-ray and Rietveld refinement data, discussion of crystal structures, pressure courses during milling, and quantum chemical data (PDF)

Additional movie of a mortar reaction (MOV)

https://doi.org/10.1021/acs.inorgchem.4c00200
Inorg. Chem. 2024, 63, 8099−8108

AUTHOR INFORMATION

Corresponding Author

Guido Kickelbick − *Inorganic Solid-State Chemistry, Saarland University, 66123 Saarbrücken, Germany; Saarene − Saarland Center for Energy Materials and Sustainability, 66123 Saarbrücken, Germany;* orcid.org/0000-0001-6813-9269; Email: guido.kickelbick@uni-saarland.de

Authors

Anna Michaely − *Inorganic Solid-State Chemistry, Saarland University, 66123 Saarbrücken, Germany*

Christopher Luckas − *Inorganic Solid-State Chemistry, Saarland University, 66123 Saarbrücken, Germany;* orcid.org/0000-0001-5167-410X

Robert Haberkorn − *Inorganic Solid-State Chemistry, Saarland University, 66123 Saarbrücken, Germany;* orcid.org/0000-0002-4605-3760

Complete contact information is available at: https://pubs.acs.org/10.1021/acs.inorgchem.4c00200

Notes

The authors declare no competing financial interest.

ACKNOWLEDGMENTS

Instrumentation and technical assistance for this work were provided by the Service Center X-ray Diffraction, with financial support from the Saarland University and German Science Foundation (project number INST 256/349-1).

REFERENCES

(1) Simard, G. L.; Steger, J. F.; Arnott, R. J.; Siegel, L. A. Vanadium Oxides as Oxidation Catalysts. *Ind. Eng. Chem.* **1955**, *47* (7), 1424−1430.

(2) (a) Hassan, N.; Riaz, J.; Qureshi, M. T.; Razaq, A.; Rahim, M.; Toufiq, A. M.; Shakoor, A. Vanadium oxide (V_2O_3) for energy storage applications through hydrothermal route. *J. Mater. Sci.: Mater. Electron.* **2018**, *29* (18), 16021−16026. (b) Liu, M.; Su, B.; Tang, Y.; Jiang, X.; Yu, A. Recent Advances in Nanostructured Vanadium Oxides and Composites for Energy Conversion. *Adv. Energy Mater.* **2017**, *7* (23), 1700885.

(3) Hu, P.; Hu, P.; Vu, T. D.; Li, M.; Wang, S.; Ke, Y.; Zeng, X.; Mai, L.; Long, Y. Vanadium Oxide: Phase Diagrams, Structures, Synthesis, and Applications. *Chem. Rev.* **2023**, *123* (8), 4353−4415.

(4) Cunha, Á.; Martins, J.; Rodrigues, N.; Brito, F. P. Vanadium redox flow batteries: a technology review. *Int. J. Energy Res.* **2015**, *39* (7), 889−918.

(5) Zhang, X.; Sun, X.; Li, X.; Hu, X.; Cai, S.; Zheng, C. Recent progress in rate and cycling performance modifications of vanadium oxides cathode for lithium-ion batteries. *J. Energy Chem.* **2021**, *59*, 343−363.

(6) Zhang, X.; Zhang, Z.; Xu, S.; Xu, C.; Rui, X. Advanced Vanadium Oxides for Sodium-Ion Batteries. *Adv. Funct. Mater.* **2023**, *33*, 2306055.

(7) Boruah, B. D.; Wen, B.; De Volder, M. Light Rechargeable Lithium-Ion Batteries Using V_2O_5 Cathodes. *Nano Lett.* **2021**, *21* (8), 3527−3532.

(8) (a) Kang, Y.-B. Critical evaluation and thermodynamic optimization of the VO-$VO_{2.5}$ system. *J. Eur. Ceram. Soc.* **2012**, *32* (12), 3187−3198. (b) Wriedt, H. A. The O-V (Oxygen-Vanadium) system. *Bull. Alloy Phase Diagrams* **1989**, *10* (3), 271−277.

(9) Schwingenschlögl, U.; Eyert, V. The vanadium Magnéli phases V_nO_{2n-1}. *Ann. Phys.* **2004**, *516* (9), 475−510.

(10) Bahlawane, N.; Lenoble, D. Vanadium Oxide Compounds: Structure, Properties, and Growth from the Gas Phase. *Chem. Vap. Deposition* **2014**, *20* (7−8-9), 299−311.

(11) Crystal Impact. *Pearson's Crystal Data: Crystal Structure Database for Inorganic Compounds. Release 2022/23*; ASM International: Materials Park: Ohio (USA), 2023.

(12) Pei, G.; Xiang, J.; Yang, L.; Jin, X.; Lv, X. Thermodynamic properties of sodium pyrovanadate ($Na_4V_2O_7$) at high temperature (298.15−873 K). *Calphad* **2020**, *70*, 101802.

(13) Petranikova, M.; Tkaczyk, A. H.; Bartl, A.; Amato, A.; Lapkovskis, V.; Tunsu, C. Vanadium sustainability in the context of innovative recycling and sourcing development. *Waste Manag.* **2020**, *113*, 521−544.

(14) Su, B.; Wu, S.; Liang, H.; Zhou, W.; Liu, J.; Goonetilleke, D.; Sharma, N.; Sit, P. H.-L.; Zhang, W.; Yu, D. Y. W. High-Performance $NaVO_3$ with Mixed Cationic and Anionic Redox Reactions for Na-Ion Battery Applications. *Chem. Mater.* **2020**, *32* (20), 8836−8844.

(15) Su, B.; Liang, H.; Liu, J.; Wu, J.; Sharma, N.; Gu, Q.; Johannessen, B.; Yu, D. Y. W. Novel structurally-stable Na-rich $Na_4V_2O_7$ cathode material with high reversible capacity by utilization of anion redox activity. *Chem. Commun.* **2020**, *56* (59), 8245−8248.

(16) (a) Didier, C.; Guignard, M.; Darriet, J.; Delmas, C. O′3-Na_xVO_2 System: A Superstructure for $Na_{1/2}VO_2$. *Inorg. Chem.* **2012**, *51* (20), 11007−11016. (b) Didier, C.; Guignard, M.; Suchomel, M. R.; Carlier, D.; Darriet, J.; Delmas, C. Thermally and Electrochemically Driven Topotactical Transformations in Sodium Layered Oxides Na_xVO_2. *Chem. Mater.* **2016**, *28* (5), 1462−1471.

(17) Lu, J.; Zhang, D.; Wang, Y.; Ni, S. Na_3VO_4 as a new anode material for lithium-ion batteries. *New J. Chem.* **2021**, *45* (26), 11506−11511.

(18) Rana, D.; Kumar, A. Is there a Role for Sodium Orthovanadate in the Treatment of Diabetes? *Curr. Diabetes Rev.* **2019**, *15* (4), 284−287.

(19) (a) Kolta, G. A.; Hewaidy, I. F.; Felix, N. S.; Girgis, N. N. Reactions between sodium carbonate and vanadium pentoxide. *Thermochim. Acta* **1973**, *6* (2), 165−177. (b) Chamberland, B. L.; Porter, S. K. A study on the preparation and physical property determination of $NaVO_2$. *J. Solid State Chem.* **1988**, *73* (2), 398−404.

(20) Barker, M. G.; Hooper, A. J. Reactions of Liquid Sodium with Transition-metal Oxides. Part VI. Oxides of Vanadium. *J. Chem. Soc., Dalton Trans.* **1973**, No. 15, 1520−1522.

(21) Barker, M. G.; Hooper, A. J. Reactions of Sodium Oxide with the Oxides VO_2, V_2O_3, VO, and Vanadium Metal. *J. Chem. Soc., Dalton Trans.* **1973**, No. 15, 1517−1519.

(22) Rüdorff, W.; Becker, H. Notizen: Über Umsetzungen des Vanadin(III)oxyds und des Vanadin(IV)oxyds mit einigen Metalloxyden. *Z. Naturforsch., B: J. Chem. Sci.* **1954**, *9* (9), 613−614.

(23) Baláž, P.; Achimovičová, M.; Baláž, M.; Billik, P.; Cherkezova-Zheleva, Z.; Criado, J. M.; Delogu, F.; Dutková, E.; Gaffet, E.; Gotor, F. J.; et al. Hallmarks of mechanochemistry: from nanoparticles to technology. *Chem. Soc. Rev.* **2013**, *42*, 7571−7637.

(24) Rojac, T.; Trtnik, Ž.; Kosec, M. Mechanochemical reactions in Na_2CO_3-M_2O_5 (M = V, Nb, Ta) powder mixtures: Influence of transition-metal oxide on reaction rate. *Solid State Ionics* **2011**, *190*, 1−7.

(25) Haberkorn, R.; Bauer, J.; Kickelbick, G. Chemical Sodiation of V_2O_5 by Na_2S. *Z. Anorg. Allg. Chem.* **2014**, *640* (15), 3197−3202.

(26) Takai, C.; Senna, M.; Hoshino, S.; Razavi-Khosroshahi, H.; Fuji, M. Chemical and thermal properties of VO_2 mechanochemically derived from V_2O_5 by co-milling with paraffin wax. *RSC Adv.* **2018**, *8* (38), 21306−21315.

(27) Yang, H.; McCormick, P. G. Mechanochemical Reduction of V_2O_5. *J. Solid State Chem.* **1994**, *110* (1), 136−141.

(28) Mukherjee, A.; Krishnamurthy, N. Phase evolution during mechanochemical coreduction of V_2O_5 and TiO_2 with Al. *Int. J. Self-Propag. High-Temp. Synth.* **2010**, *19* (4), 237−243.

(29) Michaely, A.; Janka, O.; Gießelmann, E. C. J.; Haberkorn, R.; Wiedemann, H. T. A.; Kay, C. W. M.; Kickelbick, G. Black Titania and Niobia within Ten Minutes - Mechanochemical Reduction of Metal Oxides with Alkali Metal Hydrides. *Chem.—Eur. J.* **2023**, *29* (29), No. e202300223.

(30) Hagenmuller, P.; Lesaicherre, A. La réduction de l'anhydride vanadique par l'hydrure de lithium. *Compt. Rend.* **1963**, *256*, 170−171.

https://doi.org/10.1021/acs.inorgchem.4c00200
Inorg. Chem. 2024, 63, 8099−8108

(31) *Topas 5*; Bruker AXS: Karlsruhe (Germany), 2014.
(32) Cheary, R. W.; Coelho, A. A.; Cline, J. P. Fundamental Parameters Line Profile Fitting in Laboratory Diffractometers. *J. Res. Natl. Inst. Stand. Technol.* **2004**, *109* (1), 1−25.
(33) Blöchl, P. E. Projector augmented-wave method. *Phys. Rev. B: Condens. Matter Mater. Phys.* **1994**, *50* (24), 17953−17979.
(34) (a) Kresse, G.; Furthmüller, J. Efficient iterative schemes for *ab initio* total-energy calculations using a plane-wave basis set. *Phys. Rev. B: Condens. Matter Mater. Phys.* **1996**, *54* (16), 11169−11186. (b) Kresse, G.; Furthmüller, J. Efficiency of ab-initio total energy calculations for metals and semiconductors using a plane-wave basis set. *Comput. Mater. Sci.* **1996**, *6* (1), 15−50. (c) Kresse, G.; Joubert, D. From ultrasoft pseudopotentials to the projector augmented-wave method. *Phys. Rev. B: Condens. Matter Mater. Phys.* **1999**, *59* (3), 1758−1775.
(35) Perdew, J. P.; Ruzsinszky, A.; Csonka, G. I.; Vydrov, O. A.; Scuseria, G. E.; Constantin, L. A.; Zhou, X.; Burke, K. Restoring the Density-Gradient Expansion for Exchange in Solids and Surfaces. *Phys. Rev. Lett.* **2008**, *100* (13), 136406.
(36) Jalaly, M.; Gotor, F. J.; Sayagués, M. J. Mechanochemical combustion synthesis of vanadium carbide (VC), niobium carbide (NbC) and tantalum carbide (TaC) nanoparticles. *Int. J. Refract. Met. Hard Mater.* **2019**, *79*, 177−184.
(37) Barker, M. G.; Hooper, A. J. Preparation and X-Ray Powder Diffraction Patterns of the Sodium Vanadates $NaVO_3$, $Na_4V_2O_7$, and Na_3VO_4. *J. Chem. Soc., Dalton Trans.* **1973**, No. 15, 1513−1517.
(38) Kubaschewski, O.; Hoster, T.; Schlim, R. The Heats of Formation of Some Sodium and Barium Vanadates and Molybdates. *Ber. Bunsenges. Phys. Chem.* **1981**, *85* (5), 367−369.
(39) Cheng, H.; Pez, G.; Kern, G.; Kresse, G.; Hafner, J. Hydrogen Adsorption in Potassium-Intercalated Graphite of Second Stage: An ab Initio Molecular Dynamics Study. *J. Phys. Chem. B* **2001**, *105* (3), 736−742.
(40) Kresse, G. Dissociation and sticking of H_2 on the Ni(111), (100), and (110) substrate. *Phys. Rev. B: Condens. Matter Mater. Phys.* **2000**, *62* (12), 8295−8305.
(41) Vdovin, V. V.; Edil'baev, A. I.; Kozlov, V. A.; Karpov, A. A.; Spitsyn, V. A.; Terlikbaeva, A. Z.; Pechenkina, A. A. Thermodynamic analysis of the reaction of vanadium oxides with oxides of sodium, potassium, calcium, barium, and manganese. *Steel Translat.* **2007**, *37* (9), 787−791.
(42) Munir, Z. A.; Anselmi-Tamburini, U. Self-propagating exothermic reactions: The synthesis of high-temperature materials by combustion. *Mater. Sci. Rep.* **1989**, *3* (7−8), 277−365.
(43) Takacs, L. Self-sustaining reactions induced by ball milling. *Prog. Mater. Sci.* **2002**, *47* (4), 355−414.
(44) Brauer, G. *Handbuch der Präparativen Anorganischen Chemie Dritter Band*; Ferdinand Enke Verlag, 1981.

https://doi.org/10.1021/acs.inorgchem.4c00200
Inorg. Chem. 2024, 63, 8099−8108

3.3 Mechanochemical reduction of V_2O_5: Alkali metals vs. Alkali Metal Hydrides – Which are the better Reducing Agents?

3.3.1 Introduction

As shown in the previous chapter, the mechanochemical reaction of V_2O_5 with NaH as a reducing agent occurs in a self-propagating manner in the ball mill after only a few minutes of milling, resulting in the formation of different vanadium oxides and sodium vanadates depending on the initial hydride concentration. Due to the lower standard potential of the redox pair Na^+/Na (–2.71 eV) compared to H_2/H^- (–2.23 eV),[23] elemental sodium should be an even stronger reducing agent than NaH. Furthermore, under the assumption that the same products are formed with NaH and Na, the reactions with sodium should be energetically more favored due to expected lower (more exothermic) reaction energies issuing from the lower standard enthalpy of formation from NaH (–56.3 kJ mol^{-1}) compared to Na (0 kJ mol^{-1}).[23]
The previous study is therefore extended by ball milling V_2O_5 with varying amounts of Na and by comparing the obtained sample compositions to those obtained with NaH.[65] In addition, both LiH and Li were also applied as reducing agents to evaluate the generality of this concept. In comparison to sodium, an even stronger reaction is anticipated for lithium due to the comparatively lower standard potential of the redox pair Li^+/Li (–3.04 eV).[23]

The results of this study are unpublished. Reactions with 1 and 2 eq. LiH were first carried out and characterized by Christopher Luckas during his bachelor thesis under the supervision of Anna Michaely and Guido Kickelbick.[337] Anna Michaely later revisited the Rietveld refinement of both samples and performed and characterized the remaining experiments with 3 and 4 eq. LiH, as well as all reactions with elemental lithium and sodium. She also performed the quantum chemical calculations.

3.3.2 Results and Discussion

Quantum mechanical calculations

Quantum mechanical calculations using the Vienna Ab initio Simulation Package (VASP) were initially conducted to better assess the anticipated differences in exothermicity between alkali metal hydrides (NaH and LiH) and their corresponding elemental forms (Na and Li) as mechanochemical reducing agents for V_2O_5. It was assumed that the reaction behavior, in terms of the main products formed, would be similar to that observed in the mechanochemical reduction of V_2O_5 with NaH, which could later be confirmed through ball milling experiments.

The formation enthalpies of the reactants and the expected main products were calculated (Supporting Information, Chapter 6.3, Table S1), with the lowest formation energy for each polymorph being used to determine the reaction energies. After calculating the partial reaction equations for the reduction of V_2O_5 to reduced oxides VO_2, V_3O_5 and V_2O_3, the formation energies of alkali metal vanadates from vanadium oxides with Li_2O and Na_2O were determined (Table 1). For easy comparison, all reaction energies are normalized to one mol V_2O_5 or V_2O_3. As previously shown, the formation of sodium vanadates, especially of ones with V^{5+}, seems to be the driving force for the exothermic reactions in the case of NaH and Na.[65] While the formation of lithium vanadate Li_3VO_4 with V^{5+} also shows a high exothermicity, the reduction of V_2O_5 to reduced vanadium oxides such as V_2O_3 seem to be even more energetically favorable for lithium-involving reactions compared to sodium ones. This can be attributed to the higher stability of Li_2O (–14.75 eV) compared to Na_2O (–11.94 eV).

Table 1: Reaction enthalpies per mol V_2O_5 or V_2O_3 (ΔH_r) of the possible partial reaction equations for the reduction of V_2O_5 with Na(H) and Li(H) to reduced vanadium oxides and the formation of alkali metal vanadates from vanadium oxides and the respective alkali metal oxide. Hereby, *A* represents Na and Li. For easier comparison, our previous results with NaH are shown again.[65] H_2 formation has only been considered for reactions that were performed with the respective hydride.

Nr.	Reaction	$\Delta H_{r, NaH}$ (eV)	$\Delta H_{r, Na}$ (eV)	$\Delta H_{r, LiH}$ (eV)	$\Delta H_{r, Li}$ (eV)
1	$V_2O_5 + 2\ A(H) \rightarrow 2\ VO_2 + A_2O\ (+ H_2)$	–1.16	–2.03	–2.18	–3.97
2	$3\ V_2O_5 + 10\ A(H) \rightarrow 2\ V_3O_5 + 5\ A_2O\ (+ 5\ H_2)$	–1.22	–2.66	–2.91	–5.90
3	$V_2O_5 + 4\ A(H) \rightarrow V_2O_3 + 2\ A_2O\ (+ 2\ H_2)$	–1.15	–2.89	–3.18	–6.77
4	$V_2O_5 + A(H) \rightarrow AV_2O_5\ (+ 0.5\ H_2)$	–2.39	–2.82	–2.09	–2.99
5	$V_2O_5 + A_2O \rightarrow 2\ AVO_3$	–3.43	–3.43	–1.90	–1.90
6	$V_2O_5 + 2\ A_2O \rightarrow A_4V_2O_7$[a]	–5.62	–5.62	-	-
7	$V_2O_5 + 3\ A_2O \rightarrow 2\ A_3VO_4$	–7.63	–7.63	–5.46	–5.46
9	$V_2O_3 + A_2O \rightarrow 2\ AVO_2$	–1.42	–1.42	–1.22	–1.22

[a] $Li_4V_2O_7$ is not known to literature. Therefore, no reaction enthalpies have been calculated.

Total reaction equations are then derived by combining the partial reactions tabulated in Table 1 and normalized to the atomic mass unit (u) of reactants for easier comparison. As shown in Table 2, calculated reaction enthalpies range from –5.47 to –47.63 meV u^{-1}, confirming their exothermic nature. A notable exception is the reduction of V_2O_5 with NaH to elemental vanadium with an endothermic reaction enthalpy of 4.94 meV u^{-1} (Table 2, Equation 17). This can most likely be attributed to the formation of large amounts of Na_2O, which is less stable

and therefore energetically less favored compared to Li_2O. For all established reaction equations, those involving elemental alkali metals are more exothermic compared to their respective alkali metal hydrides, which is consistent with the previous considerations. Additionally, a lower standard potential of the redox pair appears to correlate with a more exothermic reaction. Based on the quantum mechanical calculations, elemental lithium is expected to provide the highest degree of reduction and the most exothermic reactions.

Table 2: Reaction enthalpies per mol V_2O_5 (ΔH_r) of the overall reaction equations for the reactions between V_2O_5 and Na(H) and Li(H), normalized to the atomic mass unit of the reactants. Hereby, *A* stands for Na and Li. For easier comparison, our previous results for NaH are shown again.[65] H_2 formation has only been considered for reactions that were performed with the respective hydride.

Nr.	eq. *M*	Reaction	$\Delta H_{r, NaH}$ (meV u^{-1})	$\Delta H_{r, Na}$ (meV u^{-1})	$\Delta H_{r, LiH}$ (meV u^{-1})	$\Delta H_{r, Li}$ (meV u^{-1})
10	1	3 V_2O_5 + 3 *A*(H) → 2 VO_2 + 2 *A*VO_3 + *A*V_2O_5 (+ 1.5 H_2)	–11.31	–13.48	–10.83	–15.65
12	1.33	3 V_2O_5 + 4 *A*(H) → V_2O_3 + 4 *A*VO_3 (+ 2 H_2)	–12.49	–15.28	–12.09	–18.44
13	2	2 V_2O_5 + 4 *A*(H) → V_2O_3 + $A_4V_2O_7$ (+ 2 H_2)[a]	–14.72	–18.65	-	-
14	2.4	5 V_2O_5 + 12 *A*(H) → 3 V_2O_3 + 4 A_3VO_4 (+ 6 H_2)	–18.72	–20.18	–20.36	–31.47
15	3	2 V_2O_5 + 6 *A*(H) → A_3VO_4 + 3 *A*VO_2 (+ 3 H_2)	–7.68	–20.49	–22.66	–36.29
16	4	V_2O_5 + 4 *A*(H) → 2 *A*VO_2 + A_2O (+ 2 H_2)	–9.27	–15.74	–20.57	–38.10
17	10	V_2O_5 + 10 *A*(H) → 2 V + 5 A_2O (+5 H_2)	+4.94	–5.47	–11.44	–47.63

[a] $Li_4V_2O_7$ is not known to literature. Therefore, no reaction enthalpies have been calculated.

Evolution of pressure during ball milling

To compare the reaction behavior of the different reducing agents 1, 2, 3, and 4 eq. of NaH, Na sand, LiH and Li powder were milled with V_2O_5 at 300 rpm for 10 min in the mechanochemical reaction with V_2O_5. The evolution of the pressure inside the milling jar was studied using the EASY GTM system by Fritsch. As with NaH,[65] a sharp pressure increase, indicative of a combustion event, was observed for both alkali metals and LiH (Figure 18), suggesting that all reactions are self-propagating and highly exothermic. Only the reaction with 1 eq. LiH did not result in a significant pressure increase (Figure 18c) after 10 min of milling, suggesting that longer milling times would be necessary to induce a reaction and that the observed cementation inside the milling jar must be prevented.

After the strong initial pressure spike, the pressure rapidly decreases before attaining constant values between 4 and 9 bar for NaH and LiH (Figure 18a, c). The final elevated pressure is attributed to the evolution of hydrogen. The higher the initial hydride concentration, the higher the pressure increases, and the later the reaction is induced. To avoid exceeding the maximum pressure tolerance of the milling jars of 20 bar, the mass of the reaction mixture was reduced in case of 3 and 4 eq. of hydride.

In contrast, during reactions with elemental sodium and lithium, the maximum pressure did not exceed 1.4 bar and quickly returned to its original level (Figure 18b, d). This indicates that no significant amounts of gaseous byproducts such as oxygen were formed, which is consistent with the absence of an increase in oxygen inside the glovebox when the milling jar was opened. Instead, the observed pressure rise is attributed to a sudden release of energy. According to the ideal gas law, the maximum pressure increases from 0.6 to 1.4 bar, which would correspond to brief temperature spikes of approximately 180 to 420 °C. This underlines the strong exothermicity and formation of the observed thermites. Overall, the lack of elevated final pressures significantly reduces safety concerns related to excessive pressure buildup during milling, unlike in the case of the respective hydrides. As observed with alkali metal hydrides, higher maximum pressures are attained with increasing concentrations of alkali hydrides, suggesting that the reactions become more exothermic, which aligns with our calculations.

While the induction period for reactions with NaH and LiH ranged from 30 s to several minutes, all reactions with elemental sodium and lithium as reducing agents started in less than one minute of milling. In particular, the use of lithium powder resulted in an instantaneous ignition upon milling. The activation energy is so low that the highly exothermic reaction was even triggered accidentally by lightly mixing both V_2O_5 and Li powder with a spatula inside the glovebox, which was not observed for the other tested reducing agents. As evidenced by the

earlier reaction ignition, reactions with alkali metals seem to have lower activation energies than with the respective hydrides. This is in accordance with the calculated lower (more exothermic) reaction enthalpies under the assumption that similar reactions occur during milling according to the empirical Bell-Evans-Polyani principle, which states that there is a linear relationship between the activation energy and the reaction enthalpy for closely related reactions. [338, 339]

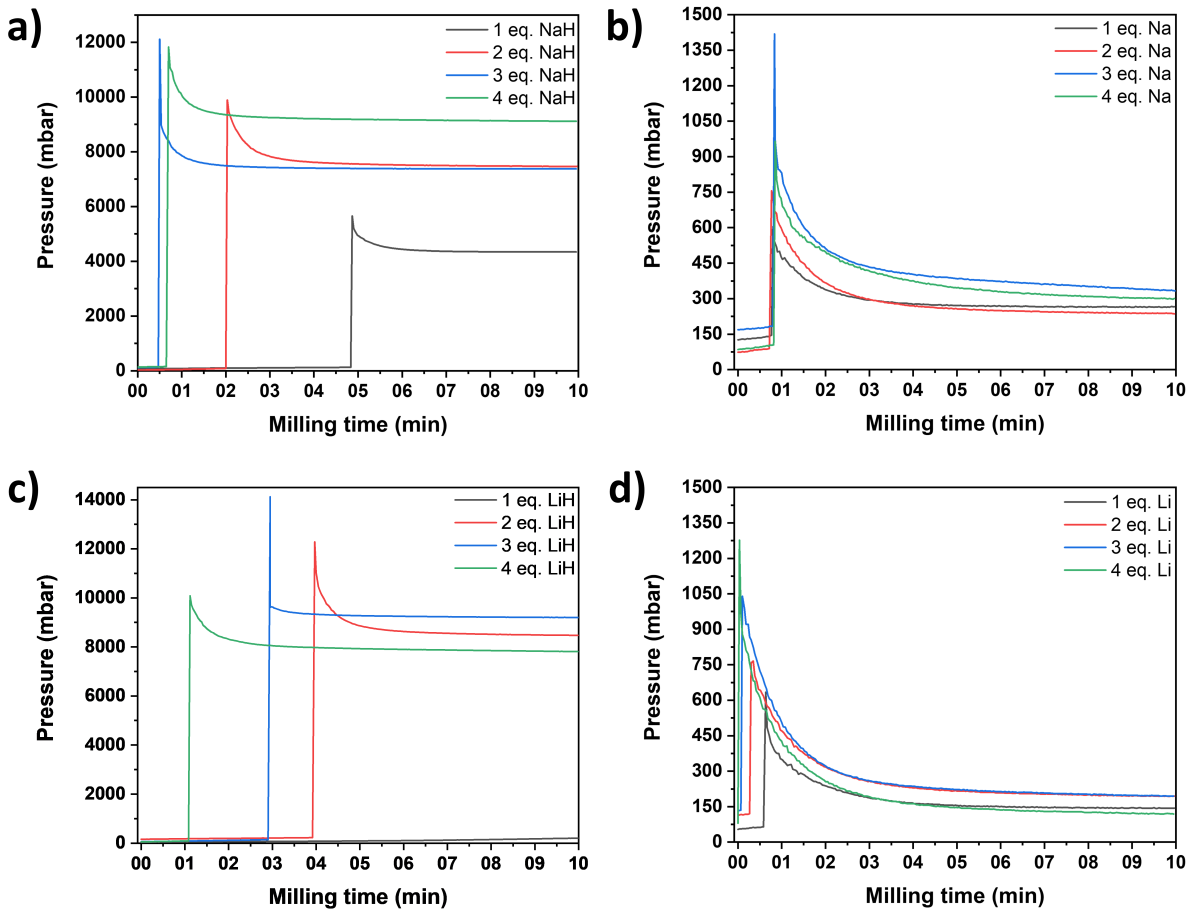

Figure 18: Evolution of the pressure inside the milling jar during milling of V_2O_5 with 1 to 4 eq. of (a) sodium hydride, (b) sodium, (c) lithium hydride, and (d) lithium. Note the different pressure scales. The pressure sensor inside the milling equipment is referenced to atmospheric pressure and initial pressures before milling therefore often range between 30 and 130 mbar. For easier comparison, our previous results with NaH are shown again in (a).[65]

Color change during ball milling and X-ray diffraction analysis

After milling, samples with colors ranging from dark green to black were obtained, depending on the type and concentration of the reducing agent, in contrast to the ochre color of the V_2O_5 starting material (Figure 19). Milling with 1 eq. NaH, Na, and Li led to a dark-greenish color, while the sample obtained with 1 eq. LiH exhibited a much lighter, ochre/brown color, supporting the hypothesis that no reaction occurred, as seen by the lack of pressure increase.

Meanwhile, the use of 2 and 3 eq. Na(H), as well as 2 to 4 eq. Li(H) led to very similar black and anthracite colorations, respectively. Only milling with 4 eq. Na at room temperature resulted in a sticky, grayish, non-homogeneous reaction mixture with milling balls trapped inside. Due to the stickiness, the reaction mixture was difficult to remove from the milling jar, suggesting that large excesses of very ductile reducing agents hinder the effective mechanical energy transfer. In contrast, cryogenic milling at 35 Hz produced an easily removable fine, black powder. This phenomenon can be attributed to the increased brittleness of sodium at these temperatures, which facilitates the milling process and represents an effective alternative to address mixing issues with sticky reactants or reaction mixtures.

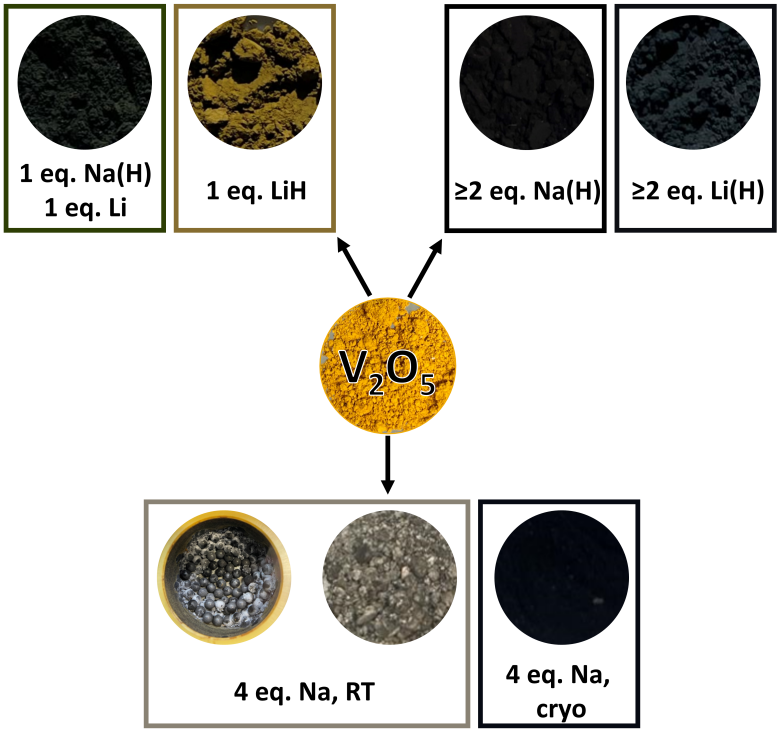

Figure 19: Observed sample coloration after milling V_2O_5 with different amounts of reducing agent at room temperature; as well as under cryogenic conditions in the case of 4 eq. sodium.

Powder X-Ray Diffraction (PXRD) measurements and Rietveld refinement were performed to analyze the sample composition. All PXRD patterns differ significantly from the diffraction pattern of pristine V_2O_5 with space group *Pmmn* after mechanochemical reaction with the tested reducing agents (Figure 20). While the reducing agent type (NaH vs. Na, LiH vs. Li) had rather minimal influence on the sample composition, the reducing agent concentration strongly influenced the number and positions of reflections and thus the sample composition (Figure 20).

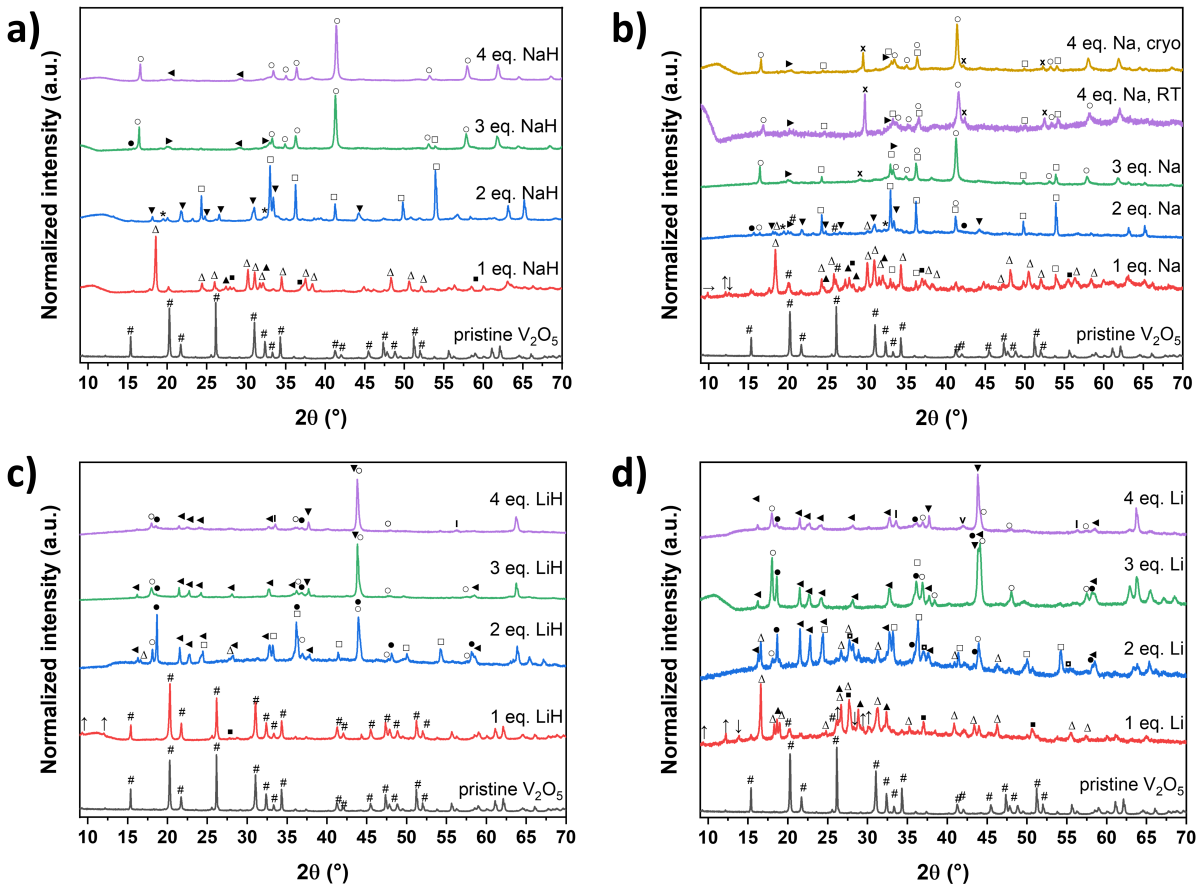

Figure 20: PXRD patterns of pristine V_2O_5 (black) and after reaction of V_2O_5 with 1 to 4 eq. of (a) sodium hydride and (b) sodium, (c) lithium hydride, and (d) lithium. For easier comparison, our previous results with NaH were adapted and are shown again in (a).[65] Unidentified reflections are marked with asterisks. Characteristic reflections corresponding to V_2O_5 (*Pmmn*) are marked with #, of VO_2 ($P4_2/mnm$) with ■, of VO_2 ($P2_1/c$) with ◘, of V_2O_3 ($R\bar{3}c$) with □, of V ($Im\bar{3}m$) with ▼, of AV_3O_8 ($P2_1/m$) with ↓, of AVO_3 ($C2/c$) with ▲, of $Na_4V_2O_7$ ($C2/c$) and $Li_2V_2O_4$ ($Fd\bar{3}m$) with ▼, of A_3VO_4 ($P2_13$) with ► and A_3VO_4 ($Pmn2_1$) with ◄, of AV_6O_{15} ($C2/m$) with ↑, of $Na_{0.56}V_2O_5$ ($C2/m$) with →, of AV_2O_5 (*Pmmn*) with Δ, of NaV_2O_4 ($C2/c$) and LiV_2O_4 ($Fd\bar{3}m$) with ●, of AVO_2 ($R\bar{3}m$) with ○, of Li_2O ($Fd\bar{3}m$) with **l**, and Na ($Im\bar{3}m$) with **x**. *A* equals Na and Li. If a phase is present as a main phase in different diffractograms, its main reflections are marked in all corresponding diffractograms. To facilitate comparison, the XRD data has been normalized between zero and one. An increased or amorphous background between ~10 and 15° 2θ originate from different dome sample holders.

Rietveld refinements confirm the strong influence of the alkali metal concentration on the reaction outcome. With sodium, the same main phases are overall formed as with NaH (Figure 21), including NaV_2O_5 (*Pmmn*) with 1 eq. Na(H), V_2O_3 ($R\bar{3}c$) and $Na_4V_2O_7$ ($C2/c$) with 2 eq. Na(H), as well as $NaVO_2$ ($R\bar{3}m$) and Na_3VO_4 ($P2_13$ and $Pmn2_1$) with even higher concentrations. As described above, milling with 4 eq. Na resulted in a poorly manageable, sticky reaction mixture at room temperature and a fine black powder under cryogenic conditions. Both milling temperatures resulted in the formation of the same main phases with $NaVO_2$ as the dominant product. In comparison, a higher percentage of unreacted sodium was

present after milling at room temperature (26%) compared to cryomilling (12%). Overall, the sample prepared at room temperature shows a very poor crystallinity compared to the other ones, as seen by the high signal-to-noise ratio (Figure 20b), making the refinement process challenging and highlighting cryomilling as a suitable alternative for milling highly ductile compounds.

With 1 eq. Na, some minor additional phases NaV_3O_8 (*P*2/*m*),[340] NaV_6O_{15} (*C*2/*c*),[341] and $Na_{0.56}V_2O_5$ (*C*2/*m*)[342] were detected, which were absent when using sodium hydride. Furthermore, both less and more reduced (sodium) vanadium oxides are observed in the reaction mixtures compared to NaH. For example, NaV_2O_5 with V^{+4}/V^{+5} is only formed with 1 eq. NaH, but with both 1 and 2 eq. Na. In contrast, more reduced NaV_2O_4 and $NaVO_2$ with V^{+3}/V^{+4} and V^{+3}, respectively, are only observed with ≥3 eq. NaH, but already with 2 eq. Na. The faster formation of more reduced phases with sodium can most likely be attributed to its lower standard potential and the more exothermic reaction enthalpies compared to NaH. However, the high ductility of sodium might reduce the local energy impact from the milling balls, which explains the formation of less reduced products.

Since the same products are mainly formed with NaH, it can be concluded that similar reactions occur simultaneously during ball milling and the general trends deduced for increasing NaH concentrations are also valid for Na reduced samples: higher percentages of sodium vanadates form due to increased sodium availability, lower vanadium oxidation states become accessible, and sodium-rich vanadates are preferentially formed.

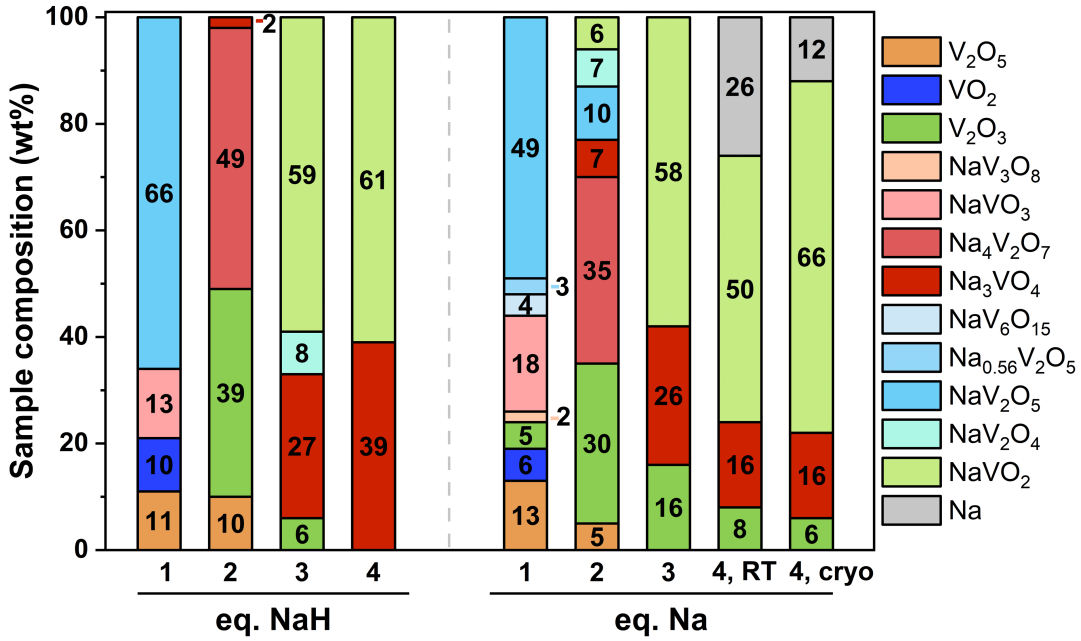

Figure 21: Sample composition in weight percent as obtained by Rietveld refinement for V_2O_5 milled with 1 to 4 eq. sodium hydride and sodium for 10 min. For easier comparison, our previous results with NaH are reshown.[65]

Lithium-based reductions mirror the trends observed for sodium-containing reducing agents and a product mixture of different (lithium) vanadium oxides is always obtained (Figure 22). As suspected, based on the missing pressure increase and cementation, no reaction occurred with 1 eq. LiH, with the sample consisting mainly of unreacted V_2O_5, only minor amounts VO_2 ($P4_2/mnm$) and LiV_6O_{15} ($C2/m$). In contrast, milling with lithium resulted in a rapid mechanochemical reduction and the formation of VO_2 ($P2_1/c$), LiV_3O_8 ($P2_1/m$), $LiVO_3$ ($C2/c$), and LiV_6O_{15} ($C2/m$) along with some unreacted V_2O_5. Overall, increasing Li(H) concentrations result in the formation of very similar phases, including V_2O_3 ($R\bar{3}c$), Li_3VO_4 ($Pmn2_1$), LiV_2O_5 ($Pmmn$), LiV_2O_4 ($Fd\bar{3}m$), $LiVO_2$ ($R\bar{3}m$) and $Li_2V_2O_4$ ($Fd\bar{3}m$). When using elemental lithium, even minor amounts of elemental vanadium can be detected, evidencing the higher reductive power of Li and the highly exothermic calculated reaction enthalpies.

In good agreement with the sodium-based results and the performed quantum chemical calculations, reactions with a low ratio of alkali metal to V_2O_5 dominate at low Li(H) concentrations such as the formation of LiV_2O_5 at 1 and 2 eq. Li(H), while lithium rich phases such as Li_3VO_4 or reduced lithium vanadates with V^{3+} such as $LiVO_2$ are only formed with 3 or 4 eq. Li(H). Again, similar findings for the obtained sample compositions suggest similar occurring reactions during ball milling, which further validates the previous assumption regarding lower activation energies in case of Li according to the Bell-Evans-Polyani principle.

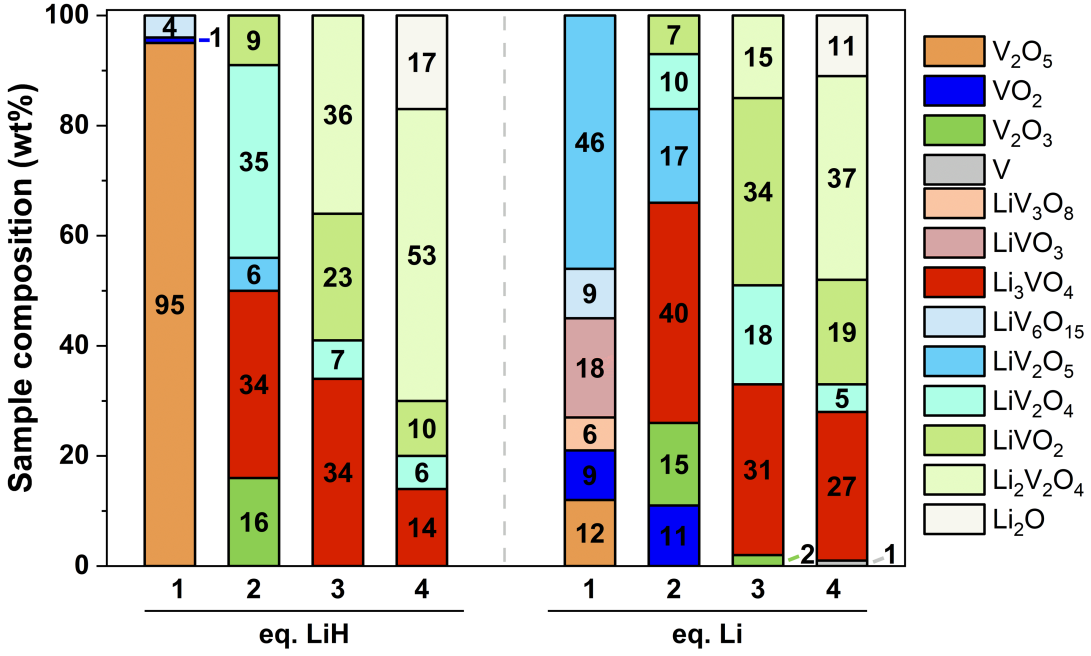

Figure 22: Sample composition in weight percent as obtained by Rietveld refinement for V_2O_5 milled with 1 to 4 eq. lithium hydride and lithium for 10 min.

3.3.3 Experimental section

Materials

V_2O_5 (abcr, Karlsruhe, Germany, 99.9%), LiH (Alfa Aesar GmbH, Karlsruhe, Germany, 99.4%), lithium powder and sodium were obtained from commercial standard suppliers and were stored in a glovebox under argon atmosphere. The purity of all solids was characterized by X-ray diffraction prior to use.

Synthetic procedures

Preparation of sodium sand

Sodium metal was heated in a Schlenk round bottom flask in paraffin oil to 105 °C under argon atmosphere. Once the sodium was melted, the reaction mixture was vigorously stirred for 15 min until small sodium beads formed. The stirring was stopped during the cooling process to avoid agglomeration. The obtained sodium sand was then washed three times with absolute toluene and three times with absolute *n*-hexane before being dried and stored in the glovebox under argon. Both solvents were dried in Solvent Purification System (MBRAUN, Garching, Germany) beforehand.

Mechanochemical syntheses

All syntheses were performed under an argon atmosphere using glovebox technique (MBraun, eco, Garching, Germany).

For syntheses in the planetary ball mill Pulverisette 7 *Premium line* (Fritsch, Idar-Oberstein, Germany), ZrO_2 grinding jars with a volume of 45 mL were used. The batch size was set to 3 g and V_2O_5 was milled with *n* eq. Li, LiH and Na (*n* = 1, 2, 3 and 4) at 300 rpm for 10 min using 90 ZrO_2 milling balls with a diameter of 5 mm. The evolution of pressure and temperature during ball milling was studied using the EASY GTM system by Fritsch (Idar-Oberstein, Germany). To avoid damage of the milling equipment, the total mass of the reaction mixture was set to 2 and 1.5 g for 3 and 4 eq. LiH, respectively.

In case of ductility issues with the alkali metals, reactions were performed in the mixer mill MM500 nano (Retsch, Haan, Germany). Since ZrO_2 milling equipment is not suitable for use in cryogenic conditions, steel grinding jars with a volume of 45 mL were used and filled with 90 steel milling balls with a diameter of 5 mm. The batch size was kept at 3 g. After initially cooling down the milling jar in a bath of liquid nitrogen, the reaction mixture was milled for 2 min at 35 Hz with 1 min of cooling in between to ensure that the cryogenic conditions are retained.

Characterization

Powder X-ray diffraction (PXRD) patterns of the pulverized samples were recorded at room temperature on a X'Pert MPD diffractometer (PANalytical, Almelo, Netherlands) in Bragg-Brentano θ-θ-geometry (goniometer radius 240 mm) with Cu $K_{\alpha 1,2}$-radiation (λ_1 = 154.055, λ_2 = 154.441 pm). A 12 µm Ni foil working as K_β filter and a variable divergence slit were mounted at the primary beam side. A PIXcel^{1D} detector was used at the secondary beam side. Experiments were carried out in a 2θ range of 7 to 120° with a step size of 0.013° and a total scan time of 2 h. Rietveld refinements of the recorded diffraction patterns were performed using Topas 5.0 (Bruker AXS, Karlsruhe, Germany) software.[325] Crystallographic structure and microstructure were refined, while instrumental line broadening was included in a fundamental parameters approach.[323] The mean crystallite size <L> was calculated as the mean volume weighted column height derived from the integral breadth. Crystal structure data were obtained from the Pearson's Crystal database.[67]

Quantum mechanical calculations

Calculation of the free energy of the (sodium) vanadium oxides was carried out using the projector-augmented wave (PAW) method by Blöchl[343] implemented in the Vienna ab initio simulation package (VASP).[344-346] Exchange and correlation effects were accommodated using the General Gradient Approximation (GGA) functional by Perdew-Burke-Ernzerhof optimized for bulk solids (PBEsol).[347] POTPAW_PBE_54 potentials were used for all calculations, more specifically Na_sv, Li_sv, V_sv, O_h, and H_h. The convergence criteria for electronic and ionic relaxation were set to 10^{-4} and 10^{-5} eV, respectively, while the cut-off energy was set to 800 eV. The Brillouin zone was sampled by automatically generating a Γ-centered *k*-point mesh with a resolution of minimum 0.035 Å^{-1} per cell. All calculations were carried out without spin-polarization.

3.3.4 Conclusion

In conclusion, mechanically induced self-propagating reactions of V_2O_5 can be performed not only with NaH, as previously investigated, but also with LiH and their elemental counterparts sodium and lithium as reducing agents. Except for an absent reaction after 10 min of milling with 1 eq. LiH due to cementation, the ignition event was either detected instantaneously (Na, Li) or after a few minutes of milling (NaH, LiH) for all other tested reducing agent concentrations.

Rietveld refinement confirmed that both hydrides and elemental alkali metals follow similar reaction pathways, yielding product mixtures of different (alkali metal) vanadium oxides with the same main phases under comparable reaction conditions. The concentration of the reducing agent strongly influences the reaction outcome. Higher concentrations favor the formation of alkali-rich vanadates, lower vanadium oxidation states, and reduced oxide formation. Both alkali metals yield larger product mixtures with both more and less reduced alkali metal vanadates compared to NaH and LiH. The formation of more reduced phases is likely due to their lower standard potential compared to the hydride one and the calculated more exothermic reaction enthalpies. The latter ones align with the apparent lower activation energy in accordance with the Bell-Evans-Polyani principle, as evidenced by the instantaneous start of the reactions.

Although elemental alkali metals can be seen as the more powerful reducing agents, their higher ductility can hinder effective energy transfer, causing the formation of less reduced products. Especially large amounts of highly ductile sodium led to unmanageable and sticky reaction mixtures, which can only be overcome by less straightforward cryomilling.

Overall, the differences in reaction outcomes when using alkali metals or hydrides as reducing agents are rather small in the mechanochemical reaction with V_2O_5 and a large product mixture is always obtained. However, despite the risk of hydrogen gas formation, alkali metal hydrides offer easier handling, better commercial availability and safer mixing. In contrast, elemental metals provide stronger reduction, but they pose practical limitations due to vigorous reactivity and ductility. For less ductile systems, such as those employing alkaline earth metal-based reducing agents, fine powders of the elemental metal should be a preferable alternative to hydrides since hydrogen gas hazards can be avoided while maintaining similar product formation.

3.4 Mechanochemical Synthesis of MgV_2O_4: Reactivity Pathways Driven by Milling Energy and Precursors

As shown in the previous chapters, ball milling of V_2O_5 with Na(H) and Li(H) always leads to fast mechanically induced self-propagating reactions and a large mixture of different vanadium oxides and alkali metal vanadates. It was also stated that less ductile alkaline earth metal powders such as magnesium might be the preferable alternative to the respective hydride to avoid damage due to hydrogen gas formation. Similarly, Yang and McCormick were able to obtain elemental vanadium in a rapid self-propagating reduction of V_2O_5 with 5 eq. Mg in the ball mill in 1994.[187]

With these intriguing findings and a rather low number of literature-known magnesium vanadates, the mechanochemical reaction of vanadium oxides with magnesium as a strong reducing agent was investigated in the last part of this thesis. Among the different magnesium vanadates, spinel-type MgV_2O_4 has been little examined until now, but is a promising electrode material for magnesium-ion[230, 231, 236, 237] or zinc-ion batteries.[232]

Since the mechanochemical synthesis and the behavior of MgV_2O_4 in the ball mill is largely unexplored in literature, the direct mechanochemical synthesis of the spinel was studied for the first time to the best of our knowledge. First, the reaction enthalpies for different reactant combinations, namely V_2O_3/MgO, $2VO_2$/Mg, V_2O_5+V_2O_3 (formally VO_2)/2Mg andV_2O_5/2Mg were calculated using a quantum chemical DFT approach. In line with these theoretical investigations, only the most exothermic reaction between V_2O_5 and 2Mg leads to the successful formation of MgV_2O_4 with MgO as a side product in a self-propagating reaction after only a few minutes. With increasing rotational speeds, the reaction is induced earlier and MgV_2O_4 with a lower crystallite size in the nanometer range and larger strain is obtained. Furthermore, it was found that harsh milling conditions induce a non-stoichiometry in both phases, leading to a magnesium-rich spinel and a vanadium containing rock salt phase, as supported by XRD and EPR measurements. After removal of MgO by acid washing, as confirmed by ICP-MS measurements, the influence of the ball milling conditions on the physical properties of the spinel were investigated by electrochemical impedance spectroscopy (EIS) (Figure 23). A positive influence of low milling speeds on conductivity was observed. This is evident by the decrease in conductivity with increasing milling intensity, which is caused by a higher number of defects.

The results of this study were published:

A. Michaely, H. Chen, O. Clemens, M. Neuberger, C. W. M. Kay, R. Haberkorn, G. Kickelbick, Mechanochemical Synthesis of MgV_2O_4: Reactivity Pathways Driven by Milling Energy and Precursors. *Inorg. Chem.* **2025**, 64, 20163-20174, DOI:10.1021/acs.inorgchem.5c03095.

The publication is published by the American Chemical Society and licensed under CC-BY 4.0.

Anna Michaely performed the experimental work, data interpretation and the theoretical calculations, along with writing the original draft. Robert Haberkorn assisted with scientific ideas, interpretation, and discussions of the acquisitioned data, as well as editing of the manuscript. Hong Chen and Oliver Clemens performed and interpreted EIS measurements, while Maxim Neuberger and Christopher Kay carried out EPR analysis and interpretation. Guido Kickelbick has contributed with scientific ideas, supervising, discussions of the results, and editing of the manuscript.

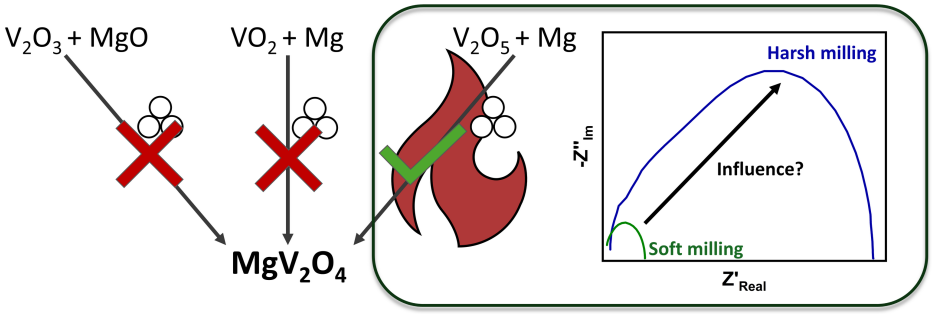

Figure 23: Table of contents graphic – Only the self-propagating reaction between V_2O_5 and Mg leads to the mechanochemical formation of MgV_2O_4, whereby the milling intensity also influences the electrochemical properties.[348]

Inorganic Chemistry

Open Access

This article is licensed under CC-BY 4.0

pubs.acs.org/IC

Article

Mechanochemical Synthesis of MgV_2O_4: Reactivity Pathways Driven by Milling Energy and Precursors

Anna Michaely, Hong Chen, Oliver Clemens, Maxim Neuberger, Christopher W. M. Kay, Robert Haberkorn, and Guido Kickelbick*

Cite This: *Inorg. Chem.* 2025, 64, 20163–20174

Read Online

ACCESS | Metrics & More | Article Recommendations | Supporting Information

ABSTRACT: Magnesium spinels such as $MgAl_2O_4$ and $MgFe_2O_4$ have been widely explored for energy storage and sensing applications, but MgV_2O_4 remains relatively unexplored despite its promising potential, e.g., as a battery electrode material. In this study, we report the first mechanochemical synthesis of MgV_2O_4 at room temperature using either MgO or Mg with various vanadium oxides as reactants. Directed by thermodynamic calculations on a DFT level, only the self-sustaining reaction between V_2O_5 and Mg led to MgV_2O_4 within 20 min of milling, along with MgO as a side product. With increasing rotational speed, an earlier reaction ignition after a few minutes of milling, smaller crystallite sizes in the nanometer range, and increased strain in MgV_2O_4 were observed. In addition, harsh milling conditions induce increasing nonstoichiometry in both phases, leading to a magnesium-rich spinel and a vanadium-containing rock salt phase, as supported by X-ray diffraction and electron paramagnetic resonance measurements. Acid washing after synthesis removed MgO, and electrochemical impedance spectroscopy showed that milder grinding conditions increased the conductivity of MgV_2O_4 due to the smaller number of defects.

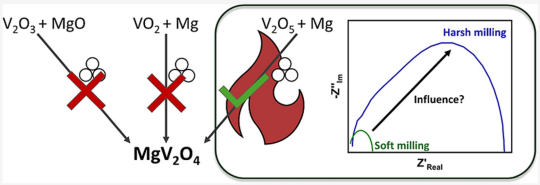

■ INTRODUCTION

With over 200 literature known compounds and minerals,[1] spinel compounds with the general sum formula AB_2X_4 (A, B = metal cation; X = O^{2-}, S^{2-}, Se^{2-}, Te^{2-}) represent an important class of materials. In the case of direct spinels with space group $Fd\bar{3}m$, the crystal structure features a robust cubic closed packed substructure of oxygen atoms with 1/8 of the resulting tetrahedral sites being occupied by A cations and half of the octahedral sites by B cations.[2] Due to their versatile elemental composition facilitated by a quite flexible cationic arrangement and incorporation of various transition metals, the resulting (redox)chemical, electronic, and magnetic properties can be tailored for use in various applications such as catalysis,[3] energy storage and batteries,[4] sensors,[5] or for oxygen reduction/evolution reactions (ORR/OER).[6] For example, while $MgAl_2O_4$, which is one of the most studied spinels, is widely used in optical applications due to its transparency and high thermal stability;[7] the magnetic properties of iron and the biocompatibility of magnesium make $MgFe_2O_4$ an ideal candidate for cancer treatment and other biomedical applications.[8] Typical synthesis routes for the preparation of spinels include solid-state high temperature reactions starting from the corresponding oxides as reactants,[9] thermal decomposition,[8a,10] sol–gel processes,[11] hydrothermal syntheses,[12] microemulsion,[13] and chemical vapor deposition.[14]

Mechanochemistry offers a greener, solvent-free, room-temperature alternative to conventional high-temperature or hydrothermal synthesis methods, which are often energy- and solvent-intensive.[15] Depending on the type of ball mill and the milling intensity, ball milling can generally be classified into two types: low-energy and high-energy ball milling.[10] Low-energy milling provides only a small energy input, is commonly carried out in tumbler mills, and primarily enables a homogeneous and uniform reduction of particle size.[16] In some cases, sequential ball milling, meaning that the powder is subjected to multiple milling steps, has been applied successfully. For example, Farhad et al. were able to produce $CuBi_2O_4$ nanopowder with a tunable band gap for use in (photo)electrochemical applications by using this approach.[17] In contrast, high-energy milling not only reduces particle sizes but can also introduce defects and increase product reactivity due to the much larger energy input. This approach is also typically used when the induction of a chemical reaction in the ball mill is envisioned, as it can shorten reaction times, improve yields, or even enable product formation unattainable by conventional synthesis routes.[15,18]

While the mechanochemical synthesis and behavior of MgV_2O_4 remain largely unexplored, related spinels such as $MgFe_2O_4$ and $MgAl_2O_4$ have been synthesized using various precursors, including metal hydroxides,[19] oxides,[19c,d,20] or a

Received: July 6, 2025
Revised: September 20, 2025
Accepted: September 23, 2025
Published: October 2, 2025

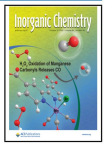

ACS Publications

© 2025 The Authors. Published by American Chemical Society

https://doi.org/10.1021/acs.inorgchem.5c03095
Inorg. Chem. 2025, 64, 20163–20174

combination of both.[19c,d,21] Compared to more traditional approaches, mechanochemical routes can lead to enhanced magnetic[19a] and catalytic properties of spinels.[20e] However, a sintering step is often required to obtain phase-pure spinels.

Compared with other magnesium-based spinels such as $MgAl_2O_4$ and $MgFe_2O_4$, MgV_2O_4 has received relatively limited attention. The reported synthesis methods are primarily hydrothermal techniques[22] or high-temperature solid-state reactions,[23] while to our knowledge, no mechanochemical synthesis has been described to date. Despite the sparse literature, MgV_2O_4 is a promising electrode material for magnesium-ion[22a,b,23d,24] or zinc-ion batteries.[22c] For example, Ding et al. demonstrated good cycling stability with a capacity of 112 mAh g^{-1} using cactus-like MgV_2O_4 structures as cathodes for Mg-ion batteries,[22b] while Tang et al. reported a capacity of 272 mAh g^{-1} at 0.2 A g^{-1} for urchin-like morphologies.[22c] Additionally, MgV_2O_4 is a key intermediate in the reduction of V_2O_5 by Mg in a self-propagating reaction to prepare elemental vanadium, which is an important additive for high-performance steels and alloys.[25]

Yang and Cormick demonstrated that milling V_2O_5 with 5 eq. Mg, Al, or Ti in a Spex 8000 mixer mill leads to the rapid and highly exothermic formation of elemental vanadium via a mechanochemical reduction reaction.[26] Depending on the size of the milling balls, a combustion event was detected after an activation period between 4 and 570 s of milling, which was reflected in a sudden increase in the vial temperature. This combustion event indicates the onset of a mechanochemically induced self-propagating reaction (MSR). Unlike traditional self-propagating high-temperature synthesis, MSRs occur at room temperature within a ball mill and are driven by mechanical energy. A key criterion for MSRs is a high adiabatic temperature T_{ad}, typically exceeding 1800 K, which can be estimated by dividing the reaction energy by the specific heat capacity.[27] Ideally, both parameters are known for the same temperature. Other reported MSRs involving V_2O_5 have been reported for the formation of alloys[28] or carbides.[29] Recently, we also showed that milling V_2O_5 with NaH induces similarly exothermic reactions, yielding various sodium vanadium oxides.[30]

In this study, we investigate the mechanochemical synthesis of MgV_2O_4 using different combinations of vanadium oxides and magnesium sources, namely, V_2O_3/MgO, $2VO_2$/Mg, V_2O_5+V_2O_3 (formally VO_2)/2Mg, and V_2O_5/2Mg. The investigation is based on quantum chemical calculations to assess the thermochemistry of possible reactions. Additionally, the electrochemical properties of the as-synthesized MgV_2O_4 are studied by electrochemical impedance spectroscopy (EIS).

EXPERIMENTAL SECTION

Materials. V_2O_5 (abcr, Karlsruhe, Germany, 99.9%), VO_2 (ChemPur, Karlsruhe, Germany, 99.5%), MgO (N50 leicht, Lehmann&Voss&Co, Hamburg, Germany), vanadium powder (Fisher Scientific, Kandel, Germany, 99.5%), and magnesium powder (Thermo Scientific, Dreieich, Germany, ≥99.8%) were used without further purification and stored in a glovebox under an argon atmosphere. All solids have been characterized by X-ray diffraction before use. Due to partial conversion of MgO into $Mg(OH)_2$, MgO was annealed at 600 °C for 48 h in air before use as a reactant.

Synthetic Procedures. *Preparation of V_2O_3 via Solid-State Reaction.* Stoichiometric amounts of V_2O_5 (3 equiv) and V (4 equiv) were mixed, placed in a porcelain boat, and heated to 900 °C under argon with a heating rate of 200 °C/h. The temperature was held for 12 h, followed by an intermediate grinding step and subsequent heating cycles at 900 C for 12 h until the retention of phase-pure V_2O_3.

Mechanochemical Syntheses. All syntheses were performed under an argon atmosphere by using a glovebox.

Stoichiometric amounts of V_2O_3/MgO, $2VO_2$/Mg, V_2O_5 + V_2O_3/2Mg, or V_2O_5/2Mg for the synthesis of MgV_2O_4 were lightly mixed with a spatula before mechanochemical treatment in the planetary ball mill Pulverisette 7 Premium line (Fritsch, Idar-Oberstein, Germany). The batch size was set to 3.0 g each time. In most experiments, the rotational speed was set to 300 rpm and the milling time was set to 20 min. Experiments that differ from the standard ones, using more intense milling conditions, are mentioned below. WC milling jars with a volume of 45 mL and 90 WC milling balls with a diameter of 5 mm were used. WC milling equipment was chosen due to small cracks of ZrO_2 milling equipment in preliminary experiments, which were most likely caused by the mechanochemical reaction of V_2O_5 and Mg.

To remove the side product MgO after the reaction of V_2O_5 and Mg, samples were treated according to a modified literature procedure.[31] After overnight stirring in 0.4 M HCl, the samples were treated with 7.5 M HCl for 1.5 h at 40 °C followed by an additional 0.5 h at room temperature. Subsequently, the samples were washed with distilled water until pH neutrality was reached and dried in a vacuum oven at 80 °C.

Characterization. Powder X-ray diffraction (PXRD) patterns of the pulverized samples were recorded at room temperature on a D8-A25-Advance diffractometer (Bruker, Karlsruhe, Germany) in Bragg–Brentano θ-θ-geometry (goniometer radius of 280 mm) with Cu K_α-radiation (λ = 154.0596 pm). A 12 μm Ni foil working as the K_β filter and a variable divergence slit were mounted at the primary beam side. A LYNXEYE detector with 192 channels was used at the secondary beam side. Experiments were carried out in a 2θ range of 7 to 120° with a step size of 0.013° and a total scan time of 2 h. Rietveld refinements of the recorded diffraction patterns were performed using TOPAS 5.0 (Bruker AXS, Karlsruhe, Germany) software.[32] Crystallographic structure and microstructure were refined. The mean crystallite size <L> was calculated as the mean volume-weighted column height derived from the integral breadth. Since the width of reflections is influenced by both the microstructure of the sample and the instrumental setup, the fundamental parameters approach[33] (implemented in Topas 5.0) was used to account for the contributions of instrumental line broadening, which enables microstructural analysis. Crystal structure data for Rietveld refinement were obtained from the Pearson's Crystal database.[34]

Electron paramagnetic resonance (EPR) spectroscopy was performed at a temperature of 5 K using an ELEXSYS E580 (Bruker, Ettlingen, Germany) spectrometer at X-band frequencies (9–10 GHz) with a modified[35] ER4118X-MD5 resonator (Bruker, Ettlingen, Germany) with symmetric long holders. For temperature control, a closed cycle helium cryostat (Cryogenic CF VTC) was used. Data evaluation and simulation were performed in MATLAB[36] using the EasySpin[37] toolbox.

The elemental quantification was conducted via inductively coupled plasma mass spectrometry (ICP–MS) with a commercial ICP–MS system (8900 Triple Quad and SPS4 autosampler, Agilent, Santa Clara, USA). Stock solutions of single-element ICP–MS standards of Mg(II) (1000 mg L^{-1} in 2–3% HNO_3, Merck Certipur, Darmstadt, Germany), V(V) (10 g L^{-1} in 5% HNO_3, Alfa Aesar, Karlsruhe, Germany), W(VI) (1 g L^{-1} in 4% HNO_3, Carl Roth, Karlsruhe, Germany), Ho(III) (1 g L^{-1} in 2–3% HNO_3, Merck Certipur, Darmstadt, Germany), and Sc(III) (1 g L^{-1} in 5% HNO_3, Alfa Aesar, Karlsruhe, Germany) were used. The last two are used as internal standards. The detector dwell time was 100 μs, the repetition was 3 times, and the measured isotopes were ^{24}Mg, ^{51}V, and ^{182}W. For the ICP–MS measurements, approximately 3 mg of the sample was dissolved in 4 mL of aqua regia (HNO_3 ROTIPURAN Supra 69%, Carl Roth, Karlsruhe, Germany; HCl Suprapur 30%, Merck, Darmstadt, Germany) before being diluted with ultrapure water. An external calibration was performed for quantification.

EIS measurements were carried under an air atmosphere using an MTZ-35 impedance analyzer (BioLogic, Seyssinet-Pariset, France)

https://doi.org/10.1021/acs.inorgchem.5c03095
Inorg. Chem. 2025, 64, 20163–20174

Inorganic Chemistry pubs.acs.org/IC Article

Table 1. Reaction Enthalpies Per mol MgV_2O_4 (ΔH_r) and Reaction Enthalpies Per Atomic Mass Unit of the Reactants ($\Delta H_{r,Reactant}$) for the Formation of MgV_2O_4 with Different Vanadium and Magnesium Sources[a]

Nr.	reaction equation	ΔH_r (eV)	$\Delta H_{r,reactant}$ (meV/u)	$\Delta H_{literature}$ (eV)
1	$V_2O_3 + MgO \rightarrow MgV_2O_4$	0.34	1.77	−0.20
2	$2\ VO_2 + Mg \rightarrow MgV_2O_4$	−2.53	−13.30	−4.31
3	$0.5\ V_2O_5 + 0.5\ V_2O_3 + Mg \rightarrow MgV_2O_4$	−3.05	−16.01	−4.72
4	$V_2O_5 + 2\ Mg \rightarrow MgV_2O_4 + MgO$	−6.43	−27.89	−9.23

[a]For comparison, the reaction enthalpies ($\Delta H_{literature}$) calculated from the standard enthalpies of formation tabulated in literature[41] are given.

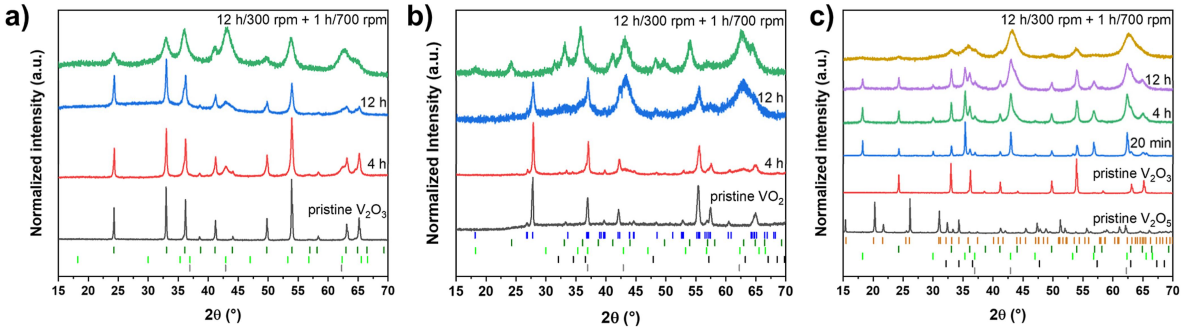

Figure 1. Normalized PXRD patterns after milling (a) an equimolar mixture of V_2O_3 and MgO, (b) VO_2 and 0.5 eq. Mg, and (c) a mixture of V_2O_5, V_2O_3, and Mg. The respective milling times are given in each graph as well as the PXRD patterns of the corresponding pristine vanadium oxides. Unless otherwise indicated, the milling speed was set to 300 rpm. Bragg reflection positions are marked as follows: ocher ticks for V_2O_5 (*Pmmn*), blue for VO_2 ($P6_3/mmc$), dark green forV_2O_3 ($R\bar{3}c$), light green for MgV_2O_4 ($Fd\bar{3}m$), black for Mg ($P6_3/mmc$), and gray for MgO ($Fm\bar{3}m$).

applying an AC signal of 100 mV amplitude (linearity of EIS data was confirmed and is demonstrated in Figure S1), with a frequency range from 1 MHz to 100 mHz. ~200 mg of the powdery sample was pressed into pellets with a diameter of 7.3 mm by applying uniaxial pressure (2 t load) followed by isostatic pressing (400 kN). Isostatic pressing results in good stability of the pellet without using additional binder materials, which can impact the resistance to charge transfer between the grains. All samples were investigated over a temperature range of 298−373 K during the heating sweep and 373−273 K during the cooling sweep. The top and bottom of the pellets were sputtered with gold to establish the electrical contact to the electrodes of the spectrometer. The data were fitted using the software RelaxIS3 (rhd instruments, Darmstadt, Germany).

Quantum Mechanical Calculations. Calculation of the free energy of the (magnesium) vanadium oxides at 0 K was carried out using the projector-augmented wave method by Blöchl[38] implemented in the Vienna ab Initio Simulation Package (VASP) version 6.4.[39] Exchange and correlation effects were accommodated using the General Gradient Approximation functional by Perdew−Burke−Ernzerhof optimized for bulk solids (PBEsol).[40] POTPAW_PBE_54 potentials were used for all calculations, more specifically Mg_sv, V_sv, and O_h. The free energy of the spinel phase as well as that of reduced vanadium oxides was obtained with spin polarization. The convergence criteria for electronic and ionic relaxation were set to 10^{-4} and 10^{-5} eV, respectively, while the cutoff energy was set to 800 eV. The Brillouin zone was sampled by automatically generating a Γ-centered *k*-point mesh with a resolution of minimum 0.035 $Å^{-1}$ per cell. For ease of comparison, the reaction enthalpies calculated from the respective free energies of the oxides are normalized to the atomic mass units (u) of the reactants.

RESULTS AND DISCUSSION

Quantum Mechanical Calculations. Apart from hydrothermal and carbothermal synthesis, the successful synthesis of (nearly) phase-pure MgV_2O_4 has frequently been reported using V_2O_3 and MgO as starting materials.[23ab−c] Given the various stable vanadium oxides, different combinations of magnesium/magnesium oxide and vanadium oxides (V_2O_5, VO_2, V_2O_3) as reactants are possible. While combinations such as V_2O_3/MgO, $2VO_2$/Mg, or $V_2O_5 + V_2O_3$ (formally VO_2)/2Mg would lead to pure MgV_2O_4, the combination of V_2O_5/2Mg would result in the formation of MgV_2O_4 and MgO as side products.

To evaluate the thermodynamic feasibility of the proposed reactant combinations and identify those most likely to proceed under mechanochemical conditions in a planetary ball mill, quantum mechanical calculations were conducted by using the Vienna Ab initio Simulation Package (VASP). As summarized in Table 1, the reaction between V_2O_3 and MgO is the only endothermic process with a reaction enthalpy of +0.34 eV. This endothermicity is attributed to the high thermodynamic stability of MgO, suggesting that this reaction is unlikely to be initiated under ball milling conditions. In contrast, all other reactant combinations are predicted to be exothermic, with reaction enthalpies ranging from −13.30 meV/u (VO_2/Mg) to −27.89 meV/u (V_2O_5/Mg), indicating a probability of successful initiation during ball milling. These theoretical findings are further supported by trends derived from standard enthalpies of formation reported in the literature,[41] which show consistent relative reaction enthalpies among the different reactant pairs. This agreement reinforces the reliability of computational predictions and highlights the potential of specific combinations for mechanochemical synthesis.

Reaction of Vanadium(III) Oxide and Magnesium Oxide. The feasibility of synthesizing MgV_2O_4 via mechanochemical activation of V_2O_3 and MgO was examined by subjecting the oxide mixture to ball milling at 300 rpm for up to 12 h, followed by an intensified milling step at 700 rpm for 1 h. Based on the calculated endothermic reaction enthalpy (Table 1), the formation of MgV_2O_4 under these conditions was considered thermodynamically unfavorable. PXRD measurements performed after 4 and 12 h of milling confirmed the persistent presence of both starting materials V_2O_3 ($R\bar{3}c$, main reflections at ~24.3, 33.0, 36.1, and 53.9° 2θ) and MgO ($Fm\bar{3}m$,

https://doi.org/10.1021/acs.inorgchem.5c03095
Inorg. Chem. 2025, 64, 20163−20174

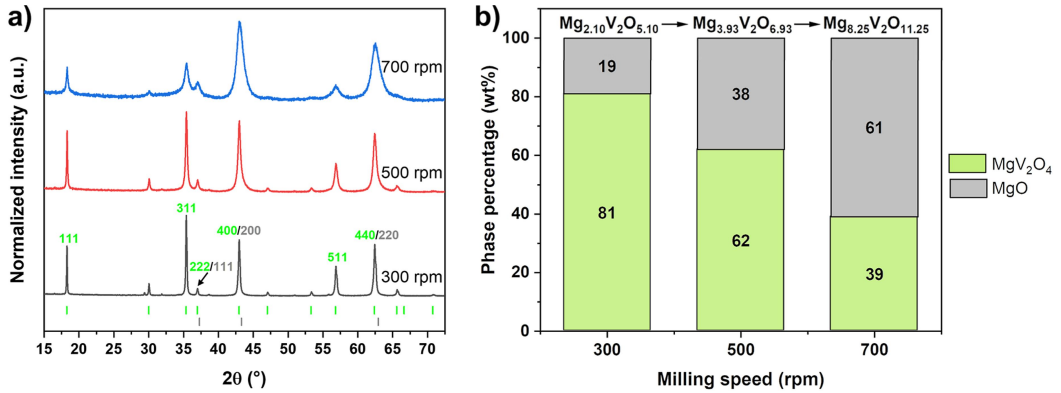

Figure 2. (a) Normalized PXRD diffractograms of MgV_2O_4 prepared mechanochemically at 300 (black), 500 rpm (red), and 700 rpm (blue) in 20 min. Bragg reflection positions are indicated by green ticks for MgV_2O_4 ($Fd\bar{3}m$) and gray ticks for MgO ($Fm\bar{3}m$). Indexing of selected reflections of MgV_2O_4 is given in green and of MgO in gray. (b) Corresponding evolution of the sample composition as a function of the milling speed as determined by Rietveld refinement, assuming stoichiometric compounds.

main reflections at ~36.9, 42.9, and 62.3° 2θ) even after prolonged milling (Figure 1a). Although reflection broadening was observed, indicative of reduced crystallite size due to the continuous impact of the milling balls, no new reflections corresponding to MgV_2O_4 ($Fd\bar{3}m$, main reflections at ~36.9°, 42.9°, and 62.3° 2θ) were detected. Even after the additional milling step at 700 rpm for 1 h, the diffraction patterns remained unchanged, confirming the absence of product formation. These experimental findings are consistent with the theoretical prediction of an endothermic reaction pathway and underscore the utility of theoretical calculations in prescreening reactant combinations for mechanochemical synthesis. The inability to induce the reaction under the applied milling conditions highlights the importance of thermodynamic driving forces in successful mechanochemical transformations.

Reaction of Vanadium(IV) Oxide and Elemental Magnesium. To further explore the mechanochemical synthesis of MgV_2O_4, a mixture of VO_2 and 0.5 eq. of magnesium powder was subjected to the same milling protocol as previously applied to V_2O_3 and MgO. PXRD measurements revealed that milling at 300 rpm for up to 12 h did not result in a significant reaction progress. The diffraction pattern remained dominated by reflections corresponding to unreacted VO_2 ($P2_1/c$), with the main reflections observed at 27.8°, 36.9°, and 55.4° 2θ (Figure 1b). Subsequent milling at 700 rpm for 1 h did not result in the anticipated mechanochemical synthesis of phase-pure MgV_2O_4. However, a broad reflection at ~18.3° 2θ suggests the possible formation of a minor fraction of highly nanocrystalline MgV_2O_4. More prominently, reflections corresponding to V_2O_3 (~24.3°, 33.0°, 36.1°, and 53.9° 2θ) and MgO (~36.9°, 42.9°, and 62.3° 2θ) were clearly detected, indicating that harsh ball milling of VO_2 and Mg leads to the formation of V_2O_3 and MgO. This observation is consistent with DFT calculations, which show that the reaction enthalpy for the formation of V_2O_3 and MgO (−2.87 eV) is more exothermic than that for the formation of MgV_2O_4 (−2.53 eV). The thermodynamic preference for V_2O_3 and MgO instead of MgV_2O_4 under harsh milling conditions explains their predominance in the PXRD pattern. The relatively small difference in reaction enthalpies also accounts for the minor formation of MgV_2O_4, likely as a secondary product.

Reaction of Vanadium(III) Oxide, Vanadium(V) Oxide, and Elemental Magnesium. Milling an equimolar mixture of V_2O_3 and V_2O_5 (formally VO_2) with Mg, as described by reaction eq 3 (Table 1) resulted in a noticeable temperature rise in the milling jar after 20 min at 300 rpm, indicating the onset of an exothermic reaction. Upon opening of the milling jar, a fine black powder was obtained, and the characteristic orange color of V_2O_5 was no longer visible. PXRD analysis revealed the complete disappearance of reflections corresponding to V_2O_5 ($Pmmn$) and Mg ($P6_3/mmc$) after just 20 min of milling, while reflections of unreacted V_2O_3 remain detectable even after 12 h (Figure 1c). Concurrently, new reflections attributed to MgV_2O_4 and MgO emerged and progressively broadened with an extended milling time and with continuous mechanical impact. The fact that only unreacted V_2O_3 was detected among the three reactants after 20 min of milling indicates that only the highly exothermic reaction between V_2O_5 and Mg proceeded. The activation energy required for the subsequent endothermic reaction between V_2O_3 and in situ formed MgO (Table 1) is again too high for induction in a ball mill.

Reaction of Vanadium(V) Oxide and Elemental Magnesium. *Influence of the Ball Milling Procedure on the Sample Composition.* Building on the promising results for the rapid mechanochemical synthesis of MgV_2O_4 with MgO as a byproduct from V_2O_5 and Mg, pure V_2O_5 and Mg were milled together at 300 rpm. No significant temperature increase in the milling jar was observed after 5 min. However, a noticeable rise in jar temperature occurred between 5 and 10 min of mechanochemical treatment, indicating the onset of an exothermic reaction and a black powder accompanied by grains of molten material were obtained. Extending the milling time to 20 min ultimately resulted in a fine black powder. The presence of molten grains and the observed temperature spike suggest a combustion event characteristic of a self-propagating reaction. This behavior aligns with our previous studies of mechanochemical self-propagating reactions between V_2O_5 and NaH,[30] the high exothermicity reported for the vanadium formation from V_2O_5 and Mg[26] and predictions from our VASP calculations. Due to prior damage to sensor and milling equipment after milling V_2O_5 with Mg, the recording of an in situ pressure and temperature curve with the EASY GTM system by Fritsch to determine the reaction onset was not performed in this case.

https://doi.org/10.1021/acs.inorgchem.5c03095
Inorg. Chem. 2025, 64, 20163−20174

Increasing the rotational speed to 500 and 700 rpm leads to earlier reaction initiation, with the milling jar feeling warm after just 5 min of mechanochemical treatment in both cases.

PXRD measurements confirm that MgV_2O_4 is successfully formed with all investigated rotational speeds, with MgO consistently appearing as a byproduct (Figure 2a). With increasing milling time, reflections progressively broaden, which indicates a decrease in the crystallite size. Rietveld refinements using both stoichiometric MgV_2O_4 and MgO phases reveal a steady increase in the MgO content, rising from 19 wt% at 300 rpm to 61 wt% at 700 rpm (Figure 2b). This trend suggests a compositional shift in the overall sample, evolving from $Mg_{2.10}V_2O_{5.10}$ at 300 rpm, which closely matches the theoretical composition of $Mg_2V_2O_5$ based on the initial reactant masses, to $Mg_{8.25}V_2O_{11.25}$ at 700 rpm, which implies an unrealistic vanadium deficiency in the sample.

In theory, this apparent deficiency might be explained by the presence of an amorphous or highly nanocrystalline phase with an unknown composition. Quantitative analysis, including the use of an internal standard, was employed to estimate the amorphous content (see the Supporting Information for further details). The results indicate that samples milled at lower rotational speeds (300 rpm) contain no or only minimal amounts of the amorphous phase (maximum 5%), whereas samples subjected to more intense milling conditions (700 rpm) exhibit an increased amorphous fraction of 12−15%. While this trend aligns with expectations for ball-milled materials, the overall amorphous content remains moderate.

However, a thorough examination of the MgO phase after milling V_2O_5 and 2 eq. Mg for 20 min further reveals a shift in the relative intensities of reflections (111) at 36.9° 2θ and (200) at 42.9° 2θ, indicating that the cationic positions scatter more than expected for pure MgO. Furthermore, the lattice parameter of MgO decreases from 421.47(1) pm at 300 rpm, consistent with literature,[42] to 419.8(3) pm at 700 rpm, which is smaller than expected. Given that VO ($Fm\bar{3}m$) exhibits a lattice parameter of 409.5 pm,[43] this contraction could imply a partial vanadium incorporation into the MgO lattice under harsh milling conditions, resulting in nonstoichiometry in MgO.

In contrast, the lattice parameter of the spinel phase shows only a slight increase from 841.11 to 841.91 pm, remaining largely consistent with reported values.[44] Assuming a non-stoichiometric, Mg-rich spinel, an increase in cell volume would be expected due to the larger cationic size of Mg^{2+} (cationic radius in octahedral geometry: 72.0 pm[45]) compared to V^{3+} (64.0 pm). However, to maintain charge neutrality, the substitution of two V^{3+} ions by one Mg^{2+} ion and one V^{4+} ion (58.0 pm) would counterbalance the expected expansion. This compensation likely accounts for the relatively stable lattice parameter and supports the hypothesis of mechanochemically induced nonstoichiometry in the spinel phase.

To account for the observed compositional variations, several mechanistic scenarios involving nonstoichiometric product phases can be proposed, each dependent on the milling intensity. These are summarized by the following reaction pathways:

1. Formation of stoichiometric MgV_2O_4 and MgO at low milling intensities:

$$V_2O_5 + 2Mg \rightarrow MgV_2O_4 + MgO \quad (1)$$

2. Formation of stoichiometric MgV_2O_4 and insertion of V(III) into MgO at intermediate milling intensities:

$$V_2O_5 + 2Mg \rightarrow \frac{1-5x}{1-4x}MgV_2O_4 + \frac{1-3x}{1-4x}Mg_{1-3x}V_{2x}O \quad (2)$$

3. Formation of nonstoichiometric MgV_2O_4 and insertion of V(II) into MgO at high milling intensities:

$$V_2O_5 + 2Mg \rightarrow Mg_{1+x}V_{2-x}O_4 + Mg_{1-x}V_xO \quad (3)$$

While the above postulated reaction pathways mainly serve as models to better understand the processes during milling, it is most likely that a combination of these reactions occurs simultaneously. However, the share of a specific pathway in the total reaction differs, according to the milling conditions.

Rietveld refinements based on these scenarios reveal that the choice of the structural model has only a minor impact on refined lattice parameters and microstructural features. However, for samples subjected to more intense milling, allowing for nonstoichiometry slightly improves the fit quality. Importantly no evidence for antisite disorder was detected in the MgV_2O_4 spinel phase.

For the sample milled at 300 rpm, refinement yields a phase composition of 81% MgV_2O_4 and 19% MgO, corresponding to an overall sample composition of $Mg_{2.10}V_2O_{5.10}$ (Supporting Information, Figure S2, and Table S1). Introducing non-stoichiometry into the refinement model does not significantly alter site occupancies, supporting the formation of stoichiometric MgV_2O_4 and MgO under mild milling conditions.

Independent of the different scenarios postulated above, a sample composition of 62% spinel and 38% rock salt was refined for the 500 rpm sample (Supporting Information, Figure S3, and Table S2). While the spinel phase remains stoichiometric, up to 26% of vanadium can be incorporated into the MgO lattice, depending on the assumed oxidation state, leading to slightly increased quality fit parameters. Hereby, the refined overall sample composition of $Mg_{1.94}V_2O_{4.94}$ for V(III) according to scenario 2 is in excellent agreement with the theoretical one. While it can be approximated that mainly V(III) is incorporated into the MgO lattice under intermediately harsh milling conditions, it is not possible to distinguish between two oxidation states by Rietveld refinement. Given that the rock-salt-type phase is considered a byproduct and will be removed in subsequent processing steps to isolate the spinel, no further structural characterization of this phase was pursued.

Allowing for nonstoichiometry in MgV_2O_4 and MgO and vanadium incorporation into the MgO lattice leads to a shift in the refined phase composition by up to 6% for the sample milled at 700 rpm, compared to the model assuming fully stoichiometric phases (Supporting Information, Table S3). Although the visual appearance of the fits remains largely unchanged across the different models (Supporting Information and Figure S4), the refinement quality indicators improve, and the overall sample compositions approach the theoretical composition. An approximate composition of $Mg_{1.5}V_{1.5}O_4$ and $Mg_{0.77}V_{0.23}O$ was refined for the spinel and rock salt structure, respectively.

These findings support the previously proposed mechanistic scenarios and indicate that magnesium-rich spinels can be accessed under high-energy milling conditions. However, further intensification of the milling process at 700 rpm revealed a significant decline in the structural integrity of the spinel phase. This is evidenced by the near-complete disappearance of spinel reflections in the PXRD pattern (Supporting Information,

https://doi.org/10.1021/acs.inorgchem.5c03095
Inorg. Chem. 2025, 64, 20163−20174

Figure S5), suggesting low mechanochemical stability under such conditions.

Consequently, while harsh milling may facilitate the formation of nonstoichiometric spinels, it is not suitable for the targeted synthesis of stoichiometric and well-crystalline MgV_2O_4. Controlled milling conditions are therefore essential to balance phase formation with structural preservation.

Analysis of Mechanochemically Induced Structural Changes by EPR Spectroscopy. EPR spectroscopy was employed to further investigate the structural modifications induced by mechanochemical treatment, with a particular focus on the local environment of vanadium species. In general, it would be expected that only the paramagnetic V^{4+} ion with its $3d^1$ electronic configuration is observed in the EPR spectra. Lower oxidation states such as V^{3+} and V^{2+} are unlikely to be observable at X-band frequencies due to strong fine structure interactions in the $3d^2$ and $3d^3$ configurations.[46] The sensitivity of EPR to local structural distortions makes it therefore a valuable tool for detecting defects introduced during the mechanochemical reaction between Mg and V_2O_5. All recorded spectra exhibit a well-resolved hyperfine structure arising from the coupling of the paramagnetic species with the ^{51}V nucleus (I = 7/2 and natural abundance of 99.75%). Additionally, a broad underlying resonance is observed, attributed to spin−spin exchange interactions between neighboring vanadium centers, consistent with previous reports on vanadium-containing systems.[47] In accordance with the PXRD results, the EPR spectra show a strong influence of the milling intensity on the vanadium environment in the sample, as the appearance of the EPR signal continuously changes as a function of the milling intensity (Figure 3a).

Milling at 700 rpm for a total time of 50 min leads to a clear axial hyperfine tensor for coupling between the unpaired electron and the ^{51}V nucleus in an octahedral environment.

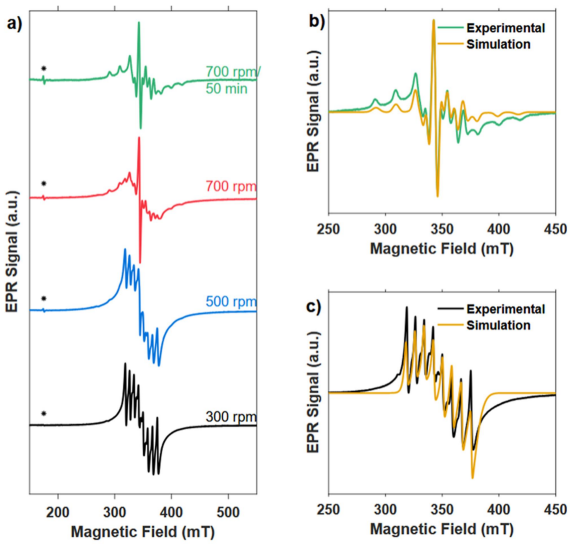

Figure 3. (a) Overview of continuous wave EPR spectra at 5 K of MgV_2O_4 prepared in 20 min at 300 (black), 500 (blue), and 700 rpm (red), and at 700 rpm in a total of 50 min of milling (green). The asterisks mark the signal from the microwave resonator. Experimental and simulated spectra of MgV_2O_4 prepared at 300 rpm in 20 min and at 700 rpm in 50 min are shown in (b) and (c), respectively.

Simulation of the obtained spectrum (Figure 3b) reveals hyperfine tensor components of $A_\perp$ = 158(1) MHz as well as $A_\parallel$ = 495(3) MHz, which align well with those reported for similar vanadate systems.[47,48] These results support the hypothesis of vanadium incorporation into the MgO matrix and the concurrent formation of a magnesium-rich spinel phase. At low and intermediate milling speeds of 300 and 500 rpm, the spectrum consists of eight resonance lines, which is expected for hyperfine coupling to the vanadium nucleus. The spectrum of the 300 rpm sample could be well simulated (Figure 3c) by assuming an axial g-tensor with $g_\perp$ = 1.940(3), $g_\parallel$ = 1.989(1) and an axial hyperfine tensor A with $A_\perp$ = 120(3) MHz and $A_\parallel$ = 227(1) MHz. More details of the simulation parameters are included in Supporting Information Tables S4 and S5. We note that a comparably large g strain had to be considered for an accurate simulation of the spectrum. Both the hyperfine coupling tensor and the significantly narrower lines of the EPR signal of the 300 rpm sample suggest a more isotropic environment of the paramagnetic centers, which is likely to arise from local defects generated during mechanochemical milling.

Although the exact nature of the paramagnetic centers remains uncertain, the significant changes in the EPR signal hyperfine coupling tensor after intense milling, suggesting the incorporation of vanadium into the crystal lattice, along with structural changes observed via Rietveld refinement, support the hypothesis that vanadium is incorporated into the MgO lattice under the formation of a defective rock salt structure and a magnesium-rich spinel. Again, intense milling is therefore not beneficial for the mechanochemical synthesis of MgV_2O_4.

Removal of MgO by Acid Washing. To remove the side product MgO, a modified literature procedure was employed involving sequential acid treatments: in 0.4 M HCl for 15 h, followed by treatment with 7.5 M HCl for 1.5 h at 40 °C and 0.5 h at room temperature. The samples were afterward washed with distilled water until neutral pH was achieved.[31]

After washing, reflections of (overlapping) MgV_2O_4 and MgO at ∼ 43° and 62° 2θ become noticeably narrower after washing (Figure 4a), indicating effective removal of MgO. However, because the main reflections completely overlap, it remains difficult to reliably quantify the remaining rock salt phase using Rietveld refinement. For samples milled at 300 and 500 rpm, Rietveld analysis suggests that less than 5% of a rock salt phase may be present, but equally good fits can be achieved without using MgO at all. In contrast, for the sample milled at 700 rpm, the use of MgO is still required for adequate refinement. Since the phase percentage of the rock salt phase decreased significantly from 55% to 21% after washing (Supporting Information, Table S7), it can be concluded that the majority of MgO was removed, which aligns with EPR and ICP−MS analysis. While EPR spectra of the 700 rpm sample still show the largest axial contribution after washing (Supporting Information, Figure S6), ICP−MS measurements reveal a decrease in the Mg to V ratio from approximately 1 to 1 in the unwashed samples to ∼0.6 to 1 after washing (Supporting Information, Table S8), showing that most of MgO is removed during acid washing.

Regarding the microstructure of unwashed samples, the crystallite size decreases from >500 to 26 nm with intensifying milling conditions (Figure 4b), which is in line with a decrease of the particle size revealed by scanning electron microscopy (SEM) measurements (Supporting Information, Figure S7). Simultaneously, the strain of the spinel increases from 0.06 to 0.40% due to the harsher milling impact, which is a well-known

https://doi.org/10.1021/acs.inorgchem.5c03095
Inorg. Chem. 2025, 64, 20163−20174

Inorganic Chemistry pubs.acs.org/IC Article

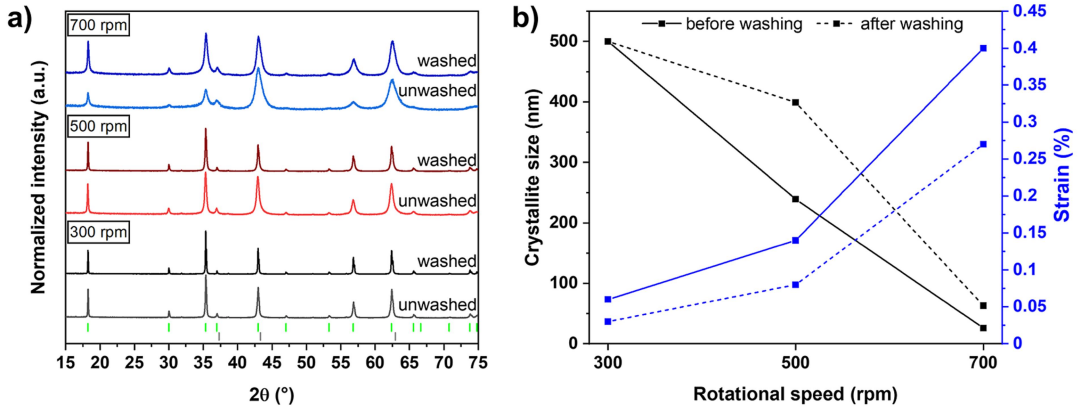

Figure 4. (a) Normalized PXRD diffractograms of MgV_2O_4 prepared mechanochemically before and after acid washing prepared at 300 (gray/black), 500 rpm (red), and 700 rpm (blue) in 20 min. Green ticks indicate the Bragg positions of MgV_2O_4 ($Fd\bar{3}m$), gray ones of MgO ($Fm\bar{3}m$). (b) Evolution of the crystallite size (black) and strain (blue) of the spinel phase as a function of the milling speed before (solid line) and after (dotted line) washing with diluted HCl. The lines in the figure connecting the points serve as orientation aids for the eye.

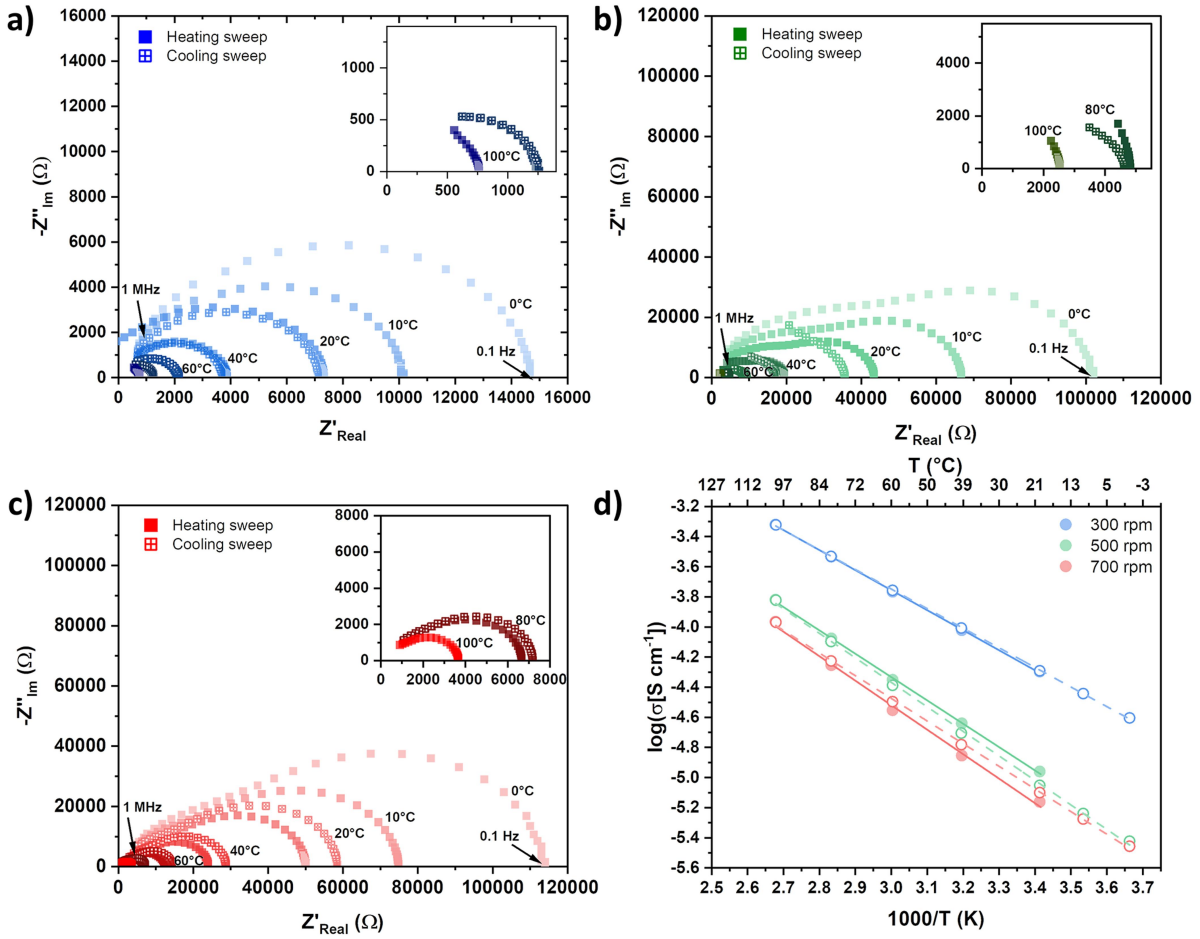

Figure 5. Nyquist plot of MgV_2O_4 prepared at (a) 300, (b) 500, and (c) 700 rpm as well as (d) the corresponding Arrhenius plot for all samples, separately for the heating (hollow circles) and cooling sweep (filled circles).

phenomenon in mechanochemistry.[49] After washing, an increase in crystallite size and a decrease in strain are observed in comparison to the unwashed samples. Rather than an improvement of the overall crystallinity due to crystal growth

https://doi.org/10.1021/acs.inorgchem.5c03095
Inorg. Chem. 2025, 64, 20163−20174

during washing, this observation is most likely caused by the dissolution of the smaller, more strained spinel crystallites in HCl as evidenced by a green coloration of the acid, which corresponds to dissolved V^{3+}. These findings suggest that prolonged washing or the use of stronger acids are not advisable even though full removal of the side product might be possible due to the undesirable dissolution of the spinel phase.

Investigation of the Electrochemical Properties by Impedance Spectroscopy. To evaluate the impact of ball milling conditions on the electrochemical performance of the synthesized MgV_2O_4 samples, alternating current EIS was conducted on pellets prepared by isostatic pressing of nonsintered powders. This method allows for the assessment of total conductivity without the influence of sintering-induced microstructural changes. It is well established that high-energy ball milling reduces the particle size and increases the defect density, which can enhance the electrochemical activity. However, excessive milling may also introduce detrimental effects, such as impaired electron transport due to defect accumulation and grain boundary proliferation.[50]

The finer particle size resulting from high-energy milling increases the number of ceramic−ceramic interfaces in the pressed pellets, which can significantly influence both electronic and ionic transport. Although isostatic pressing improves pellet densification and mechanical integrity, samples still contain large amounts of grain boundaries in comparison to well-sintered ones.

As shown in the Nyquist plots of the MgV_2O_4 samples (Figure 5a−c), the shape of the semicircle as well as the frequency dependence of phase angles strongly depend on the milling speed. The absent blocking tail in all spectra in the low-frequency range indicates the electron conducting nature of the samples. Among the samples, the 300 rpm sample exhibits the lowest total resistivity over the temperature range from 0 to 100 °C. Increasing the milling speed from 300 to 700 rpm leads to a noticeable decrease of the conductivity from 52.2 to 8.59 μS/cm, respectively.

Arrhenius plots for all samples (Figure 5d) show excellent linearity ($R^2 > 0.999$), confirming thermally activated conduction behavior. Notably, the total conductivity decreases by approximately 1 order of magnitude with increasing milling speed. This trend correlates with the increased point defect density and grain boundaries introduced by the high-energy ball milling process, which is in line with the increase in strain and decrease in crystallite size as well as the nonstoichiometry observed by PXRD and EPR measurements. The accumulation of point defects and grain boundaries likely acts as scattering centers and barriers to charge transport, thereby reducing conductivity.[50,51] This negative impact is also indicated by the higher activation energies for the 500 and 700 rpm samples (Table 2). Interestingly, the heating process affects the overall conductivity of the three samples differently. The 300 rpm sample shows negligible thermal hysteresis, while 500 and 700 rpm samples show either a slightly enhanced conductivity or a reduction of conductivity in a subsequent cooling sweep. The maximum deviation in conductivity reaches approximately 20%. Although the exact mechanism remains unclear, this behavior may be linked to milling-induced nonstoichiometry, defect dynamics, or moisture interactions at grain boundaries during thermal cycling in air.

Table 2. Calculated Activation Energy for All Samples, with Values Shown Separately for Heating and Cooling Cycles

milling speed (rpm)	measurement condition	E_a (eV)
300	heating sweep	0.26
	cooling sweep	0.26
500	heating sweep	0.32 ($E_{a,grain}$: 0.28; $E_{a,gb}$: 0.36)
	cooling sweep	0.31
700	heating sweep	0.30
	cooling sweep	0.32

To understand the rpm-dependent conductivity of different electron transport phenomena, the impedance data were evaluated by using equivalent circuit models consisting of R-CPE elements or series of them. The fitting examples for the three samples are shown in Figure 6a−c. As illustrated in the inset, R is a resistor and CPE is the constant phase element, which represents the nonideal capacitor response from samples due to surface roughness, porosity, and other microstructural imperfections of the pellet. The corresponding capacitances of CPE were determined using the Brug equation

$$C = Q^{1/\alpha} \times R^{1-\alpha/\alpha}$$

Q is the CPE constant, R is the resistance in parallel with the CPE, and α is the CPE exponent ($0 \leq \alpha \leq 1$). Q, R, and α can be extracted from the fitted spectra.

For the sample milled at 300 rpm, only a single R-CPE element was sufficient to model the data. Associated capacitance values in the range of 10^{-11} F were observed (Figure 6d), which exhibit a small dependence on temperature. For 500 and 700 rpm samples, equivalent circuits consisting of two single R-CPE elements were used (for the 500 rpm sample, at temperature above 80 °C, a single R-CPE element was used). The capacitance corresponding to the semicircle in the high-frequency range is also in the order of 10^{-11} F. Given the comparable temperature-dependence of the capacitances (Figure 6d), the associated resistance is attributed to the bulk transport.[52] Figure 6e shows the grain resistance as a function of temperature (logarithmic scale) for the three samples during the heating sweep. A significant reduction in bulk conductivity by 1 order of magnitude, similar to the trend of overall conductivity, is observed. However, the 500 rpm sample shows marginal differences in bulk resistance to the 700 rpm sample, suggesting that the total conductivity differences among the samples are mainly due to nonbulk contributions.

For the 500 rpm sample (at temperatures below 80 °C) and 700 rpm sample, a second semicircle in the midfrequency range can be assigned to grain boundary contribution with capacitances in the range of ~10^{-10} F. Figure S8 displays the grain, grain boundary, and total resistance as a function of temperature (logarithmic scale) for the 500 rpm sample. During the heating sweep, the electron-conducting phenomena are dominated by both bulk and grain boundary contributions at low temperatures, but by bulk resistance at high temperatures. This is consistent with the higher activation energy for grain boundary contribution as compared to the bulk contribution shown in Table 2. As illustrated in Figure 6f, the 700 rpm sample exhibits significantly increased grain boundary resistance (lower conductivity) compared to the 500 rpm sample, which is attributed to the increased density of grain boundary resulting from higher milling energy.[53] The increased grain boundary resistance explains the lowest overall conductivity of the 700 rpm sample, especially given that the bulk resistance of this sample is comparable to that of the 500 rpm sample.

https://doi.org/10.1021/acs.inorgchem.5c03095
Inorg. Chem. 2025, 64, 20163−20174

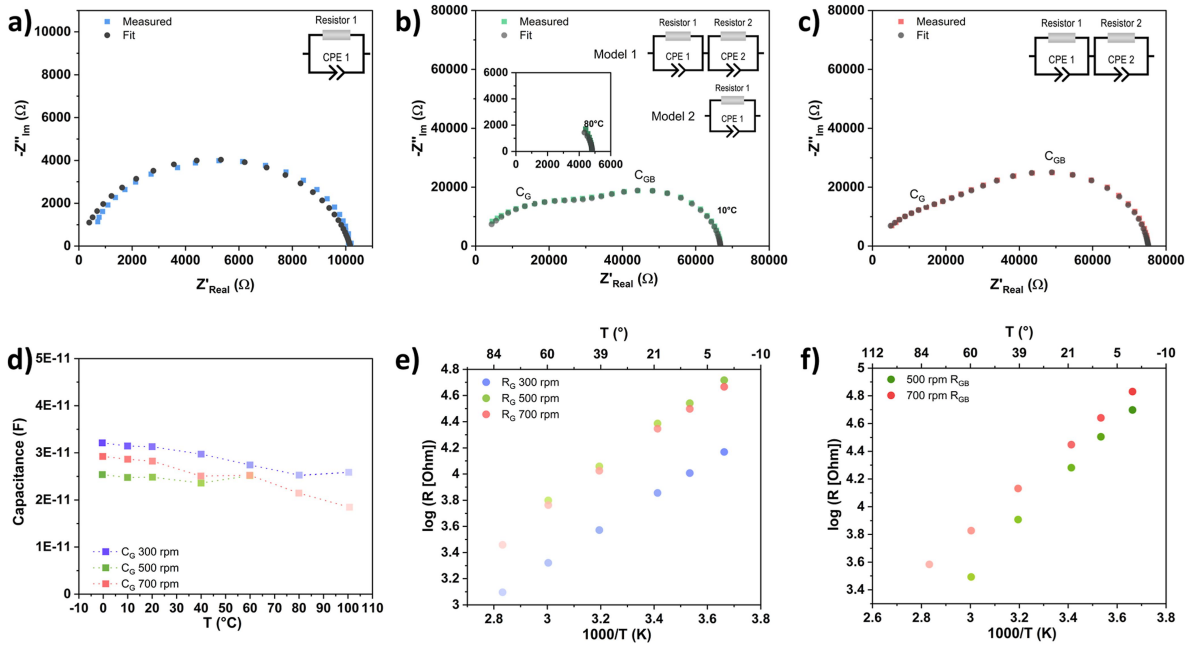

Figure 6. Fitting examples and models used for MgV_2O_4 prepared at (a) 300 rpm, (b) 500 rpm, (c) 700 rpm; (d) temperature-dependent bulk(grain) capacitance for different samples; (e) temperature-dependent logarithm plot of bulk (grain) resistance and (f) grain boundary resistance for different samples.

As the temperature increased, also during the subsequent cooling sweep, the 500 rpm sample exhibits only a single depressed and partial semicircle. Therefore, model 2 with only one R-CPE element was applied, as no indication of the presence of two semicircles was observed in the Bode plot either (Supporting Information, Figure S9). The corresponding capacitance was around 10^{-10} F. Despite this, it did not follow the tendency seen in model 2, neither for bulk resistance nor for grain boundary resistance (Supporting Information, Figure S8). This implies that the complexity of spectra and the mixed frequency domain of bulk and grain boundary contributions could not be fully deconvoluted with the current data set, and further investigations would be needed. However, a clear influence of the milling speed was observed by EIS measurements, revealing the positive influence of rather soft milling conditions, which further agrees with the observed low mechanochemical stability of the spinel.

CONCLUSION

This study presents the first systematic investigation of the mechanochemical synthesis of MgV_2O_4 at room temperature, evaluating various combinations of vanadium oxides and Mg or MgO as precursors. Among the tested systems, only the highly exothermic reaction between V_2O_5 and Mg led to the successful formation of MgV_2O_4, accompanied by MgO as a side product, in agreement with the DFT calculations. In contrast, no reaction occurred between V_2O_3 and MgO due to the endothermic nature of the process, while reactions involving VO_2/Mg and $V_2O_5 + V_2O_3$/Mg primarily resulted in partial reduction to V_2O_3 and selective reactivity of V_2O_5, respectively.

The self-propagating reaction between V_2O_5 and Mg was found to be sensitive to the milling intensity. Higher rotational speeds accelerated reaction initiation and led to reduced crystallite sizes and increased strain in the resulting MgV_2O_4. However, excessive milling introduced nonstoichiometry and structural instability, as evidenced by PXRD and EPR analyses, indicating that harsh milling conditions are detrimental to phase purity and structural integrity.

Following acid washing to remove MgO, the electrochemical properties of the as-prepared MgV_2O_4 pellets were evaluated by using EIS. While all samples showed capacitances of $3.0 \pm 0.5 \times 10^{-11}$ F, the results revealed that moderate milling conditions (e.g., 300 rpm) yielded the highest conductivity, while higher milling speeds led to increased resistivity. This decline in performance is attributed to the accumulation of structural defects and elevated grain boundary resistance, highlighting the importance of optimizing milling parameters to balance reactivity and material quality.

Overall, this work demonstrates the feasibility of synthesizing MgV_2O_4 via a rapid, room-temperature mechanochemical route and underscores the critical role of milling conditions in tailoring the structural and electrochemical properties of the resulting material for potential battery applications.

ASSOCIATED CONTENT

Supporting Information

The Supporting Information is available free of charge at https://pubs.acs.org/doi/10.1021/acs.inorgchem.5c03095.

Additional powder X-ray and Rietveld refinement data as well as additional EPR, ICP–MS, SEM, and EIS data (PDF)

AUTHOR INFORMATION

Corresponding Author

Guido Kickelbick – *Inorganic Solid-State Chemistry, Saarland University, 66123 Saarbrücken, Germany;* orcid.org/

https://doi.org/10.1021/acs.inorgchem.5c03095
Inorg. Chem. 2025, 64, 20163−20174

0000-0001-6813-9269; Email: guido.kickelbick@uni-saarland.de

Authors

Anna Michaely − *Inorganic Solid-State Chemistry, Saarland University, 66123 Saarbrücken, Germany*

Hong Chen − *Institute for Materials Science, Materials Synthesis Group, University of Stuttgart, 70569 Stuttgart, Germany;* orcid.org/0000-0002-3211-9896

Oliver Clemens − *Institute for Materials Science, Materials Synthesis Group, University of Stuttgart, 70569 Stuttgart, Germany;* orcid.org/0000-0002-0860-0911

Maxim Neuberger − *Physical Chemistry and Didactics of Chemistry, Saarland University, 66123 Saarbrücken, Germany*

Christopher W. M. Kay − *Physical Chemistry and Didactics of Chemistry, Saarland University, 66123 Saarbrücken, Germany; London Centre for Nanotechnology, University College London, London WC1H 0AH, U.K.;* orcid.org/0000-0002-5200-6004

Robert Haberkorn − *Inorganic Solid-State Chemistry, Saarland University, 66123 Saarbrücken, Germany;* orcid.org/0000-0002-4605-3760

Complete contact information is available at: https://pubs.acs.org/10.1021/acs.inorgchem.5c03095

Notes

The authors declare no competing financial interest.

■ ACKNOWLEDGMENTS

Instrumentation and technical assistance for this work were provided by the Service Center X-ray Diffraction, with financial support from Saarland University and German Science Foundation (project number INST 256/349-1). ICP−MS instrumentation for this work was provided by the Elemental analysis group, with financial support from Saarland University and German Science Foundation (project number INST 256/553-1). We thank Aaron Haben and Lena Ruck for performing the ICP−MS measurements.

■ REFERENCES

(1) Hill, R. J.; Craig, J. R.; Gibbs, G. V. Systematics of the spinel structure type. *Phys. Chem. Miner.* **1979**, *4*, 317−339.

(2) Bragg, W. H. XXX. The structure of the spinel group of crystals. *Lond. Edinb. Dubl. Phil. Mag. J. Sci.* **1915**, *30*, 305−315.

(3) (a) Shan, C.; Wang, Y.; Li, J.; Zhao, Q.; Han, R.; Liu, C.; Liu, Q. Recent Advances of VOCs Catalytic Oxidation over Spinel Oxides: Catalyst Design and Reaction Mechanism. *Environ. Sci. Technol.* **2023**, *57*, 9495−9514. (b) Aznam, I.; Muchtar, A.; Somalu, M. R.; Baharuddin, N. A.; Rosli, N. A. H. Advanced materials for heterogeneous catalysis: A comprehensive review of spinel materials for direct internal reforming of methane in solid oxide fuel cell. *Chem. Eng. J.* **2023**, *471*, 144751.

(4) (a) Yuan, J.; Li, Y.; Xu, H.; Qiao, Y.; He, G.; Chen, H. Engineering improved strategies for spinel cathodes in high-performing zinc-ion batteries. *Nanoscale* **2024**, *16*, 1025−1037. (b) Yuan, C.; Wu, H. B.; Xie, Y.; Lou, X. W. Mixed Transition-Metal Oxides: Design, Synthesis, and Energy-Related Applications. *Angew. Chem., Int. Ed.* **2014**, *53*, 1488−1504.

(5) Li, Y.; Yuan, Z.; Meng, F. Spinel-Type Materials Used for Gas Sensing: A Review. *Sensors* **2020**, *20*, 5413.

(6) Zhao, Q.; Yan, Z.; Chen, C.; Chen, J. Spinels: Controlled Preparation, Oxygen Reduction/Evolution Reaction Application, and Beyond. *Chem. Rev.* **2017**, *117*, 10121−10211.

(7) Rubat du Merac, M.; Kleebe, H.-J.; Müller, M. M.; Reimanis, I. E. Fifty Years of Research and Development Coming to Fruition; Unraveling the Complex Interactions during Processing of Transparent Magnesium Aluminate ($MgAl_2O_4$) Spinel. *J. Am. Ceram. Soc.* **2013**, *96*, 3341−3365.

(8) (a) Shahjuee, T.; Masoudpanah, S. M.; Mirkazemi, S. M. Thermal Decomposition Synthesis of $MgFe_2O_4$ Nanoparticles for Magnetic Hyperthermia. *J. Supercond. Novel Magn.* **2019**, *32*, 1347−1352. (b) Shunmuga Priya, R.; Ranjith Kumar, E.; Balamurugan, A.; Srinivas, C. Green synthesized $MgFe_2O_4$ ferrites nanoparticles for biomedical applications. *Appl. Phys. A: Mater. Sci. Process.* **2021**, *127*, 538.

(9) (a) Carter, R. E. Mechanism of Solid-state Reaction Between Magnesium Oxide and Aluminum Oxide and Between Magnesium Oxide and Ferric Oxide. *J. Am. Ceram. Soc.* **1961**, *44*, 116−120. (b) Shimada, S.; Furuichi, R.; Ishii, T. Effects of Additives on Solid State Reaction. I. A Kinetic Study of the Effects of Halides of the Formation of $MgAl_2O_4$. *Bull. Chem. Soc. Jpn.* **1974**, *47*, 2026−2030.

(10) Gusmano, G.; Nunziante, P.; Traversa, E.; Chiozzini, G. The mechanism of $MgAl_2O_4$ spinel formation from the thermal decomposition of coprecipitated hydroxides. *J. Eur. Ceram. Soc.* **1991**, *7*, 31−39.

(11) (a) Parmentier, J.; Richard-Plouet, M.; Vilminot, S. Influence of the sol-gel synthesis on the formation of spinel $MgAl_2O_4$. *Mater. Res. Bull.* **1998**, *33*, 1717−1724. (b) Huang, Y.; Tang, Y.; Wang, J.; Chen, Q. Synthesis of $MgFe_2O_4$ nanocrystallites under mild conditions. *Mater. Chem. Phys.* **2006**, *97*, 394−397.

(12) (a) Verma, S.; Joy, P. A.; Khollam, Y. B.; Potdar, H. S.; Deshpande, S. B. Synthesis of nanosized $MgFe_2O_4$ powders by microwave hydrothermal method. *Mater. Lett.* **2004**, *58*, 1092−1095. (b) Zhang, X. Hydrothermal synthesis and catalytic performance of high-surface-area mesoporous nanocrystallite $MgAl_2O_4$ as catalyst support. *Mater. Chem. Phys.* **2009**, *116*, 415−420.

(13) (a) Vestal, C. R.; Zhang, Z. J. Normal micelle synthesis and characterization of $MgAl_2O_4$ spinel nanoparticles. *J. Solid State Chem.* **2003**, *175*, 59−62. (b) Holec, P.; Plocek, J.; Nižňanský, D.; Poltierová Vejpravová, J. Preparation of $MgFe_2O_4$ nanoparticles by microemulsion method and their characterization. *J. Sol-Gel Sci. Technol.* **2009**, *51*, 301−305.

(14) (a) Koh, W.; Ku, S.-J.; Kim, Y. Single-Source CVD of $MgAl_2O_4$. *Chem. Vap. Deposition* **1998**, *4*, 192−195. (b) Mathur, S.; Veith, M.; Ruegamer, T.; Hemmer, E.; Shen, H. Chemical Vapor Deposition of $MgAl_2O_4$ Thin Films Using Different Mg−Al Alkoxides: Role of Precursor Chemistry. *Chem. Mater.* **2004**, *16*, 1304−1312.

(15) Baláž, P.; Achimovičová, M.; Baláž, M.; Billik, P.; Cherkezova-Zheleva, Z.; Criado, J. M.; Delogu, F.; Dutková, E.; Gaffet, E.; Gotor, F. J.; Kumar, R.; Mitov, I.; Rojac, T.; Senna, M.; Streletskii, A.; Wieczorek-Ciurowa, K. Hallmarks of mechanochemistry: from nanoparticles to technology. *Chem. Soc. Rev.* **2013**, *42*, 7571−7637.

(16) El-Eskandarany, M. S.; Al-Hazza, A.; Al-Hajji, L. A.; Ali, N.; Al-Duweesh, A. A.; Banyan, M.; Al-Ajmi, F. Mechanical Milling: A Superior Nanotechnological Tool for Fabrication of Nanocrystalline and Nanocomposite Materials. *Nanomaterials* **2021**, *11*, 2484.

(17) Farhad, S. F. U.; Naher, M. I.; Tanvir, N. I.; Quddus, M. S.; Jahan, S. A.; Shaikh, M. A. A. Facile Top-Down Synthesis of Phase-Pure and Tunable Bandgap $CuBi_2O_4$ Photocathode Materials by Low-Energy Sequential Ball Milling. *ACS Appl. Energy Mater.* **2024**, *7*, 8278−8287.

(18) Howard, J. L.; Cao, Q.; Browne, D. L. Mechanochemistry as an emerging tool for molecular synthesis: What can it offer? *Chem. Sci.* **2018**, *9*, 3080−3094.

(19) (a) Antic, B.; Jovic, N.; Pavlovic, M. B.; Kremenovic, A.; Manojlović, D.; Vucinic-Vasic, M.; Nikolić, A. S. Magnetization enhancement in nanostructured random type $MgFe_2O_4$ spinel prepared by soft mechanochemical route. *J. Appl. Phys.* **2010**, *107*, 043525. (b) Yalamaç, E.; Akkurt, S.; Çiftçioğlu, M. Low Temperature Synthesis of Spinel Powders by Mechanical Grinding. *Key Eng. Mater.* **2004**, *264−268*, 53−56. (c) Plešingerová, B.; Števulová, N.; Luxová, M.; Boldižárová, E. Mechanochemical Synthesis of Magnesium Aluminate Spinel in Oxide-Hydroxide Systems. *J. Mater. Synth. Process.* **2000**, *8*,

287−293. (d) Kril'ová, L.; Števulová, N. The kinetic study of the synthesis of magnesium aluminate spinel from mechanochemically treated mixtures of oxide-hydroxide. *J. Mater. Sci.* **2004**, *39*, 5403−5405.
(20) (a) Bar-On, P.; Lin, I. J.; Nadiv, S.; Melamud, M. Formation of partially inverse Mg−Al spinel by grinding MgO with γ-Al_2O_3. *J. Therm. Anal.* **1994**, *42*, 207−217. (b) Šepelák, V.; Feldhoff, A.; Heitjans, P.; Krumeich, F.; Menzel, D.; Litterst, F. J.; Bergmann, I.; Becker, K. D. Nonequilibrium Cation Distribution, Canted Spin Arrangement, and Enhanced Magnetization in Nanosized $MgFe_2O_4$ Prepared by a One-Step Mechanochemical Route. *Chem. Mater.* **2006**, *18*, 3057−3067. (c) Bergmann, I.; Šepelák, V.; Becker, K. D. Preparation of nanoscale $MgFe_2O_4$ via non-conventional mechanochemical route. *Solid State Ionics* **2006**, *177*, 1865−1868. (d) Domanski, D.; Urretavizcaya, G.; Castro, F. J.; Gennari, F. C. Mechanochemical Synthesis of Magnesium Aluminate Spinel Powder at Room Temperature. *J. Am. Ceram. Soc.* **2004**, *87*, 2020−2024. (e) Bocanegra, S. A.; Ballarini, A. D.; Scelza, O. A.; de Miguel, S. R. The influence of the synthesis routes of $MgAl_2O_4$ on its properties and behavior as support of dehydrogenation catalysts. *Mater. Chem. Phys.* **2008**, *111*, 534−541.
(21) (a) Pavlović, M.; Jovalekić, C.; Nikolić, A. S.; Manojlović, D.; Šojić, N. Mechanochemical synthesis of stoichiometric $MgFe_2O_4$ spinel. *J. Mater. Sci.: Mater. Electron.* **2009**, *20*, 782−787. (b) Sekulić, D. L.; Lazarević, Z. Z.; Jovalekić, C.; D.; Milutinović, A. N.; Romčević, N. Z. Impedance Spectroscopy of Nanocrystalline $MgFe_2O_4$ and $MnFe_2O_4$ Ferrite Ceramics: Effect of Grain Boundaries on the Electrical Properties. *Sci. Sintering* **2016**, *48*, 17−28.
(22) (a) Hu, L.; Jokisaari, J. R.; Kwon, B. J.; Yin, L.; Kim, S.; Park, H.; Lapidus, S. H.; Klie, R. F.; Key, B.; Zapol, P.; Ingram, B. J.; Vaughey, J. T.; Cabana, J. High Capacity for Mg^{2+} Deintercalation in Spinel Vanadium Oxide Nanocrystals. *ACS Energy Lett.* **2020**, *5*, 2721−2727. (b) Ding, Q.; Han, T.; Zhou, T.; Lin, X.; Liu, J. A Temperature-Tolerant Magnesium-Ion Battery Using Ball Cactus-like MgV_2O_4 as High-Performance Cathode. *Chem.—Eur. J.* **2024**, *30*, No. e202302978. (c) Tang, W.; Lan, B.; Tang, C.; An, Q.; Chen, L.; Zhang, W.; Zuo, C.; Dong, S.; Luo, P. Urchin-like Spinel MgV_2O_4 as a Cathode Material for Aqueous Zinc-Ion Batteries. *ACS Sustain. Chem. Eng.* **2020**, *8*, 3681−3688.
(23) (a) Rüdorff, W.; Reuter, B. Über Verbindungen des Vanadin-(III)oxyds und des Vanadin(IV)oxyds mit einigen zweiwertigen basischen Oxyden. *Z. Anorg. Chem.* **1947**, *253*, 177−193. (b) Mamiya, H.; Onoda, M. Electronic states of vanadium spinels MgV_2O_4 and ZnV_2O_4. *Solid State Commun.* **1995**, *95*, 217−221. (c) Riedel, E.; Alisch, C. Verteilung und Valenz der Kationen in Spinellsystemen mit Eisen und Vanadium, V Röntgenographische und Mößbauer-spektroskopische Untersuchung des Spinellsystems FeV_2O_4—MgV_2O_4. *Z. Naturforsch., B* **1987**, *42*, 1549−1552. (d) Lee, J.; Dey, S.; Dutton, S. E.; Grey, C. P. Synthesis and Characterization of Magnesium Vanadates as Potential Magnesium-Ion Cathode Materials through an Ab Initio Guided Carbothermal Reduction Approach. *Angew. Chem., Int. Ed.* **2022**, *61*, No. e202112688.
(24) Lee, J.; Seymour, I. D.; Pell, A. J.; Dutton, S. E.; Grey, C. P. A systematic study of ^{25}Mg NMR in paramagnetic transition metal oxides: applications to Mg-ion battery materials. *Phys. Chem. Chem. Phys.* **2017**, *19*, 613−625.
(25) (a) Inazu, N.; Suzuki, E.; Fujii, S.; Tsubaki, S.; Wada, Y. A. Facile Formation of Vanadium(0) by the Reduction of Vanadium Pentoxide Pelletized with Magnesium Oxide Enabled by Microwave Irradiation. *ChemistrySelect* **2020**, *5*, 2949−2953. (b) Jisen, Y.; Zhihe, D.; Ting'an, Z. Preparation of vanadium by the magnesiothermic self-propagating reduction and process control. *Nanotechnol. Rev.* **2022**, *11*, 1237−1247.
(26) Yang, H.; McCormick, P. G. Mechanochemical Reduction of V_2O_5. *J. Solid State Chem.* **1994**, *110*, 136−141.
(27) Takacs, L. Self-sustaining reactions induced by ball milling. *Prog. Mater. Sci.* **2002**, *47*, 355−414.
(28) Mukherjee, A.; Krishnamurthy, N. Phase evolution during mechanochemical coreduction of V_2O_5 and TiO_2 with Al. *Int. J. Self-Propag. High-Temp. Synth.* **2010**, *19*, 237−243.
(29) Jalaly, M.; Gotor, F. J.; Sayagués, M. J. Mechanochemical combustion synthesis of vanadium carbide (VC), niobium carbide (NbC) and tantalum carbide (TaC) nanoparticles. *Int. J. Refract. Met. Hard Mater.* **2019**, *79*, 177−184.
(30) Michaely, A.; Luckas, C.; Haberkorn, R.; Kickelbick, G. Highly Exothermic and Fast Mechanochemical Redox and Intercalation Reactions of V_2O_5 with Sodium Hydride. *Inorg. Chem.* **2024**, *63*, 8099−8108.
(31) Choi, S. H.; Sim, J. J.; Lim, J. H.; Seo, S.-J.; Kim, D.-W.; Hyun, S.-K.; Park, K.-T. Removal of Mg and MgO By-Products through Magnesiothermic Reduction of Ti Powder in Self-Propagating High-Temperature Synthesis. *Metals* **2019**, *9*, 169.
(32) *Topas Bruker AXS Inc.: Karlsruhe (Germany)*, 2014.
(33) Cheary, R. W.; Coelho, A. A fundamental parameters approach to X-ray line-profile fitting. *J. Appl. Crystallogr.* **1992**, *25*, 109−121.
(34) *Pearson's Crystal Data: Crystal Structure Database for Inorganic Compounds. Release 2022/23*; ASM International: Materials Park: Ohio (USA), 2023.
(35) Wiedemann, H. T. A.; Ruloff, S.; Richter, R.; Zollitsch, C. W.; Kay, C. W. M. Towards high performance dielectric microwave resonators for X-band EPR spectroscopy. *J. Magn. Reson.* **2023**, *354*, 107519.
(36) *MATLAB*; The MathWorks Inc.: Natick, Massachusetts (USA), 2024.
(37) Stoll, S.; Schweiger, A. EasySpin, a comprehensive software package for spectral simulation and analysis in EPR. *J. Magn. Reson.* **2006**, *178*, 42−55.
(38) Blöchl, P. E. Projector augmented-wave method. *Phys. Rev. B* **1994**, *50*, 17953−17979.
(39) (a) Kresse, G.; Furthmüller, J. Efficient iterative schemes for *ab initio* total-energy calculations using a plane-wave basis set. *Phys. Rev. B* **1996**, *54*, 11169−11186. (b) Kresse, G.; Furthmüller, J. Efficiency of ab-initio total energy calculations for metals and semiconductors using a plane-wave basis set. *Comput. Mater. Sci.* **1996**, *6*, 15−50. (c) Kresse, G.; Joubert, D. From ultrasoft pseudopotentials to the projector augmented-wave method. *Phys. Rev. B* **1999**, *59*, 1758−1775.
(40) Perdew, J. P.; Ruzsinszky, A.; Csonka, G. I.; Vydrov, O. A.; Scuseria, G. E.; Constantin, L. A.; Zhou, X.; Burke, K. Restoring the Density-Gradient Expansion for Exchange in Solids and Surfaces. *Phys. Rev. Lett.* **2008**, *100*, 136406.
(41) (a) Haynes, W. M. *CRC Handbook of Chemistry and Physics*; CRC Press, 2016. (b) Kijima, N.; Toba, M.; Yoshimura, Y. A. Chemical Potential Diagram and an In-situ X-ray Diffraction Analysis of a V−Mg−O Catalyst Used in the Oxidative Dehydrogenation of n-Butane. *Catal. Lett.* **2009**, *127*, 63−69.
(42) Hazen, R. M. Effects of temperature and pressure on the cell dimension and X-ray temperature factors of periclase. *Am. Mineral.* **1976**, *61*, 266−271.
(43) Reuter, B.; Weber, R.; Jaskowsky, J. Über Oxidsysteme mit Übergangsmetallen in verschiedenen Oxydationsstufen und ihr elektrisches Verhalten I. Das System VO—$LiVO_2$. *Z. Elektrochem., Ber. Bunsenges. Phys. Chem.* **1962**, *66*, 832−838.
(44) Plumier, R.; Tardieu, A. Étude par diffraction des neutrons du composé spinelle MgV_2O_4. *Compt. Rend* **1963**, *257*, 3858−3859.
(45) Shannon, R. D. Revised effective ionic radii and systematic studies of interatomic distances in halides and chalcogenides. *Acta Crystallogr., Sect. A* **1976**, *32*, 751−767.
(46) Dinse, A.; Ozarowski, A.; Hess, C.; Schomäcker, R.; Dinse, K.-P. Potential of High-Frequency EPR for Investigation of Supported Vanadium Oxide Catalysts. *J. Phys. Chem. C* **2008**, *112*, 17664−17671.
(47) Zolnierkiewicz, G.; Typek, J.; Guskos, N.; Bosacka, M. EPR Study of Defect Centers in New $Mg_2InV_3O_{11}$ Vanadate. *Appl. Magn. Reson.* **2008**, *34*, 101−109.
(48) Rybarczyk, P.; Berndt, H.; Radnik, J.; Pohl, M.-M.; Buyevskaya, O.; Baerns, M.; Brückner, A. The Structure of Active Sites in *Me*−V−O Catalysts (*Me* = Mg, Zn, Pb) and Its Influence on the Catalytic Performance in the Oxidative Dehydrogenation (ODH) of Propane. *J. Catal.* **2001**, *202*, 45−58.
(49) (a) Krupa, B. R. V.; Dasgupta, A.; Ghosh, C.; Sinha, S. K. Analysis of structural transformation in nanocrystalline Y_2O_3 during high energy ball milling. *J. Alloys Compd.* **2022**, *900*, 163550. (b) Pradhan, S. K.;

https://doi.org/10.1021/acs.inorgchem.5c03095
Inorg. Chem. 2025, 64, 20163−20174

Shee, S. K.; Chanda, A.; Bose, P.; De, M. X-ray studies on the kinetics of microstructural evolution of Ni_3Al synthesized by ball milling elemental powders. *Mater. Chem. Phys.* **2001**, *68*, 166−174. (c) Hadef, F.; Ans, M. X-ray analysis and Rietveld refinement of ball milled $Fe_{50}Al_{35}Ni_{15}$ powder. *Surf. Interfaces* **2021**, *26*, 101303.

(50) Stein, M., IV; Chen, C.-F.; Mullings, M.; Jaime, D.; Zaleski, A.; Mukherjee, P. P.; Rhodes, C. P. Probing the Effect of High Energy Ball Milling on the Structure and Properties of $LiNi_{1/3}Mn_{1/3}Co_{1/3}O_2$ Cathodes for Li-Ion Batteries. *J. Electrochem. Energy Convers. Storage* **2016**, *13*, 031001.

(51) Malyk, O. P.; Syrotyuk, S. V. Local Electron Interaction with Point Defects in Sphalerite Zinc Selenide: Calculation from First Principles. *J. Electron. Mater.* **2018**, *47*, 4212−4218.

(52) (a) Irvine, J. T. S.; Sinclair, D. C.; West, A. R. Electroceramics: Characterization by Impedance Spectroscopy. *Adv. Mater.* **1990**, *2*, 132−138. (b) Delacourt, C.; Laffont, L.; Bouchet, R.; Wurm, C.; Leriche, J.-B.; Morcrette, M.; Tarascon, J.-M.; Masquelier, C. Toward Understanding of Electrical Limitations (Electronic, Ionic) in $LiMPO_4$ (M = Fe, Mn) Electrode Materials. *J. Electrochem. Soc.* **2005**, *152*, A913.

(53) (a) Di, L.; Pan, J.; Gao, L.; Zhu, J.; Wang, L.; Wang, X.; Su, Q.; Gao, S.; Zou, R.; Zhao, Y.; Han, S. Effect of grain boundary resistance on the ionic conductivity of amorphous xLi_2S-(100-x)LiI binary system. *Front. Chem.* **2023**, *11*, 1230187. (b) Shindrov, A. A.; Skachilova, M. G.; Shapovalova, A. A.; Kosova, N. V. Application of dry high-energy ball-milling to increase the density and grain boundary conductivity of solid ceramic electrolytes: $Li_{1.3}Al_{0.3}Ti_{1.7}(PO_4)_3$ as a case study. *Ionics* **2025**, *31*, 1351−1360.

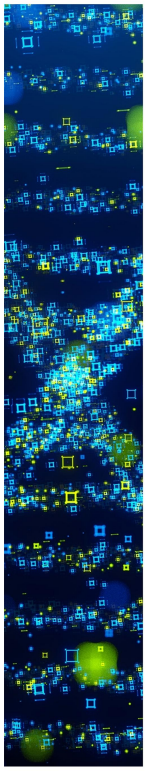

https://doi.org/10.1021/acs.inorgchem.5c03095
Inorg. Chem. 2025, 64, 20163−20174

4 Conclusion and Outlook

In this thesis, the use of group 1 and 2 metal (hydrides) as highly effective reducing agents for the mechanochemical reduction of group 4 and 5 transition metal oxides TiO_2, Nb_2O_5, and V_2O_5 has been extensively explored. In contrast to traditional high-temperature solid-state reductions, it was shown that mechanochemistry enables rapid, solvent-free reduction reactions at room temperature. Depending on the milling conditions (reducing agent concentration and milling time) and the investigated transition metal oxide, different reaction behaviors were observed.

Mechanochemical treatment of white rutile-type TiO_2 and monoclinic H-Nb_2O_5 with LiH and NaH for up to 60 min yielded powders with a color ranging from light gray to black, indicating a reduction of Ti^{4+} to Ti^{3+} and of Nb^{5+} to Nb^{4+}. PXRD analysis and Rietveld refinement showed that the crystal structures of the pristine oxides were retained, but an increase of the cell volume of several $Å^3$ was observed in case of LiH due to the intercalation of lithium. Additionally, the formation of rock-salt type $Li_{0.5}Ti_{0.5}O$ was observed in the case of TiO_2. The presence of unpaired electrons by EPR spectroscopy further confirms the successful partial reduction of TiO_2 and Nb_2O_5 to black titania and black niobia, respectively. The incorporation of Li is further supported by ^{6}Li SPE-MAS NMR spectroscopy, which also shows an interaction of the formed paramagnetic Ti^{3+} ions with the Li nucleus in case of LiH-reduced TiO_2. Both NMR and Raman spectroscopy reveal a significant amount of structural disorder with increasing milling time and increasing hydride concentrations. Due to the present disorder and defects, as well as a decrease of the optical band gap of up to 0.4 eV, the as-synthesized black oxides exhibited significantly enhanced photocatalytic performance compared to pristine ones under illumination with UV and visible light for methylene blue degradation. Further investigations and optimization of the milling conditions might give a more profound understanding of the ball milling reduction and might further improve the photocatalytic performance. Additionally, their suitability for other applications such as battery materials could be explored.

In contrast, V_2O_5 displayed a different reaction behavior during ball milling with NaH. While a continuous pressure increase indicates a continuous formation of hydrogen gas during the reduction of TiO_2 and Nb_2O_5 with the tested hydrides, a rapid and large increase in pressure is observed with V_2O_5 after a few minutes of milling. This sudden release of hydrogen gas, confirmed by a positive oxyhydrogen test, as well as the presence of larger pieces of molten particles at the maximum pressure increase, suggest that the mechanochemical reaction between V_2O_5 and NaH occurred in a highly exothermic, self-propagating manner. Depending

on the synthesis conditions, a mixture of different vanadium oxides and sodium vanadates with vanadium oxidation states ranging from +III to +V was identified by Rietveld refinement. Hereby, the hydride concentration has a greater influence on the final sample composition than the milling time. In general, with increasing amounts of reducing agent, higher percentages of vanadates are formed instead of vanadium oxides, sodium vanadates with V^{5+} become richer in sodium and lower oxidation states of vanadium are accessed. DFT calculations confirmed the high exothermicity of the studied systems, showing that higher NaH concentrations lead to more exothermic reaction enthalpies, which agrees nicely with the experimental observations. Furthermore, the formation of alkali metal vanadates with V^{5+} appears to be energetically favorable, causing the reduction of V_2O_5 to V_2O_3 to be more favorable than the reduction to VO_2 and can be seen as the driving force for these highly exothermic reactions.
The general validity of these mechanochemical reduction reactions of V_2O_5 were extended to LiH as reducing agent, as well as the theoretically even more powerful reducing agents Na and Li. While all observed reactions were highly exothermic, those induced with elemental alkali metals ignited earlier. This suggests lower activation energies, which is consistent with the calculated lower (more exothermic) reaction enthalpies. Overall, the tested hydrides and their elemental counterparts gave similar product mixtures of (alkali metal) vanadium oxides. It can therefore be concluded that similar reactions occur simultaneously independent of the reducing agent. However, both Na and Li produce mixtures with both more and less reduced alkali metal vanadates compared to NaH and LiH. While the formation of more reduced phases is likely due to their higher reductive strength, their higher ductility hinders the effective energy transfer, causing the formation of less reduced products. Problems with ductility occurred especially with large amounts of sodium, resulting in a sticky and unmanageable reaction mixture. Although cryomilling can overcome this issue, alkali metal hydrides offer easier handling and safer mixing, despite hydrogen gas formation risks. These ductility issues become less prominent when less ductile reducing agents are used, as shown in last part of this thesis for the mechanochemical reduction of V_2O_5 with Mg.

In the last part of this thesis, the mechanochemical synthesis of spinel-type MgV_2O_4, a promising electrode material for batteries, was investigated by testing the suitability of different reactant combinations: V_2O_3/MgO, $2VO_2$/Mg, V_2O_5+V_2O_3 (formally VO_2)/2Mg andV_2O_5/2Mg. In accordance with DFT calculations, only the most exothermic reactant combination resulted in the successful formation of MgV_2O_4. While the endothermic reaction between V_2O_3 and MgO could not be induced at all, mechanochemical treatment of VO_2 and

Mg eventually led to the formation of mainly nanocrystalline V_2O_3 and MgO and only little amounts of MgV_2O_4. This can be explained with slightly more exothermic reaction enthalpy for the formation of V_2O_3 and MgO (–2.73 eV) compared to the one of MgV_2O_4 (–2.12 eV). When employing a combination of V_2O_5, V_2O_3 and 2Mg, only a self-propagating reaction between V_2O_5 and Mg occurred first, while the endothermic reaction between V_2O_3 and freshly formed MgO did not proceed. As for the mechanically induced self-propagating reaction of V_2O_5 and 2 eq. Mg, MgV_2O_4 and MgO were obtained as fine powders in less than 20 min of milling. Increasing milling speeds led to an earlier ignition of the reaction and a lower crystallite size, as well as larger strain in MgV_2O_4 due to the larger impact of mechanical energy. Under harsh milling conditions, a non-stoichiometry of the formed products and formation of a magnesium-rich spinel and a vanadium containing rock salt phase were observed, as supported by XRD and EPR measurements. After removal of the majority of MgO by acid washing, as confirmed by ICP-MS measurements, EIS measurements were performed to study the influence of the ball milling conditions on the conductivity of the as-prepared samples. Hereby, the sample milled at 300 rpm showed the highest conductivity, due to the lowest number of defects and grain boundaries. Thus, intense milling is not always favorable for achieving optimal material properties.

5 References

(1) Takacs, L. The historical development of mechanochemistry. *Chem. Soc. Rev.* **2013**, *42*, 7649-7659, DOI: 10.1039/c2cs35442j.
(2) Takacs, L. Quicksilver from cinnabar: The first documented mechanochemical reaction? *JOM* **2000**, *52*, 12-13, DOI: 10.1007/s11837-000-0106-0.
(3) Lea, M. C. Disruption of the silver haloid molecule by mechanical force. *Am. J. Sci.* **1892**, *s3-43*, 527-531, DOI: 10.2475/ajs.s3-43.258.527.
(4) Heinicke, G. *Tribochemistry*; Carl Hanser Verlag, München, 1984.
(5) 'Mechano-chemical reaction' in *IUPAC Compendium of Chemical Terminology*, 5th ed. International Union of Pure and Applied Chemistry; 2025. Online version 5.0.0, 2025. DOI: 10.1351/goldbook.MT07141.
(6) Gomollón-Bel, F. Ten Chemical Innovations That Will Change Our World: IUPAC identifies emerging technologies in Chemistry with potential to make our planet more sustainable. *Chem. Int.* **2019**, *41*, 12-17, DOI: 10.1515/ci-2019-0203.
(7) Ardila-Fierro, K. J.; Hernández, J. G. Sustainability Assessment of Mechanochemistry by Using the Twelve Principles of Green Chemistry. *ChemSusChem* **2021**, *14*, 2145-2162, DOI: 10.1002/cssc.202100478.
(8) Han, G.-F.; Li, F.; Chen, Z.-W.; Coppex, C.; Kim, S.-J.; Noh, H.-J.; Fu, Z.; Lu, Y.; Singh, C. V.; Siahrostami, S.; et al. Mechanochemistry for ammonia synthesis under mild conditions. *Nat. Nanotechnol.* **2021**, *16*, 325-330, DOI: 10.1038/s41565-020-00809-9.
(9) Kim, J.-H.; Dai, T.-Y.; Yang, M.; Seo, J.-M.; Lee, J. S.; Kweon, D. H.; Lang, X.-Y.; Ihm, K.; Shin, T. J.; Han, G.-F.; et al. Achieving volatile potassium promoted ammonia synthesis via mechanochemistry. *Nat. Commun.* **2023**, *14*, 2319, DOI: 10.1038/s41467-023-38050-2.
(10) Howard, J. L.; Cao, Q.; Browne, D. L. Mechanochemistry as an emerging tool for molecular synthesis: What can it offer? *Chem. Sci.* **2018**, *9*, 3080-3094, DOI: 10.1039/C7SC05371A.
(11) Tan, D.; García, F. Main group mechanochemistry: from curiosity to established protocols. *Chem. Soc. Rev.* **2019**, *48*, 2274-2292, DOI: 10.1039/c7cs00813a.
(12) Chen, Y.; Mellot, G.; Van Luijk, D.; Creton, C.; Sijbesma, R. P. Mechanochemical tools for polymer materials. *Chem. Soc. Rev.* **2021**, *50*, 4100-4140, DOI: 10.1039/D0CS00940G.
(13) Šepelák, V.; Düvel, A.; Wilkening, M.; Becker, K. D.; Heitjans, P. Mechanochemical reactions and syntheses of oxides. *Chem. Soc. Rev.* **2013**, *42*, 7507-7520, DOI: 10.1039/c2cs35462d.
(14) Chen, D.; Zhao, J.; Zhang, P.; Dai, S. Mechanochemical synthesis of metal–organic frameworks. *Polyhedron* **2019**, *162*, 59-64, DOI: 10.1016/j.poly.2019.01.024.
(15) Suryanarayana, C. Mechanical alloying and milling. *Prog. Mater Sci.* **2001**, *46*, 1-184, DOI: 10.1016/S0079-6425(99)00010-9.
(16) Fuentes, A. F.; Takacs, L. Preparation of multicomponent oxides by mechanochemical methods. *J. Mater. Sci.* **2013**, *48*, 598-611, DOI: 10.1007/s10853-012-6909-x.
(17) Broseghini, M.; Gelisio, L.; D'Incau, M.; Azanza Ricardo, C. L.; Pugno, N. M.; Scardi, P. Modeling of the planetary ball-milling process: The case study of ceramic powders. *J. Eur. Ceram. Soc.* **2016**, *36*, 2205-2212, DOI: 10.1016/j.jeurceramsoc.2015.09.032.
(18) Burgio, N.; Iasonna, A.; Magini, M.; Martelli, S.; Padella, F. Mechanical alloying of the Fe-Zr system. Correlation between input energy and end products. *Il Nuovo Cimento D* **1991**, *13*, 459-476, DOI: 10.1007/BF02452130.
(19) Rogachev, A. S.; Moskovskikh, D. O.; Nepapushev, A. A.; Sviridova, T. A.; Vadchenko, S. G.; Rogachev, S. A.; Mukasyan, A. S. Experimental investigation of milling regimes in planetary ball mill and their influence on structure and reactivity of gasless powder exothermic mixtures. *Powder Technol.* **2015**, *274*, 44-52, DOI: 10.1016/j.powtec.2015.01.009.

(20) Begin-Colin, S.; Le Caër, G.; Zandona, M.; Bouzy, E.; Malaman, B. Influence of the nature of milling media on phase transformations induced by grinding in some oxides. *J. Alloys Compd.* **1995**, *227*, 157-166, DOI: 10.1016/0925-8388(95)01596-5.
(21) B.R, V. K.; Dasgupta, A.; Ghosh, C.; Sinha, S. K. Analysis of structural transformation in nanocrystalline Y_2O_3 during high energy ball milling. *J. Alloys Compd.* **2022**, *900*, 163550, DOI: 10.1016/j.jallcom.2021.163550.
(22) Betke, A.; Kickelbick, G. Important reaction parameters in the synthesis of phenylphosphonic acid functionalized titania particles by reactive milling. *New J. Chem.* **2014**, *38*, 1264-1270, DOI: 10.1039/C3NJ01291C.
(23) Haynes, W. M. *CRC Handbook of Chemistry and Physics*; CRC Press, Boca Raton, 2016.
(24) Lennox, C. B.; Borchers, T. H.; Gonnet, L.; Barrett, C. J.; Koenig, S. G.; Nagapudi, K.; Friščić, T. Direct mechanocatalysis by resonant acoustic mixing (RAM). *Chem. Sci.* **2023**, *14*, 7475-7481, DOI: 10.1039/D3SC01591B.
(25) Wohlgemuth, M.; Mayer, M.; Rappen, M.; Schmidt, F.; Saure, R.; Grätz, S.; Borchardt, L. From Inert to Catalytically Active Milling Media: Galvanostatic Coating for Direct Mechanocatalysis. *Angew. Chem. Int. Ed.* **2022**, *61*, e202212694, DOI: 10.1002/anie.202212694.
(26) Belenguer, A. M.; Lampronti, G. I.; Michalchuk, A. A. L.; Emmerling, F.; Sanders, J. K. M. Quantitative reversible one pot interconversion of three crystalline polymorphs by ball mill grinding. *CrystEngComm* **2022**, *24*, 4256-4261, DOI: 10.1039/D2CE00393G.
(27) Krusenbaum, A.; Grätz, S.; Bimmermann, S.; Hutsch, S.; Borchardt, L. The mechanochemical Scholl reaction as a versatile synthesis tool for the solvent-free generation of microporous polymers. *RSC Adv.* **2020**, *10*, 25509-25516, DOI: 10.1039/D0RA05279E
(28) Bolt, R. R. A.; Raby-Buck, S. E.; Ingram, K.; Leitch, J. A.; Browne, D. L. Temperature-Controlled Mechanochemistry for the Nickel-Catalyzed Suzuki–Miyaura-Type Coupling of Aryl Sulfamates via Ball Milling and Twin-Screw Extrusion. *Angew. Chem. Int. Ed.* **2022**, *61*, e202210508, DOI: 10.1002/anie.202210508.
(29) Cindro, N.; Tireli, M.; Karadeniz, B.; Mrla, T.; Užarević, K. Investigations of Thermally Controlled Mechanochemical Milling Reactions. *ACS Sustain. Chem. Eng.* **2019**, *7*, 16301-16309, DOI: 10.1021/acssuschemeng.9b03319.
(30) Kumar, N.; Biswas, K. Cryomilling: An environment friendly approach of preparation large quantity ultra refined pure aluminium nanoparticles. *J. Mater. Res. Technol.* **2019**, *8*, 63-74, DOI: 10.1016/j.jmrt.2017.05.017.
(31) Abdellaoui, M.; Gaffet, E. The physics of mechanical alloying in a planetary ball mill: Mathematical treatment. *Acta metall. mater.* **1995**, *43*, 1087-1098, DOI: 10.1016/0956-7151(95)92625-7.
(32) Rojac, T.; Kosec, M.; Malič, B.; Holc, J. The application of a milling map in the mechanochemical synthesis of ceramic oxides. *J. Eur. Ceram. Soc.* **2006**, *26*, 3711-3716, DOI: 10.1016/j.jeurceramsoc.2005.11.013.
(33) Chattopadhyay, P. P.; Manna, I.; Talapatra, S.; Pabi, S. K. Mathematical analysis of milling mechanics in a planetary ball mill. *Mater. Chem. Phys.* **2001**, *68*, 85-94, DOI: 10.1016/S0254-0584(00)00289-3.
(34) Kozma, G.; Puskás, R.; Papp, I. Z.; Bélteky, P.; Kónya, Z.; Kukovecz, Á. Experimental validation of the Burgio–Rojac model of planetary ball milling by the length control of multiwall carbon nanotubes. *Carbon* **2016**, *105*, 615-621, DOI: 10.1016/j.carbon.2016.05.005.
(35) Jafter, O. F.; Lee, S.; Park, J.; Cabanetos, C.; Lungerich, D. Navigating Ball Mill Specifications for Theory-to-Practice Reproducibility in Mechanochemistry. *Angew. Chem. Int. Ed.* **2024**, *63*, e202409731, DOI: 10.1002/anie.202409731.
(36) Delogu, F.; Cocco, G. Weakness of the "hot spots" approach to the kinetics of mechanically induced phase transformations. *J. Alloys Compd.* **2008**, *465*, 540-546, DOI: 10.1016/j.jallcom.2007.11.024.

(37) Bowden, F.; Yoffe, A. *Fast Reactions in Solids*; Butterworths, London, 1958.
(38) Bowden, F. P.; Tabor, D. *The Friction and Lubrication of Solids*; Clarendon Press, Oxford, 1958.
(39) Bowden, F. P.; Yoffe, A. D.; Hudson, G. E. *Initiation and Growth of Explosion in Liquids and Solids*; Cambridge University Press, Cambridge, 1952.
(40) Thiessen, P. A.; Meyer, K.; Heinicke, G. *Grundlagen der Tribochemie*; Akademie-Verlag, Berlin, 1967.
(41) Ma, X.; Yuan, W.; Bell, S. E. J.; James, S. L. Better understanding of mechanochemical reactions: Raman monitoring reveals surprisingly simple 'pseudo-fluid' model for a ball milling reaction. *Chem. Commun.* **2014**, *50*, 1585-1587, DOI: 10.1039/C3CC47898J.
(42) Carta, M.; Delgou, F.; Porcheddu, A. A phenomenological kinetic equation for mechanochemical reactions involving highly deformable molecular solids *Phys. Chem. Chem. Phys.* **2021**, *23*, 14178-14194, DOI: 10.1039/D1CP01361K
(43) Sukhomlinov, S. V.; Kickelbick, G.; Müser, M. H. Mechanochemical Ionization: Differentiating Pressure-, Shear-, and Temperature-Induced Reactions in a Model Phosphate. *Tribol. Lett.* **2022**, *70*, 102, DOI: 10.1007/s11249-022-01644-w.
(44) Pladevall, B. S.; de Aguirre, A.; Maseras, F. Understanding Ball Milling Mechanochemical Processes with DFT Calculations and Microkinetic Modeling. *ChemSusChem* **2021**, *14*, 2763-2768, DOI: 10.1002/cssc.202100497.
(45) Bhuiyan, F. H.; Li, Y.-S.; Kim, S. H.; Martini, A. Shear-activation of mechanochemical reactions through molecular deformation. *Sci. Rep.* **2024**, *14*, 2992, DOI: 10.1038/s41598-024-53254-2.
(46) Begin-Colin, S.; Le Caer, G.; Mocellin, A.; Zandona, M. Polymorphic transformations of titania induced by ball milling. *Philos. Mag. Lett.* **1994**, *69*, 1-7, DOI: 10.1080/09500839408242430.
(47) Straub, T. B.; Haberkorn, R.; Kickelbick, G. Mechanochemical Activation of Mn_3O_4: Implications for Lithium Intercalation. *Inorg. Chem.* **2025**, *64*, 6420-6433, DOI: 10.1021/acs.inorgchem.4c04660.
(48) Gauthier, R.; Scott, B.; Bennett, J. C.; Salehabadi, M.; Wang, J.; Sainuddin, T.; Obrovac, M. N. The amorphization of crystalline silicon by ball milling. *Heliyon* **2024**, *10*, e34881, DOI: 10.1016/j.heliyon.2024.e34881.
(49) Fan, G. J.; Guo, F. Q.; Hu, Z. Q.; Quan, M. X.; Lu, K. Amorphization of selenium induced by high-energy ball milling. *Phys. Rev. B* **1997**, *55*, 11010-11013, DOI: 10.1103/PhysRevB.55.11010.
(50) Wang, C.; Hu, H.; Yan, S.; Zhang, Q. Activating Bi_2O_3 by ball milling to induce efficiently oxygen vacancy for incorporating iodide anions to form BiOI. *Chem. Phys.* **2020**, *533*, 110739, DOI: 10.1016/j.chemphys.2020.110739.
(51) Zheng, R.; Zhu, L.; Li, C.; Wu, Z.; Huang, Y.; Yang, J.; Wei, R.; Zhu, X.; Sun, Y. Ball milling as an effective method for improving oxygen evolution reaction electrocatalyst $Ca_3Co_4O_9$. *J. Electroanal. Chem.* **2023**, *931*, 117182, DOI: 10.1016/j.jelechem.2023.117182.
(52) Daiko, Y.; Schmidt, J.; Kawamura, G.; Romeis, S.; Segets, D.; Iwamoto, Y.; Peukert, W. Mechanochemically induced sulfur doping in ZnO via oxygen vacancy formation. *Phys. Chem. Chem. Phys.* **2017**, *19*, 13838-13845, DOI: 10.1039/c7cp01489a.
(53) Baláž, P.; Achimovičová, M.; Baláž, M.; Billik, P.; Cherkezova-Zheleva, Z.; Criado, J. M.; Delogu, F.; Dutková, E.; Gaffet, E.; Gotor, F. J.; et al. Hallmarks of mechanochemistry: from nanoparticles to technology. *Chem. Soc. Rev.* **2013**, *42*, 7571-7637, DOI: 10.1039/C3CS35468G.
(54) Boldyrev, V. V.; Tkáčová, K. Mechanochemistry of solids: Past, present, and prospects. *J. Mater. Synth. Process.* **2000**, *8*, 121-132, DOI: 10.1023/A:1011347706721.

(55) Khalameida, S.; Sydorchuk, V.; Leboda, R.; Skubiszewska-Zięba, J.; Zazhigalov, V. Mechanochemical synthesis and some properties of dispersed lithium niobate. *Russ. J. Inorg. Chem.* **2014**, *59*, 419-423, DOI: 10.1134/S003602361405009X.
(56) Becker, D.; Haberkorn, R.; Kickelbick, G. Mechanochemical Induced Structure Transformations in Lithium Titanates: A Detailed PXRD and ^{6}Li MAS NMR Study. *Inorganics* **2018**, *6*, 117, DOI: 10.3390/inorganics6040117.
(57) Iwaniak, W.; Fritzsche, J.; Zukalová, M.; Winter, R.; Wilkening, M.; Heitjans, P. Li Conductivity of Nanocrystalline $Li_4Ti_5O_{12}$ Prepared by a Sol-Gel Method and High-Energy Ball Milling. *Defect Diffus. Forum* **2009**, *289-292*, 565-570, DOI: 10.4028/www.scientific.net/DDF.289-292.565.
(58) Martinez, V.; Stolar, T.; Karadeniz, B.; Brekalo, I.; Užarević, K. Advancing mechanochemical synthesis by combining milling with different energy sources. *Nat. Rev. Chem.* **2023**, *7*, 51-65, DOI: 10.1038/s41570-022-00442-1.
(59) Užarević, K.; Halasz, I.; Friščić, T. Real-Time and In Situ Monitoring of Mechanochemical Reactions: A New Playground for All Chemists. *J. Phys. Chem. Lett.* **2015**, *6*, 4129-4140, DOI: 10.1021/acs.jpclett.5b01837.
(60) Lukin, S.; Germann, L. S.; Friščić, T.; Halasz, I. Toward Mechanistic Understanding of Mechanochemical Reactions Using Real-Time In Situ Monitoring. *Acc. Chem. Res.* **2022**, *55*, 1262-1277, DOI: 10.1021/acs.accounts.2c00062.
(61) Weidenthaler, C. In Situ Analytical Methods for the Characterization of Mechanochemical Reactions. *Crystals* **2022**, *12*, 345, DOI: 10.3390/cryst12030345.
(62) Michalchuk, A. A. L.; Emmerling, F. Time-Resolved In Situ Monitoring of Mechanochemical Reactions. *Angew. Chem. Int. Ed.* **2022**, *61*, e202117270, DOI: 10.1002/anie.202117270.
(63) Julien, P. A.; Užarević, K.; Katsenis, A. D.; Kimber, S. A. J.; Wang, T.; Farha, O. K.; Zhang, Y.; Casaban, J.; Germann, L. S.; Etter, M.; et al. In Situ Monitoring and Mechanism of the Mechanochemical Formation of a Microporous MOF-74 Framework. *J. Am. Chem. Soc.* **2016**, *138*, 2929-2932, DOI: 10.1021/jacs.5b13038.
(64) Pallone, E. M. J. A.; Trombini, V.; Botta F, W. J.; Tomasi, R. Synthesis of Al_2O_3–NbC by reactive milling and production of nanocomposites. *J. Mater. Process. Technol.* **2003**, *143-144*, 185-190, DOI: 10.1016/S0924-0136(03)00411-4.
(65) Michaely, A.; Luckas, C.; Haberkorn, R.; Kickelbick, G. Highly Exothermic and Fast Mechanochemical Redox and Intercalation Reactions of V_2O_5 with Sodium Hydride. *Inorg. Chem.* **2024**, *63*, 8099-8108, DOI: 10.1021/acs.inorgchem.4c00200.
(66) Wachs, I. E.; Chen, Y.; Jehng, J.-M.; Briand, L. E.; Tanaka, T. Molecular structure and reactivity of the Group V metal oxides. *Catal. Today* **2003**, *78*, 13-24, DOI: 10.1016/S0920-5861(02)00337-1.
(67) *Pearson's Crystal Data: Crystal Structure Database for Inorganic Compounds. Release 2022/23*; ASM International®: Materials Park: Ohio (USA), 2023.
(68) Kulkarni, D.; Wachs, I. E. Isopropanol oxidation by pure metal oxide catalysts: number of active surface sites and turnover frequencies. *Appl. Catal. A: Gen.* **2002**, *237*, 121-137, DOI: 10.1016/S0926-860X(02)00325-3.
(69) Andersson, S.; Collén, B.; Kuylenstierna, U.; Magnéli, A. Phase Analysis Studies on the Titanium-Oxygen System. *Acta Chem. Scand.* **1957**, *11*, 1641-1652, DOI: 10.3891/acta.chem.scand.11-1641.
(70) Okamoto, H. O-Ti (Oxygen-Titanium). *J. Phase Equilib. Diffus.* **2011**, *32*, 473-474, DOI: 10.1007/s11669-011-9935-5.
(71) Arlt, T.; Bermejo, M.; Blanco, M. A.; Gerward, L.; Jiang, J. Z.; Staun Olsen, J.; Recio, J. M. High-pressure polymorphs of anatase *Phys. Rev. B* **2000**, *61*, 14414-14419, DOI: 10.1103/PhysRevB.61.14414.

(72) Dubrovinsky, L. S.; Dubrovinskaia, N. A.; Swamy, V.; Muscat, J.; Harrison, N. M.; Ahuja, R.; Holm, B.; Johansson, B. The hardest known oxide. *Nature* **2001**, *410*, 653-654, DOI: 10.1038/35070650.
(73) Swamy, V.; Muddle, B. C. Ultrastiff Cubic TiO_2 Identified via First-Principles Calculations. *Phys. Rev. Lett.* **2007**, *98*, 035502, DOI: 10.1103/PhysRevLett.98.035502.
(74) Wang, Q.; Watanabe, M.; Edalati, K. Visible-Light Photocurrent in Nanostructured High-Pressure TiO_2-II (Columbite) Phase. *J. Phys. Chem. C* **2020**, *124*, 13930-13935, DOI: 10.1021/acs.jpcc.0c03923.
(75) Dachille, F.; Simons, P. Y.; Roy, R. Pressure-temperature studies of anatase, brookite, rutile and TiO_2-II. *Am. Mineral.* **1968**, *53*, 1929-1939.
(76) Di Paola, A.; Bellardita, M.; Palmisano, L. Brookite, the Least Known TiO_2 Photocatalyst. *Catalysts* **2013**, *3*, 36-73, DOI: 10.3390/catal3010036.
(77) Greenwood, G. LXVI. The crystal structure of cuprite and rutile. *Phil. Mag.* **1924**, *48*, 654-663, DOI: 10.1080/14786442408634528.
(78) Cromer, D. T.; Herrington, K. The Structures of Anatase and Rutile. *J. Am. Chem. Soc.* **1955**, *77*, 4708-4709, DOI: 10.1021/ja01623a004.
(79) Macwan, D. P.; Dave, P. N.; Chaturvedi, S. A review on nano-TiO_2 sol–gel type syntheses and its applications. *J. Mater. Sci.* **2011**, *46*, 3669-3686, DOI: 10.1007/s10853-011-5378-y.
(80) Noman, M. T.; Ashraf, M. A.; Ali, A. Synthesis and applications of nano-TiO_2: a review. *Environ. Sci. Pollut. Res.* **2019**, *26*, 3262-3291, DOI: 10.1007/s11356-018-3884-z.
(81) Wang, J.; Wang, Z.; Wang, W.; Wang, Y.; Hu, X.; Liu, J.; Gong, X.; Miao, W.; Ding, L.; Li, X.; et al. Synthesis, modification and application of titanium dioxide nanoparticles: a review. *Nanoscale* **2022**, *14*, 6709-6734, DOI: 10.1039/D1NR08349J
(82) Matthews, A. The crystallization of anatase and rutile from amorphous titanium dioxide under hydrothermal conditions. *Am. Mineral.* **1976**, *61*, 419-424.
(83) Zhang, H.; Banfield, J. F. Thermodynamic analysis of phase stability of nanocrystalline titania. *J. Mater. Chem.* **1998**, *8*, 2073-2076, DOI: 10.1039/A802619J
(84) Terabe, K.; Kato, K.; Miyazaki, H.; Yamaguchi, S.; Imai, A.; Iguchi, Y. Microstructure and crystallization behaviour of TiO_2 precursor prepared by the sol-gel method using metal alkoxide. *J. Mater. Sci.* **1994**, *29*, 1617-1622, DOI: 10.1007/BF00368935.
(85) Wang, C.-C.; Ying, J. Y. Sol−Gel Synthesis and Hydrothermal Processing of Anatase and Rutile Titania Nanocrystals. *Chem. Mater.* **1999**, *11*, 3113-3120, DOI: 10.1021/cm990180f.
(86) Arnal, P.; Corriu, R. J. P.; Leclercq, D.; Mutin, P. H.; Vioux, A. Preparation of anatase, brookite and rutile at low temperature by non-hydrolytic sol–gel methods. *J. Mater. Chem.* **1996**, *6*, 1925-1932, DOI: 10.1039/JM9960601925.
(87) Zhu, Y.; Zhang, L.; Gao, C.; Cao, L. The synthesis of nanosized TiO_2 powder using a sol-gel method with $TiCl_4$ as a precursor. *J. Mater. Sci.* **2000**, *35*, 4049-4054, DOI: 10.1023/A:1004882120249.
(88) Cheng, H.; Ma, J.; Zhao, Z.; Qi, L. Hydrothermal Preparation of Uniform Nanosize Rutile and Anatase Particles. *Chem. Mater.* **1995**, *7*, 663-671, DOI: 10.1021/cm00052a010.
(89) Keesmann, I. Zur hydrothermalen Synthese von Brookit. *Z. Anorg. Allg. Chem.* **1966**, *346*, 30-43, DOI: 10.1002/zaac.19663460105.
(90) Wang, C.; Deng, Z.-X.; Zhang, G.; Fan, S.; Li, Y. Synthesis of nanocrystalline TiO_2 in alcohols. *Powder Technol.* **2002**, *125*, 39-44, DOI: 10.1016/S0032-5910(01)00523-X.
(91) Li Bassi, A.; Cattaneo, D.; Russo, V.; Bottani, C. E.; Barborini, E.; Mazza, T.; Piseri, P.; Milani, P.; Ernst, F. O.; Wegner, K.; et al. Raman spectroscopy characterization of titania nanoparticles produced by flame pyrolysis: The influence of size and stoichiometry. *J. Appl. Phys.* **2005**, *98*, 074305, DOI: 10.1063/1.2061894.
(92) Byun, D.; Jin, Y.; Kim, B.; Kee Lee, J.; Park, D. Photocatalytic TiO_2 deposition by chemical vapor deposition. *J. Hazard. Mater.* **2000**, *73*, 199-206, DOI: 10.1016/S0304-3894(99)00179-X.

(93) Jung, S.-C.; Imaishi, N. Preparation, crystal structure, and photocatalytic activity of TiO_2 films by chemical vapor deposition. *Korean J. Chem. Eng.* **2001**, *18*, 867-872, DOI: 10.1007/BF02705610.
(94) Giolli, C.; Borgioli, F.; Credi, A.; Fabio, A. D.; Fossati, A.; Miranda, M. M.; Parmeggiani, S.; Rizzi, G.; Scrivani, A.; Troglio, S.; et al. Characterization of TiO_2 coatings prepared by a modified electric arc-physical vapour deposition system. *Surf. Coat. Technol.* **2007**, *202*, 13-22, DOI: 10.1016/j.surfcoat.2007.04.043.
(95) Anuradha, T. V.; Ranganathan, S. Nanocrystalline TiO_2 by three different synthetic approaches: A comparison. *Bull. Mater. Sci.* **2007**, *30*, 263-269, DOI: 10.1007/s12034-007-0046-1.
(96) Salari, M.; Mousavi khoie, S. M.; Marashi, P.; Rezaee, M. Synthesis of TiO_2 nanoparticles via a novel mechanochemical method. *J. Alloys Compd.* **2009**, *469*, 386-390, DOI: 10.1016/j.jallcom.2008.01.112.
(97) Billik, P.; Plesch, G. Mechanochemical synthesis of anatase and rutile nanopowders from $TiOSO_4$. *Mater. Lett.* **2007**, *61*, 1183-1186, DOI: 10.1016/j.matlet.2006.06.080.
(98) Billik, P.; Plesch, G. Mechanochemical synthesis of nanocrystalline TiO_2 from liquid $TiCl_4$. *Scr. Mater.* **2007**, *56*, 979-982, DOI: 10.1016/j.scriptamat.2007.01.048.
(99) Hu, W.; Li, L.; Li, G.; Tang, C.; Sun, L. High-Quality Brookite TiO_2 Flowers: Synthesis, Characterization, and Dielectric Performance. *Cryst. Growth Des.* **2009**, *9*, 3676-3682, DOI: 10.1021/cg9004032.
(100) Kavan, L.; Grätzel, M.; Gilbert, S. E.; Klemenz, C.; Scheel, H. J. Electrochemical and Photoelectrochemical Investigation of Single-Crystal Anatase. *J. Am. Chem. Soc.* **1996**, *118*, 6716-6723, DOI: 10.1021/ja954172l.
(101) Ekuma, C. E.; Bagayoko, D. Ab-initio Electronic and Structural Properties of Rutile Titanium Dioxide. *Jpn. J. Appl. Phys.* **2011**, *50*, 101103, DOI: 10.1143/JJAP.50.101103.
(102) Tang, H.; Berger, H.; Schmid, P. E.; Lévy, F.; Burri, G. Photoluminescence in TiO_2 anatase single crystals. *Solid State Commun.* **1993**, *87*, 847-850, DOI: 10.1016/0038-1098(93)90427-O.
(103) Zhang, J.; Zhou, P.; Liu, J.; Yu, J. New understanding of the difference of photocatalytic activity among anatase, rutile and brookite TiO_2. *Phys. Chem. Chem. Phys.* **2014**, *16*, 20382-20386, DOI: 10.1039/C4CP02201G
(104) Žerjav, G.; Žižek, K.; Zavašnik, J.; Pintar, A. Brookite vs. rutile vs. anatase: What`s behind their various photocatalytic activities? *J. Environ. Chem. Eng.* **2022**, *10*, 107722, DOI: 10.1016/j.jece.2022.107722.
(105) Li, W.; Bai, Y.; Liu, C.; Yang, Z.; Feng, X.; Lu, X.; van der Laak, N. K.; Chan, K.-Y. Highly Thermal Stable and Highly Crystalline Anatase TiO_2 for Photocatalysis. *Environ. Sci. Technol.* **2009**, *43*, 5423-5428, DOI: 10.1021/es8037005.
(106) Paz, Y.; Luo, Z.; Rabenberg, L.; Heller, A. Photooxidative self-cleaning transparent titanium dioxide films on glass. *J. Mater. Res.* **1995**, *10*, 2842-2848, DOI: 10.1557/JMR.1995.2842.
(107) Wang, R.; Hashimoto, K.; Fujishima, A.; Chikuni, M.; Kojima, E.; Kitamura, A.; Shimohigoshi, M.; Watanabe, T. Light-induced amphiphilic surfaces. *Nature* **1997**, *388*, 431-432, DOI: 10.1038/41233.
(108) O'Regan, B.; Grätzel, M. A low-cost, high-efficiency solar cell based on dye-sensitized colloidal TiO_2 films. *Nature* **1991**, *353*, 737-740, DOI: 10.1038/353737a0.
(109) Rams, J.; Tejeda, A.; Cabrera, J. M. Refractive indices of rutile as a function of temperature and wavelength. *J. Appl. Phys.* **1997**, *82*, 994-997, DOI: 10.1063/1.365938.
(110) Braun, J. H.; Baidins, A.; Marganski, R. E. TiO_2 pigment technology: a review. *Prog. Org. Coat.* **1992**, *20*, 105-138, DOI: 10.1016/0033-0655(92)80001-D.

(111) Morsy, F. A.; El-Sherbiny, S.; Samir, M.; Fouad, O. A. Application of nanostructured titanium dioxide pigments in paper coating: a comparison between prepared and commercially available ones. *J. Coat. Technol. Res.* **2016**, *13*, 307-316, DOI: 10.1007/s11998-015-9735-7.
(112) Allen, N. S.; McIntyre, R.; Kerrod, J. M.; Hill, C.; Edge, M. Photo-Stabilisation and UV Blocking Efficacy of Coated Macro and Nano-Rutile Titanium Dioxide Particles in Paints and Coatings. *J. Polym. Environ.* **2018**, *26*, 4243-4257, DOI: 10.1007/s10924-018-1298-0.
(113) Phillips, L. G.; Barbano, D. M. The Influence of Fat Substitutes Based on Protein and Titanium Dioxide on the Sensory Properties of Lowfat Milks1. *J. Dairy Sci.* **1997**, *80*, 2726-2731, DOI: 10.3168/jds.S0022-0302(97)76234-9.
(114) Weir, A.; Westerhoff, P.; Fabricius, L.; Hristovski, K.; von Goetz, N. Titanium Dioxide Nanoparticles in Food and Personal Care Products. *Environ. Sci. Technol.* **2012**, *46*, 2242-2250, DOI: 10.1021/es204168d.
(115) Lu, P.-J.; Huang, S.-C.; Chen, Y.-P.; Chiueh, L.-C.; Shih, D. Y.-C. Analysis of titanium dioxide and zinc oxide nanoparticles in cosmetics. *J. Food Drug Anal.* **2015**, *23*, 587-594, DOI: 10.1016/j.jfda.2015.02.009.
(116) Shakeel, M.; Jabeen, F.; Shabbir, S.; Asghar, M. S.; Khan, M. S.; Chaudhry, A. S. Toxicity of Nano-Titanium Dioxide (TiO_2-NP) Through Various Routes of Exposure: a Review. *Biol. Trace Elem. Res.* **2016**, *172*, 1-36, DOI: 10.1007/s12011-015-0550-x.
(117) Ayorinde, T.; Sayes, C. M. An updated review of industrially relevant titanium dioxide and its environmental health effects. *J. Hazard. Mater. Lett.* **2023**, *4*, 100085, DOI: 10.1016/j.hazl.2023.100085.
(118) Pfanzelt, M.; Kubiak, P.; Fleischhammer, M.; Wohlfahrt-Mehrens, M. TiO_2 rutile—An alternative anode material for safe lithium-ion batteries. *J. Power Sources* **2011**, *196*, 6815-6821, DOI: 10.1016/j.jpowsour.2010.09.109.
(119) Wang, X.; Liang, S.; Cheng, Y.-J.; Xia, Y.; Müller-Buschbaum, P. Rutile TiO_2's odyssey into the post-lithium ion battery horizon. *Renew. Sust. Energy Rev.* **2025**, *209*, 115101, DOI: 10.1016/j.rser.2024.115101.
(120) Borghols, W. J. H.; Wagemaker, M.; Lafont, U.; Kelder, E. M.; Mulder, F. M. Impact of Nanosizing on Lithiated Rutile TiO_2. *Chem. Mater.* **2008**, *20*, 2949-2955, DOI: 10.1021/cm703376e.
(121) Vijayakumar, M.; Kerisit, S.; Wang, C.; Nie, Z.; Rosso, K. M.; Yang, Z.; Graff, G.; Liu, J.; Hu, J. Effect of Chemical Lithium Insertion into Rutile TiO_2 Nanorods. *J. Phys. Chem. C* **2009**, *113*, 14567-14574, DOI: 10.1021/jp904148z.
(122) Nico, C.; Monteiro, T.; Graça, M. P. F. Niobium oxides and niobates physical properties: Review and prospects. *Prog. Mater Sci.* **2016**, *80*, 1-37, DOI: 10.1016/j.pmatsci.2016.02.001.
(123) Brauer, G. Die Oxyde des Niobs. *Z. Anorg. Allg. Chem.* **1941**, *248*, 1-31, DOI: 10.1002/zaac.19412480101.
(124) Schäfer, H.; Gruehn, R.; Schulte, F. The Modifications of Niobium Pentoxide. *Angew. Chem. Int. Ed.* **1966**, *5*, 40-52, DOI: 10.1002/anie.196600401.
(125) Zibrov, I. P.; Filonenko, V. P.; Werner, P.-E.; Marinder, B.-O.; Sundberg, M. A New High-Pressure Modification of Nb_2O_5. *J. Solid State Chem.* **1998**, *141*, 205-211, DOI: 10.1006/jssc.1998.7954.
(126) Valencia-Balvín, C.; Pérez-Walton, S.; Dalpian, G. M.; Osorio-Guillén, J. M. First-principles equation of state and phase stability of niobium pentoxide. *Comput. Mater. Sci.* **2014**, *81*, 133-140, DOI: 10.1016/j.commatsci.2013.07.032.
(127) Cava, R. J.; Murphy, D. W.; Zahurak, S. M. Lithium Insertion in Wadsley-Roth Phases Based on Niobium Oxide. *J. Electrochem. Soc.* **1983**, *130*, 2345-2351, DOI: 10.1149/1.2119583.
(128) Chen, H.; Zhang, H.; Wu, Y.; Zhang, T.; Guo, Y.; Zhang, Q.; Zeng, Y.; Lu, J. Nanostructured Nb_2O_5 cathode for high-performance lithium-ion battery with Super-P and

graphene compound conductive agents. *J. Electroanal. Chem.* **2018**, *827*, 112-119, DOI: 10.1016/j.jelechem.2018.08.037.
(129) Raba, A. M.; Bautista-Ruíz, J.; Joya, M. R. Synthesis and Structural Properties of Niobium Pentoxide Powders: A Comparative Study of the Growth Process. *Mater. Res.* **2016**, *19*, 1381-1387, DOI: 10.1590/1980-5373-mr-2015-0733.
(130) Avellaneda, C. O.; Pawlicka, A.; Aegerter, M. A. Two methods of obtaining sol–gel Nb_2O_5 thin films for electrochromic devices. *J. Mater. Sci.* **1998**, *33*, 2181-2185, DOI: 10.1023/A:1004339723987.
(131) Ristić, M.; Popović, S.; Musić, S. Sol–gel synthesis and characterization of Nb_2O_5 powders. *Mater. Lett.* **2004**, *58*, 2658-2663, DOI: 10.1016/j.matlet.2004.03.041.
(132) Rosario, A. V.; Pereira, E. C. The effect of composition variables on precursor degradation and their consequence on Nb_2O_5 film properties prepared by the Pecchini Method. *J. Sol-Gel Sci. Technol.* **2006**, *38*, 233-240, DOI: 10.1007/s10971-006-7997-3.
(133) Tsuzuki, T.; McCormick, P. G. Mechanochemical Synthesis of Niobium Pentoxide Nanoparticles. *Mater. Trans.* **2001**, *42*, 1623-1628, DOI: 10.2320/matertrans.42.1623.
(134) Terao, N. Structures des Oxydes de Niobium. *Jpn. J. Appl. Phys.* **1963**, *2*, 156-174, DOI: 10.1143/jjap.2.156.
(135) Valeeva, A. A.; Schroettner, H.; Rempel, A. A. NbO disintegration by surfactant-assisted high-energy ball milling. *Inorg. Mater.* **2014**, *50*, 398-403, DOI: 10.1134/S0020168514040177.
(136) Brauer, G. *Handbuch der Präparativen Anorganischen Chemie Dritter Band*; Ferdinand Enke Verlag, Stuttgart, 1981.
(137) Grube, G.; Kubaschewski, O.; Zwiauer, K. Die Reduktion des Niobpentoxyds mit Wasserstoff. *Ztschr. Elektrochem.* **1939**, *45*, 885-888, DOI: 10.1002/bbpc.19390451207.
(138) Waldron, J. E. L.; Green, M. A.; Neumann, D. A. Structure and electronic properties of monoclinic $Nb_{12}O_{29}$. *J. Phys. Chem. Solids* **2004**, *65*, 79-86, DOI: 10.1016/j.jpcs.2003.09.001.
(139) Cava, R. J.; Batlogg, B.; Krajewski, J. J.; Gammel, P.; Poulsen, H. F.; Peck Jr, W. F.; Rupp Jr, L. W. Antiferromagnetism and metallic conductivity in $Nb_{12}O_{29}$. *Nature* **1991**, *350*, 598-600, DOI: 10.1038/350598a0.
(140) Hibst, H.; Gruehn, R. Neue Beobachtungen zur mechanischen und thermischen Umwandlung von Nioboxiden. *Z. Anorg. Allg. Chem.* **1978**, *440*, 137-154, DOI: 10.1002/zaac.19784400114.
(141) Ikeya, T.; Senna, M. Amorphization and phase transformation of niobium pentoxide by fine grinding. *J. Mater. Sci.* **1987**, *22*, 2497-2502, DOI: 10.1007/BF01082136.
(142) Ikeya, T.; Senna, M. Change in the structure of niobium pentoxide due to mechanical and thermal treatments. *J. Non-Cryst. Solids* **1988**, *105*, 243-250, DOI: 10.1016/0022-3093(88)90313-4.
(143) Gaffet, E.; Michel, D.; Mazerolles, L.; Berthet, P. Effects of high energy ball milling on ceramic oxides. *Mater. Sci. Forum* **1997**, *235-238*, 103-108, DOI: 10.4028/www.scientific.net/MSF.235-238.103.
(144) Tsuiki, H.; Shimanouchi, T.; Takahashi, N.; Kakuta, N.; Ueno, A. Preparation of Niobium Oxide Films as Humidity Sensor. *Chem. Lett.* **1990**, *19*, 1729-1732, DOI: 10.1246/cl.1990.1729.
(145) Chambon, L.; Maleysson, C.; Pauly, A.; Germain, J. P.; Demarne, V.; Grisel, A. Investigation, for NH_3 gas sensing applications, of the Nb_2O_5 semiconducting oxide in the presence of interferent species such as oxygen and humidity. *Sens. Actuator B Chem.* **1997**, *45*, 107-114, DOI: 10.1016/S0925-4005(97)00281-5.
(146) Chambon, L.; Pauly, A.; Germain, J. P.; Maleysson, C.; Demarne, V.; Grisel, A. A model for the responses of Nb_2O_5 sensors to CO and NH_3 gases. *Sens. Actuator B Chem.* **1997**, *43*, 60-64, DOI: 10.1016/S0925-4005(97)00136-6.

(147) Royon, A.; Canioni, L.; Bousquet, B.; Rodriguez, V.; Couzi, M.; Rivero, C.; Cardinal, T.; Fargin, E.; Richardson, M.; Richardson, K. Strong nuclear contribution to the optical Kerr effect in niobium oxide containing glasses. *Phys. Rev. B: Condens. Matter Mater. Phys.* **2007**, *75*, 104207, DOI: 10.1103/PhysRevB.75.104207.
(148) Liu, J.; Xue, D.; Li, K. Single-crystalline nanoporous Nb_2O_5 nanotubes. *Nanoscale Res. Lett.* **2011**, *6*, 138, DOI: 10.1186/1556-276X-6-138.
(149) Soares, M. R. N.; Leite, S.; Nico, C.; Peres, M.; Fernandes, A. J. S.; Graça, M. P. F.; Matos, M.; Monteiro, R.; Monteiro, T.; Costa, F. M. Effect of processing method on physical properties of Nb_2O_5. *J. Eur. Ceram. Soc.* **2011**, *31*, 501-506, DOI: 10.1016/j.jeurceramsoc.2010.10.024.
(150) Le Viet, A.; Reddy, M. V.; Jose, R.; Chowdari, B. V. R.; Ramakrishna, S. Nanostructured Nb_2O_5 Polymorphs by Electrospinning for Rechargeable Lithium Batteries. *J. Phys. Chem. C* **2010**, *114*, 664-671, DOI: 10.1021/jp9088589.
(151) Cao, D.; Yao, Z.; Liu, J.; Zhang, J.; Li, C. H-Nb_2O_5 wired by tetragonal tungsten bronze related domains as high-rate anode for Li-ion batteries. *Energy Storage Mater.* **2018**, *11*, 152-160, DOI: 10.1016/j.ensm.2017.10.005.
(152) Ding, H.; Song, Z.; Feng, K.; Zhang, H.; Zhang, H.; Li, X. Controlled synthesis of pure-phase metastable tetragonal Nb_2O_5 anode material for high-performance lithium batteries. *J. Solid State Chem.* **2021**, *299*, 122136, DOI: 10.1016/j.jssc.2021.122136.
(153) Kong, L.; Liu, X.; Wei, J.; Wang, S.; Xu, B. B.; Long, D.; Chen, F. T-Nb_2O_5 nanoparticle enabled pseudocapacitance with fast Li-ion intercalation. *Nanoscale* **2018**, *10*, 14165-14170, DOI: 10.1039/C8NR03495H.
(154) Catti, M.; Ghaani, M. R. On the lithiation reaction of niobium oxide: Structural and electronic properties of $Li_{1.714}Nb_2O_5$. *Phys. Chem. Chem. Phys.* **2014**, *16*, 1385-1392, DOI: 10.1039/C3CP54215G.
(155) Störmer, H.; Weber, A.; Fischer, V.; Ivers-Tiffée, E.; Gerthsen, D. Anodically formed oxide films on niobium: Microstructural and electrical properties. *J. Eur. Ceram. Soc.* **2009**, *29*, 1743-1753, DOI: 10.1016/j.jeurceramsoc.2008.10.019.
(156) Grishin, A. M.; Velichko, A. A.; Jalalian, A. Nb_2O_5 nanofiber memristor. *Appl. Phys. Lett.* **2013**, *103*, 053111, DOI: 10.1063/1.4817302.
(157) Grossman, E. N.; Harvey, T. E.; Reintsema, C. D. Controlled barrier modification in Nb/NbO_x/Ag metal insulator metal tunnel diodes. *J. Appl. Phys.* **2002**, *91*, 10134-10139, DOI: 10.1063/1.1471385.
(158) Kukli, K.; Ritala, M.; Leskelä, M. Development of Dielectric Properties of Niobium Oxide, Tantalum Oxide, and Aluminum Oxide Based Nanolayered Materials. *J. Electrochem. Soc.* **2001**, *148*, F35-F41, DOI: 10.1149/1.1343106.
(159) Kang, Y.-B. Critical evaluation and thermodynamic optimization of the VO–$VO_{2.5}$ system. *J. Eur. Ceram. Soc.* **2012**, *32*, 3187-3198, DOI: 10.1016/j.jeurceramsoc.2012.04.045.
(160) Wriedt, H. A. The O-V (Oxygen-Vanadium) system. *Bull. Alloy Phase Diagr.* **1989**, *10*, 271-277, DOI: 10.1007/BF02877512.
(161) Hu, P.; Hu, P.; Vu, T. D.; Li, M.; Wang, S.; Ke, Y.; Zeng, X.; Mai, L.; Long, Y. Vanadium Oxide: Phase Diagrams, Structures, Synthesis, and Applications. *Chem. Rev.* **2023**, *123*, 4353-4415, DOI: 10.1021/acs.chemrev.2c00546.
(162) Balog, P.; Orosel, D.; Cancarevic, Z.; Schön, C.; Jansen, M. V_2O_5 phase diagram revisited at high pressures and high temperatures. *J. Alloys Compd.* **2007**, *429*, 87-98, DOI: 10.1016/j.jallcom.2006.04.042.
(163) Cocciantelli, J. M.; Gravereau, P.; Doumerc, J. P.; Pouchard, M.; Hagenmuller, P. On the preparation and characterization of a new polymorph of V_2O_5. *J. Solid State Chem.* **1991**, *93*, 497-502, DOI: 10.1016/0022-4596(91)90323-A.

(164) Shklover, V.; Haibach, T.; Ried, F.; Nesper, R.; Novák, P. Crystal Structure of the Product of Mg^{2+} Insertion into V_2O_5 Single Crystals. *J. Solid State Chem.* **1996**, *123*, 317-323, DOI: 10.1006/jssc.1996.0186.
(165) Ren, X.; Jiang, Y.; Zhang, P.; Liu, J.; Zhang, Q. Preparation and electrochemical properties of V_2O_5 submicron-belts synthesized by a sol–gel H_2O_2 route. *J. Sol-Gel Sci. Technol.* **2009**, *51*, 133-138, DOI: 10.1007/s10971-009-2002-6.
(166) Gotić, M.; Popović, S.; Ivanda, M.; Musić, S. Sol–gel synthesis and characterization of V_2O_5 powders. *Mater. Lett.* **2003**, *57*, 3186-3192, DOI: 10.1016/S0167-577X(03)00022-3.
(167) Mu, J.; Wang, J.; Hao, J.; Cao, P.; Zhao, S.; Zeng, W.; Miao, B.; Xu, S. Hydrothermal synthesis and electrochemical properties of V_2O_5 nanomaterials with different dimensions. *Ceram. Int.* **2015**, *41*, 12626-12632, DOI: 10.1016/j.ceramint.2015.06.091.
(168) Pan, A.; Wu, H. B.; Yu, L.; Zhu, T.; Lou, X. W. Synthesis of Hierarchical Three-Dimensional Vanadium Oxide Microstructures as High-Capacity Cathode Materials for Lithium-Ion Batteries. *ACS Appl. Mater. Interfaces* **2012**, *4*, 3874-3879, DOI: 10.1021/am3012593.
(169) Chen, R.-S.; Wang, W.-C.; Chan, C.-H.; Hsu, H.-P.; Tien, L.-C.; Chen, Y.-J. Photoconductivities in monocrystalline layered V_2O_5 nanowires grown by physical vapor deposition. *Nanoscale Res. Lett.* **2013**, *8*, 443, DOI: 10.1186/1556-276X-8-443.
(170) Sharma, R. K.; Kumar, P.; Reddy, G. B. Synthesis of vanadium pentoxide (V_2O_5) nanobelts with high coverage using plasma assisted PVD approach. *J. Alloys Compd.* **2015**, *638*, 289-297, DOI: 10.1016/j.jallcom.2015.02.178.
(171) George, A.; Raj, A. D.; Yang, Q. Structural characteristics and gas sensing response of V_2O_5 nanorod thinfilms deposited by hot filament CVD. *Sens. Actuator B Chem.* **2023**, *378*, 133078, DOI: 10.1016/j.snb.2022.133078.
(172) Zhang, X.; Wu, M.; Gao, S.; Xu, Y.; Cheng, X.; Zhao, H.; Huo, L. Facile synthesis of uniform flower-like V_2O_5 hierarchical architecture for high-performance Li-ion battery. *Mater. Res. Bull.* **2014**, *60*, 659-664, DOI: 10.1016/j.materresbull.2014.09.046.
(173) Wang, Y.; Li, Z.; Sheng, X.; Zhang, Z. Synthesis and optical properties of V_2O_5 nanorods. *J. Chem. Phys.* **2007**, *126*, 164701, DOI: 10.1063/1.2722746.
(174) Liu, X.; Huang, C.; Yi, S.; Xie, G.; Li, H.; Luo, Y. A new solvothermal method of preparing VO_2 nanosheets and petaloid clusters. *Solid State Commun.* **2007**, *144*, 259-263, DOI: 10.1016/j.ssc.2007.08.013.
(175) El-Shobaky, G. A.; El-Barawy, K. A.; Abdalla, F. H. A. Thermal decomposition of ammonium metavanadate supported on Al_2O_3. *Thermochim. Acta* **1985**, *96*, 129-137, DOI: 10.1016/0040-6031(85)80015-0.
(176) Glushenkov, A. M.; Stukachev, V. I.; Hassan, M. F.; Kuvshinov, G. G.; Liu, H. K.; Chen, Y. A Novel Approach for Real Mass Transformation from V_2O_5 Particles to Nanorods. *Cryst. Growth Des.* **2008**, *8*, 3661-3665, DOI: 10.1021/cg800257d.
(177) Guimarães, J. L.; Abbate, M.; Betim, S. B.; Alves, M. C. M. Preparation and characterization of TiO_2 and V_2O_5 nanoparticles produced by ball-milling. *J. Alloys Compd.* **2003**, *352*, 16-20, DOI: 10.1016/S0925-8388(02)01112-X.
(178) Chatterjee, P.; Sen Gupta, S. P.; Sen, S. Particle fracture and plastic deformation in vanadium pentoxide powders induced by high energy vibrational ball-mill. *Bull. Mater. Sci.* **2001**, *24*, 173-180, DOI: 10.1007/BF02710097.
(179) Chatterjee, P.; Sen Gupta, S. P.; Sen, S. Microstructural transformation of vanadium pentoxide powder obtained by high-energy vibrational ball-milling. *J. Appl. Crystallogr.* **2001**, *34*, 381-385, DOI: 10.1107/S0021889801004009.
(180) Dutta, H.; Pradhan, S. K. Microstructure characterization of high energy ball-milled nanocrystalline V_2O_5 by Rietveld analysis. *Mater. Chem. Phys.* **2003**, *77*, 868-877, DOI: 10.1016/S0254-0584(02)00169-4.

(181) Shubin, A. A.; Lapina, O. B.; Bosch, E.; Spengler, J.; Knözinger, H. Effect of Milling of V_2O_5 on the Local Environment of Vanadium as Studied by Solid-State ^{51}V NMR and Complementary Methods. *J. Phys. Chem. B* **1999**, *103*, 3138-3144, DOI: 10.1021/jp984513s.
(182) Su, D. S.; Roddatis, V.; Willinger, M.; Weinberg, G.; Kitzelmann, E.; Schlögl, R.; Knözinger, H. Tribochemical Modification of the Microstructure of V_2O_5. *Catal. Lett.* **2001**, *74*, 169-175, DOI: 10.1023/A:1016689231883.
(183) Zazhigalov, V. A.; Kharlamov, A. I.; Bacherikova, I. V.; Komashko, G. A.; Khalameida, S. V.; Bogutskaya, L. V.; Byl', O. G.; Stoch, J.; Koval, A. Changes in structure and catalytic properties of V_2O_5 caused by mechanochemical treatment. *Theor. Exp. Chem.* **1998**, *34*, 162-164, DOI: 10.1007/BF02764462.
(184) Petranikova, M.; Tkaczyk, A. H.; Bartl, A.; Amato, A.; Lapkovskis, V.; Tunsu, C. Vanadium sustainability in the context of innovative recycling and sourcing development. *Waste Manag.* **2020**, *113*, 521-544, DOI: 10.1016/j.wasman.2020.04.007.
(185) Takai, C.; Senna, M.; Hoshino, S.; Razavi-Khosroshahi, H.; Fuji, M. Chemical and thermal properties of VO_2 mechanochemically derived from V_2O_5 by co-milling with paraffin wax. *RSC Adv.* **2018**, *8*, 21306-21315, DOI: 10.1039/C8RA02159G.
(186) Zhang, D. L.; Zhang, Y. J. Chemical Reactions Between Vanadium Oxides and Carbon During High Energy Ball Milling. *J. Mater. Sci. Lett.* **1998**, *17*, 1113-1115, DOI: 10.1023/A:1006688117629.
(187) Yang, H.; McCormick, P. G. Mechanochemical Reduction of V_2O_5. *J. Solid State Chem.* **1994**, *110*, 136-141, DOI: 10.1006/jssc.1994.1147.
(188) Weber, R.; Sakurai, T.; Hagenmaier, H. Low temperature decomposition of PCDD/PCDF, chlorobenzenes and PAHs by TiO_2-based V_2O_5–WO_3 catalysts. *Appl. Catal. B* **1999**, *20*, 249-256, DOI: 10.1016/S0926-3373(98)00115-5.
(189) Ponzi, M.; Duschatzky, C.; Carrascull, A.; Ponzi, E. Obtaining benzaldehyde via promoted V_2O_5 catalysts. *Appl. Catal. A: Gen.* **1998**, *169*, 373-379, DOI: 10.1016/S0926-860X(98)00026-X.
(190) Simard, G. L.; Steger, J. F.; Arnott, R. J.; Siegel, L. A. Vanadium Oxides as Oxidation Catalysts. *Ind. Eng. Chem.* **1955**, *47*, 1424-1430, DOI: 10.1021/ie50547a047.
(191) Klencke, H.; Göhre, K. R.; Siecke, W. Verfahren und Vorrichtung zur Herstellung von Schwefelsaeure nach dem Kontaktverfahren. DE682915, 1939.
(192) Zhang, K.; Gao, G.; Sun, W.; Liang, X.; Liu, Y.; Wu, G. Large interlayer spacing vanadium oxide nanotubes as cathodes for high performance sodium ion batteries. *RSC Adv.* **2018**, *8*, 22053-22061, DOI: 10.1039/C8RA03514H
(193) Boruah, B. D.; Wen, B.; De Volder, M. Light Rechargeable Lithium-Ion Batteries Using V_2O_5 Cathodes. *Nano Lett.* **2021**, *21*, 3527-3532, DOI: 10.1021/acs.nanolett.1c00298.
(194) Ali, G.; Lee, J. H.; Oh, S. H.; Cho, B. W.; Nam, K.-W.; Chung, K. Y. Investigation of the Na Intercalation Mechanism into Nanosized V_2O_5/C Composite Cathode Material for Na-Ion Batteries. *ACS Appl. Mater. Interfaces* **2016**, *8*, 6032-6039, DOI: 10.1021/acsami.5b11954.
(195) Wang, G.; Cui, X.; Yang, Z.; Liu, J.; Shi, X.; Zhang, Y.; Zhao, Z.; Wang, J.; Song, J.; Wang, X.; et al. Quasi-Solid-State All-V_2O_5 Battery. *Small* **2024**, *20*, 2304786, DOI: 10.1002/smll.202304786.
(196) Zhang, Y.; Lai, J.; Gong, Y.; Hu, Y.; Liu, J.; Sun, C.; Wang, Z. L. A Safe High-Performance All-Solid-State Lithium–Vanadium Battery with a Freestanding V_2O_5 Nanowire Composite Paper Cathode. *ACS Appl. Mater. Interfaces* **2016**, *8*, 34309-34316, DOI: 10.1021/acsami.6b10358.
(197) Cunha, Á.; Martins, J.; Rodrigues, N.; Brito, F. P. Vanadium redox flow batteries: a technology review. *Int. J. Energy Res.* **2015**, *39*, 889-918, DOI: 10.1002/er.3260.
(198) Colton, R. J.; Guzman, A. M.; Rabalais, J. W. Electrochromism in some thin-film transition-metal oxides characterized by x-ray electron spectroscopy. *J. Appl. Phys.* **1978**, *49*, 409-416, DOI: 10.1063/1.324349.

(199) Colton, R. J.; Guzman, A. M.; Rabalais, J. W. Photochromism and electrochromism in amorphous transition metal oxide films. *Acc. Chem. Res.* **1978**, *11*, 170-176, DOI: 10.1021/ar50124a008.
(200) Prasad, A. K.; Park, J.-Y.; Kang, S.-H.; Ahn, K.-S. Electrochemically co-deposited WO_3-V_2O_5 composites for electrochromic energy storage applications. *Electrochim. Acta* **2022**, *422*, 140340, DOI: 10.1016/j.electacta.2022.140340.
(201) Cheng, K.-C.; Chen, F.-R.; Kai, J.-J. V_2O_5 nanowires as a functional material for electrochromic device. *Sol. Energy Mater. Sol. Cells* **2006**, *90*, 1156-1165, DOI: 10.1016/j.solmat.2005.07.006.
(202) Zhang, L.; Jiang, C.; Wu, C.; Ju, H.; Jiang, G.; Liu, W.; Zhu, C.; Chen, T. V_2O_5 as Hole Transporting Material for Efficient All Inorganic Sb_2S_3 Solar Cells. *ACS Appl. Mater. Interfaces* **2018**, *10*, 27098-27105, DOI: 10.1021/acsami.8b09843.
(203) Mutta, G. R.; Popuri, S. R.; Maciejczyk, M.; Robertson, N.; Vasundhara, M.; Wilson, J. I. B.; Bennett, N. S. V_2O_5 as an inexpensive counter electrode for dye sensitized solar cells. *Mater. Res. Express* **2016**, *3*, 035501, DOI: 10.1088/2053-1591/3/3/035501.
(204) Alrammouz, R.; Lazerges, M.; Pironon, J.; Bin Taher, I.; Randi, A.; Halfaya, Y.; Gautier, S. V_2O_5 gas sensors: A review. *Sens. Actuators A: Phys.* **2021**, *332*, 113179, DOI: 10.1016/j.sna.2021.113179.
(205) Shannon, R. D. Revised effective ionic radii and systematic studies of interatomic distances in halides and chalcogenides. *Acta Crystallogr. A* **1976**, *32*, 751-767, DOI: 10.1107/S0567739476001551.
(206) Yang, G.; Feng, J.; Zhang, B.; Aravindan, V.; Peng, D.; Cao, X.; Yu, H.; Madhavi, S.; Huang, Y. Solvothermal synthesis of Li_3VO_4: Morphology control and electrochemical performance as anode for lithium-ion batteries. *Int. J. Hydrogen Energy* **2017**, *42*, 22167-22174, DOI: 10.1016/j.ijhydene.2017.02.186.
(207) Yang, K.; Fang, G.; Zhou, J.; Qin, M.; Tang, Y.; Pan, A.; Liang, S. Hydrothermal synthesis of sodium vanadate nanobelts as high-performance cathode materials for lithium batteries. *J. Power Sources* **2016**, *325*, 383-390, DOI: 10.1016/j.jpowsour.2016.06.023.
(208) Zhang, Z.; Kaneti, Y. V.; Jiang, X.; Yu, A. Hydrothermal synthesis of sodium vanadium oxide nanorods for gas sensing application. *Sens. Actuator B Chem.* **2014**, *202*, 803-809, DOI: 10.1016/j.snb.2014.05.064.
(209) Kolta, G. A.; Hewaidy, I. F.; Felix, N. S.; Girgis, N. N. Reactions between sodium carbonate and vanadium pentoxide. *Thermochim. Acta* **1973**, *6*, 165-177, DOI: 10.1016/0040-6031(73)85023-3.
(210) Chamberland, B. L.; Porter, S. K. A study on the preparation and physical property determination of $NaVO_2$. *J. Solid State Chem.* **1988**, *73*, 398-404, DOI: 10.1016/0022-4596(88)90124-7.
(211) Barker, M. G.; Hooper, A. J. Reactions of Sodium Oxide with the Oxides VO_2, V_2O_3, VO, and Vanadium Metal. *J. Chem. Soc., Dalton Trans.* **1973**, 1517-1519, DOI: 10.1039/DT9730001517.
(212) Barker, M. G.; Hooper, A. J. Reactions of Liquid Sodium with Transition-metal Oxides. Part VI. Oxides of Vanadium. *J. Chem. Soc., Dalton Trans.* **1973**, 1520-1522, DOI: 10.1039/DT9730001520.
(213) Rüdorff, W.; Becker, H. Über Umsetzungen des Vanadin(III)oxyds und des Vanadin(IV)oxyds mit einigen Metalloxyden. *Z. Naturforsch. B* **1954**, *9*, 613-614, DOI: 10.1515/znb-1954-0910.
(214) Rüdorff, W.; Becker, H. Notizen: Die Strukturen von $LiVO_2$, $NaVO_2$, $LiCrO_2$ und $NaCrO_2$. *Z. Naturforsch. B* **1954**, *9*, 614-615, DOI: 10.1515/znb-1954-0911.
(215) Pei, G.; Xiang, J.; Yang, L.; Jin, X.; Lv, X. Thermodynamic properties of sodium pyrovanadate ($Na_4V_2O_7$) at high temperature (298.15–873 K). *Calphad* **2020**, *70*, 101802, DOI: 10.1016/j.calphad.2020.101802.

(216) Barker, M. G.; Hooper, A. J. Preparation and X-Ray Powder Diffraction Patterns of the Sodium Vanadates $NaVO_3$, $Na_4V_2O_7$, and Na_3VO_4. *J. Chem. Soc., Dalton Trans.* **1973**, 1513-1517, DOI: 10.1039/DT9730001513.
(217) Kubaschewski, O.; Hoster, T.; Schlim, R. The Heats of Formation of Some Sodium and Barium Vanadates and Molybdates. *Ber. Bunsenges. Phys. Chem.* **1981**, *85*, 367-369, DOI: 10.1002/bbpc.19810850505.
(218) Hagenmuller, P.; Lesaicherre, A. La réduction de l'anhydride vanadique par l'hydrure de lithium. *Compt. Rend.* **1963**, *256*, 170-171.
(219) Rojac, T.; Trtnik, Ž.; Kosec, M. Mechanochemical reactions in Na_2CO_3-M_2O_5 (M = V, Nb, Ta) powder mixtures: Influence of transition-metal oxide on reaction rate. *Solid State Ion.* **2011**, *190*, 1-7, DOI: 10.1016/j.ssi.2011.03.011.
(220) Haberkorn, R.; Bauer, J.; Kickelbick, G. Chemical Sodiation of V_2O_5 by Na_2S. *Z. Anorg. Allg. Chem.* **2014**, *640*, 3197-3202, DOI: 10.1002/zaac.201400381.
(221) Zhang, J.; Su, B.; Kitajou, A.; Fujita, M.; Cui, Y.; Oda, M.; Zhou, W.; Sit, P. H.-L.; Yu, D. Y. W. Activating abnormal capacity in stoichiometric $NaVO_3$ as cathode material for sodium-ion battery. *J. Power Sources* **2018**, *400*, 377-382, DOI: 10.1016/j.jpowsour.2018.08.042.
(222) Zhang, M.; Zhang, X.; Liu, Z.; Peng, H.; Wang, G. Ball milling-derived nanostructured Li_3VO_4 anode with enhanced surface-confined capacitive contribution for lithium ion capacitors. *Ionics* **2020**, *26*, 4129-4140, DOI: 10.1007/s11581-020-03537-1.
(223) Kim, H.-S.; Cho, B.-W. Electrochemical Characteristics of Lithium Vanadium Oxide for Lithium Secondary Battery. *Bull. Korean Chem. Soc.* **2010**, *31*, 1267-1269, DOI: 10.5012/BKCS.2010.31.5.1267.
(224) Su, B.; Liang, H.; Liu, J.; Wu, J.; Sharma, N.; Gu, Q.; Johannessen, B.; Yu, D. Y. W. Novel structurally-stable Na-rich $Na_4V_2O_7$ cathode material with high reversible capacity by utilization of anion redox activity. *Chem. Commun.* **2020**, *56*, 8245-8248, DOI: 10.1039/D0CC02816A.
(225) Jian, X. M.; Tu, J. P.; Qiao, Y. Q.; Lu, Y.; Wang, X. L.; Gu, C. D. Synthesis and electrochemical performance of $LiVO_3$ cathode materials for lithium ion batteries. *J. Power Sources* **2013**, *236*, 33-38, DOI: 10.1016/j.jpowsour.2013.02.004.
(226) Su, B.; Wu, S.; Liang, H.; Zhou, W.; Liu, J.; Goonetilleke, D.; Sharma, N.; Sit, P. H.-L.; Zhang, W.; Yu, D. Y. W. High-Performance $NaVO_3$ with Mixed Cationic and Anionic Redox Reactions for Na-Ion Battery Applications. *Chem. Mater.* **2020**, *32*, 8836-8844, DOI: 10.1021/acs.chemmater.0c02244.
(227) Asakura, R.; Bolli, C.; Novák, P.; Robert, R. Insights into the Charge Storage Mechanism of Li_3VO_4 Anode Materials for Li-Ion Batteries. *ChemElectroChem* **2020**, *7*, 2033-2041, DOI: 10.1002/celc.202000161.
(228) Lu, J.; Zhang, D.; Wang, Y.; Ni, S. Na_3VO_4 as a new anode material for lithium-ion batteries. *New J. Chem.* **2021**, *45*, 11506-11511, DOI: 10.1039/D1NJ01797G.
(229) Niitaka, S.; Lee, S.; Oshima, Y.; Kato, K.; Hashizume, D.; Takata, M.; Takagi, H. Synchrotron X-ray powder diffraction and convergent beam electron diffraction studies on the cubic phase of MgV_2O_4 spinel. *J. Solid State Chem.* **2014**, *215*, 184-188, DOI: 10.1016/j.jssc.2014.03.037.
(230) Hu, L.; Jokisaari, J. R.; Kwon, B. J.; Yin, L.; Kim, S.; Park, H.; Lapidus, S. H.; Klie, R. F.; Key, B.; Zapol, P.; et al. High Capacity for Mg^{2+} Deintercalation in Spinel Vanadium Oxide Nanocrystals. *ACS Energy Lett.* **2020**, *5*, 2721-2727, DOI: 10.1021/acsenergylett.0c01189.
(231) Ding, Q.; Han, T.; Zhou, T.; Lin, X.; Liu, J. A Temperature-Tolerant Magnesium-Ion Battery Using Ball Cactus-like MgV_2O_4 as High-Performance Cathode. *Chem. Eur. J.* **2024**, *30*, e202302978, DOI: 10.1002/chem.202302978.

(232) Tang, W.; Lan, B.; Tang, C.; An, Q.; Chen, L.; Zhang, W.; Zuo, C.; Dong, S.; Luo, P. Urchin-like Spinel MgV_2O_4 as a Cathode Material for Aqueous Zinc-Ion Batteries. *ACS Sustain. Chem. Eng.* **2020**, *8*, 3681-3688, DOI: 10.1021/acssuschemeng.9b06613.
(233) Rüdorff, W.; Reuter, B. Über Verbindungen des Vanadin(III)oxyds und des Vanadin(IV)oxyds mit einigen zweiwertigen basischen Oxyden. *Z. anorg. Chemie* **1947**, *253*, 177-193, DOI: 10.1002/zaac.19472530310.
(234) Mamiya, H.; Onoda, M. Electronic states of vanadium spinels MgV_2O_4 and ZnV_2O_4. *Solid State Commun.* **1995**, *95*, 217-221, DOI: 10.1016/0038-1098(95)00253-7.
(235) Riedel, E.; Alisch, C. Verteilung und Valenz der Kationen in Spinellsystemen mit Eisen und Vanadium, V Röntgenographische und Mößbauer-spektroskopische Untersuchung des Spinellsystems FeV_2O_4—MgV_2O_4 *Z. Naturforsch. B* **1987**, *42*, 1549-1552, DOI: 10.1515/znb-1987-1210.
(236) Lee, J.; Dey, S.; Dutton, S. E.; Grey, C. P. Synthesis and Characterization of Magnesium Vanadates as Potential Magnesium-Ion Cathode Materials through an Ab Initio Guided Carbothermal Reduction Approach. *Angew. Chem. Int. Ed.* **2022**, *61*, e202112688, DOI: 10.1002/anie.202112688.
(237) Lee, J.; Seymour, I. D.; Pell, A. J.; Dutton, S. E.; Grey, C. P. A systematic study of ^{25}Mg NMR in paramagnetic transition metal oxides: applications to Mg-ion battery materials. *Phys. Chem. Chem. Phys.* **2017**, *19*, 613-625, DOI: 10.1039/C6CP06338A.
(238) Chen, X.; Liu, L.; Huang, F. Black titanium dioxide (TiO_2) nanomaterials. *Chem. Soc. Rev.* **2015**, *44*, 1861-1885, DOI: 10.1039/C4CS00330F.
(239) Chen, X.; Liu, L.; Yu, P. Y.; Mao, S. S. Increasing Solar Absorption for Photocatalysis with Black Hydrogenated Titanium Dioxide Nanocrystals. *Science* **2011**, *331*, 746-750, DOI: 10.1126/science.1200448.
(240) Myung, S.-T.; Kikuchi, M.; Yoon, C. S.; Yashiro, H.; Kim, S.-J.; Sun, Y.-K.; Scrosati, B. Black anatase titania enabling ultra high cycling rates for rechargeable lithium batteries. *Energy Environ. Sci.* **2013**, *6*, 2609-2614, DOI: 10.1039/C3EE41960F.
(241) Santara, B.; Giri, P. K.; Imakita, K.; Fujii, M. Evidence of oxygen vacancy induced room temperature ferromagnetism in solvothermally synthesized undoped TiO_2 nanoribbons. *Nanoscale* **2013**, *5*, 5476-5488, DOI: 10.1039/C3NR00799E.
(242) Sinhamahapatra, A.; Jeon, J.-P.; Yu, J.-S. A new approach to prepare highly active and stable black titania for visible light-assisted hydrogen production. *Energy Environ. Sci.* **2015**, *8*, 3539-3544, DOI: 10.1039/C5EE02443A
(243) Ye, M.; Jia, J.; Wu, Z.; Qian, C.; Chen, R.; O'Brien, P. G.; Sun, W.; Dong, Y.; Ozin, G. A. Synthesis of Black TiO_x Nanoparticles by Mg Reduction of TiO_2 Nanocrystals and their Application for Solar Water Evaporation. *Adv. Energy Mater.* **2017**, *7*, 1601811, DOI: 10.1002/aenm.201601811.
(244) Li, J.; Wu, E.-H.; Hou, J.; Huang, P.; Xu, Z.; Jiang, Y.; Liu, Q.-S.; Zhong, Y.-Q. A facile method for the preparation of black TiO_2 by Al reduction of TiO_2 and their visible light photocatalytic activity. *RSC Adv.* **2020**, *10*, 34775-34780, DOI: 10.1039/D0RA06784A.
(245) Song, H.; Li, C.; Lou, Z.; Ye, Z.; Zhu, L. Effective Formation of Oxygen Vacancies in Black TiO_2 Nanostructures with Efficient Solar-Driven Water Splitting. *ACS Sustain. Chem. Eng.* **2017**, *5*, 8982-8987, DOI: 10.1021/acssuschemeng.7b01774.
(246) Fang, W.; Xing, M.; Zhang, J. A new approach to prepare Ti^{3+} self-doped TiO_2 via $NaBH_4$ reduction and hydrochloric acid treatment. *Appl. Catal. B* **2014**, *160-161*, 240-246, DOI: 10.1016/j.apcatb.2014.05.031.
(247) Jiang, X.; Yan, Z.; Zhang, J.; Gao, J.; Huang, W.; Shi, Q.; Zhang, H. Mesoporous hollow black TiO_2 with controlled lattice disorder degrees for highly efficient visible-light-driven photocatalysis. *RSC Adv.* **2019**, *9*, 36907-36914, DOI: 10.1039/C9RA08148H.

(248) Kang, Q.; Cao, J.; Zhang, Y.; Liu, L.; Xu, H.; Ye, J. Reduced TiO_2 nanotube arrays for photoelectrochemical water splitting. *J. Mater. Chem. A* **2013**, *1*, 5766-5774, DOI: 10.1039/C3TA10689F.
(249) Plaça, L. F.; Vital, P.-L. S.; Gomes, L. E.; Roveda, A. C., Jr.; Cardoso, D. R.; Martins, C. A.; Wender, H. Black TiO_2 Photoanodes for Direct Methanol Photo Fuel Cells. *ACS Appl. Mater. Interfaces* **2023**, *15*, 43259-43271, DOI: 10.1021/acsami.2c04802.
(250) Tan, H.; Zhao, Z.; Niu, M.; Mao, C.; Cao, D.; Cheng, D.; Feng, P.; Sun, Z. A facile and versatile method for preparation of colored TiO_2 with enhanced solar-driven photocatalytic activity. *Nanoscale* **2014**, *6*, 10216-10223, DOI: 10.1039/c4nr02677b.
(251) Zhu, G.; Yin, H.; Yang, C.; Cui, H.; Wang, Z.; Xu, J.; Lin, T.; Huang, F. Black Titania for Superior Photocatalytic Hydrogen Production and Photoelectrochemical Water Splitting. *ChemCatChem* **2015**, *7*, 2614-2619, DOI: 10.1002/cctc.201500488.
(252) Liu, X.; Carvalho, P.; Getz, M. N.; Norby, T.; Chatzitakis, A. Black Anatase TiO_2 Nanotubes with Tunable Orientation for High Performance Supercapacitors. *J. Phys. Chem. C* **2019**, *123*, 21931-21940, DOI: 10.1021/acs.jpcc.9b05070.
(253) Wang, M.; Nie, B.; Yee, K.-K.; Bian, H.; Lee, C.; Lee, H. K.; Zheng, B.; Lu, J.; Luo, L.; Li, Y. Y. Low-temperature fabrication of brown TiO_2 with enhanced photocatalytic activities under visible light. *Chem. Commun.* **2016**, *52*, 2988-2991, DOI: 10.1039/C5CC09176D.
(254) Cui, H.; Zhu, G.; Xie, Y.; Zhao, W.; Yang, C.; Lin, T.; Gu, H.; Huang, F. Black nanostructured Nb_2O_5 with improved solar absorption and enhanced photoelectrochemical water splitting. *J. Mater. Chem. A* **2015**, *3*, 11830-11837, DOI: 10.1039/C5TA01544H.
(255) Zhao, W.; Zhao, W.; Zhu, G.; Lin, T.; Xu, F.; Huang, F. Black Nb_2O_5 nanorods with improved solar absorption and enhanced photocatalytic activity. *Dalton Trans.* **2016**, *45*, 3888-3894, DOI: 10.1039/c5dt04578a.
(256) Tong, Z.; Yang, R.; Wu, S.; Shen, D.; Jiao, T.; Zhang, K.; Zhang, W.; Lee, C.-S. Surface-Engineered Black Niobium Oxide@Graphene Nanosheets for High-Performance Sodium-/Potassium-Ion Full Batteries. *Small* **2019**, *15*, 1901272, DOI: 10.1002/smll.201901272.
(257) Yang, P.; Fan, Y.; Hu, K.; Jiang, L.; Tan, L.; Wang, Z.; Li, A.; Yang, S.; Hu, Y.; Gu, H. Fast, Sensitive, and Highly Selective Room-Temperature Hydrogen Sensing of Defect-Rich Orthorhombic Nb_2O_{5-x} Nanobelts with an Abnormal *p*-Type Sensor Response. *ACS Appl. Mater. Interfaces* **2022**, *14*, 25937-25948, DOI: 10.1021/acsami.2c05786.
(258) Cheng, S.; Wang, J.; Duan, S.; Zhang, J.; Wang, Q.; Zhang, Y.; Li, L.; Liu, H.; Xiao, Q.; Lin, H. Anionic oxygen vacancies in Nb_2O_{5-x}/carbon hybrid host endow rapid catalytic behaviors for high-performance high areal loading lithium sulfur pouch cell. *Chem. Eng. J.* **2021**, *417*, 128172, DOI: 10.1016/j.cej.2020.128172.
(259) Li, S.; Cui, Y.; Kang, R.; Zou, B.; Ng, D. H. L.; El-Khodary, S. A.; Liu, X.; Qiu, J.; Lian, J.; Li, H. Oxygen vacancies boosted the electrochemical kinetics of Nb_2O_{5-x} for superior lithium storage. *Chem. Commun.* **2021**, *57*, 8182-8185, DOI: 10.1039/D1CC02299G.
(260) Luo, D.; Zhang, Z.; Li, G.; Cheng, S.; Li, S.; Li, J.; Gao, R.; Li, M.; Sy, S.; Deng, Y.-P.; et al. Revealing the Rapid Electrocatalytic Behavior of Ultrafine Amorphous Defective Nb_2O_{5-x} Nanocluster toward Superior Li-S Performance. *ACS Nano* **2020**, *14*, 4849-4860, DOI: 10.1021/acsnano.0c00799.
(261) de Araújo, M. A.; Gromboni, M. F.; Marken, F.; Parker, S. C.; Peter, L. M.; Turner, J.; Aspinall, H. C.; Black, K.; Mascaro, L. H. Contrasting transient photocurrent characteristics for thin films of vacuum-doped "grey" TiO_2 and "grey" Nb_2O_5. *Appl. Catal. B* **2018**, *237*, 339-352, DOI: 10.1016/j.apcatb.2018.05.065.
(262) Zhou, X.; Liu, N.; Schmidt, J.; Kahnt, A.; Osvet, A.; Romeis, S.; Zolnhofer, E. M.; Marthala, V. R. R.; Guldi, D. M.; Peukert, W.; et al. Noble-Metal-Free Photocatalytic Hydrogen Evolution Activity: The Impact of Ball Milling Anatase Nanopowders with TiH_2. *Adv. Mater.* **2017**, *29*, 1604747, DOI: 10.1002/adma.201604747.

(263) Zhang, X.; Xiao, J.; Peng, C.; Xiang, Y.; Chen, H. Enhanced photocatalytic hydrogen production over conjugated polymer/black TiO_2 hybrid: The impact of constructing active defect states. *Appl. Surf. Sci.* **2019**, *465*, 288-296, DOI: 10.1016/j.apsusc.2018.09.105.
(264) Ou, G.; Xu, Y.; Wen, B.; Lin, R.; Ge, B.; Tang, Y.; Liang, Y.; Yang, C.; Huang, K.; Zu, D.; et al. Tuning defects in oxides at room temperature by lithium reduction. *Nat. Commun.* **2018**, *9*, 1302, DOI: 10.1038/s41467-018-03765-0.
(265) Zhang, M.; Pei, Q.; Chen, W.; Liu, L.; He, T.; Chen, P. Room temperature synthesis of reduced TiO_2 and its application as a support for catalytic hydrogenation. *RSC Adv.* **2017**, *7*, 4306-4311, DOI: 10.1039/c6ra26667c.
(266) Sarkar, A.; Khan, G. G. The formation and detection techniques of oxygen vacancies in titanium oxide-based nanostructures. *Nanoscale* **2019**, *11*, 3414-3444, DOI: 10.1039/C8NR09666J.
(267) Deluca, M.; Hu, H.; Popov, M. N.; Spitaler, J.; Dieing, T. Advantages and developments of Raman spectroscopy for electroceramics. *Commun. Mater.* **2023**, *4*, 78, DOI: 10.1038/s43246-023-00400-4.
(268) Rambadey, O. V.; Gupta, M.; Kumar, A.; Sagdeo, P. R. Analysis of structural disorder on Raman spectra of semiconductors. *J. Appl. Phys.* **2023**, *133*, 131101, DOI: 10.1063/5.0145442.
(269) Serrano-Sevillano, J.; Carlier, D.; Saracibar, A.; Lopez del Amo, J. M.; Casas-Cabanas, M. DFT-Assisted Solid-State NMR Characterization of Defects in Li_2MnO_3. *Inorg. Chem.* **2019**, *58*, 8347-8356, DOI: 10.1021/acs.inorgchem.9b00394.
(270) Su, Y.; Lang, J.; Li, L.; Guan, K.; Du, C.; Peng, L.; Han, D.; Wang, X. Unexpected catalytic performance in silent tantalum oxide through nitridation and defect chemistry. *J. Am. Chem. Soc.* **2013**, *135*, 11433-11436, DOI: 10.1021/ja404239z.
(271) Kim, H.-S.; Cook, J. B.; Lin, H.; Ko, J. S.; Tolbert, S. H.; Ozolins, V.; Dunn, B. Oxygen vacancies enhance pseudocapacitive charge storage properties of MoO_{3-x}. *Nat. Mater.* **2017**, *16*, 454-462, DOI: 10.1038/NMAT4810.
(272) Zhang, S.; Liu, G.; Qiao, W.; Wang, J.; Ling, L. Oxygen vacancies enhance the lithium ion intercalation pseudocapacitive properties of orthorhombic niobium pentoxide. *J. Colloid Interface Sci.* **2020**, *562*, 193-203, DOI: 10.1016/j.jcis.2019.12.015.
(273) Tan, H.; Zhao, Z.; Zhu, W. B.; Coker, E. N.; Li, B.; Zheng, M.; Yu, W.; Fan, H.; Sun, Z. Oxygen vacancy enhanced photocatalytic activity of pervoskite $SrTiO_3$. *ACS Appl. Mater. Interfaces* **2014**, *6*, 19184-19190, DOI: 10.1021/am5051907.
(274) Landi Jr., S.; Segundo, I. R.; Freitas, E.; Vasilevskiy, M.; Carneiro, J.; Tavares, C. J. Use and misuse of the Kubelka-Munk function to obtain the band gap energy from diffuse reflectance measurements. *Solid State Commun.* **2022**, *341*, 114573, DOI: 10.1016/j.ssc.2021.114573.
(275) Yamamoto, T.; Kageyama, H. Hydride Reductions of Transition Metal Oxides. *Chem. Lett.* **2013**, *42*, 946-953, DOI: 10.1246/cl.130581.
(276) Hayward, M. A.; Green, M. A.; Rosseinsky, M. J.; Sloan, J. Sodium Hydride as a Powerful Reducing Agent for Topotactic Oxide Deintercalation: Synthesis and Characterization of the Nickel(I) Oxide $LaNiO_2$. *J. Am. Chem. Soc.* **1999**, *121*, 8843-8854, DOI: 10.1021/ja991573i.
(277) Dixon, E.; Hadermann, J.; Ramos, S.; Goodwin, A. L.; Hayward, M. A. Mn(I) in an Extended Oxide: The Synthesis and Characterization of $La_{1-x}Ca_xMnO_{2+\delta}$ ($0.6 \leq x \leq 1$). *J. Am. Chem. Soc.* **2011**, *133*, 18397-18405, DOI: 10.1021/ja207616c.
(278) Kobayashi, Y.; Li, Z.; Hirai, K.; Tassel, C.; Loyer, F.; Ichikawa, N.; Abe, N.; Yamamoto, T.; Shimakawa, Y.; Yoshimura, K.; et al. Gas phase contributions to topochemical hydride reduction reactions. *J. Solid State Chem.* **2013**, *207*, 190-193, DOI: 10.1016/j.jssc.2013.09.006.
(279) Hernden, B. C.; Lussier, J. A.; Bieringer, M. Topotactic Solid-State Metal Hydride Reductions of Sr_2MnO_4. *Inorg. Chem.* **2015**, *54*, 4249-4256, DOI: 10.1021/ic502932x.

(280) Zhang, H.; Gao, S.; Zhang, Q.; Wu, J.; Liang, J.; Dong, C.; Gu, L.; Dong, S.; Sun, J.; Liao, F.; et al. Topotactic Reduction toward a Noncentrosymmetric Deficient Perovskite $Tb_{0.50}Ca_{0.50}Mn_{0.96}O_{2.37}$ with Ordered Mn Vacancies and Piezoelectric Behavior. *Chem. Mater.* **2017**, *29*, 9840-9850, DOI: 10.1021/acs.chemmater.7b04115.
(281) Nedumkandathil, R.; Jaworski, A.; Grins, J.; Bernin, D.; Karlsson, M.; Eklöf-Österberg, C.; Neagu, A.; Tai, C.-W.; Pell, A. J.; Häussermann, U. Hydride Reduction of $BaTiO_3$ − Oxyhydride Versus O Vacancy Formation. *ACS Omega* **2018**, *3*, 11426-11438, DOI: 10.1021/acsomega.8b01368.
(282) Guo, H.; Jaworski, A.; Ma, Z.; Slabon, A.; Bacsik, Z.; Nedumkandathil, R.; Häussermann, U. Trapping of different stages of $BaTiO_3$ reduction with LiH. *RSC Adv.* **2020**, *10*, 35356-35365, DOI: 10.1039/D0RA07276A.
(283) Barker, M. G.; Hooper, A. J. Reactions of liquid sodium with transition-metal oxides. Part VIII. The oxides of chromium-(III),-(IV), and -(VI) and disodium chromium(VI) tetraoxide. *J. Chem. Soc., Dalton Trans.* **1976**, 1093-1095, DOI: 10.1039/DT9760001093.
(284) Barker, M. G.; Hooper, A. J.; Wood, D. J. Reactions of liquid sodium with transition-metal oxides. Part VII. The oxides of niobium and tantalum. *J. Chem. Soc., Dalton Trans.* **1974**, 55-58, DOI: 10.1039/DT9740000055.
(285) Barker, M. G.; Hooper, A. J.; Lintonbon, R. M. Reactions of the oxides of vanadium with liquid potassium. *J. Chem. Soc., Dalton Trans.* **1973**, 2618-2620, DOI: 10.1039/DT9730002618.
(286) Addison, C. C.; Braker, M. G.; Hooper, A. J. Reactions of liquid sodium with transition-metal oxides. Part IV. Oxides of iron, cobalt, nickel, and copper. *J. Chem. Soc., Dalton Trans.* **1972**, 1017-1019, DOI: 10.1039/DT9720001017.
(287) Qvick, J. Influence of sodium on the reduction of tungsten(VI) oxide. *Reactivity of Solids* **1987**, *4*, 73-91, DOI: 10.1016/0168-7336(87)80088-8.
(288) Belyakova, D. A.; Udalova, T. A. Synthesis of highly dispersed tungsten by mechanochemical reduction of magnesium tungstate. *Mater. Today: Proc.* **2020**, *31*, 476-478, DOI: 10.1016/j.matpr.2020.05.614.
(289) Davison, N.; Khatun, T.; Arce-Garcia, I.; Gould, J. A.; Dawson, J. A.; Lu, E. Facile Mechanochemical Reduction and Lithium-Ion Doping of Transition-Metal Oxides. *Eur. J. Inorg. Chem.* **2023**, *26*, e202300344, DOI: 10.1002/ejic.202300344.
(290) Welham, N. J. Mechanochemical reduction of $FeTiO_3$ by Si. *J. Alloys Compd.* **1998**, *274*, 303-307, DOI: 10.1016/S0925-8388(98)00590-8.
(291) Yang, H.; Nguyen, G.; McCormick, P. G. Mechanochemical reduction of CuO by graphite. *Scr. Metall. Mater.* **1995**, *32*, 681-684, DOI: 10.1016/0956-716X(95)91585-D.
(292) Matteazzi, P.; Le Caër, G. Mechanochemical reduction of hematite by room temperature ball milling. *Hyperfine Interact.* **1992**, *68*, 177-180, DOI: 10.1007/BF02396465.
(293) Grohn, H.; Paudert, R.; Friedrich, H. Über die mechanochemische Reduktion einiger Metalloxide durch Kohlenstoff. *Z. Anorg. Allg. Chem.* **1966**, *348*, 21-29, DOI: 10.1002/zaac.19663480104.
(294) Zakeri, M.; Yazdani-Rad, R.; Enayati, M. H.; Rahimipour, M. R.; Mobasherpour, I. Mechanochemical reduction of MoO_3/SiO_2 powder mixtures by Al and carbon for the synthesis of nanocrystalline $MoSi_2$. *J. Alloys Compd.* **2007**, *430*, 170-174, DOI: 10.1016/j.jallcom.2006.05.016.
(295) Zou, R.; Li, J.; Cui, J.; Zhang, W.; Lei, G.; Cao, H.; Chen, P. Catalyst-free synthesis of lithium hydride at room temperature. *Chem. Commun.* **2023**, *59*, 2660-2663, DOI: 10.1039/D2CC06849D
(296) Felderhoff, M.; Pommerin, A.; Mamatha, M.; Bogdanović, B.; Schüth, F. Tribochemische Synthese von Hydriden durch Hochenergie-Kugelvermahlung. *Chem. Ing. Tech.* **2007**, *79*, 907-911, DOI: 10.1002/cite.200700049.

(297) Baran, A.; Jensen, T. R.; Polański, M. Synthesis of Mg_2FeH_6 by High-Temperature High-Pressure Reactive Planetary Ball Milling. *Adv. Eng. Mater.* **2024**, 2400425, DOI: 10.1002/adem.202400425.
(298) Bilen, M.; Yılmaz, O.; Gürü, M. Synthesis of $LiBH_4$ from $LiBO_2$ as hydrogen carrier and its catalytic dehydrogenation. *Int. J. Hydrogen Energy* **2015**, *40*, 15213-15217, DOI: 10.1016/j.ijhydene.2015.02.085.
(299) Çakanyildirim, Ç.; Gürü, M. The Production of $NaBH_4$ from Its Elements by Mechanochemical Reaction and Usage in Hydrogen Recycle. *Energy Sources A: Recovery Util. Environ. Eff.* **2011**, *33*, 1912-1920, DOI: 10.1080/15567030903503175.
(300) Chłopek, K.; Frommen, C.; Léon, A.; Zabara, O.; Fichtner, M. Synthesis and properties of magnesium tetrahydroborate, $Mg(BH_4)_2$. *J. Mater. Chem.* **2007**, *17*, 3496-3503, DOI: 10.1039/B702723K.
(301) Rongeat, C.; Llamas Jansa, I.; Oswald, S.; Schultz, L.; Gutfleisch, O. Mechanochemical synthesis and XPS analysis of sodium alanate with different additives. *Acta Mater.* **2009**, *57*, 5563-5570, DOI: 10.1016/j.actamat.2009.07.053.
(302) Kabbour, H.; Ahn, C. C.; Hwang, S.-J.; Bowman, R. C.; Graetz, J. Direct synthesis and NMR characterization of calcium alanate. *J. Alloys Compd.* **2007**, *446-447*, 264-266, DOI: 10.1016/j.jallcom.2006.12.050.
(303) Kojima, Y.; Kawai, Y.; Haga, T.; Matsumoto, M.; Koiwai, A. Direct formation of $LiAlH_4$ by a mechanochemical reaction. *J. Alloys Compd.* **2007**, *441*, 189-191, DOI: 10.1016/j.jallcom.2006.08.343.
(304) Pu, K.; Yang, Y.; Qu, X.; Gao, M.; Liu, Y.; Pan, H. Room Temperature Conversion of Carbon Dioxide into Fuel Gases by Mechanochemically Reacting with Metal Hydrides. *ChemistrySelect* **2017**, *2*, 5244-5247, DOI: 10.1002/slct.201700834.
(305) Buzanov, G. A.; Nipan, G. D.; Zhizhin, K. Y.; Kuznetsov, N. T. Hydride lithiation of spinels $LiMn_2O_4$. *Dokl. Chem.* **2016**, *471*, 330-333, DOI: 10.1134/S0012500816110082.
(306) Wang, K.; Wang, Y.; Wang, J.; Gan, Y.; He, X.; Xia, Y.; Zhang, J.; Huang, H.; Zhang, W.; Liang, C. Milling Time-Dependent Lithium/Sodium Storage Performance of Carbons Synthesized by a Mechanochemical Reaction. *Energy & Fuels* **2021**, *35*, 4596-4603, DOI: 10.1021/acs.energyfuels.1c00089.
(307) Mulas, G.; Loiselle, S.; Schiffini, L.; Cocco, G. The Mechanochemical Self-Propagating Reaction between Hexachlorobenzene and Calcium Hydride. *J. Solid State Chem.* **1997**, *129*, 263-270, DOI: 10.1006/jssc.1996.7238.
(308) Zhou, C.; Bowman, R. C., Jr.; Fang, Z. Z.; Lu, J.; Xu, L.; Sun, P.; Liu, H.; Wu, H.; Liu, Y. Amorphous TiCu-Based Additives for Improving Hydrogen Storage Properties of Magnesium Hydride. *ACS Appl. Mater. Interfaces* **2019**, *11*, 38868-38879, DOI: 10.1021/acsami.9b16076.
(309) Ikeda, T.; Mikami, Y.; Haruki, T. Mg-Promoted LiH−$LiNH_2$ Hydrogen Storage System Synthesized by Using the Mechanochemical Method. *J. Phys. Chem. C* **2007**, *111*, 8389-8396, DOI: 10.1021/jp071223f.
(310) Cao, H.; Chua, Y.; Zhang, Y.; Xiong, Z.; Wu, G.; Qiu, J.; Chen, P. Releasing 9.6 wt% of H_2 from $Mg(NH_2)_2$–3LiH–NH_3BH_3 through mechanochemical reaction. *Int. J. Hydrogen Energy* **2013**, *38*, 10446-10452, DOI: 10.1016/j.ijhydene.2013.06.036.
(311) Pukazhselvan, D.; Nasani, N.; Pérez, J.; Hortigüela, M. J.; Yang, T.; Bdikin, I.; Fagg, D. P. Two step mechanochemical synthesis of Nb doped MgO rock salt nanoparticles and its application for hydrogen storage in MgH_2. *Int. J. Hydrogen Energy* **2016**, *41*, 11716-11722, DOI: 10.1016/j.ijhydene.2015.11.175.
(312) de Oliveira, P. F. M.; Michalchuk, A. A. L.; Marquardt, J.; Feiler, T.; Prinz, C.; Torresi, R. M.; Camargo, P. H. C.; Emmerling, F. Investigating the role of reducing agents on mechanosynthesis of Au nanoparticles. *CrystEngComm* **2020**, *22*, 6261-6267, DOI: 10.1039/D0CE00826E.

(313) Johnson Humphrey, E. L. B.; Kennedy, A. R.; Sproules, S.; Nelson, D. J. Evaluating a Dispersion of Sodium in Sodium Chloride for the Synthesis of Low-Valent Nickel Complexes. *Eur. J. Inorg. Chem.* **2022**, *2022*, e202101006, DOI: 10.1002/ejic.202101006.
(314) Gao, Y.; Kubota, K.; Ito, H. Mechanochemical Approach for Air-Tolerant and Extremely Fast Lithium-Based Birch Reductions in Minutes. *Angew. Chem. Int. Ed.* **2023**, *62*, e202217723, DOI: 10.1002/anie.202217723.
(315) Takacs, L. Self-sustaining reactions induced by ball milling. *Prog. Mater Sci.* **2002**, *47*, 355-414, DOI: 10.1016/S0079-6425(01)00002-0.
(316) Takacs, L. Self-sustaining reactions as a tool to study mechanochemical activation. *Faraday Discuss.* **2014**, *170*, 251-265, DOI: 10.1039/C3FD00133D.
(317) Jalaly, M.; Gotor, F. J.; Sayagués, M. J. Mechanically induced combustion synthesis of niobium carbonitride nanoparticles. *J. Solid State Chem.* **2018**, *267*, 106-112, DOI: 10.1016/j.jssc.2018.08.027.
(318) Jalaly, M.; Gotor, F. J.; Sayagués, M. J. Mechanochemical combustion synthesis of vanadium carbide (VC), niobium carbide (NbC) and tantalum carbide (TaC) nanoparticles. *Int. J. Refract. Met. Hard Mater.* **2019**, *79*, 177-184, DOI: 10.1016/j.ijrmhm.2018.12.011.
(319) Jalaly, M.; Tamizifar, M.; Bafghi, M. S.; Gotor, F. J. Mechanochemical synthesis of ZrB_2–SiC–ZrC nanocomposite powder by metallothermic reduction of zircon. *J. Alloys Compd.* **2013**, *581*, 782-787, DOI: 10.1016/j.jallcom.2013.07.142.
(320) Abdellahi, M.; Zakeri, M.; Bahmanpour, H. Events and reaction mechanisms during the synthesis of an Al_2O_3-TiB_2 nanocomposite via high energy ball milling. *Front. Chem. Sci. Eng.* **2013**, *7*, 123-129, DOI: 10.1007/s11705-013-1325-6.
(321) Mukherjee, A.; Krishnamurthy, N. Phase evolution during mechanochemical coreduction of V_2O_5 and TiO_2 with Al. *Int. J. Self-Propag. High-Temp Synth.* **2010**, *19*, 237-243, DOI: 10.3103/S1061386210040023.
(322) Bragg, W. H.; Bragg, W. L. The reflection of X-rays by crystals. *Proc. R. Soc. A Math. Phys. Eng. Sci.* **1913**, *88*, 428-438, DOI: 10.1098/rspa.1913.0040.
(323) Cheary, R. W.; Coelho, A. A fundamental parameters approach to X-ray line-profile fitting. *J. Appl. Crystallogr.* **2004**, *25*, 109-121, DOI: 10.1107/S0021889891010804.
(324) Spieß, L.; Teichert, G.; Schwarzer, R.; Behnken, H.; Genzel, C. *Moderne Röntgenbeugung - Röntgendiffraktometrie für Materialwissenschaftler, Physiker und Chemiker*; Springer Spektrum, Wiesbaden, Germany, 2019.
(325) *Topas* Bruker AXS Inc.: Karlsruhe (Germany), 2014.
(326) Rietveld, H. M. Line profiles of neutron powder-diffraction peaks for structure refinement. *Acta Crystallogr.* **1967**, *22*, 151-152, DOI: 10.1107/S0365110X67000234.
(327) Rietveld, H. M. A profile refinement method for nuclear and magnetic structures. *J. Appl. Crystallogr.* **1969**, *2*, 65-71, DOI: 10.1107/S0021889869006558.
(328) McCusker, L. B.; Von Dreele, R. B.; Cox, D. E.; Louër, D.; Scardi, P. Rietveld refinement guidelines. *J. Appl. Crystallogr.* **1999**, *32*, 36-50, DOI: 10.1107/S0021889898009856.
(329) Scherrer, P. Bestimmung der Größe und der inneren Struktur von Kolloidteilchen mittels Röntgenstrahlen. *Nachr. Ges. Wiss. Göttingen* **1918**, 98-100.
(330) Hassanzadeh-Tabrizi, S. A. Precise calculation of crystallite size of nanomaterials: A review. *J. Alloys Compd.* **2023**, *968*, 171914, DOI: 10.1016/j.jallcom.2023.171914.
(331) Williamson, G. K.; Hall, W. H. X-ray line broadening from filed aluminium and wolfram. *Acta Metall.* **1953**, *1*, 22-31, DOI: 10.1016/0001-6160(53)90006-6.
(332) Stephens, P. Phenomenological model of anisotropic peak broadening in powder diffraction. *J. Appl. Crystallogr.* **1999**, *32*, 281-289, DOI: 10.1107/S0021889898006001.
(333) Pradhan, S. K.; Shee, S. K.; Chanda, A.; Bose, P.; De, M. X-ray studies on the kinetics of microstructural evolution of Ni_3Al synthesized by ball milling elemental powders. *Mater. Chem. Phys.* **2001**, *68*, 166-174, DOI: 10.1016/S0254-0584(00)00347-3.

(334) Hadef, F.; Ans, M. X-ray analysis and Rietveld refinement of ball milled $Fe_{50}Al_{35}Ni_{15}$ powder. *Surf. Interfaces* **2021**, *26*, 101303, DOI: 10.1016/j.surfin.2021.101303.
(335) Michaely, A. Mechanochemical synthesis and characterization of partially reduced niobium pentoxide. Universität des Saarlandes, 2021.
(336) Michaely, A.; Janka, O.; Gießelmann, E. C. J.; Haberkorn, R.; Wiedemann, H. T. A.; Kay, C. W. M.; Kickelbick, G. Black Titania and Niobia within Ten Minutes – Mechanochemical Reduction of Metal Oxides with Alkali Metal Hydrides. *Chem. Eur. J.* **2023**, *29*, e202300223, DOI: 10.1002/chem.202300223.
(337) Luckas, C. Mechanochemische Reduktion von Vanadium(V)oxid mit Hydriden. Universität des Saarlandes, 2022.
(338) Bell, R. P.; Hinshelwood, C. N. The theory of reactions involving proton transfers. *Proc. R. Soc. Lond. Ser. A - Math. Phys. Sci.* **1936**, *154*, 414-429, DOI: 10.1098/rspa.1936.0060.
(339) Evans, M. G.; Polanyi, M. Inertia and driving force of chemical reactions. *Trans. Faraday Soc.* **1938**, *34*, 11-24, DOI: 10.1039/TF9383400011.
(340) Jo, J. H.; Aniskevich, Y.; Kim, J.; Choi, J. U.; Kim, H. J.; Jung, Y. H.; Ahn, D.; Jeon, T.-Y.; Lee, K.-S.; Song, S. H.; et al. New Insight on Open-Structured Sodium Vanadium Oxide as High-Capacity and Long Life Cathode for Zn–Ion Storage: Structure, Electrochemistry, and First-Principles Calculation. *Adv. Energy Mater.* **2020**, *10*, 2001595, DOI: 10.1002/aenm.202001595.
(341) Grzechnik, A.; Ueda, Y.; Yamauchi, T.; Hanfland, M.; Hering, P.; Potapkin, V.; Friese, K. Pressure-induced non-superconducting phase of β-$Na_{0.33}V_2O_5$ and the mechanism of high-pressure phase transitions in β-$Na_{0.33}V_2O_5$ and β-$Li_{0.33}V_2O_5$ at room temperature. *J. Phys. Condens. Matter.* **2016**, *28*, 035401, DOI: 10.1088/0953-8984/28/3/035401.
(342) Kanke, Y.; Kato, K.; Takayama-Muromachi, E.; Isobe, M. Structure of $Na_{0.56}V_2O_5$. *Acta Cryst. C* **1990**, *46*, 536-538, DOI: 10.1107/S0108270189008589.
(343) Blöchl, P. E. Projector augmented-wave method. *Phys. Rev. B* **1994**, *50*, 17953-17979, DOI: 10.1103/PhysRevB.50.17953.
(344) Kresse, G.; Furthmüller, J. Efficient iterative schemes for *ab initio* total-energy calculations using a plane-wave basis set. *Phys. Rev. B* **1996**, *54*, 11169-11186, DOI: 10.1103/PhysRevB.54.11169.
(345) Kresse, G.; Furthmüller, J. Efficiency of ab-initio total energy calculations for metals and semiconductors using a plane-wave basis set. *Comput. Mater. Sci.* **1996**, *6*, 15-50, DOI: 10.1016/0927-0256(96)00008-0.
(346) Kresse, G.; Joubert, D. From ultrasoft pseudopotentials to the projector augmented-wave method. *Phys. Rev. B* **1999**, *59*, 1758-1775, DOI: 10.1103/PhysRevB.59.1758.
(347) Perdew, J. P.; Ruzsinszky, A.; Csonka, G. I.; Vydrov, O. A.; Scuseria, G. E.; Constantin, L. A.; Zhou, X.; Burke, K. Restoring the Density-Gradient Expansion for Exchange in Solids and Surfaces. *Phys. Rev. Lett.* **2008**, *100*, 136406, DOI: 10.1103/PhysRevLett.100.136406.
(348) Michaely, A.; Chen, H.; Clemens, O.; Neuberger, M.; Kay, C. W. M.; Haberkorn, R.; Kickelbick, G. Mechanochemical Synthesis of MgV_2O_4: Reactivity Pathways Driven by Milling Energy and Precursors. *Inorg. Chem.* **2025**, *64*, 20163-20174, DOI: 10.1021/acs.inorgchem.5c03095.

6 Supplementary Information

6.1 Supporting Information – Black Titania and Niobia within Ten Minutes – Mechanochemical Reduction of Metal Oxides with Alkali Metal Hydrides

Chemistry–A European Journal

Supporting Information

Black Titania and Niobia within Ten Minutes – Mechanochemical Reduction of Metal Oxides with Alkali Metal Hydrides

Anna Michaely, Oliver Janka, Elias C. J. Gießelmann, Robert Haberkorn, Haakon T. A. Wiedemann, Christopher W. M. Kay, and Guido Kickelbick*

Table of contents

1 Temperature-pressure increase during ball milling 1

2 Powder X-ray diffraction analysis and Rietveld refinement of reduced titania and niobia ... 2

Rietveld plots of reduced titania and niobia 2

Ball milling anatase TiO_2 with 1 eq. LiH 9

PXRD analysis and Rietveld refinement of reduced Nb_2O_5 9

Estimation of the Li content based on the change of the cell volume of Nb_2O_5 10

3 Reoxidation by Thermogravimetric Analysis 11

Results of the thermogravimetric analysis (TGA) and subsequent PXRD measurements 11

Indication of oxygen vacancies 13

4 ^{6}Li SPE/MAS NMR 15

5 UV-Vis absorbance spectra and Kubelka-Munk plots of niobia 16

6 Testing of the photocatalytic activity 17

7 References 17

1 Temperature-pressure increase during ball milling

The EASY GTM System by Fritsch allows to measure the pressure and temperature increase inside the milling jar during ball milling. The EASY GTM system was used to investigate the evolution of pressure and temperature inside the milling jar for some reactions. The pressure and temperature increase is exemplarily shown in Figure S1 for the reaction of Nb_2O_5 with 1 eq. LiH for 60 min. During milling, the pressure increases up to 3.1 bar and the maximum temperature measured inside the jar was around 35 °C. While the pressure increase strongly depends on the amount of added hydride, the measured temperature inside the milling jar always remained under 36 °C under the chosen milling conditions. Since no additional heating is required and the measurable overall temperature inside the jar is only slightly above room temperature, the developed method drastically lowers the required temperatures and therefore the energy consumption for the reduction.

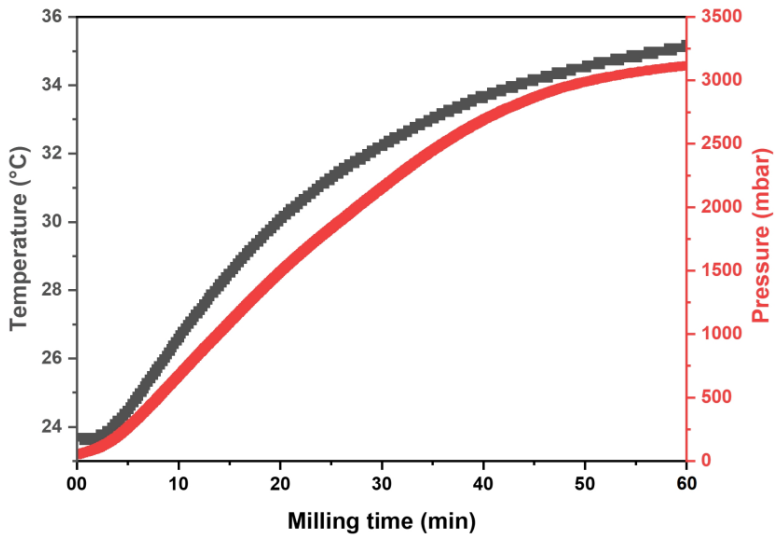

Figure S1: Pressure - temperature increase during the mechanochemical reaction of Nb_2O_5 and 1 eq. LiH. The milling time was set to 60 min.

2 Powder X-ray diffraction analysis and Rietveld refinement of reduced titania and niobia

Rietveld plots of reduced titania and niobia

Reactions via ball-milling usually do not lead to homogeneous reaction products and can produce significant amounts of strain in the material. Therefore, a multi-fraction model has been used for the Rietveld refinements to obtain a satisfying fit and accommodate structural changes, different amounts of strain and changes of the lattice parameters. In the case of TiO_2, a two-fraction model was used to describe the remaining starting material and the NaH reduced material. In contrast, four fractions of TiO_2 were used for all LiH reduced samples due to the larger structural changes occurring during to the reaction with LiH. Since only the *a* lattice parameter is significantly affected by the reduction, the value of the *c* lattice parameter was constrained to one value and refined equally for all fractions while the *a* lattice parameter was refined individually. The first TiO_2 fraction represents crystallites with the larger size, the second one the smaller crystallite sizes. To avoid over-parametrization, the strain for all but the first fractions (fractions II, III and IV) were constrained to one value and the ratio of the Gaussian-to-Lorentz contribution to the crystallite size/shape of the reflection was kept constant for these (if used at all).

In the case of Nb_2O_5, a two-fraction model was used. At Bragg angles around 25, 32 and 44° 2θ, the observed reflections are diffusely broadened, which indicates the presence of stacking faults inside the material.[1] The *b* lattice parameter was constrained for both fractions, while the other lattice parameters were refined individually.

Table S1: Overview of the sample composition as obtained by Rietveld refinement of all samples discussed in the course of the manuscript, the fit quality parameters *weighted profile R-factors (R_{wp})* and *goodness of fit (GOF)* as well as the number of the figure containing the corresponding Rietveld plot.

Sample	Composition	R_{wp}	GOF	Figure
TN_2:1_60	80% TiO_2_I	7.25	1.51	S2
	20% TiO_2_II			
TN_1:2_10	70% TiO_2_I	7.49	1.56	S3
	30% TiO_2_II			
TN_1:2_60	74% TiO_2_I	8.49	1.35	S4
	26% TiO_2_II			
TL_1:2_10	9% $Li_{0.5}Ti_{0.5}O$	6.23	1.36	S5
	58% TiO_2_I			
	25% TiO_2_II			
	7% TiO_2_III			
	1% TiO_2_IV			
TL_1:2_60	40% $Li_{0.5}Ti_{0.5}O$	8.19	1.26	S6
	33% TiO_2_I			
	10% TiO_2_II			
	6% TiO_2_III			
	11% TiO_2_IV			
NN_2:1_60	89% Nb_2O_5_I	5.07	2.16	S7
	11% Nb_2O_5_II			
NN_1:2_10	84% Nb_2O_5_I	7.18	3.04	S8
	16% Nb_2O_5_II			
NN_1:2_60	86% Nb_2O_5_I	5.78	2.42	S9
	14% Nb_2O_5_II			
NL_1:2_10	85% Nb_2O_5_I	7.42	4.99	S10
	15% Nb_2O_5_II			
NL_1:2_60	86% Nb_2O_5_I	4.47	1.81	S11
	14% Nb_2O_5_II			

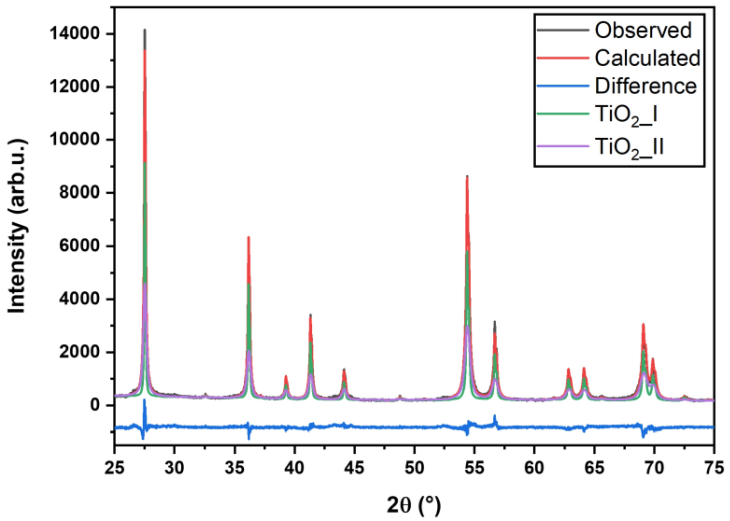

Figure S2: Rietveld refinement of rutile TiO_2 milled with 0.5 eq. NaH for 60 min.

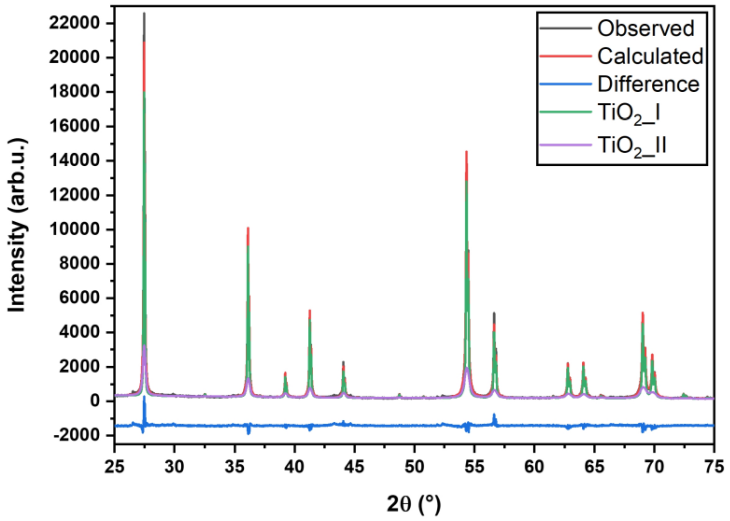

Figure S3: Rietveld refinement of rutile TiO_2 milled with 2 eq. NaH for 10 min.

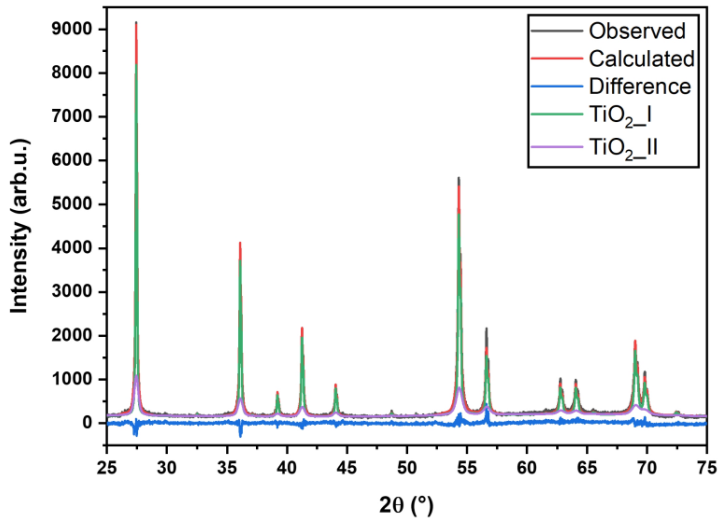

Figure S4: Rietveld refinement of rutile TiO_2 milled with 2 eq. NaH for 60 min.

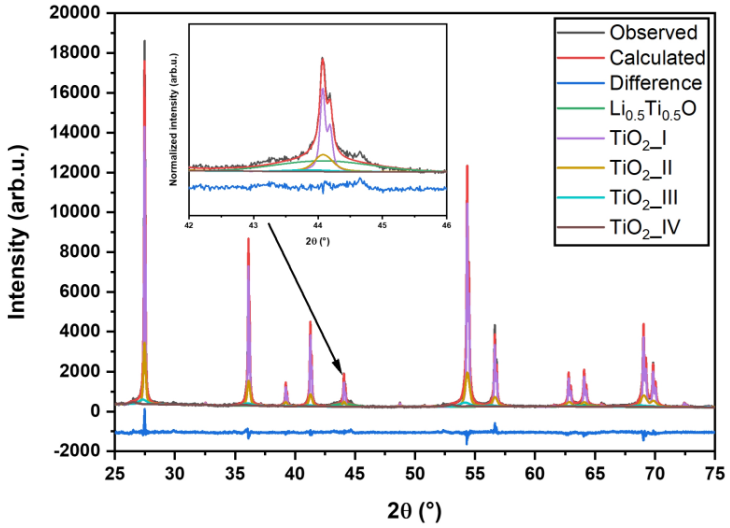

Figure S5: Rietveld refinement of rutile TiO_2 milled with 2 eq. LiH for 10 min. The inset shows the angle range, where the most intense reflection of $Li_{0.5}Ti_{0.5}O$ (200) is located and overlaps with a reflection of TiO_2 (210).

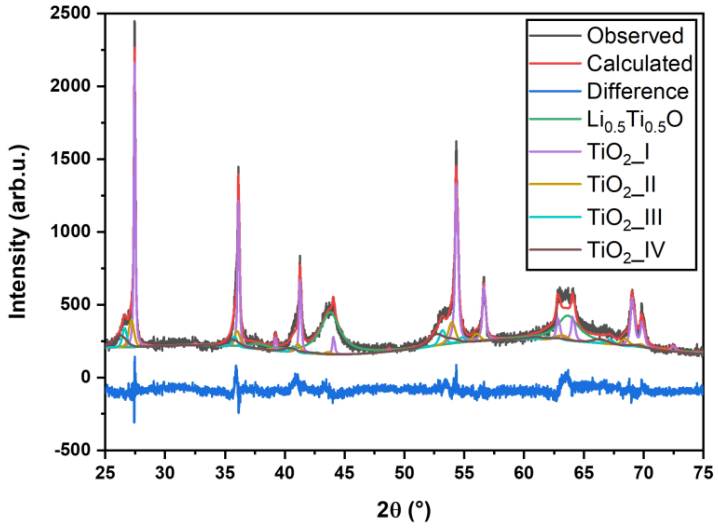

Figure S6: Rietveld refinement of rutile TiO_2 milled with 2 eq. LiH for 60 min.

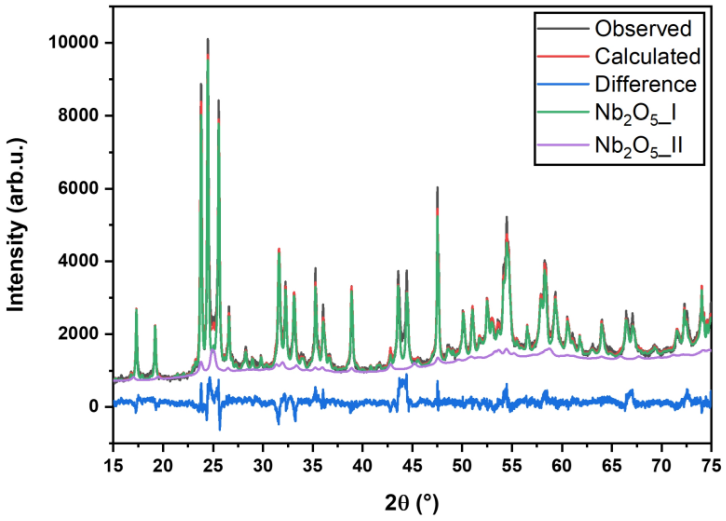

Figure S 7: Rietveld refinement of monoclinic H-Nb_2O_5 milled with 0.5 eq. NaH for 60 min.

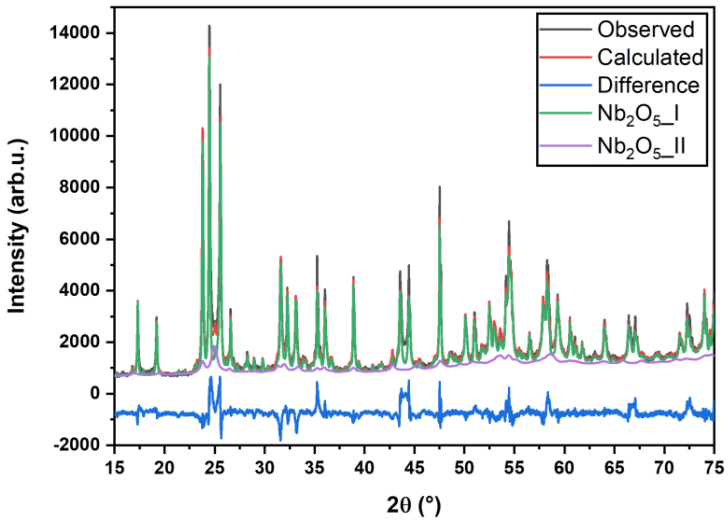

Figure S8: Rietveld refinement of monoclinic H-Nb_2O_5 milled with 2 eq. NaH for 10 min.

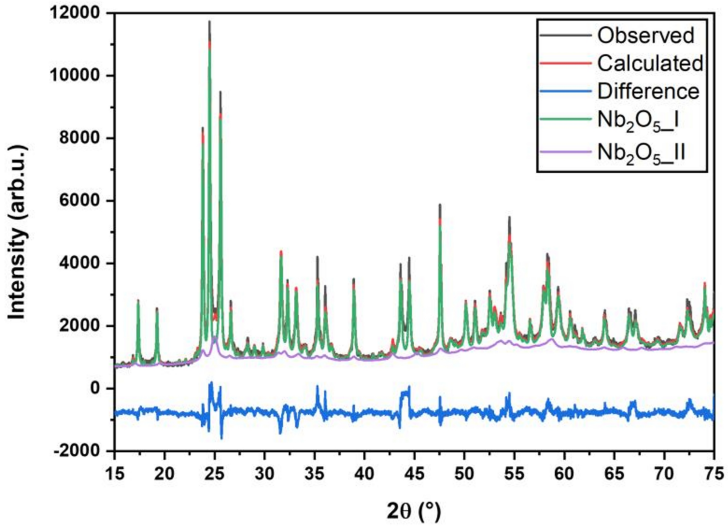

Figure S9: Rietveld refinement of monoclinic H-Nb_2O_5 milled with 2 eq. NaH for 60 min.

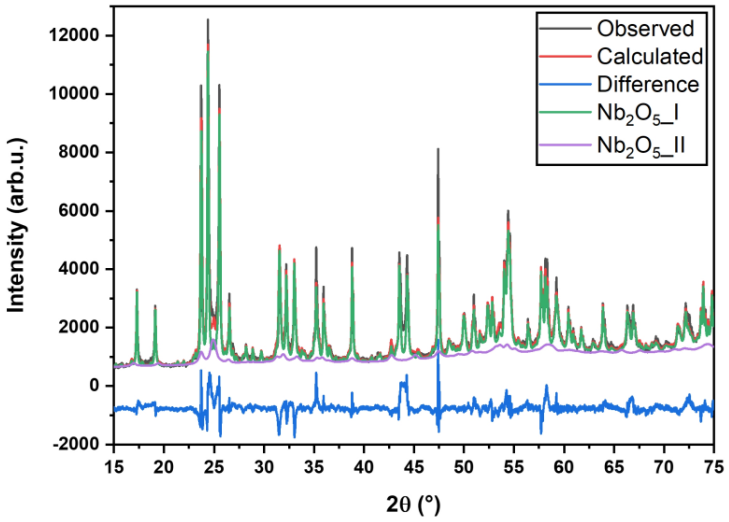

Figure S10: Rietveld refinement of monoclinic H-Nb_2O_5 milled with 2 eq. LiH for 10 min.

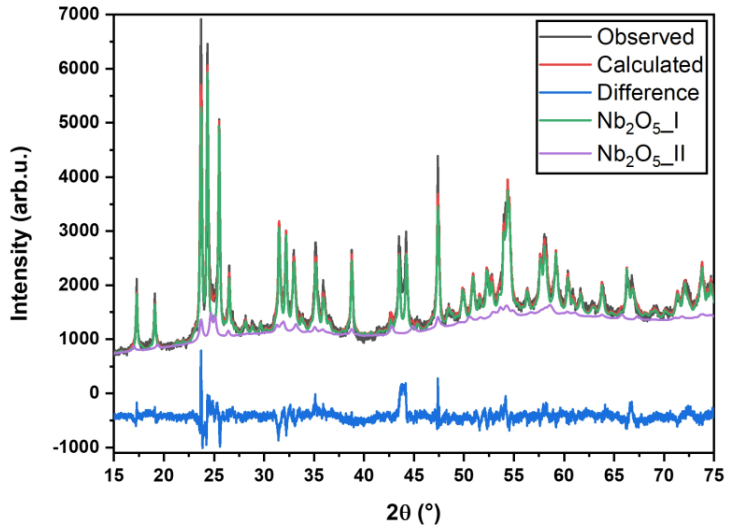

Figure S11: Rietveld refinement of monoclinic H-Nb_2O_5 milled with 2 eq. LiH for 60 min.

Ball milling anatase TiO_2 with 1 eq. LiH

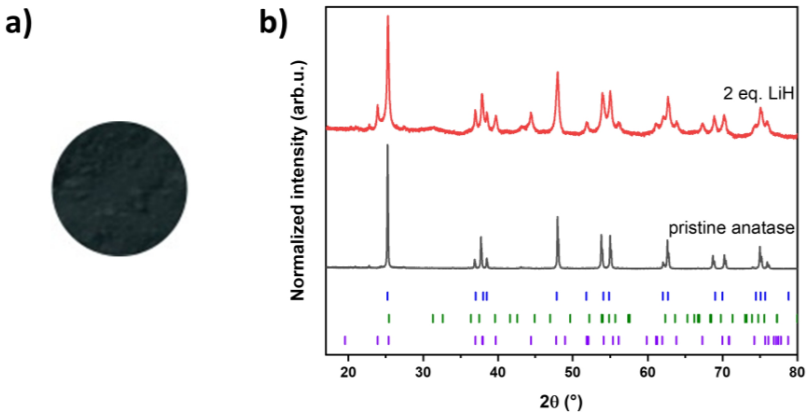

Figure S12: (a) Color change after ball milling anatase TiO_2 with 2 eq. LiH for 60 min at 300 rpm. (b) PXRD patterns of pristine and LiH-reduced anatase. Blue ticks indicate the Bragg positions of anatase type TiO_2, green ones of hp-TiO_2, and purple ones of $Li_{0.5}TiO_2$.

PXRD analysis and Rietveld refinement of reduced Nb_2O_5

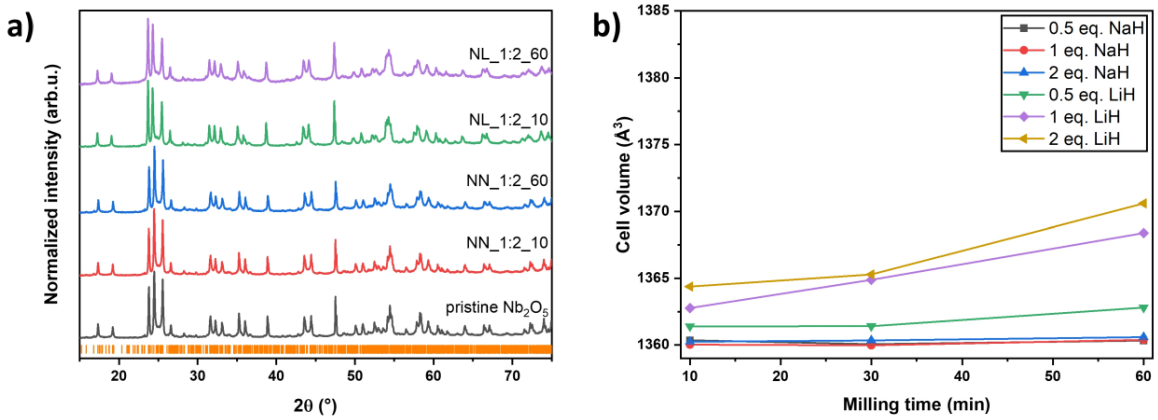

Figure S13: (a) PXRD patterns of pristine and reduced niobia. Orange ticks indicate the Bragg positions of monoclinic H-Nb_2O_5. (b) Unit cell volumes of NaH and LiH reduced Nb_2O_5 obtained by Rietveld refinement.

Estimation of the Li content based on the change of the cell volume of Nb_2O_5

The cell volume V_0 of pristine H-Nb_2O_5 is equal to 1360.46(6) Å^3 as obtained by Rietveld refinement. Catti *et al.*[2] report a cell volume of 1430.42 Å^3 for $Li_{1.74}Nb_2O_5$, a highly lithiated H-Nb_2O_5. Assuming a linear dependency of the cell volume of $Li_xNb_2O_5$ on the Li content x the value of x may be easily estimated from its cell volume V_x, according to equation (1).[2]

$$x = \frac{1.74 \cdot (V_x - V_0)}{V_{1.74} - V_0} \qquad (1)$$

With increasing milling time and higher amounts of LiH, a higher Li content x was estimated, which ranges from 0.02 to 0.25 depending on the milling conditions (Table S2).

Table S2: Unit cell volumes obtained by Rietveld refinement for Nb_2O_5 reduced with LiH and estimation of their lithium content using the obtained unit cell volumes.

Ratio Nb_2O_5 : LiH	Milling time (min)	Cell volume (Å^3)	$x_{Li_xNb_2O_5}$
no LiH	0	1360.46(6)	0
2 : 1	10	1361.40(6)	0.02
2 : 1	30	1361.41(8)	0.02
2 : 1	60	1362.82(8)	0.06
1 : 1	10	1362.78(8)	0.06
1 : 1	30	1364.89(9)	0.11
1 : 1	60	1368.39(10)	0.19
1 : 2	10	1364.38(8)	0.10
1 : 2	30	1365.29(10)	0.12
1 : 2	60	1370.59(13)	0.25

3 Reoxidation by Thermogravimetric Analysis

Results of the thermogravimetric analysis (TGA) and subsequent PXRD measurements

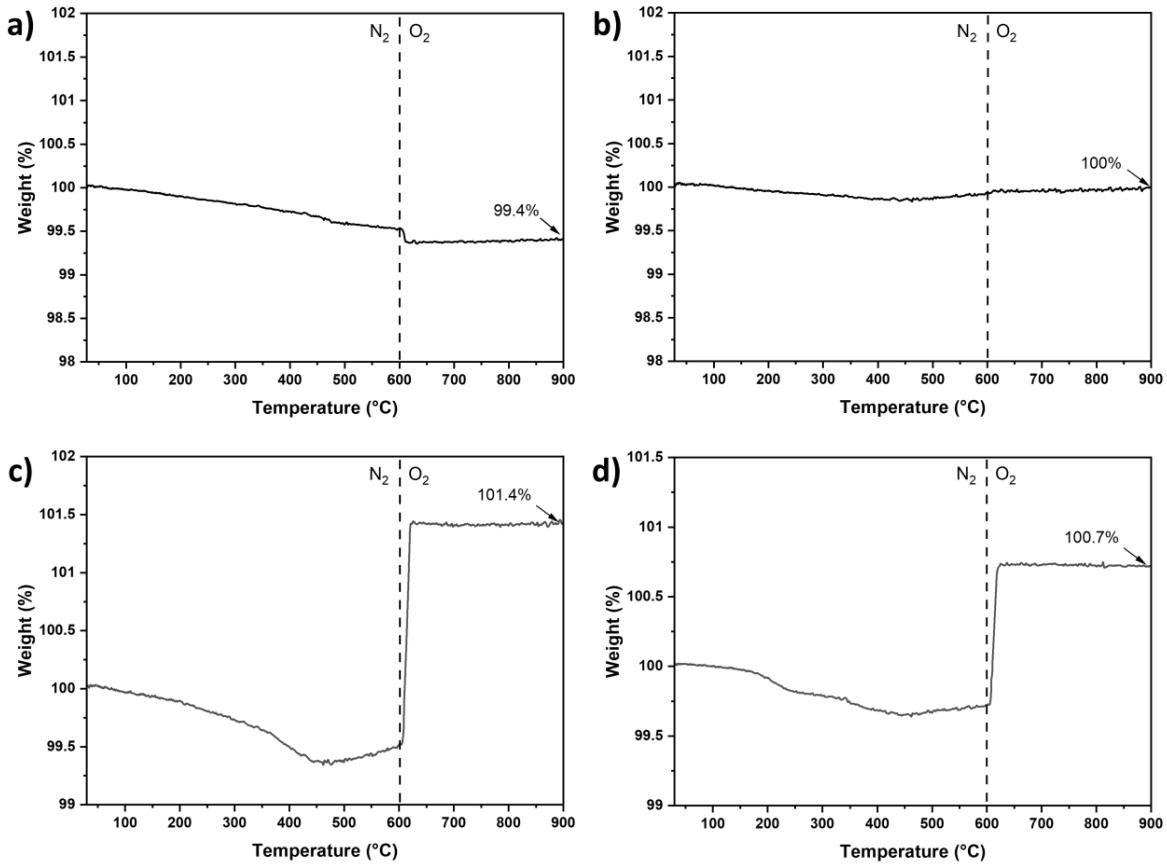

Figure S14: TGA curve in air of (a) TiO_2 and (b) Nb_2O_5 obtained after milling with 2 eq. NaH for 60 min. TGA curves of (c) TiO_2 and (d) Nb_2O_5 obtained after milling with 2 eq. LiH for 60 min. The samples were first heated under nitrogen to 600 °C followed by heating to 900 °C under synthetic air.

After TGA treatment, the samples were analyzed by PXRD measurements.

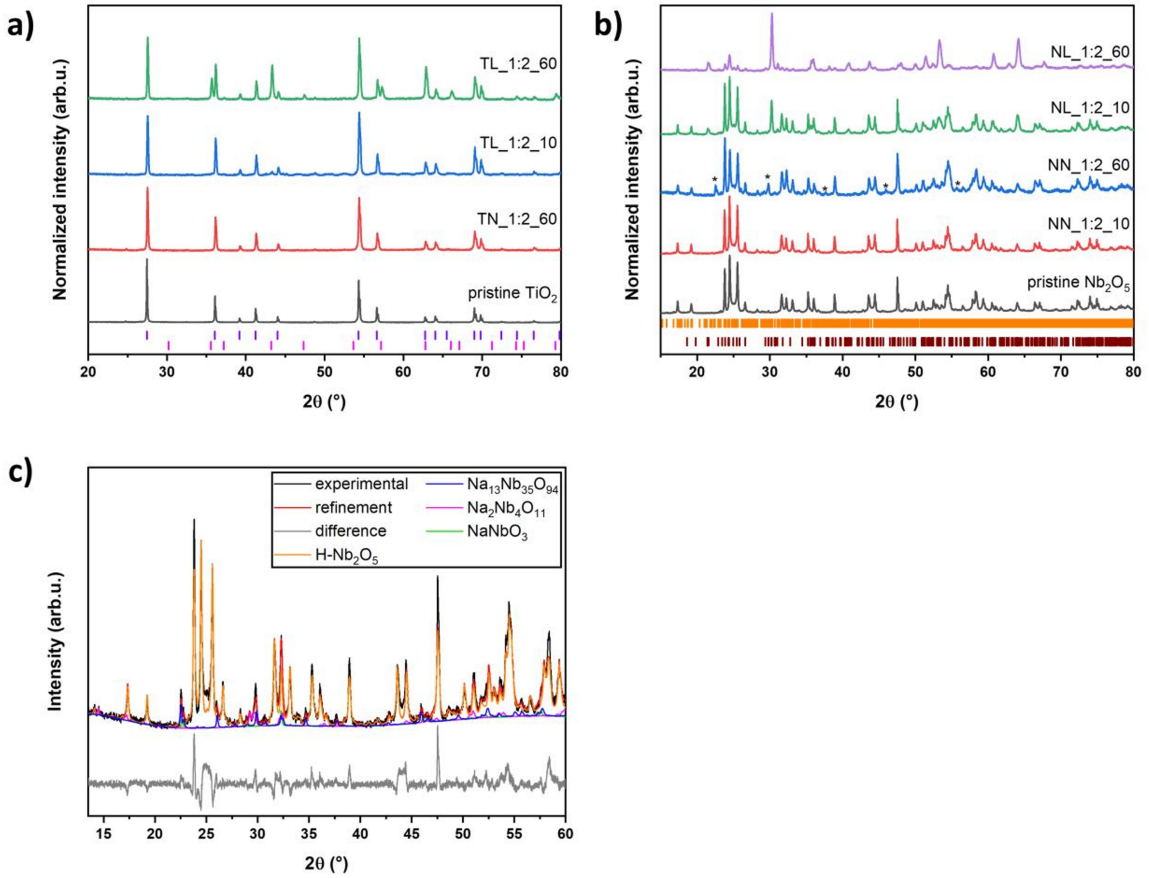

Figure S15: PXRD patterns of the pristine oxides and reduced (a) titania and (b) niobia. Reduced oxides were heated in the TGA under nitrogen to 600 °C followed by heating to 900 °C under oxygen. (a)Violet ticks indicate the Bragg positions of rutile TiO_2, and pink ones of $Li_{1.33}Ti_{1.667}O_4$. (b) Orange ticks indicate the Bragg positions of Nb_2O_5, brown ones of $LiNb_3O_8$. (c) Rietveld plot of sample NN_1:2_60 after TGA treatment.

Table S3: Percentage composition of reduced titania after TGA measurements as obtained by Rietveld refinement.

Sample	wt% TiO_2	wt% $Li_4Ti_5O_{12}$
TN_1:2_60	100	-
TL_1:2_10	91	9
TL_1:2_60	54	46

Table S4: Percentage composition of reduced niobia after TGA measurements as obtained by Rietveld refinement.

Sample	wt% Nb_2O_5	wt% $LiNb_3O_8$	wt% $NaNbO_3$	wt% $Na_2Nb_4O_{11}$	wt% $Na_{13}Nb_{35}O_{95}$
NN_1:2_10	100	-	-	-	-
NN_1:2_60	90	-	1	6	3
NL_1:2_10	74	26	-	-	-
NL_1:2_60	16	84	-	-	-

Indication of oxygen vacancies

As already stated in the manuscript, during the reduction of Ti^{4+}/Nb^{5+} to Ti^{3+}/Nb^{4+} charge neutrality can be respected by the formation of oxygen vacancies, the intercalation of Li^+ or a combination of both. However, it is hard to distinguish between the two effects.

The sample obtained after milling TiO_2 with 2 eq. NaH for 60 min was investigated more closely by TGA and PXRD measurements to possibly get an indication for the presence of oxygen vacancies. When being heated to 600 °C under N_2 followed by heating to 900 °C under synthetic air, an overall slight mass loss of 0.6% is observed and the sample turned from light gray to white again due to reoxidation (Figure S16a). Similarly, a slight decrease of the mass can be observed when the sample is heated to 800 °C either under N_2 or synthetic air (Figure S16b), possibly due to the desorption of adsorbed molecules. Overall, the total mass loss is smaller when being heated under nitrogen than under synthetic air. PXRD measurements revealed that only rutile TiO_2 and no sodiated titanates are present after thermal treatment in the TGA in both cases (Figure S16c). However, only the sample heated under air turned white again, while the light gray coloration was retained during heating under nitrogen (Figure S16d). Thus, the smaller mass decrease coupled with the color change back to white if heated under air indicates that oxygen vacancies are refilled with oxygen during the reoxidation, which does not take place, if the sample is heated under N_2. This leads to the conclusion that oxygen vacancies according to TiO_{2-x} can form in principle, but a full differentiation between reduction via lithium intercalation and reduction due to oxygen vacancies remains impossible.

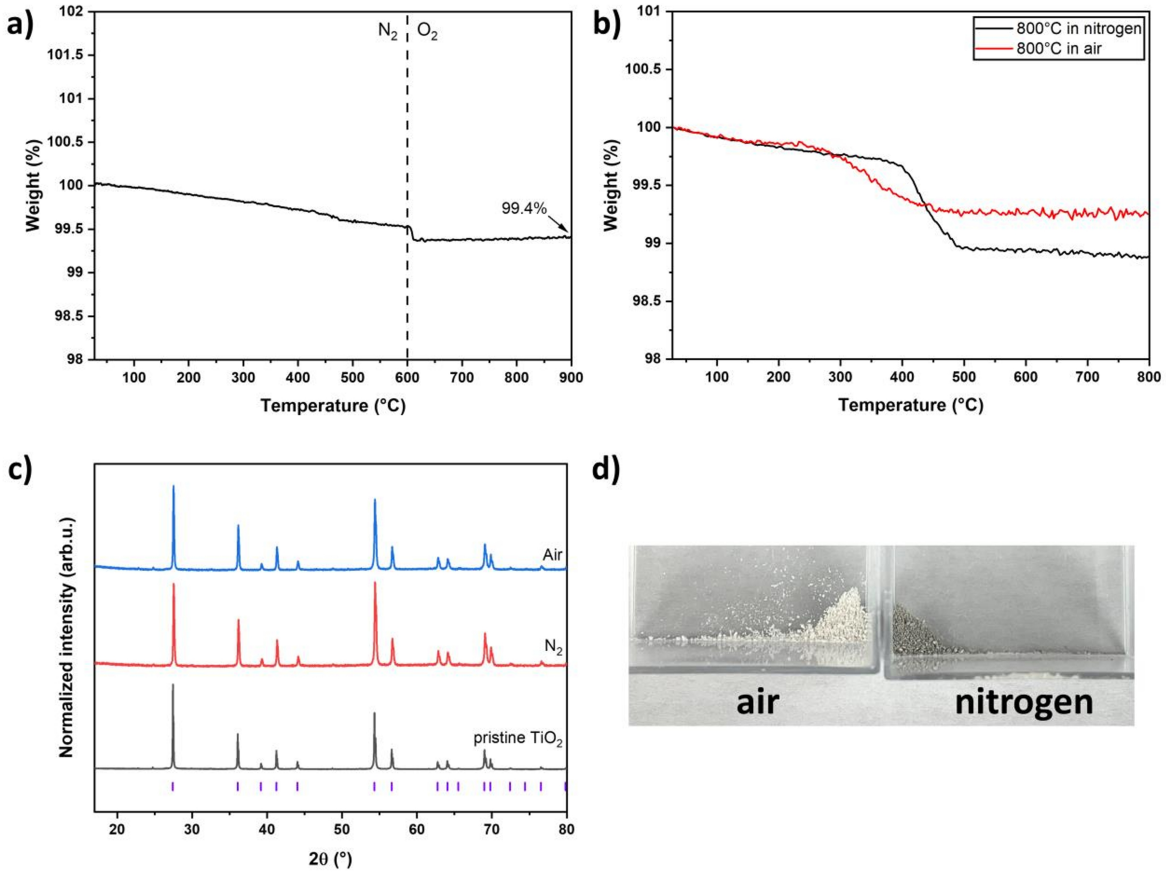

Figure S16: TGA curve of TiO_2 milled with 2 eq. NaH for 60 min obtained (a) by heating under nitrogen to 600 °C followed by heating to 900 °C under synthetic air and (b) by heating to 800 °C either under nitrogen or synthetic air. (c) XRD patterns of pristine TiO_2 (black) and TiO_2 milled with 2 eq. NaH for 60 min after TGA treatment up to 800 °C under nitrogen (red) and under synthetic air (blue). Violet ticks indicate the Bragg positions of rutile TiO_2. (d) Sample coloration after thermal treatment up to 800 °C under air (left) and under nitrogen (right).

4 ^{6}Li SPE/MAS NMR

Table S5: Summary of NMR observables of the LiH + TiO_2 (10, 30 and 60 min) and LiH + Nb_2O_5 (60 min) samples extracted from the DMFit simulation of the ^{6}Li MAS NMR spectra with δ being the resonance shift (in ppm) and FWHM being the full-width at half-maximum parameter (in ppm).

Sample		δ (ppm)	FWHM (ppm)
TL_1:2_10		1.00	2.88
TL_1:2_30	single line	1.05	4.48
	two lines	1.01	4.17
		7.52	7.23
TL_1:2_60	single line	0.84	5.36
	two lines	0.80	5.08
		8.36	6.57
NL_1:2_60		0.78	2.99

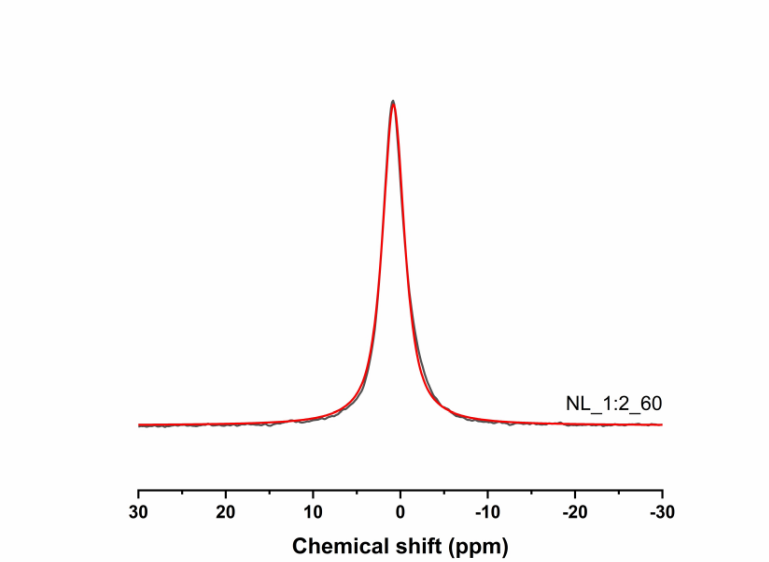

Figure S17: ^{6}Li MAS NMR spectrum of Nb_2O_5 + LiH (1:2) after 60 minutes with a single line shape simulation.

5 UV-Vis absorbance spectra and Kubelka-Munk plots of niobia

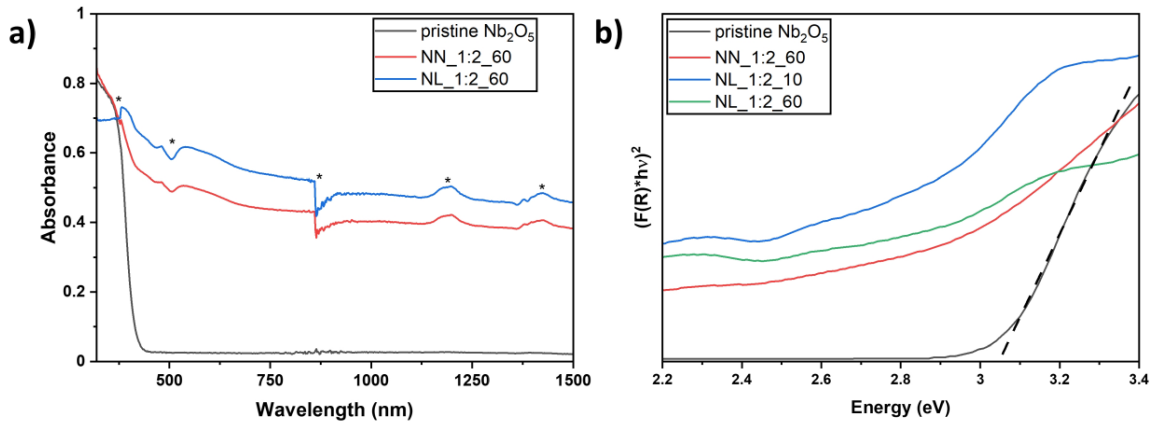

Figure S18: (a) DRS-UV-Vis absorbance spectra and (b) Kubelka-Munk plot of pristine and reduced niobia. Lamp, detector, and filter changes are marked with an asterisk, the evaluation of the band gap is shown by the dashed line in b).

Table S6: Optical band gaps of pristine and reduced titania and niobia determined using the Kubelka-Munk function.

Oxide	Reducing agent	Milling time (min)	E_g (direct) (eV)
TiO_2	-	0	3.11
TiO_2	0.5 eq. NaH	60	3.11
TiO_2	2 eq. NaH	60	3.11
TiO_2	2 eq. LiH	10	3.08
TiO_2	2 eq. LiH	60	2.89
Nb_2O_5	-	0	3.17
Nb_2O_5	0.5 eq. NaH	60	2.99
Nb_2O_5	2 eq. NaH	60	3.03
Nb_2O_5	2 eq. LiH	10	3.01
Nb_2O_5	2 eq. LiH	60	2.81

6 Testing of the photocatalytic activity

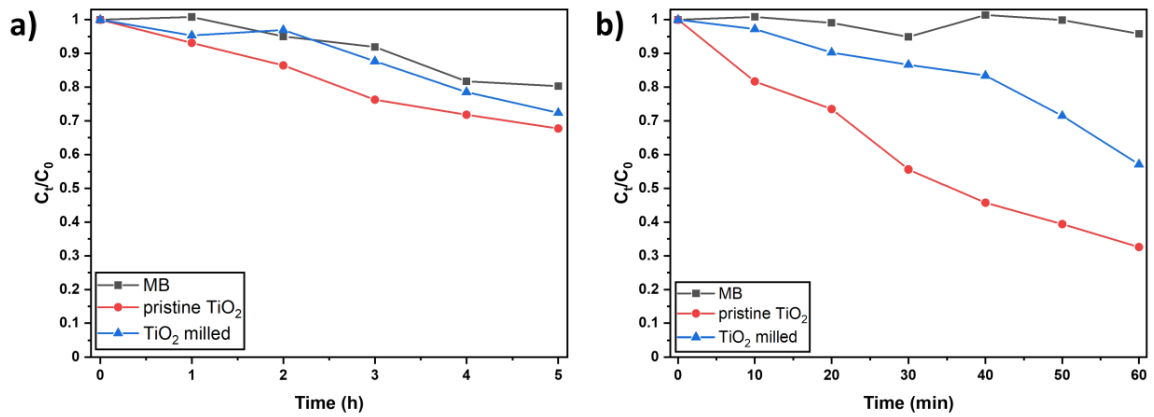

Figure S19: Photocatalytic degradation of MB without catalyst (black), with pristine TiO_2 (red) and ball-milled (300 rpm, 60 min) TiO_2 (blue) under (a) visible and (b) UV (365 nm) light.

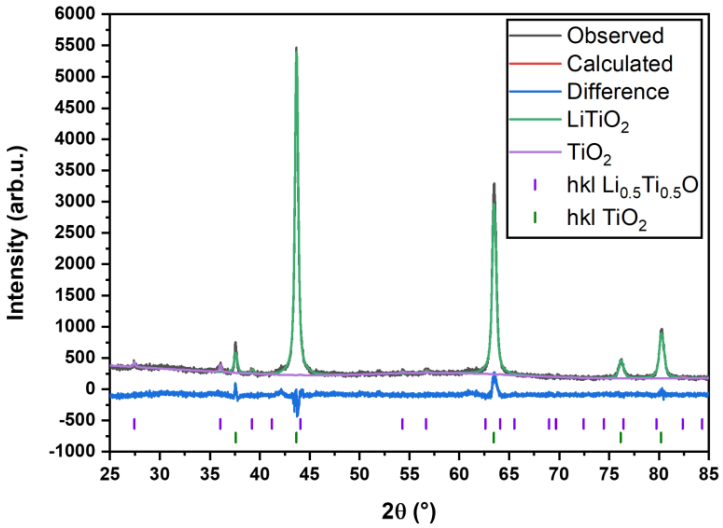

Figure S20: Rietveld refinement of $Li_{0.5}Ti_{0.5}O$ obtained via solid-state reaction of TiO_2 and LiH at 600 °C. Violet ticks indicate the Bragg positions of rutile type TiO_2 ($P4_2/mnm$) and green ones of $Li_{0.5}Ti_{0.5}O$ ($Fm\bar{3}m$).

7 References

[1] a) L. Balogh, G. Ribárik, T. Ungár, *J. Appl. Phys.* **2006**, *100*, 023512; b) Ö. Budak, M. Geißler, D. Becker, A. Kruth, A. Quade, R. Haberkorn, G. Kickelbick, B. J. M. Etzold, V. Presser, *ACS Appl. Energy Mater.* **2020**, *3*, 4275-4285.
[2] M. Catti, M. R. Ghaani, *Phys. Chem. Chem. Phys.* **2014**, *16*, 1385-1392.

6.2 Supporting Information – Highly Exothermic and Fast Mechanochemical Redox and Intercalation Reactions of V_2O_5 with Sodium Hydride

Supporting Information

Highly Exothermic and Fast Mechanochemical Redox and Intercalation Reactions of V_2O_5 with Sodium Hydride

Anna Michaely[1], Christopher Luckas[1], Robert Haberkorn[1], Guido Kickelbick[1,2]*

[1] Saarland University, Inorganic Solid-State Chemistry, Campus, Building C4.1, 66123 Saarbrücken, Germany

[2] Saarene - Saarland Center for Energy Materials and Sustainability, Campus C4 2, 66123 Saarbrücken, Germany

E-mail: guido.kickelbick@uni-saarland.de

Table of contents

1. Crystal chemistry of (sodium) vanadium oxides S1

2. Effect of ball milling on V_2O_5 ..... S7

3. Mechanochemical reaction with sodium hydride S8

3.1. Temperature-pressure course during ball milling S8

3.2. Stopping the reaction at maximum pressure S10

3.3. Performing the reaction in a mortar S11

3.4. Powder X-Ray diffraction analysis and Rietveld refinement S11

3.5. Testing of the reproducibility S20

3.6. Reoxidation of reduced samples S25

3.7. Rietveld refinement of the reaction with 6 eq. NaH S25

3.8. Quantum mechanical calculations using VASP S26

4. References S29

1. Crystal chemistry of (sodium) vanadium oxides

Vanadium oxides

Many stable and metastable vanadium oxides are known in literature. To facilitate the discussion of possible reaction pathways and why certain oxides are formed during ball milling, the crystal structure of the experimentally observed oxides is briefly discussed below.

Orthorhombic α-V_2O_5 crystallizes in the space group *Pmmn* with lattice parameters of $a = 357.1$ pm, $b = 1154.4$ pm, and $c = 438.3$ pm.[1] Each V^{5+} is coordinated by five oxygen anions forming VO_5 square pyramids. The structure consists of layers of alternating VO_5 square pyramids stacked along [001] held together by Van der Waals interactions (Figure S1a). In these layers, each square pyramid is connected to one neighboring pyramid via corner sharing and to two pyramids via edge sharing (Figure S1b).

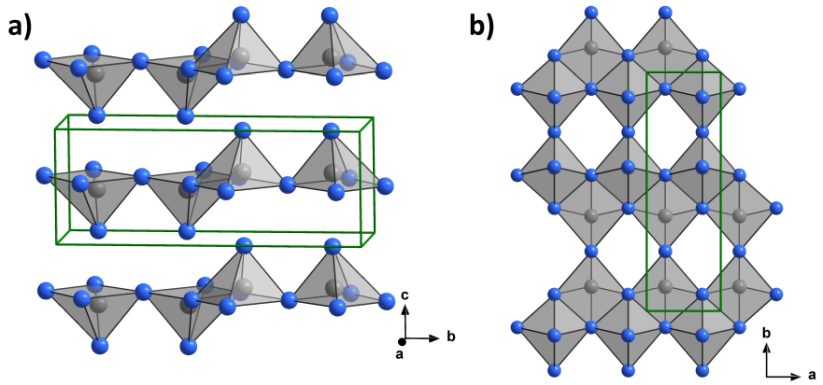

Figure S1: Crystal structure of α-V_2O_5 (*Pmmn*)[1] along (a) [100] and (b) [001]. Vanadium atoms are displayed in gray, oxygen atoms in blue and the unit cell edges in green.

Vanadium dioxide (VO_2) has a rich variety of polymorphs such as VO_2(B), VO_2(A), VO_2(M), VO_2(R), VO_2(D), and VO_2(P).[2] Experimentally, only the rutile-type high-temperature polymorph VO_2(R) was observed, which crystallizes in the tetragonal space group $P4_2/mnm$ with lattice parameters of $a = 455.61$ pm and $c = 285.98$ pm.[3] The V^{4+} cations are octahedrally surrounded by oxygen anions. Along [001] the VO_6 octahedra are linked by *cis*-edge sharing, while the other two corners are connected to adjacent strands (Figure S2).

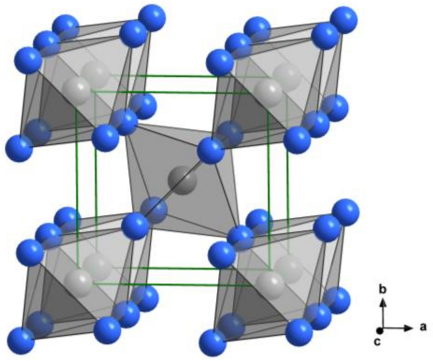

Figure S2: Crystal structure of rutile-type VO_2 ($P4_2/mnm$)[3] along [001]. Vanadium atoms are displayed in gray, oxygen atoms in blue and the unit cell edges in green.

In the Magnéli phase V_3O_5, vanadium is present in two oxidations states, namely +III and +IV. The high-temperature modification crystallizes in the monoclinic space group $C2/c$ with lattice parameters of $a = 999.6$ pm, $b = 5026.8$ pm, $c = 700.9$ pm and $\beta = 111.8°$.[4] As in VO_2, the vanadium cations are also octahedrally coordinated by oxygen anions. Two types of strands formed along [001] are found in the structure (Figure S3a). The first one consists of edge sharing double octahedra, which are each formed by two face sharing octahedra (Figure S3b, light blue octahedra). Meanwhile, the second strand is formed by corner sharing octahedra (Figure S3b, dark blue octahedra). The two types of strands are connected by both corner and edge sharing (Figure S3c).

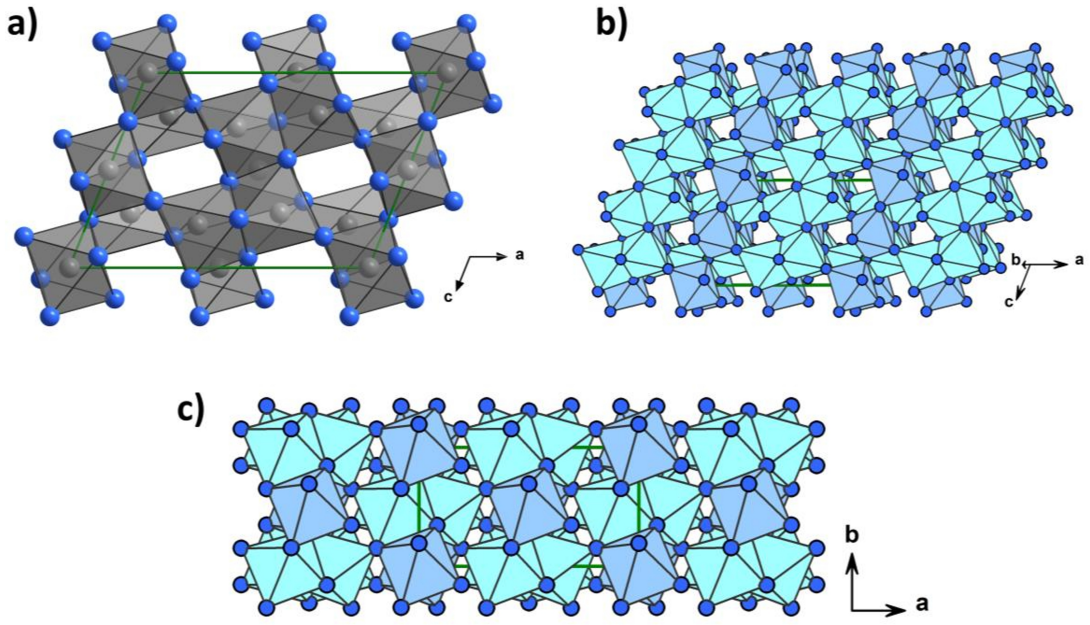

Figure S3: Crystal structure of V_3O_5 ($C2/c$)[4] along (a), (b) [010], and (c) [001]. Vanadium atoms are displayed in gray, oxygen atoms in blue and the unit cell edges in green. For better understanding, the double octahedra are marked in light blue in (b) and (c), while the corner sharing octahedra of the second type of strand are marked in darker blue.

Divanadium trioxide (V_2O_3) with vanadium in the oxidation state +III crystallizes in the rhombohedral space group R$\bar{3}c$ with the lattice parameters a = 490.2 pm and c = 1396.9 pm.[5] In the corundum-type structure, the oxygen anions are arranged in a distorted hexagonal close packing, while the V^{3+} cations sit in two-thirds of the octahedral sites. The VO_6 octahedra are connected via edge sharing and form hexagonal six-membered rings, which are stacked to *A'B'C'* layers along [001] (Figure S4).

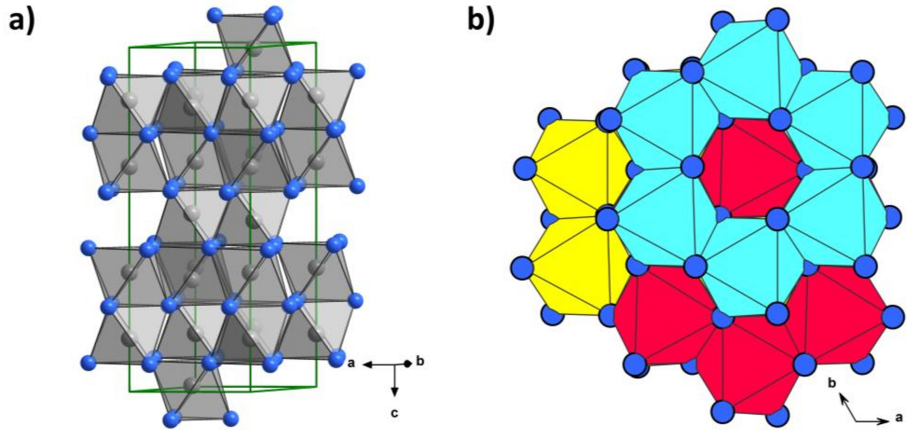

Figure S4: Crystal structure of V_2O_3 (R$\bar{3}c$)[5] along (a) [110], and (b) [001]. Vanadium atoms are displayed in gray, oxygen atoms in blue and the unit cell edges in green. For better understanding, the hexagonal *A'B'C'* layers along [001] are marked in blue, red and yellow (b).

Sodium vanadates

In addition to the wide range of literature known vanadium oxides, there are also numerous known ternary sodium vanadium oxides differing in the amount of sodium and the oxidation state of vanadium. The crystal structure of the experimentally observed sodium vanadates is described below.

For sodium metavanadate ($NaVO_3$) with vanadium in the oxidation state +V, the two modifications α-$NaVO_3$ and β-$NaVO_3$ are known. While β-$NaVO_3$ crystallizes in the orthorhombic space group *Pnma* with the lattice parameters a = 1414.7 pm, b = 365.0 pm and c = 536.4 pm,[6] α-$NaVO_3$ undergoes a ferroelectric - paraelectric transition at 380 °C with a change of the space group from *Cc* to *C*2/*c*.[7] However, the structural changes during the transition of α-$NaVO_3$ are only minor and both space group can be used to satisfactorily refine their PXRD pattern.[8] We opted to use the paraelectric phase in the space group *C*2/*c* with lattice parameters of a = 1055.2 pm, b = 946.8 pm, c = 587.9 pm, and β = 108.47°.[9] In α-$NaVO_3$, the vanadium atoms are tetrahedrally surrounded by oxygen anions. These tetrahedra are linked by

corner sharing and form infinite chains along [001]. The chains are stacked along [100] with the sodium ions being located in between those layers (Figure S5a). Similarly, orthorhombic β-$NaVO_3$ is also a layered compound. Each vanadium is surrounded by five oxygen anions in a square pyramidal manner. Along [010], these square pyramids share two edges with adjacent polyhedral, forming zigzag chains. The layers of VO_5 square pyramids are stacked along [100] with the sodium ions in between (Figure S5b).

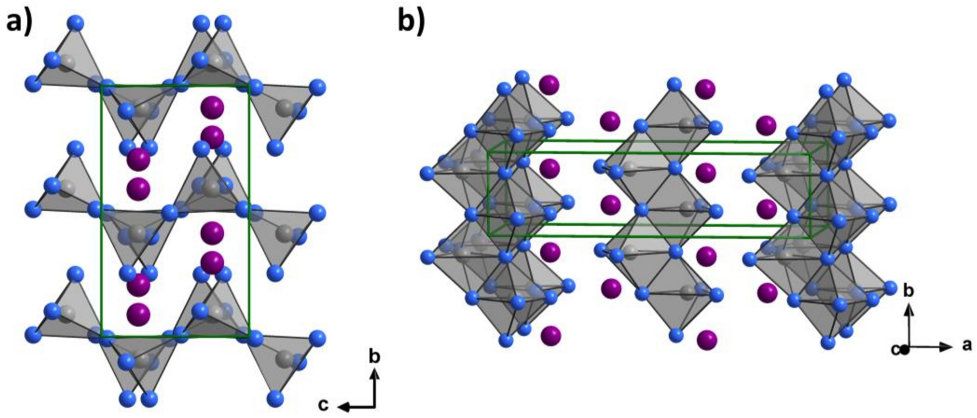

Figure S5: Crystal structure of (a) α-$NaVO_3$ ($C2/c$)[9] along [100] and (b) β-$NaVO_3$ ($Pnma$)[6] along [001]. Vanadium atoms are displayed in gray, oxygen atoms in blue, sodium atoms in purple and the unit cell edges in green.

Sodium pyrovanadate ($Na_4V_2O_7$) with vanadium in the oxidation state +V crystallizes in the monoclinic space group $C2/c$ with lattice parameters of a = 1537.6 pm, b = 575.7 pm, c = 3256.4 pm, and β = 95.08°.[10] The structure consists of isolated $V_2O_7^{4-}$ anions formed by two corner sharing tetrahedra with sodium atoms being in between the $V_2O_7^{4-}$ units (Figure S6).

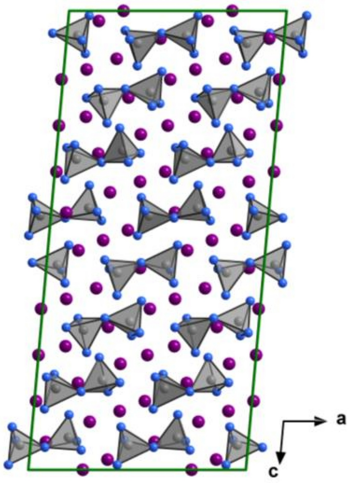

Figure S6: Crystal structure of $Na_4V_2O_7$ ($C2/c$)[10] along [010]. Vanadium atoms are displayed in gray, oxygen atoms in blue, sodium atoms in purple and the unit cell edges in green.

Three different modifications of sodium orthovanadate (Na_3VO_4) with vanadium in the oxidation state +V have been observed experimentally, all consisting of isolated VO_4 tetrahedra, forming different stacking sequences. In each layer, the vanadium and sodium atoms are on the same plane/level, differing only in their ratio to each other.

α-Na_3VO_4 crystallizes in the orthorhombic space group $Pmn2_1$ with lattice parameters of a = 708.8 pm, b = 610.9 pm, and c = 555.6 pm.[11] The VO_4 tetrahedra are stacked in an *ABA* stacking sequence along [001] in which the tetrahedra all point in the same direction (Figure S7a). All the layers are occupied by $^3/_4$ sodium ions and $^1/_4$ vanadium atoms, giving an overall ratio of sodium to vanadium of 3:1.

High temperature γ-Na_3VO_4 crystallizes in the cubic space group $P2_13$ with a lattice parameter of a = 762.0 pm.[12] In γ-Na_3VO_4, the structure consists of an *ABCBA* stacking sequence with a sodium to vanadium ratio of 1:1 in the *A* and *C* layers and a ratio of 4:0 in the *B* layer. The tetrahedra point in alternating directions both within and in between layers (Figure S7b).

At 450 °C, γ-Na_3VO_4 can be reversibly transformed into the low temperature form β-Na_3VO_4 crystallizing in the orthorhombic space group *Pnma* with lattice parameters of a = 1210.0 pm, b = 704.0 pm, and c = 557.0 pm.[12] The sodium to vanadium ratio in each layer is 3:1. The layers stack along [001] and the tetrahedra point in opposite directions within the layer (Figure S7c).

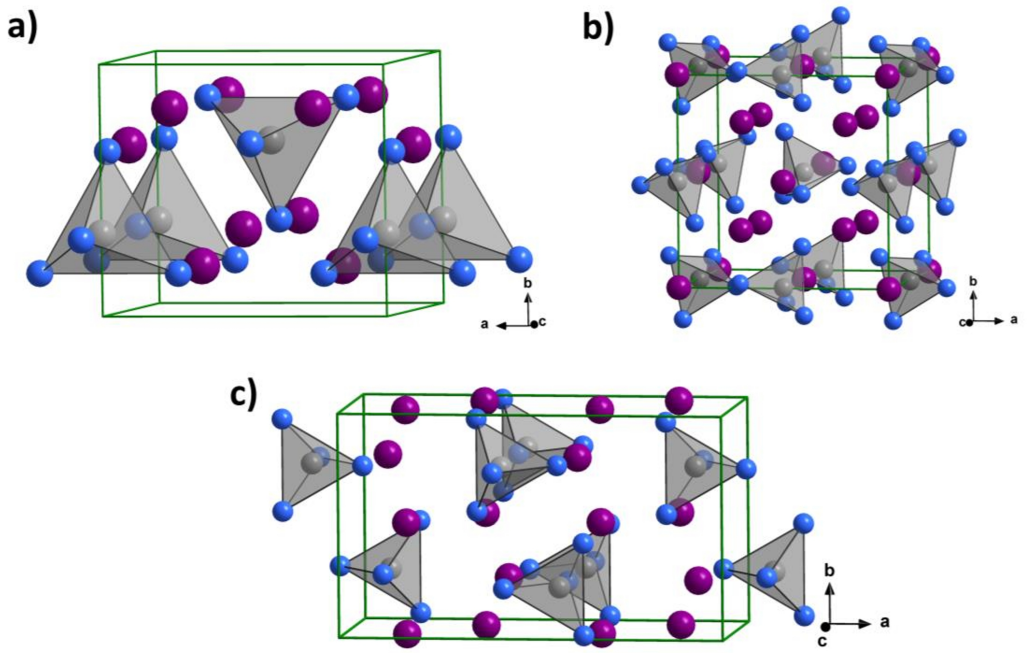

Figure S7: Crystal structure of (a) α-Na_3VO_4 ($Pmn2_1$),[11] (b) γ-Na_3VO_4 ($P2_13$),[12] and (c) β-Na_3VO_4 (*Pnma*)[12] along [100]. Vanadium atoms are displayed in gray, oxygen atoms in blue, sodium atoms in purple and the unit cell edges in green.

The crystal structure of α-NaV_2O_5 (*Pmmn*, a = 361.0 pm, b = 1131.1 pm, and c = 480.0 pm)[13] is similar to the host-structure of orthorhombic α-V_2O_5 (vide supra). The sodium cations are located between the vanadium oxygen layers, which are slightly distorted compared to α-V_2O_5 (Figure S8).

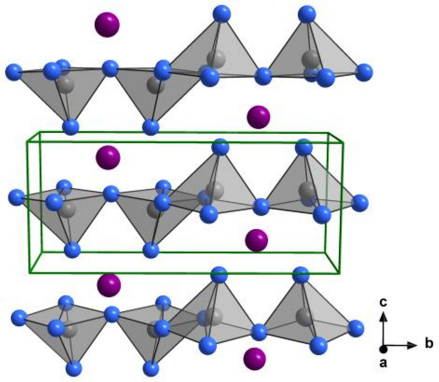

Figure S8: Crystal structure of α-NaV_2O_5 (*Pmmn*)[13] along [100]. Vanadium atoms are displayed in gray, oxygen atoms in blue, sodium atoms in purple and the unit cell edges in green.

NaV_2O_4 crystallizes in the monoclinic space group *C*2/*c* with lattice parameters of a = 1329.9 pm, b = 571.0 pm, c = 497.1 pm, and β = 120.8°.[14] It can also be expressed as O'3-$Na_{0.5}VO_2$ and has a similar layered structure as rhombohedral $NaVO_2$ (vide infra). During electrochemical desodiation of O3-$NaVO_2$ and formation of O'3-$Na_{0.5}VO_2$ a reduction of symmetric from rhombohedral R$\bar{3}$*m* to monoclinic *C*2/*c* takes place.[14, 15] During the symmetry reduction the octahedral surrounding of sodium and the layers of edge-sharing VO_6 octahedra ($(VO_2)_n$) with sodium in between the layers are retained (Figure S9). Compared to $NaVO_2$, the VO_6 octahedra in the $(VO_2)_n$ layers are slightly distorted and tilted in NaV_2O_4.

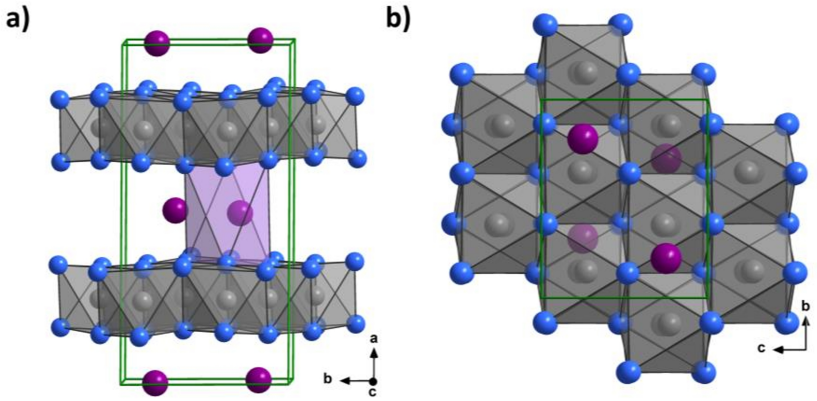

Figure S9: Crystal structure of NaV_2O_4 (*C*2/*c*)[14] along (a) [110], and (b) [001]. Vanadium atoms are displayed in gray, oxygen atoms in blue, sodium atoms in purple and the unit cell edges in green.

$NaVO_2$ crystallizes in a trigonal crystal system with the space group $R\bar{3}m$ with lattice parameters of a = 299.5 pm and c = 1629.0 pm.[16] Both sodium and vanadium, which is in the oxidation state +III are octahedrally surrounded by oxygen anions. The edge sharing octahedra form hexagonal layers in the *ab*-plane and are stacked along [001] with sodium ions being in between the layers (Figure S10).

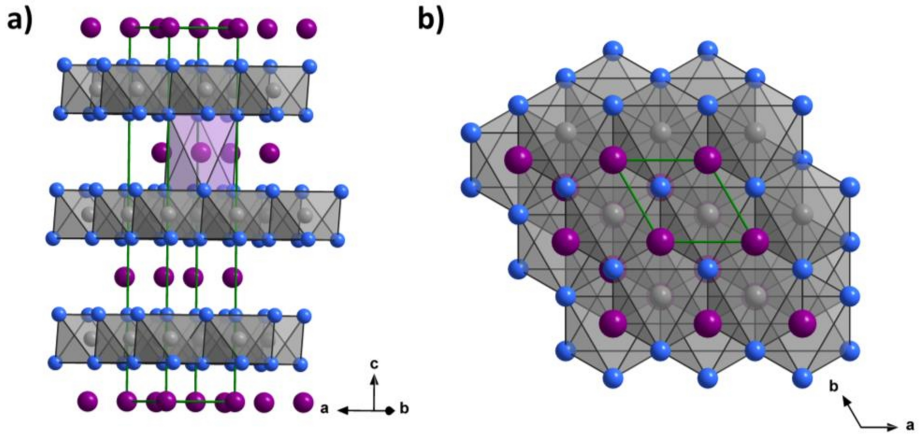

Figure S10: Crystal structure of $NaVO_2$ ($R\bar{3}m$)[16] along (a) [110], and (b) [001]. Vanadium atoms are displayed in gray, oxygen atoms in blue, sodium atoms in purple and the unit cell edges in green.

2. Effect of ball milling on V_2O_5

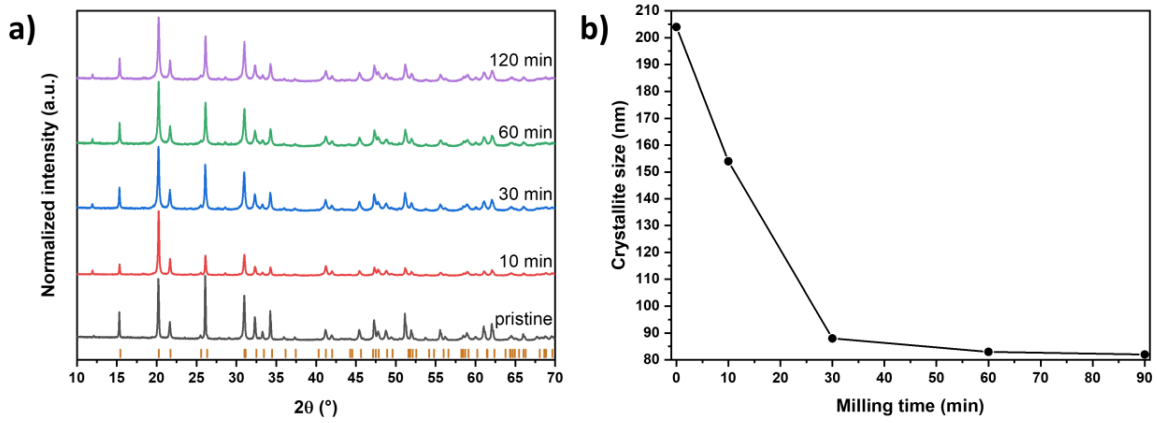

Figure S11: (a) PXRD patterns of pristine V_2O_5 (black) and V_2O_5 milled at 300 rpm for 10 (red), 30 (blue), 60 (green), and 90 min (purple). Ochre ticks indicate the Bragg positions of V_2O_5 (*Pmmn*). (b) Evolution of the crystallite during milling as obtained by Rietveld refinement.

3. Mechanochemical reaction with sodium hydride

3.1. Temperature-pressure course during ball milling

To avoid damage of the milling jar due to excessive pressure, the total mass of the reactants was decreased from 3.0 g to 2.4690 and 2.3163 g for 3 and 4 eq. of NaH, respectively. For all tested V_2O_5 to NaH ratios, a steep, sudden increase in pressure was observed between ~30 s and 5 min of milling, followed by a rapid decrease to a constant pressure value ranging from 4.34 in the case of 1 eq. NaH to 9.11 bar in the case of 4 eq. NaH (Figure S12). As stated in the experimental section, the mass of NaH was limited to 0.6 g and 0.8 g for 3 and 4 eq. NaH, respectively, to avoid damage of the milling material. Since 0.6264 g NaH were used for the reactions with 2 eq. NaH, similar amounts of hydrogen were formed, and similar steady state pressures are observable.

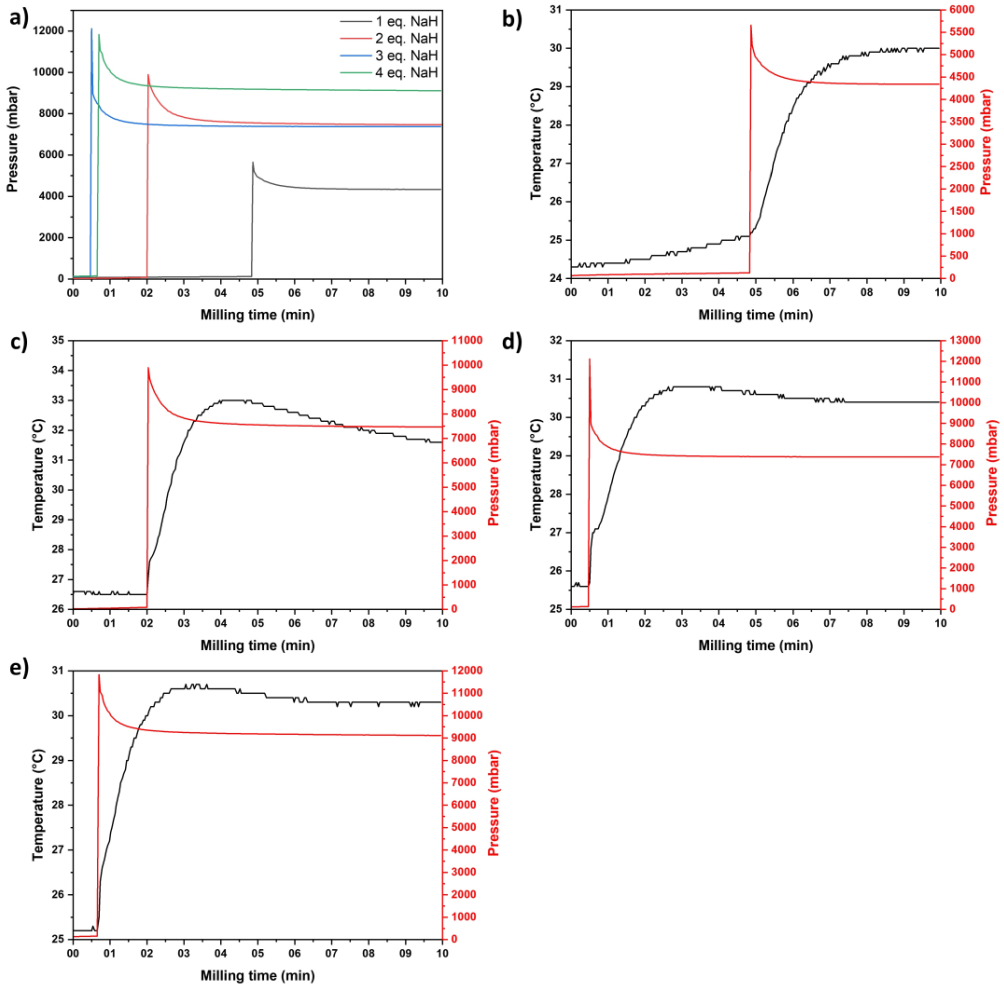

Figure S12: (a) Recorded pressure curve for the reaction of V_2O_5 with 1 (black), 2 (red), 3 (blue), and 4 eq. (green) NaH. The milling time was set to 10 min and the milling speed to 300 rpm. Corresponding recorded pressure-temperature curves for the reaction of V_2O_5 with (b) 1, (c) 2, (d) 3, and (e) 4 eq. sodium hydride. Note the different scales on the y-axes.

Based on the volume of the milling jar (45 mL), the volume of the milling balls (90 balls with a diameter of 5 mm), and the volume of the reactants (calculated based on their respective mass and density), the volume of the gas space in the milling jar can be calculated. Using this calculated volume, the initial temperature inside the milling jar and the ideal gas law, the theoretically achievable final pressure ($p_{expected}$) that would occur if all hydride ions (depends on the mass of used sodium hydride) were converted to hydrogen can be calculated (Table S1). Compared to the theoretical pressure, the experimentally observed pressure (p_{final}) inside the jar after 10 min of milling is lower, especially for large hydride concentrations. This is most likely caused by non-tightness of the milling jar. Especially at high NaH concentrations, the lid of the milling jar shows signs of some gas escaping due to the rapid increase in pressure.

Table S1: Overview of the initial and final temperature inside the milling jar after milling V_2O_5 with different hydride concentrations for 10 min of minutes, as well as the expected pressure if all initial NaH is transformed in H_2. The initial temperature inside the milling jar was used to calculate the expected pressure. The final temperature inside the milling jar (T_{final}) was taken after 10 min of milling.

eq. NaH	T_{inital} (°C)	$p_{initial}$ (bar)	T_{final} (°C)	p_{final} (bar)	$p_{expected}$ (bar)
1	24.3	0.07	30	4.34	4.73
1.5	23.3	0.13	32.5	6.12	6.69
2	23.4	0.12	29.3	7.93	8.48
2.4	24.1	0.07	29.8	8.77	9.80
3	24.9	0.08	31.9	7.38	8.10
4	25.2	0.14	30.3	9.11	10.85

3.2.Stopping the reaction at maximum pressure

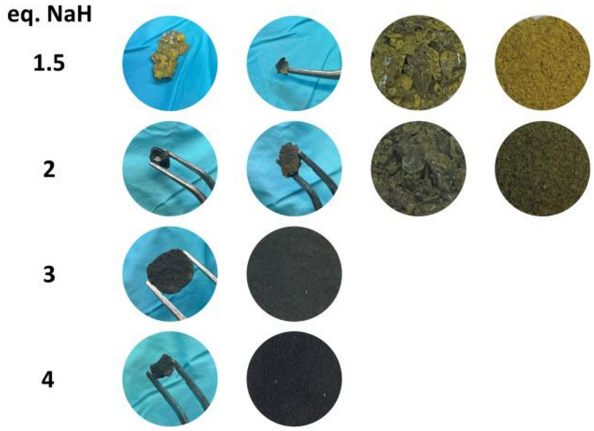

Figure S13: Photographs of the (inhomogeneous) samples obtained, when the mechanochemical reaction of V_2O_5 with 1.5 to 4 eq. NaH is stopped at the maximum pressure.

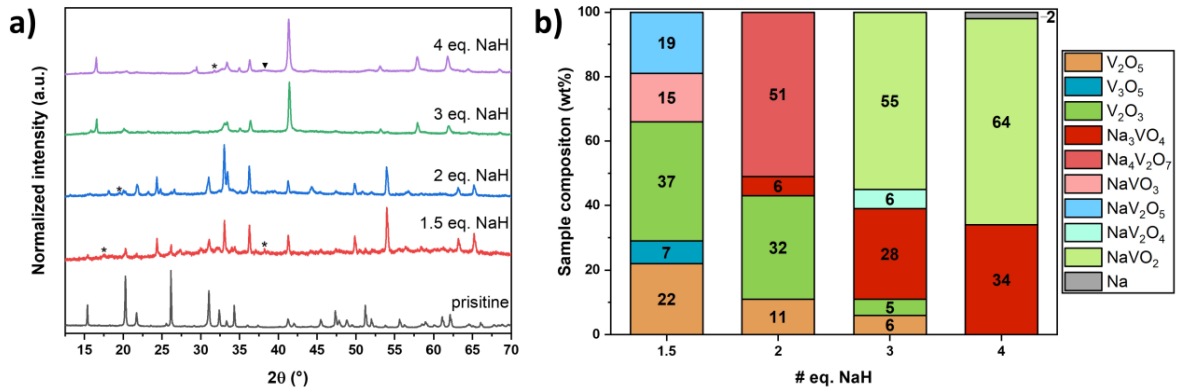

Figure S14: (a) PXRD patterns of pristine V_2O_5 (black) and V_2O_5 milled with 1.5 (red), 2 (blue), 3 (green), and 4 eq. NaH (purple) until the maximum pressure was reached. Unidentified reflections are marked with asterisks and NaOH with a triangle. (b) Corresponding sample composition of the whole sample obtained at maximum pressure for sodium concentrations between 1.5 and 4 eq. sodium hydride. NaOH was not taken into account in the case of 4 eq. NaH since it was formed during the acquisition of the diffractogram (vide infra).

3.3. Performing the reaction in a mortar

After grinding V_2O_5 with 4 eq. NaH in a mortar, a sample composition of 29% V_2O_5, 4% V_2O_3, 21% Na_3VO_4, 24% $NaVO_2$, 21% NaH, and 1% Na was obtained from Rietveld refinement.

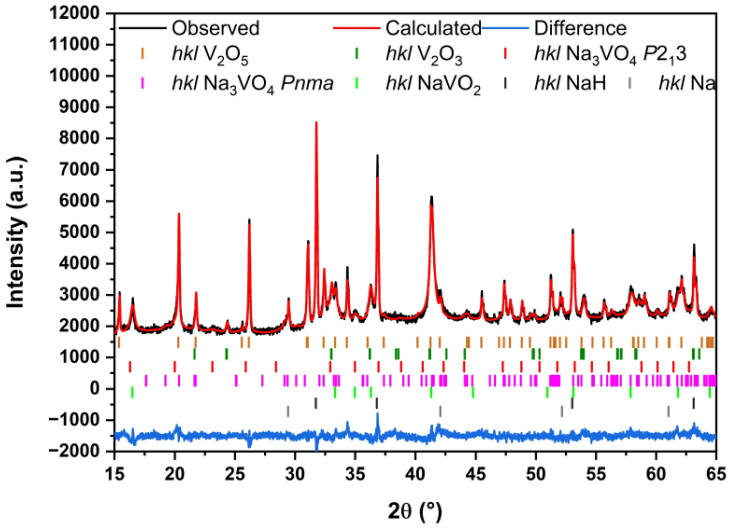

Figure S15: PXRD pattern (black) and Rietveld refinement (red) of the sample obtained after grinding V_2O_5 with 4 eq. NaH in a mortar until a reaction occurred. Ochre ticks indicate the Bragg positions of V_2O_5 (*Pmmn*), olive ones of V_2O_3 ($R\bar{3}c$), red ones of Na_3VO_4 ($P2_13$), lavender ones of Na_3VO_4 (*Pnma*), light green ones of $NaVO_2$ ($R\bar{3}m$), black ones of NaH ($Fm\bar{3}m$), and gray ones of Na ($Im\bar{3}m$).

3.4. Powder X-Ray diffraction analysis and Rietveld refinement

The following figures show the powder diffractograms for all samples prepared with NaH. While the PXRD patterns change significantly as a function of the sodium hydride concentration, they vary only little with the milling time (Figure S16a - Figure S21a). Therefore, the Rietveld refinement is exemplarily shown for all samples milled for 10 min. Overall, the refined diffractograms are in good agreement with the experimental ones, and only a few small reflections could not be assigned to any literature-known phase (Figure S16b - Figure S21b). Since the unidentified reflections occur at a different value of 2θ for the different reactant ratios tested, it can be concluded that different unknown phases are formed depending on the hydride concentration. Due to their low intensity, the refined sample composition should not be affected significantly and general trends for the mechanochemical reaction can still be derived. The sample compositions as obtained by Rietveld refinement and the corresponding fit quality parameters *weighted profile R-factors* (R_{wp}) and *goodness of fit* (GOF) are given in Table S2-Table S7.

1 eq. NaH

Table S2: Overview of the sample composition in weight percent as obtained by Rietveld refinement and the resulting composition formula of the crystalline sample (CFS) of samples prepared with 1 eq. NaH between 10 and 120 min of milling. The fit quality parameters *weighted profile R-factors* (R_{wp}) and *goodness of fit* (GOF) of the corresponding Rietveld refinements are also given.

Milling time (min)	V_2O_5 (*Pmmn*)	VO_2 ($P4_2/mnm$)	$NaVO_3$ ($C2/c$)	NaV_2O_5 (*Pmmn*)	CFS	R_{wp}	GOF
10	11	10	13	66	$Na_{0.87}V_2O_{4.32}$	3.22	1.45
30	5	12	10	73	$Na_{0.89}V_2O_{4.2}$	3.41	1.53
60	4	13	8	75	$Na_{0.87}V_2O_{4.17}$	3.27	1.42
120	3	14	8	75	$Na_{0.86}V_2O_{4.15}$	2.31	1.27

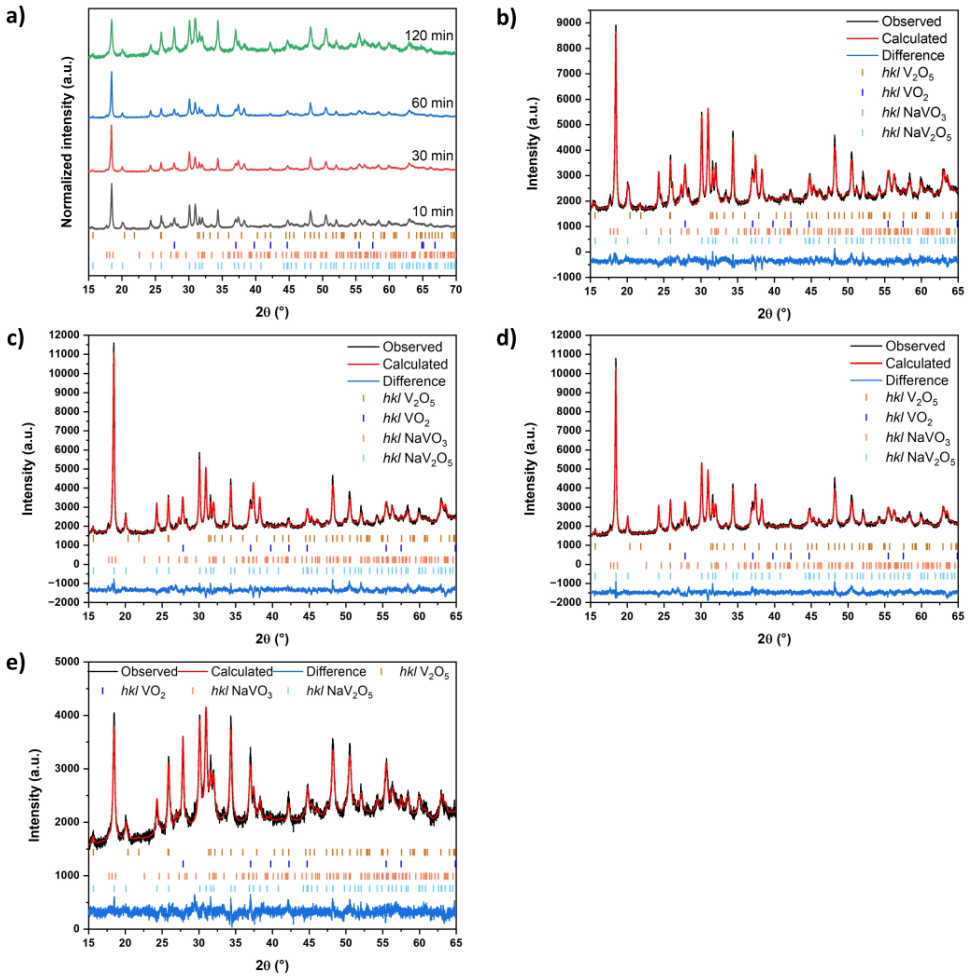

Figure S16: (a) PXRD patterns of V_2O_5 milled with 1 eq. NaH for 10 (black), 30 (red), 60 (blue), and 120 min (green) at 300 rpm. Corresponding Rietveld refinement after milling for (b) 10 min, (c) 30 min, (d) 60 min, and (e) 120 min. Ochre ticks indicate the Bragg positions of V_2O_5 (*Pmmn*), blue ones of VO_2 ($P4_2/mnm$), coral ones of $NaVO_3$ ($C2/c$), and cerulean ones of NaV_2O_5 (*Pmmn*).

1.5 eq. NaH

Table S3: Overview of the sample composition in weight percent as obtained by Rietveld refinement and the resulting composition formula of the crystalline sample (CFS) of samples prepared with 1.5 eq. NaH between 10 and 120 min of milling. The fit quality parameters *weighted profile R-factors* (R_{wp}) and *goodness of fit* (GOF) of the corresponding Rietveld refinements are also given. Standard deviations for the refined weight percentages are typically ±1 %.

Milling time (min)	V_2O_5 (*Pmmn*)	V_3O_5 (*C*2/*c*)	V_2O_3 ($R\bar{3}c$)	$NaVO_3$ (*C*2/*c*)	NaV_2O_5 (*Pmmn*)	CFS	R_{wp}	GOF
10	16	3	38	27	16	$Na_{0.50}V_2O_{4.21}$	2.94	1.31
30	17	2	38	28	15	$Na_{0.50}V_2O_{4.24}$	3.32	1.32
60	10	3	61	13	13	$Na_{0.27}V_2O_{3.07}$	3.33	1.44
120	7	9	63	-	21	$Na_{0.20}V_2O_{3.59}$	2.86	1.33

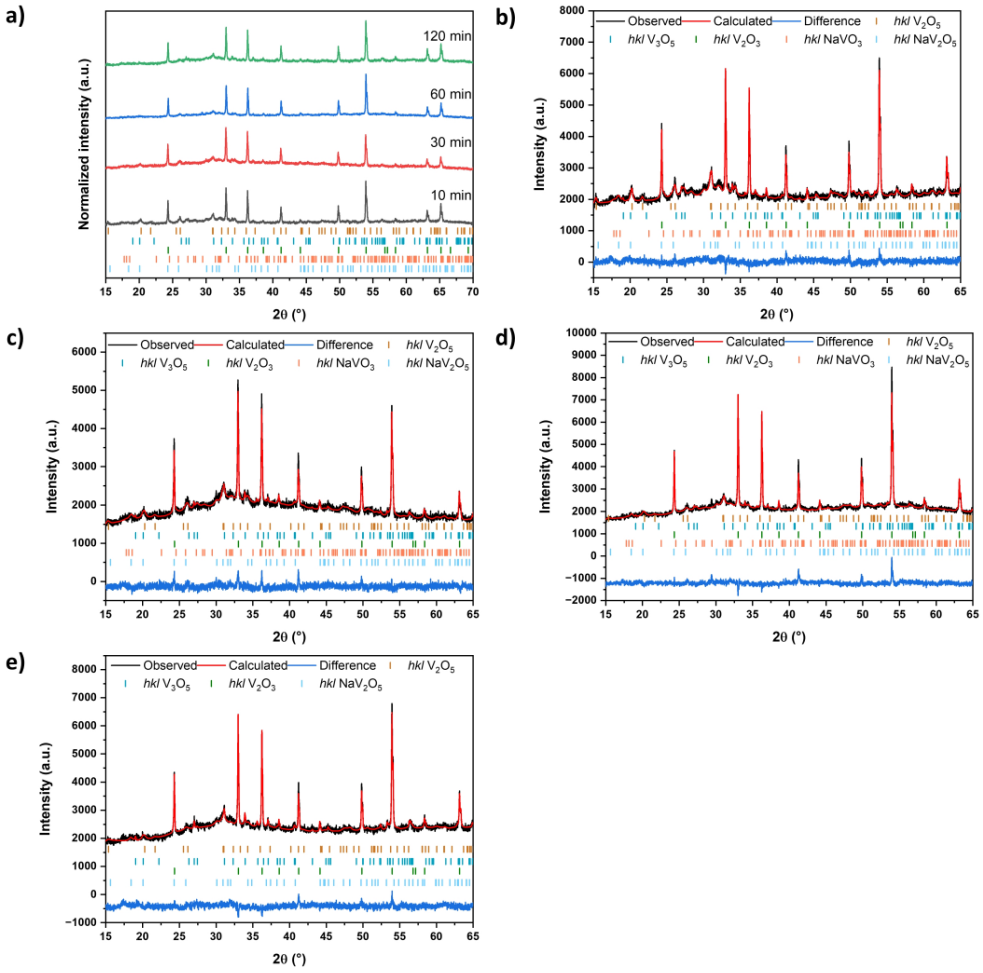

Figure S17: (a) PXRD patterns of V_2O_5 milled with 1.5 eq. NaH for 10 (black), 30 (red), 60 (blue), and 120 min (green) at 300 rpm. Corresponding Rietveld refinement after milling for (b) 10 min, (c) 30 min, (d) 60 min, and (e) 120 min. Ochre ticks indicate the Bragg positions of V_2O_5 (*Pmmn*), turquoise ones of V_3O_5 (*C*2/*c*), olive ones of V_2O_3 ($R\bar{3}c$), coral ones of $NaVO_3$ (*C*2/*c*), and cerulean ones of NaV_2O_5 (*Pmmn*).

2 eq. NaH

Table S4: Overview of the sample composition in weight percent as obtained by Rietveld refinement and the resulting composition formula of the crystalline sample (CFS) of samples prepared with 2 eq. NaH between 10 and 120 min of milling. The fit quality parameters *weighted profile R-factors* (R_{wp}) and *goodness of fit* (GOF) of the corresponding Rietveld refinements are also given.

Milling time (min)	V_2O_5 (*Pmmn*)	V_2O_3 ($R\bar{3}c$)	$Na_4V_2O_7$ (*C*2/*c*)	Na_3VO_4 ($P2_13$)	CFS	R_{wp}	GOF
10	10	39	49	2	$Na_{1.40}V_2O_{4.62}$	3.13	1.79
30	6	49	45	-	$Na_{1.61}V_2O_{4.29}$	2.94	1.41
60	12	50	38	-	$Na_{0.95}V_2O_{4.20}$	3.06	1.75
120	10	56	34	-	$Na_{0.82}V_2O_{4.03}$	2.8	1.64

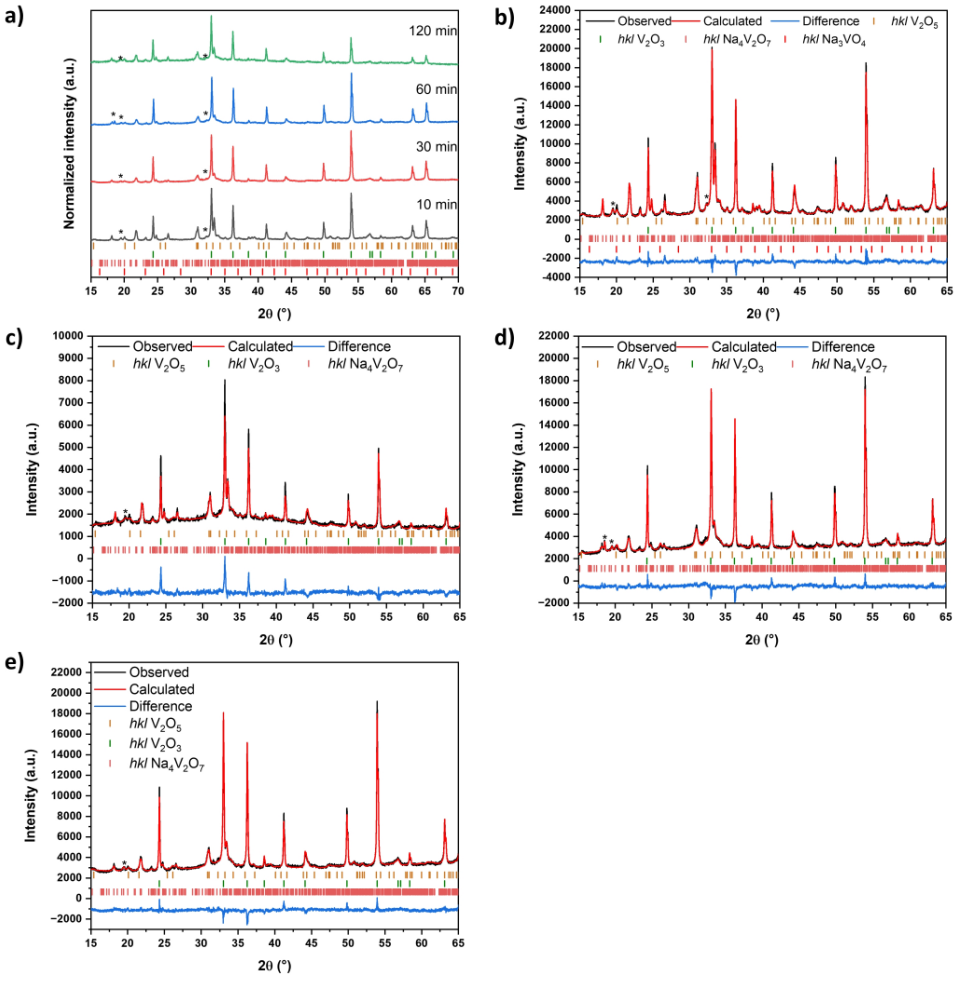

Figure S18: (a) PXRD patterns of V_2O_5 milled with 2 eq. NaH for 10 (black), 30 (red), 60 (blue), and 120 min (green) at 300 rpm. Corresponding Rietveld refinement after milling for (b) 10 min, (c) 30 min, (d) 60 min, and (e) 120 min. Ochre ticks indicate the Bragg positions of V_2O_5 (*Pmmn*), olive ones of V_2O_3 ($R\bar{3}c$), roman ones of $Na_4V_2O_7$ (*C*2/*c*), and red ones of Na_3VO_4 ($P2_13$). Unknown reflections are marked with asterisks and were refined using single peaks during the Rietveld refinement.

2.5 eq. NaH

Table S5: Overview of the sample composition in weight percent as obtained by Rietveld refinement and the resulting composition formula of the crystalline sample (CFS) of samples prepared with 2.5 eq. NaH between 10 and 120 min of milling. The fit quality parameters *weighted profile R-factors* (R_{wp}) and *goodness of fit* (GOF) of the corresponding Rietveld refinements are also given.

Milling time (min)	V_2O_3 ($R\bar{3}c$)	$Na_4V_2O_7$ ($C2/c$)	Na_3VO_4 ($P2_13$)	NaV_2O_4 ($C2/c$)	$NaVO_2$ ($R\bar{3}m$)	*CFS*	R_{wp}	GOF
10	28	18	11	20	23	$Na_{1.51}V_2O_{4.22}$	3.49	1.73
30	22	18	9	26	25	$Na_{1.56}V_2O_{4.26}$	3.24	1.50
60	19	14	4	22	41	$Na_{1.52}V_2O_{4.11}$	3.36	1.51
120	18	9	2	12	59	$Na_{1.55}V_2O_{3.98}$	2.88	1.34

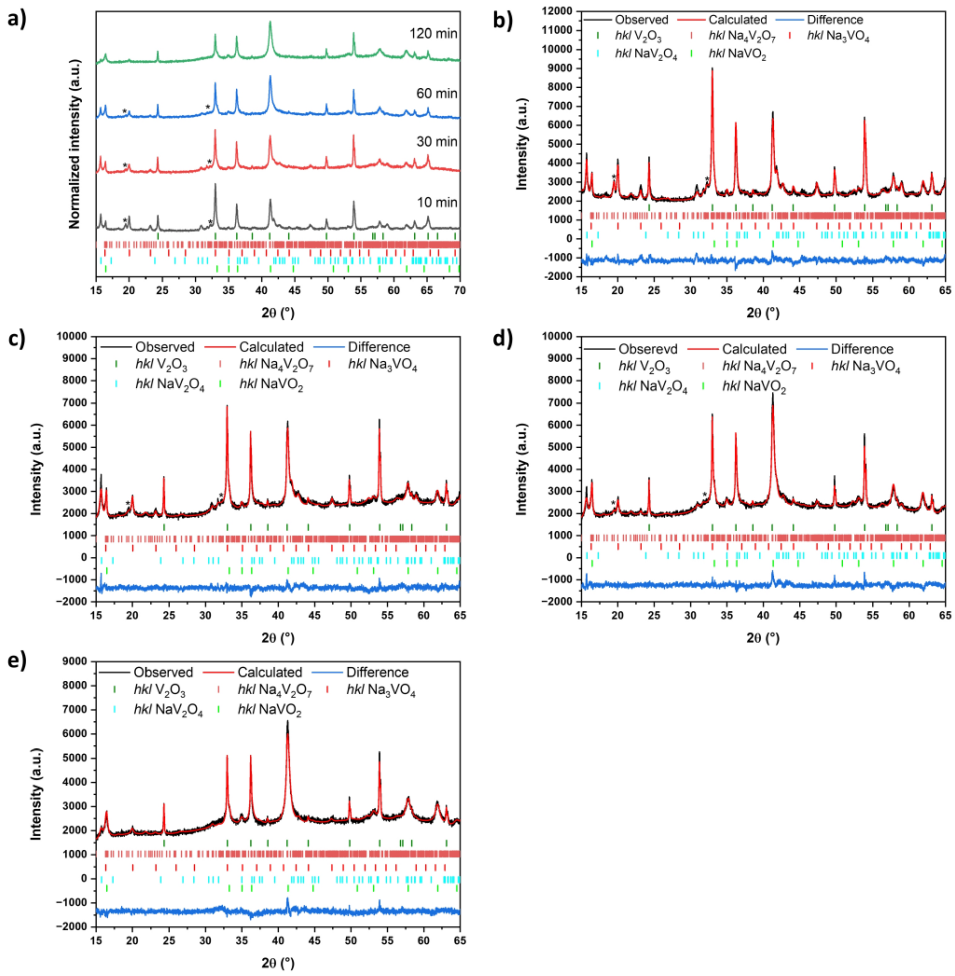

Figure S19: (a) PXRD patterns of V_2O_5 milled with 2.5 eq. NaH for 10 (black), 30 (red), 60 (blue), and 120 min (green) at 300 rpm. Corresponding Rietveld refinement after milling for (b) 10 min, (c) 30 min, (d) 60 min, and (e) 120 min. Olive ticks indicate the Bragg positions of V_2O_3 ($R\bar{3}c$), roman ones of $Na_4V_2O_7$ ($C2/c$), red ones of Na_3VO_4 ($P2_13$), cyan ones of NaV_2O_4 ($C2/c$), and light green ones of $NaVO_2$ ($R\bar{3}m$). Unknown reflections are marked with asterisks and were refined using single peaks.

3 eq. NaH

Table S6: Overview of the sample composition in weight percent as obtained by Rietveld refinement and the resulting composition formula of the crystalline sample (CFS) of samples prepared with 3 eq. NaH between 10 and 120 min of milling. The fit quality parameters *weighted profile R-factors* (R_{wp}) and *goodness of fit* (GOF) of the corresponding Rietveld refinements are also given.

Milling time (min)	V_2O_3 ($R\bar{3}c$)	Na_3VO_4 ($P2_13$)	Na_3VO_4 ($Pmn2_1$)	NaV_2O_4 ($C2/c$)	$NaVO_2$ ($R\bar{3}m$)	CFS	R_{wp}	GOF
10	7	16	13	9	55	$Na_{2.40}V_2O_{4.62}$	3.82	1.68
30	6	16	9	7	62	$Na_{2.35}V_2O_{4.53}$	3.91	1.79
60	5	17	10	5	63	$Na_{2.47}V_2O_{4.61}$	3.88	1.66
120	2	13	9	3	73	$Na_{2.45}V_2O_{4.52}$	3.07	1.41

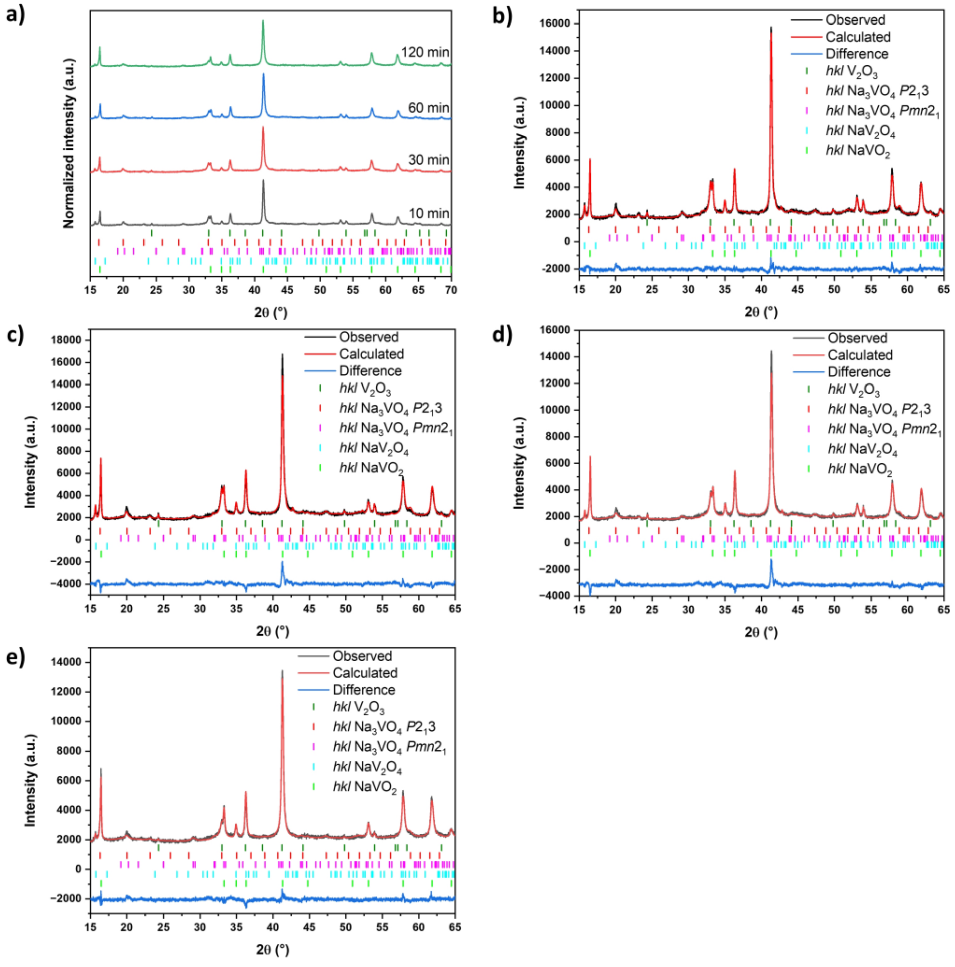

Figure S20: (a) PXRD patterns of V_2O_5 milled with 3 eq. NaH for 10 (black), 30 (red), 60 (blue), and 120 min (green) at 300 rpm. Corresponding Rietveld refinement after milling for (b) 10 min, (c) 30 min, (d) 60 min, and (e) 120 min. Olive ticks indicate the Bragg positions of V_2O_3 ($R\bar{3}c$), red ones of Na_3VO_4 ($P2_13$), magenta ones of Na_3VO_4 ($Pmn2_1$), cyan ones of NaV_2O_4 ($C2/c$), and light green ones of $NaVO_2$ ($R\bar{3}m$).

4 eq. NaH

In the case of 4 eq. NaH, two broad reflections at around 38 and 54° 2θ were attributed to NaOH. However, the formation of NaOH during the ball milling process could only be explained if water was formed during milling, which could then react with Na_2O or NaH to NaOH. Since this scenario is unlikely, NaOH is most likely formed during the PXRD measurement because the dome sample holder is not completely airtight. A PXRD measurement in the range of 35 to 45° 2θ with a step size of 0.013° in 4 min (instead of 7 to 120° 2θ in 2 h) on a sample fresh from the glovebox confirms the previous hypothesis. No reflection was detectable at 38° 2θ when the measuring time was reduced to 4 min, suggesting that NaOH is indeed not formed during ball milling, but by further reactions of possibly unreacted NaH, Na_2O or elemental sodium with moisture from the air during PXRD analysis.

Since NaOH is not formed during the ball milling process itself, NaOH was not included in the determination of the sample composition by Rietveld refinement. For this purpose, two single peaks were used to refine the two reflections at around 38 and 54° 2θ corresponding to NaOH, which are marked with asterisks in Figure S21.

Table S7: Overview of the sample composition in weight percent as obtained by Rietveld refinement and the resulting composition formula of the crystalline sample (CFS) of samples prepared with 4 eq. NaH between 10 and 120 min of milling. The fit quality parameters *weighted profile R-factors* (R_{wp}) and *goodness of fit* (GOF) of the corresponding Rietveld refinements are also given.

Milling time (min)	Na_3VO_4 ($P2_13$)	Na_3VO_4 (*Pnma*)	$NaVO_2$ ($R\bar{3}m$)	CFS	R_{wp}	GOF
10	19	20	61	$Na_{3.08}V_2O_{5.08}$	3.64	2.08
30	19	17	64	$Na_{2.62}V_2O_{4.62}$	3.24	1.77
60	11	18	71	$Na_{2.76}V_2O_{4.76}$	3.33	1.95
120	18	16	66	$Na_{2.92}V_2O_{4.92}$	3.30	1.89

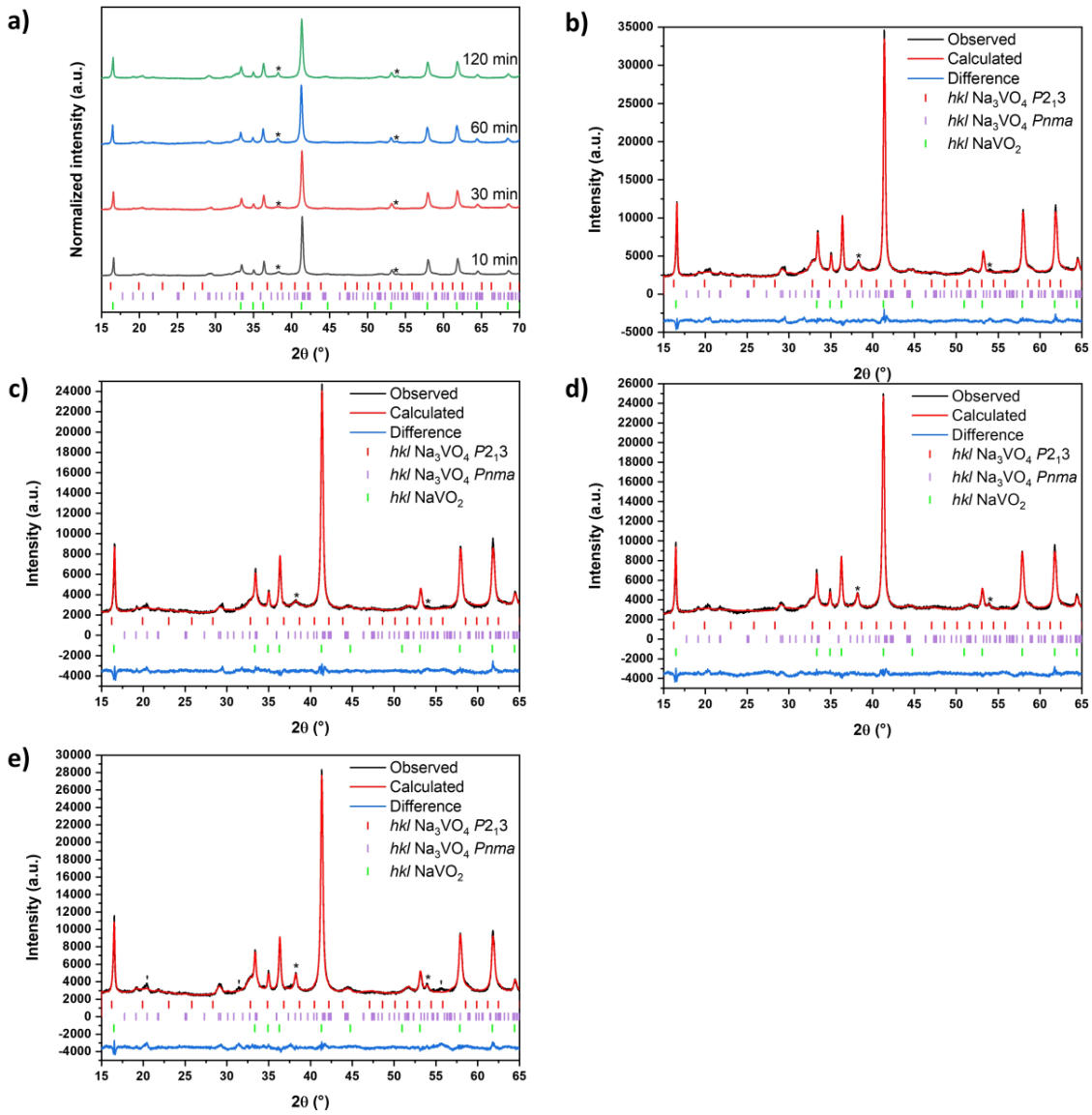

Figure S21: (a) PXRD patterns of V_2O_5 milled with 4 eq. NaH for 10 (black), 30 (red), 60 (blue), and 120 min (green) at 300 rpm. Corresponding Rietveld refinement after milling for (b) 10 min, (c) 30 min, (d) 60 min, and (e) 120 min. Red ticks indicate the Bragg positions of Na_3VO_4 ($P2_13$), lavender ones of Na_3VO_4 (*Pnma*), and light green ones of $NaVO_2$ ($R\bar{3}m$). The reflections corresponding to NaOH are marked with asterisks and were refined using single peaks. Unknown reflections are marked with ‘.

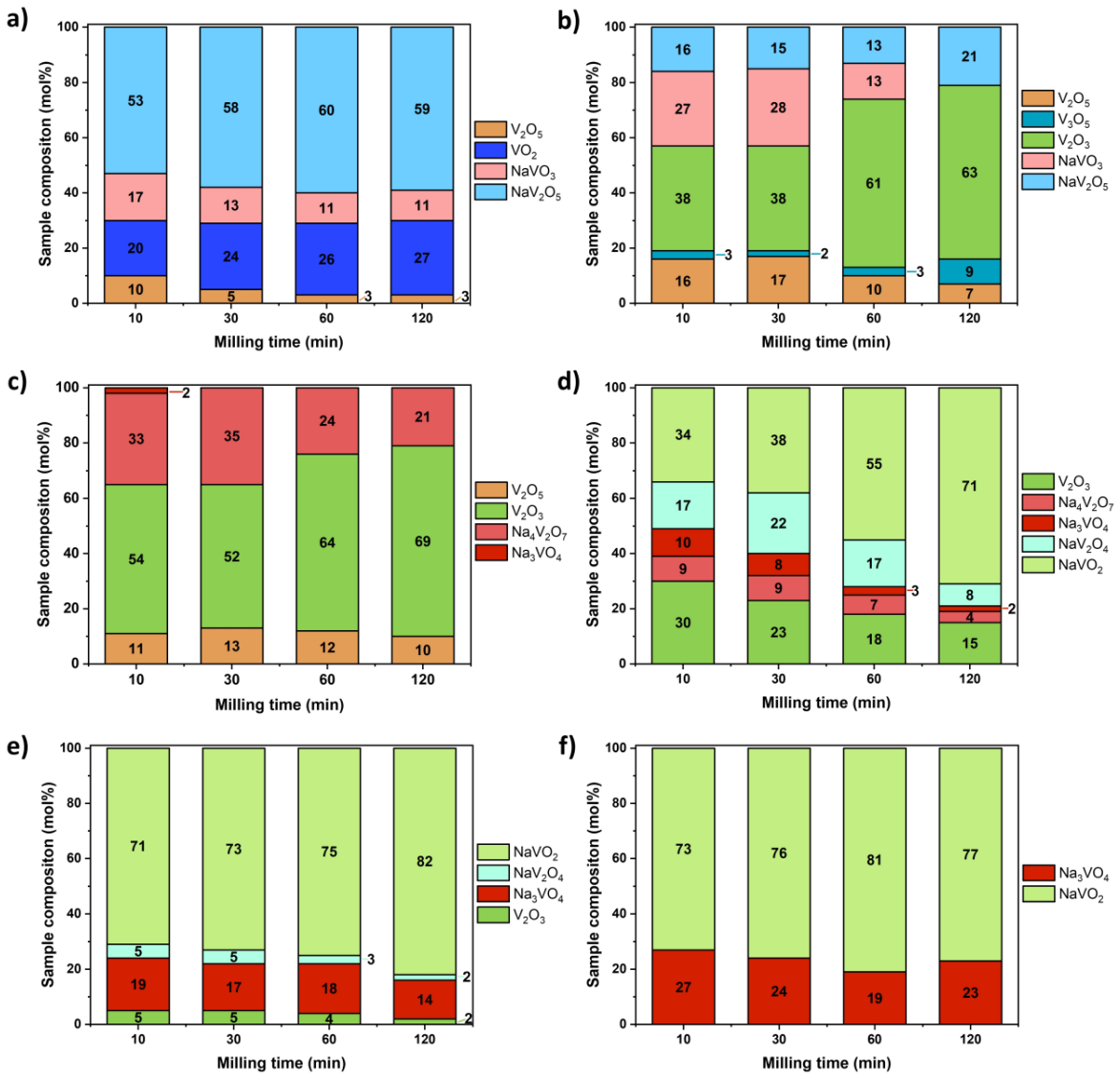

Figure S22: Sample composition in mol percent calculated from Rietveld refinement for V_2O_5 milled with (a) 1, (b) 1.5, (c) 2, (d) 2.5, (e) 3, and (f) 4 eq. NaH for different milling times. For simplicity, if different polymorphs of an oxide were found in a sample, they were added together in this figure, but are detailed in the supporting information.

3.5. Testing of the reproducibility

To test the reproducibility of the syntheses and to validate the observed trends, the syntheses with 1 eq. NaH for 10 and 120 min of milling, as well as with 2 and 3 eq. NaH for 10 min of milling have been performed three times. As shown in Figure S23, all samples show a good reproducibility with standard deviations for the phase percentages of less than 5%, confirming the observed trends.

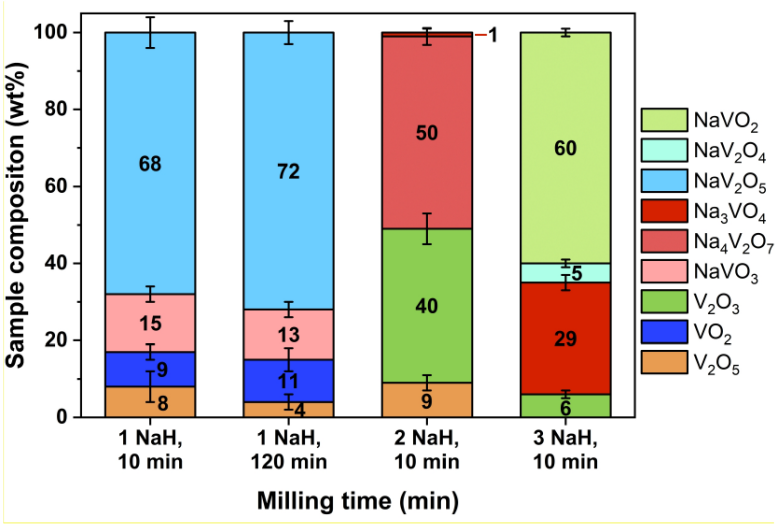

Figure S23: Average sample composition as obtained by Rietveld refinement of the triplicates prepared with the following milling conditions: 1 eq. NaH for 10 and 120 min, as well as 2 and 3 eq. NaH for 10 min. Error bars indicate the standard deviations of the mean values experiments of the sample composition of the triplicate tests.

The exact sample composition of each triplicate and the corresponding Rietveld refinements are shown in Tables S8-S11 and Figures S24-S27. Hereby, the samples that form a triplicate are referred to as sample 1, sample 2 and sample 3 for each of the grinding conditions tested in Tables S8-S11 and Figures S24-S27.

1 eq. NaH – 10 min

Table S8: Overview of the sample composition in weight percent as obtained by Rietveld refinement of the triplicate prepared with 1 eq. NaH for 10 min of milling.

Sample	Milling time (min)	V_2O_5 (*Pmmn*)	VO_2 ($P4_2/mnm$)	$NaVO_3$ ($C2/c$)	NaV_2O_5 (*Pmmn*)
1	10	11	10	13	66
2	10	9	10	15	66
3	10	3	7	17	73

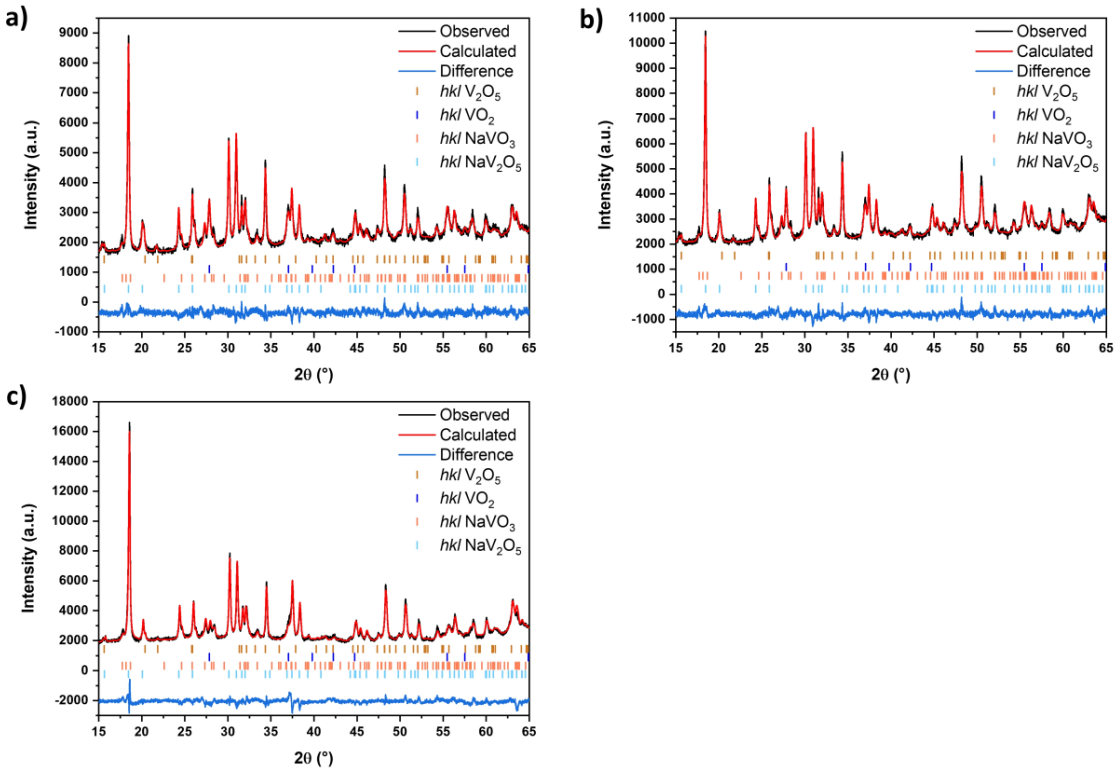

Figure S24: Rietveld refinement of the triplicate test for V_2O_5 milled with 1 eq. NaH for 10 min consisting of (a) sample 1, (b) sample 2, and (c) sample 3. Ochre ticks indicate the Bragg positions of V_2O_5 (*Pmmn*), blue ones of VO_2 ($P4_2/mnm$), coral ones of $NaVO_3$ ($C2/c$), and cerulean ones of NaV_2O_5 (*Pmmn*).

1 eq. NaH – 120 min

Table S9: Overview of the sample composition in weight percent as obtained by Rietveld refinement of the triplicate prepared with 1 eq. NaH for 120 min of milling.

Sample	Milling time (min)	V_2O_5 (*Pmmn*)	VO_2 ($P4_2/mnm$)	$NaVO_3$ ($C2/c$)	NaV_2O_5 (*Pmmn*)
1	120	3	14	8	75
2	120	4	12	12	72
3	120	2	8	14	76

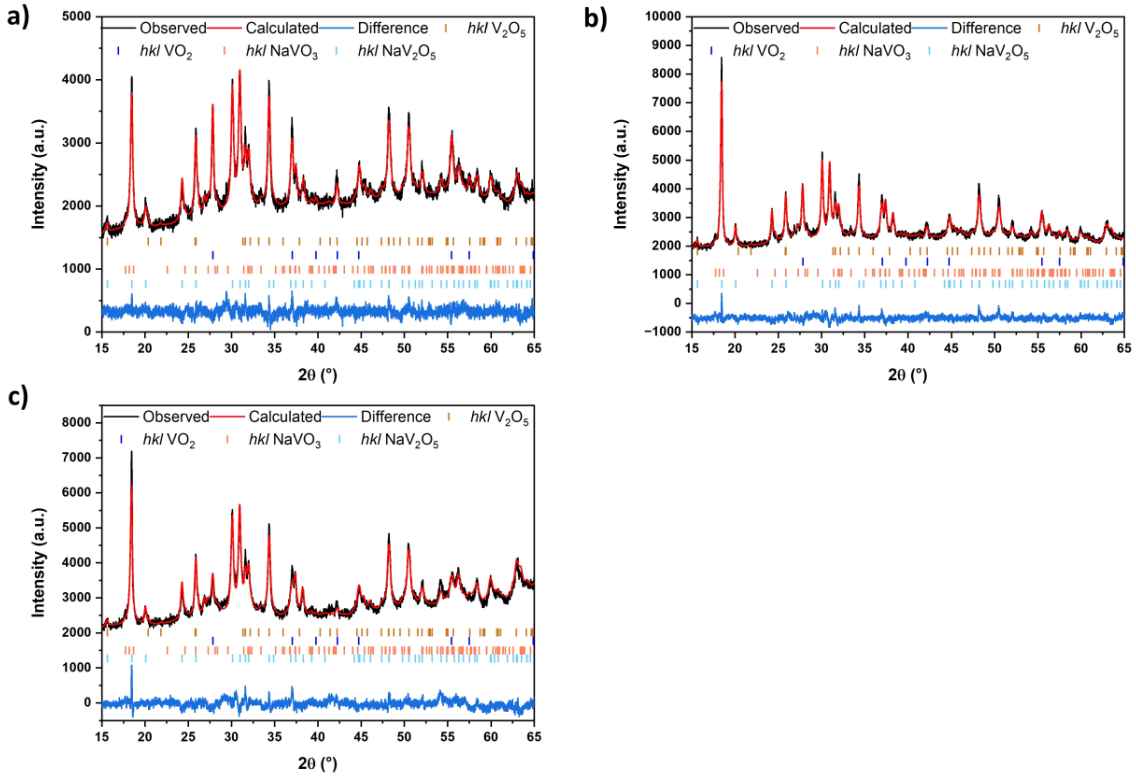

Figure S25: Rietveld refinement of the triplicate test for V_2O_5 milled with 1 eq. NaH for 120 min consisting of (a) sample 1, (b) sample 2, and (c) sample 3. Ochre ticks indicate the Bragg positions of V_2O_5 (*Pmmn*), blue ones of VO_2 ($P4_2/mnm$), coral ones of $NaVO_3$ ($C2/c$), and cerulean ones of NaV_2O_5 (*Pmmn*).

2 eq. NaH – 10 min

Table S10: Overview of the sample composition in weight percent as obtained by Rietveld refinement of the triplicate prepared with 2 eq. NaH for 10 min of milling.

Sample	Milling time (min)	V_2O_5 (*Pmmn*)	V_2O_3 ($R\bar{3}c$)	$Na_4V_2O_7$ ($C2/c$)	Na_3VO_4 ($P2_13$)
1	10	10	39	49	2
2	10	6	45	49	0
3	10	10	37	53	0

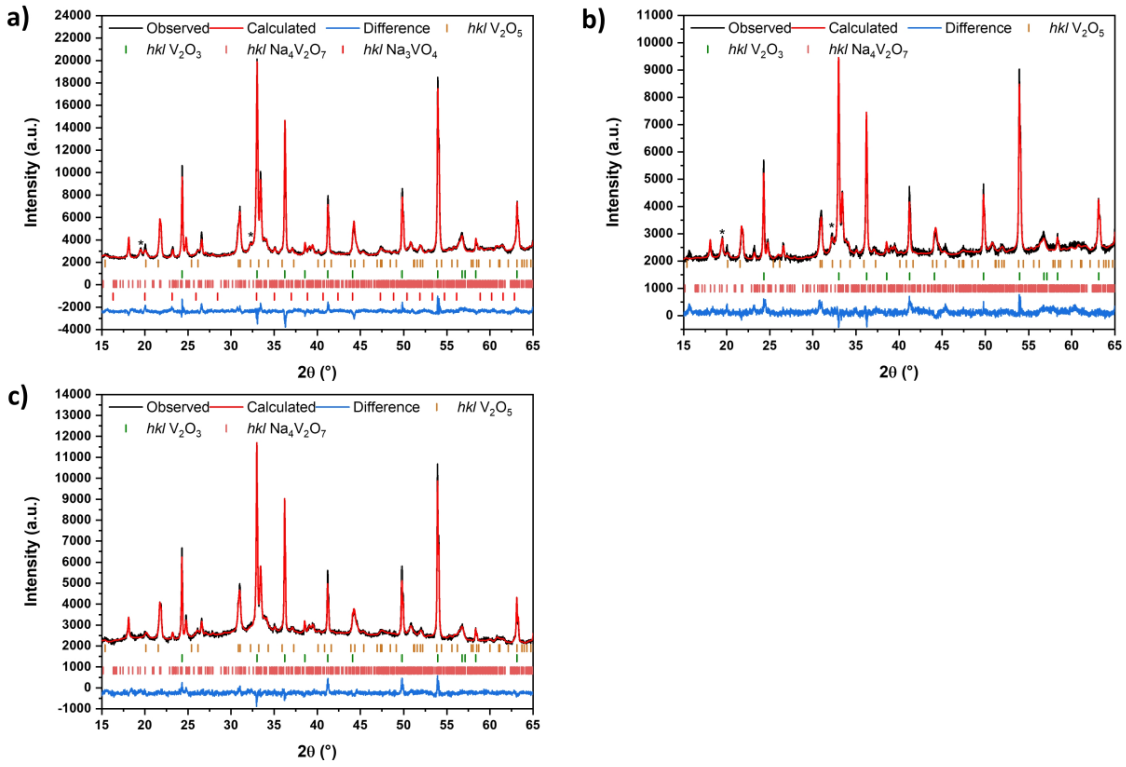

Figure S26: Rietveld refinement of the triplicate test for V_2O_5 milled with 2 eq. NaH for 10 min consisting of (a) sample 1, (b) sample 2, and (c) sample 3. Ochre ticks indicate the Bragg positions of V_2O_5 (*Pmmn*), olive ones of V_2O_3 ($R\bar{3}c$), roman ones of $Na_4V_2O_7$ ($C2/c$), and red ones of Na_3VO_4 ($P2_13$). Unknown reflections are marked with asterisks and were refined using single peaks during the Rietveld refinement.

3 eq. NaH – 10 min

Table S11: Overview of the sample composition in weight percent as obtained by Rietveld refinement of the triplicate prepared with 3 eq. NaH for 10 min of milling.

Sample	Milling time (min)	V_2O_3 ($R\bar{3}c$)	Na_3VO_4 ($P2_13$)	Na_3VO_4 ($Pmn2_1$)	NaV_2O_4 ($C2/c$)	$NaVO_2$ ($R\bar{3}m$)
1	10	7	16	13	9	55
2	10	6	18	14	5	57
3	10	6	14	13	6	61

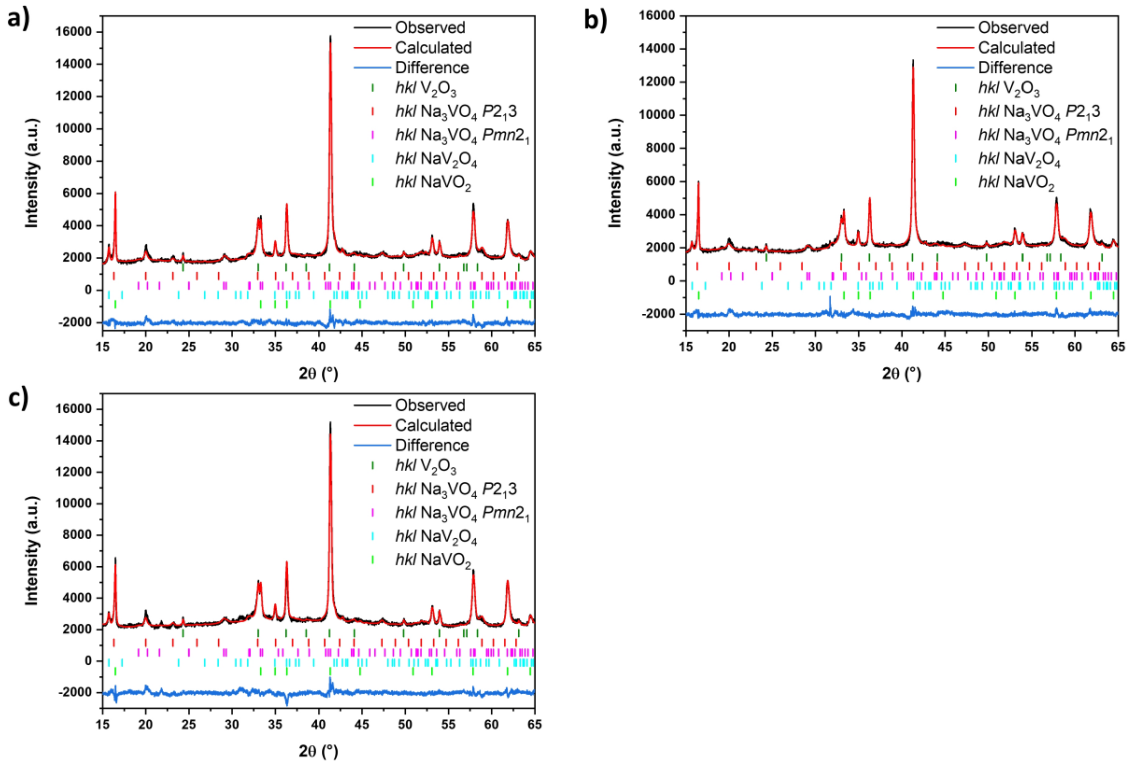

Figure S27: Rietveld refinement of the triplicate test for V_2O_5 milled with 3 eq. NaH for 10 min consisting of (a) sample 1, (b) sample 2, and (c) sample 3. Olive ticks indicate the Bragg positions of V_2O_3 ($R\bar{3}c$), red ones of Na_3VO_4 ($P2_13$), magenta ones of Na_3VO_4 ($Pmn2_1$), cyan ones of NaV_2O_4 ($C2/c$), and light green ones of $NaVO_2$ ($R\bar{3}m$).

3.6. Reoxidation of reduced samples

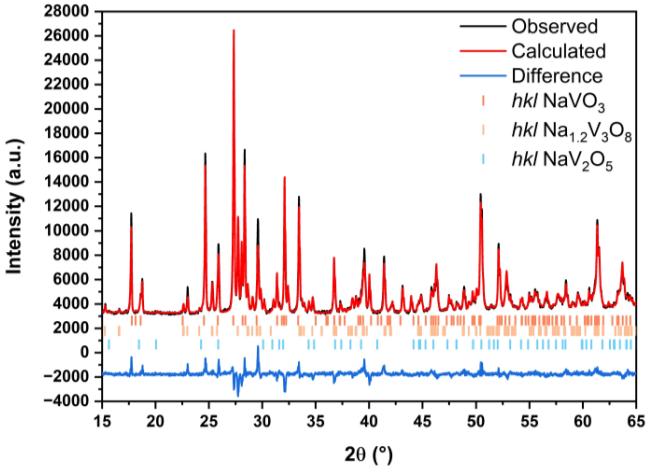

Figure S28: Rietveld refinement of V_2O_5 milled with 1.5 eq. NaH for 10 min followed by thermal treatment under argon up to 350 °C, followed by heating under a mixture of oxygen and argon to 550°C. Coral ticks indicate the Bragg positions of $NaVO_3$ (*C*2/*c*), light orange ones of $Na_{1.2}V_3O_8$ (*P*2$_1$/*m*1) and cerulean ones of NaV_2O_5 (*Pmmn*).

3.7. Rietveld refinement of the reaction with 6 eq. NaH

As with 4 eq. NaH, two broad reflections at around 38 and 54° 2θ could be attributed to NaOH, which formed during the PXRD measurement and not during ball milling. Therefore, NaOH was not included in the determination of the sample composition by Rietveld refinement and two single peaks were used again to refine the two reflections at around 38 and 54° 2θ.

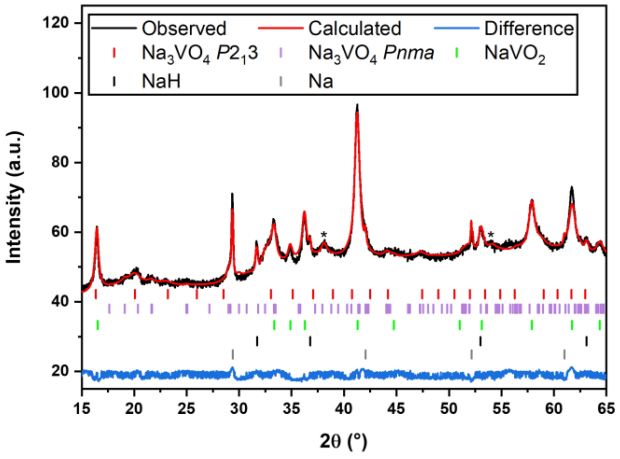

Figure S29: PXRD pattern (black) and Rietveld refinement (red) of the sample obtained after milling V_2O_5 with 6 eq. NaH for 10 min. Red ticks indicate the Bragg positions of Na_3VO_4 (*P*2$_1$3), lavender ones of Na_3VO_4 (*Pnma*), light green ones of $NaVO_2$ ($R\bar{3}m$), black ones of NaH ($Fm\bar{3}m$), and gray ones of Na ($Im\bar{3}m$). The reflections corresponding to NaOH are marked with asterisks and were refined using single peaks.

3.8. Quantum mechanical calculations using VASP

Table S12: Calculated formation enthalpies of both reactants and products per formula unit *Z*

Compound	Space group	Enthalpy/*Z* (eV)
V_2O_5	*Pmmn*	-61.40
VO_2	$P4_2/mnm$	-27.27
V_3O_5	*C*2/*c*	-73.90
V_2O_3	$R\bar{3}c$	-46.53
$NaVO_3$	*Pnma*	-38.26
$NaVO_3$	*C*2/*c*	-38.25
$Na_4V_2O_7$	*C*2/*c*	-90.42
Na_3VO_4	$P2_13$	-51.50
Na_3VO_4	*Pnma*	-52.04
NaV_2O_5	*Pmmn*	-65.63
NaV_2O_4	*C*2/*c*	-57.66
$NaVO_2$	$R\bar{3}m$	-29.83
Na_2O	$Fm\bar{3}m$	-11.70
NaOH	*Cmcm*	-13.88
NaH	$Fm\bar{3}m$	-5.05
Na	$Im\bar{3}m$	-1.41
H_2 (gaseous)	-	-6.41

Table S13: Comparison of our calculated reaction enthalpies (H_r) with those tabulated by Vdovin *et al.* (H_{Vdovin}).[17]

Reaction	H_r (eV)	H_r (kJ/mol)	H_{Vdovin} (kJ/mol)
$V_2O_5 + Na_2O \rightarrow 2\ NaVO_3$	-3.43	-330.9	-326.3
$V_2O_5 + 2\ Na_2O \rightarrow Na_4V_2O_7$	-5.62	-542.2	540.3
$V_2O_5 + 3\ Na_2O \rightarrow 2\ Na_3VO_4$	-7.63	-736.1	712.7

Table S14: Literature values for the molar heat capacity c_m of several (sodium) vanadium oxides[18] and their calculated corresponding specific heat capacities c_p.

Compound	$c_{m,298.15\ K}$ ($Jmol^{-1}K^{-1}$)	c_p ($Jg^{-1}K^{-1}$)
V_2O_5	132.69	0.73
V_2O_3	104.95	0.70
$NaVO_3$	97.57	0.80
$Na_4V_2O_7$	269.74	0.88
Na_3VO_4	164.85	0.90

Table S15: Comparison of the reaction enthalpies for the reduction of V_2O_5 with 1.5 eq. NaH to VO_2, V_3O_5 and V_2O_3 and after subsequent formation of $NaVO_3$.

Nr.	Reaction	ΔH_r (eV)
16	$V_2O_5 + 1.5\ NaH \rightarrow 0.25\ V_2O_5 + 1.5\ VO_2 + 0.75\ Na_2O + 0.75\ H_2$	-0. 87
17	$V_2O_5 + 1.5\ NaH \rightarrow 0.55\ V_2O_5 + 0.3\ V_3O_5 + 0.75\ Na_2O + 0.75\ H_2$	-0.55
18	$V_2O_5 + 1.5\ NaH \rightarrow 0.625\ V_2O_5 + 0.375\ V_2O_3 + 0.75\ Na_2O + 0.75\ H_2$	-0.43
19	$V_2O_5 + 1.5\ NaH \rightarrow 1.5\ VO_2 + 1\ NaVO_3 + 0.5\ Na_2O + 0.75\ H_2$	-1.73
20	$V_2O_5 + 1.5\ NaH \rightarrow 0.2\ V_2O_5 + 0.3\ V_3O_5 + 1.1\ NaVO_3 + 0.2\ Na_2O + 0.75\ H_2$	-2.43
21	$V_2O_5 + 1.5\ NaH \rightarrow 0.25\ V_2O_5 + 0.375\ V_2O_3 + 1.25\ NaVO_3 + 0.125\ Na_2O + 0.75\ H_2$	-2.58

Table S16: Possible partial and corresponding total reaction equations occurring during ball milling with 2 eq. NaH, as well as the reaction enthalpies for the total reaction equations.

Nr.	Reaction	ΔH_r (eV)
22	$V_2O_5 + 2\ NaH \rightarrow 0\ V_2O_5 + 2\ VO_2 + 1\ Na_2O + 1\ H_2$ → no further reaction possible	-1.16
23	$V_2O_5 + 2\ NaH \rightarrow 0.4\ V_2O_5 + 0.4\ V_3O_5 + 1\ Na_2O + 1\ H_2$	-0.73
24	$0.4\ V_2O_5 + 0.8\ Na_2O \rightarrow 0.4\ Na_4V_2O_7$	-2.24
25	$V_2O_5 + 2\ NaH \rightarrow 0.4\ V_3O_5 + 0.4\ Na_4V_2O_7 + 0.2\ Na_2O + H_2$	-2.97
26	$V_2O_5 + 2\ NaH \rightarrow 0.5\ V_2O_5 + 0.5\ V_2O_3 + 1\ Na_2O + 1\ H_2$	-0.58
27	$0.5\ V_2O_5 + 1\ Na_2O \rightarrow 0.5\ Na_4V_2O_7$	-2.80
28	$V_2O_5 + 2\ NaH \rightarrow 0.5\ V_2O_3 + 0.5\ Na_4V_2O_7 + 0\ Na_2O + H_2$	-3.38

Table S17: Possible partial and corresponding total reaction equations occurring during ball milling with 2.5 eq. NaH.

Nr.	Reaction	ΔH_r (eV)
29	$V_2O_5 + {}^5/_2\ NaH \rightarrow {}^3/_8\ V_2O_5 + {}^5/_8\ V_2O_3 + {}^5/_4\ Na_2O + {}^5/_4\ H_2$	-0.72
30	${}^1/_8\ V_2O_5 + {}^1/_4\ Na_2O \rightarrow {}^1/_8\ Na_4V_2O_7$	-0.70
31	${}^1/_8\ V_2O_5 + {}^3/_8\ Na_2O \rightarrow {}^1/_4\ Na_3VO_4$	-0.96
32	${}^1/_8\ V_2O_5 + {}^3/_8\ V_2O_3 + {}^1/_4\ Na_2O \rightarrow {}^1/_2\ NaV_2O_4$	-0.78
33	${}^1/_8\ V_2O_3 + {}^1/_8\ Na_2O \rightarrow {}^1/_4\ NaVO_2$	-0.18
34	$V_2O_5 + {}^5/_2\ NaH \rightarrow {}^1/_8\ V_2O_3 + {}^1/_4\ Na_2O + {}^1/_8\ Na_3VO_4 + {}^1/_4\ Na_3VO_4 + {}^1/_2\ NaV_2O_4 + {}^1/_8\ NaV_2O_4 + {}^5/_4\ H_2$	-3.34

Table S18: Possible partial and corresponding total reaction equations occurring during ball milling with more than 3 eq. NaH.

Nr.	Reaction
35	$x\ V_2O_5 + 4x\ NaH \rightarrow x\ V_2O_3 + 2x\ Na_2O + 2x\ H_2$
36	$(1\text{-}x)\ V_2O_5 + 3(1\text{-}x)\ Na_2O \rightarrow 2(1\text{-}x)\ Na_3VO_4$
37	$x\ V_2O_3 + x\ Na_2O \rightarrow 2x\ NaVO_2$
38	$V_2O_5 + 4x\ NaH \rightarrow 2(1\text{-}x)\ Na_3VO_4 + 2x\ NaVO_2 + (4x\text{-}3)\ Na_2O + 2x\ H_2$

4. References

(1) Shklover, V.; Haibach, T.; Ried, F.; Nesper, R.; Novák, P. Crystal Structure of the Product of Mg^{2+} Insertion into V_2O_5 Single Crystals. *J. Solid State Chem.* **1996**, *123* (2), 317-323.
(2) Li, M.; Magdassi, S.; Gao, Y.; Long, Y. Hydrothermal Synthesis of VO_2 Polymorphs: Advantages, Challenges and Prospects for the Application of Energy Efficient Smart Windows. *Small* **2017**, *13* (36), 1701147.
(3) McWhan, D. B.; Marezio, M.; Remeika, J. P.; Dernier, P. D. X-ray diffraction study of metallic VO_2. *Phys. Rev. B* **1974**, *10* (2), 490-495.
(4) Hong, S.-H.; Åsbrink, S. The structure of the high-temperature modification of V_3O_5 at 458 K. *Acta Cryst. B* **1982**, *38* (3), 713-719.
(5) Finger, L. W.; Hazen, R. M. Crystal structure and isothermal compression of Fe_2O_3, Cr_2O_3, and V_2O_3 to 50 kbars. *J. Appl. Phys.* **1980**, *51* (10), 5362-5367.
(6) Kato, K.; Takayama, E. Das Entwässerungsverhalten des Natriummetavanadatdihydrats und die Kristallstruktur des β-Natriummetavanadats. *Acta Cryst. B* **1984**, *40* (2), 102-105.
(7) Ramani, K.; Shaikh, A. M.; Reddy, B. S.; Viswamitra, M. A. Crystal structure of ferroelectric sodium meta vanadate, $NaVO_3$. *Ferroelectrics* **1975**, *9* (1), 49-56.
(8) Shaikh, A. M. Crystal chemistry of vanadate pyroxenes: Crystal structure refinement, Na anisotropy and rigid body analysis of the thermal vibration in ferroelectric $NaVO_3$. *Ferroelectrics* **1990**, *107* (1), 219-224.
(9) Marumo, F.; Isobe, M.; Iwai, S.; Kondō, Y. α Form of sodium metavanadate. *Acta Cryst. B* **1974**, *30* (6), 1628-1630.
(10) Kato, K.; Takayama, E. Tetrasodium divanadate, $Na_4[V_2O_7]$. *Acta Cryst. C* **1983**, *39* (11), 1480-1482.
(11) Kerp, O.; Möller, A. Synthesis and Characterization of $Na_5[VO_4][O]$ and $Na_4[VO_4][OH]$. *Z. Anorg. Allg. Chem.* **2006**, *632* (7), 1187-1194.
(12) Olazcuaga, R.; Le Flem, G.; Hagenmuller, P. Mise en évidence du chrome ou du manganèse au degré d'oxydation +V dans quelques nouveaux composés oxygénés. *Rev. Chim. Min.* **1976**, *13*, 9-23.
(13) Meetsma, A.; de Boer, J. L.; Damascelli, A.; Jegoudez, J.; Revcolevschi, A.; Palstra, T. T. M. Inversion Symmetry in the Spin-Peierls Compound α'-NaV_2O_5. *Acta Cryst. C* **1998**, *54* (11), 1558-1561.
(14) Didier, C.; Guignard, M.; Darriet, J.; Delmas, C. O′3–Na_xVO_2 System: A Superstructure for $Na_{1/2}VO_2$. *Inorg. Chem.* **2012**, *51* (20), 11007-11016.
(15) Didier, C.; Guignard, M.; Suchomel, M. R.; Carlier, D.; Darriet, J.; Delmas, C. Thermally and Electrochemically Driven Topotactical Transformations in Sodium Layered Oxides Na_xVO_2. *Chem. Mater.* **2016**, *28* (5), 1462-1471.
(16) Chamberland, B. L.; Porter, S. K. A study on the preparation and physical property determination of $NaVO_2$. *J. Solid State Chem.* **1988**, *73* (2), 398-404.
(17) Vdovin, V. V.; Edil'baev, A. I.; Kozlov, V. A.; Karpov, A. A.; Spitsyn, V. A.; Terlikbaeva, A. Z.; Pechenkina, A. A. Thermodynamic analysis of the reaction of vanadium oxides with oxides of sodium, potassium, calcium, barium, and manganese. *Steel Transl.* **2007**, *37* (9), 787-791.
(18) Barin, I. *Thermochemical Data of Pure Substances*; VCH Verlagsgesellschaft, 1989.

6.3 Supporting Information – Mechanochemical reduction of V_2O_5: Alkali metals vs. Alkali Metal Hydrides – Which are the better Reducing Agents?

Table S1: Overview of the calculated formation enthalpies per formula unit *Z* of different vanadium oxides, alkali metal vanadates, alkali metal oxides and hydrides as well as their elemental counterparts for the respective sodium and lithium compounds that are relevant for this work. Hereby, *A* represents Na and Li.

Compound	$Enthalpy_{Na\text{-}Compounds}/Z$ (eV)	$Enthalpy_{Li\text{-}Compounds}/Z$ (eV)
V_2O_5	–61.40	–61.40
VO_2	–27.27	–27.27
V_2O_3	–46.53	–46.53
V	–11.61	–11.61
H_2	–6.41	–6.41
AVO_3	–38.26	–39.02
$Na_4V_2O_7$	–90.42	Unknown to literature
A_3VO_{42}	–52.07	–55.57
AV_2O_5	–65.63	–66.35
AV_2O_4	–57.66	–58.48
AVO_2	–29.83	–31.25
A_2O	–11.94	–14.75
AH	–5.05	–6.07
A	–1.41	–3.93

6.4 Supporting Information – Mechanochemical Synthesis of MgV_2O_4: Reactivity Pathways Driven by Milling Energy and Precursors

Supporting Information

Mechanochemical Synthesis of MgV_2O_4: Reactivity Pathways Driven by Milling Energy and Precursors

Anna Michaely[1], Hong Chen[2], Oliver Clemens[2], Maxim Neuberger[3], Christopher W. M. Kay[3, 4], Robert Haberkorn[1], Guido Kickelbick[1]*

[1] Saarland University, Inorganic Solid-State Chemistry, Campus, Building C4.1, 66123 Saarbrücken, Germany

[2] Institute for Materials Science, Materials Synthesis Group, University of Stuttgart, Heisenbergstraße 3, 70569 Stuttgart, Germany

[3] Physical Chemistry and Didactics of Chemistry, Saarland University, Campus, Building B2.2, 66123 Saarbrücken (Germany)

[4] University College London, London Centre for Nanotechnology, 17–19 Gordon Street, London WC1H 0AH (UK)

E-mail: guido.kickelbick@uni-saarland.de

1 Experimental Section – Testing of Linearity

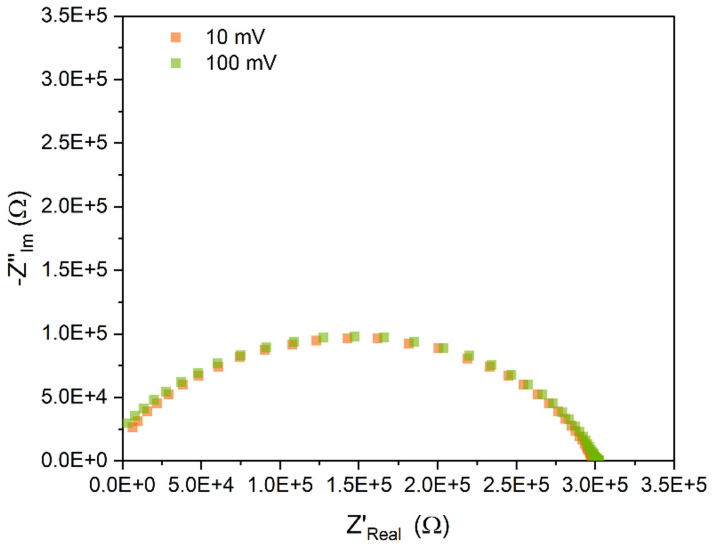

Figure S1: Nyquist plot of MgV_2O_4 sample measured with different amplitude values: 10 mV and 100 mV at 27 °C, respectively. The linearity of EIS data obtained by 100 mV in the manuscript is confirmed by the fact that no distorted data is observed between measurements using different perturbations.

2 Rietveld Refinement after ball milling V_2O_5 and Mg

2.1 Estimation of an amorphous phase

To estimate the phase percentage of an amorphous phase via Rietveld refinement, the well-established method of an internal standard can be used. After addition of a known weight percentage of a well crystalline, fine-grained compound such as CaF_2 (*wt% of spiked*), the percentage of amorphous phase in the sample (*wt% in original sample*) can be calculated via the following equation. Hereby, *wt% in spiked sample* represents the "absolute phase amount in the spiked sample after considering amorphous phase amounts" given in Topas 5.0.[1]

$$wt\%\ in\ original\ sample = \frac{wt\%\ in\ spiked\ sample}{1 - wt\%\ of\ spiked}$$

For harshly milled samples, estimation of the amorphous phase was also done via an interpretation of the background profile with a method related to PONKS.[2]

2.2 300 rpm

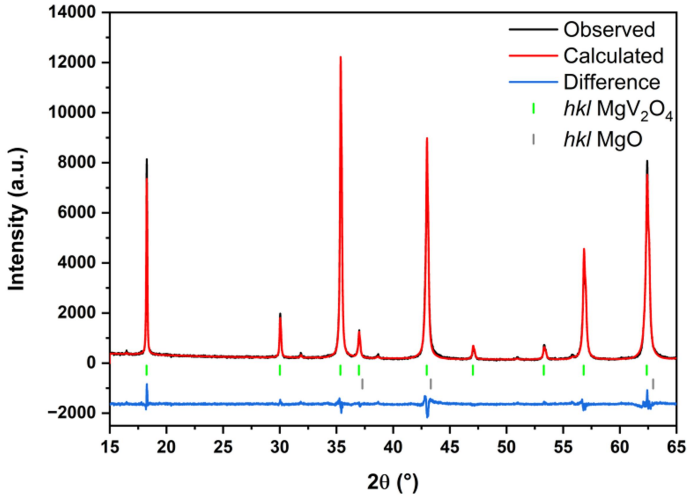

Figure S2: PXRD pattern (black) and Rietveld refinement (red) of MgV_2O_4 prepared mechanochemically at 300 rpm. Green ticks indicate the Bragg positions of MgV_2O_4 ($Fd\bar{3}m$), gray ones of MgO ($Fm\bar{3}m$).

Table S1: Refinement parameters for the 300 rpm sample using both stoichiometric MgV_2O_4 and MgO. The background polynomial is set to the 15th degree.

Phase	wt%	*a* (pm)	cry size (nm)	strain (%)	R_{wp}	GOF	composition
MgO	19	421.47(1)	32(2)	0.07(1)	7.20	1.37	$Mg_{2.10}V_2O_{5.10}$
MgV_2O_4	81	841.11(1)	>500	0.06(1)			

2.3 500 rpm

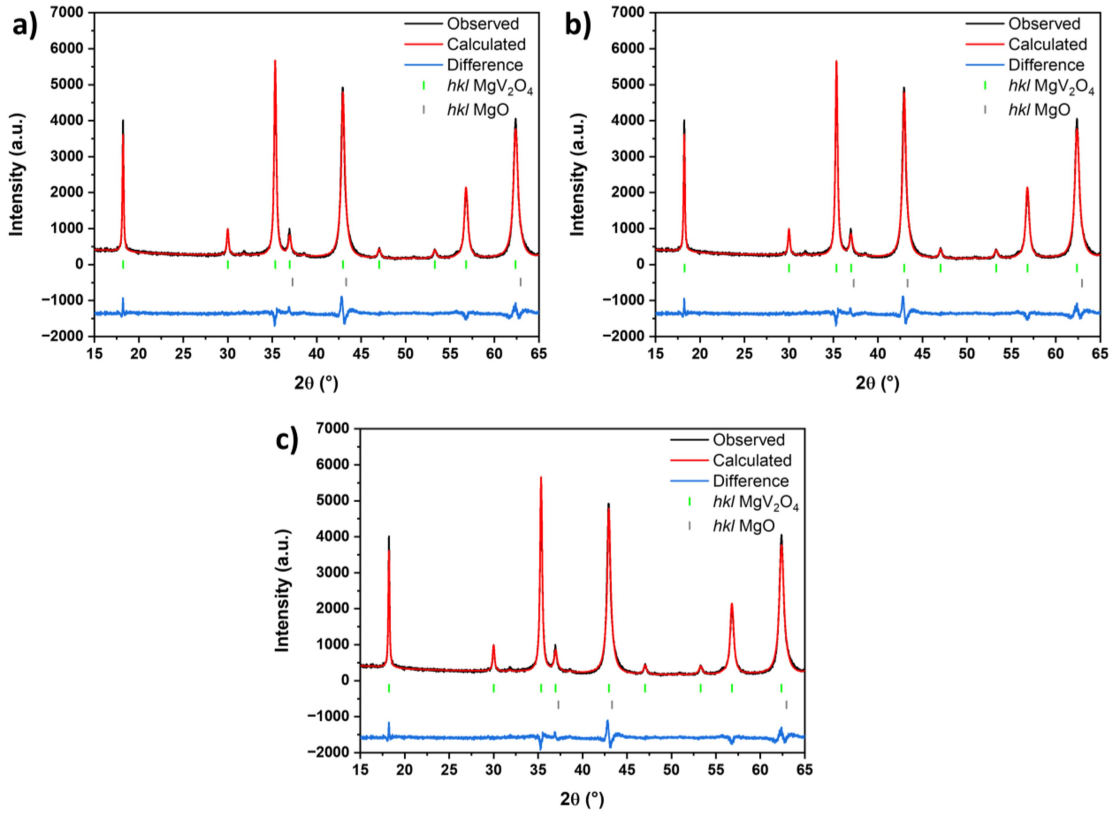

Figure S3: Different Rietveld refinements performed for MgV_2O_4 at 500 rpm, including (a) the use of stoichiometric MgV_2O_4 and MgO and using MgV_2O_4, while also allowing an insertion of (b) V(III) or (c) V(II) into MgO. In all figures, the experimental diffraction pattern is shown in black, the Rietveld refinement in red and the difference between both in blue. Green ticks indicate the Bragg positions of MgV_2O_4 ($Fd\bar{3}m$), gray ones of MgO ($Fm\bar{3}m$).

Table S2: Refinement parameters for the 500 rpm sample using both stoichiometric MgV_2O_4 and MgO, stoichiometric MgV_2O_4 and $Mg_{1-3x}V_{2x}O$ (V(III) insertion into MgO) and non-stoichiometric MgV_2O_4 and $Mg_{1-x}V_xO$ (V(II) insertion into MgO). The background polynomial is set to the 15th degree.

Phase	wt%	*a* (pm)	cry size (nm)	strain (%)	R_{wp}	GOF	composition
MgO	38	420.34(2)	16(1)	0.25(2)	7.34	1.41	$Mg_{3.93}V_2O_{6.93}$
MgV_2O_4	62	841.77(2)	222(24)	0.14(1)			
$Mg_{0.61}V_{0.26}O$	38	420.34(2)	16(1)	0.26(2)	7.21	1.40	$Mg_{1.94}V_2O_{4.94}$
MgV_2O_4	62	841.75(2)	239(28)	0.14(1)			
$Mg_{0.89}V_{0.11}O$	37	420.35(2)	16(1)	0.26(2)	7.22	1.40	$Mg_{2.97}V_2O_{5.84}$
MgV_2O_4	63	841.75(2)	237(27)	0.14(1)			

2.4 700 rpm

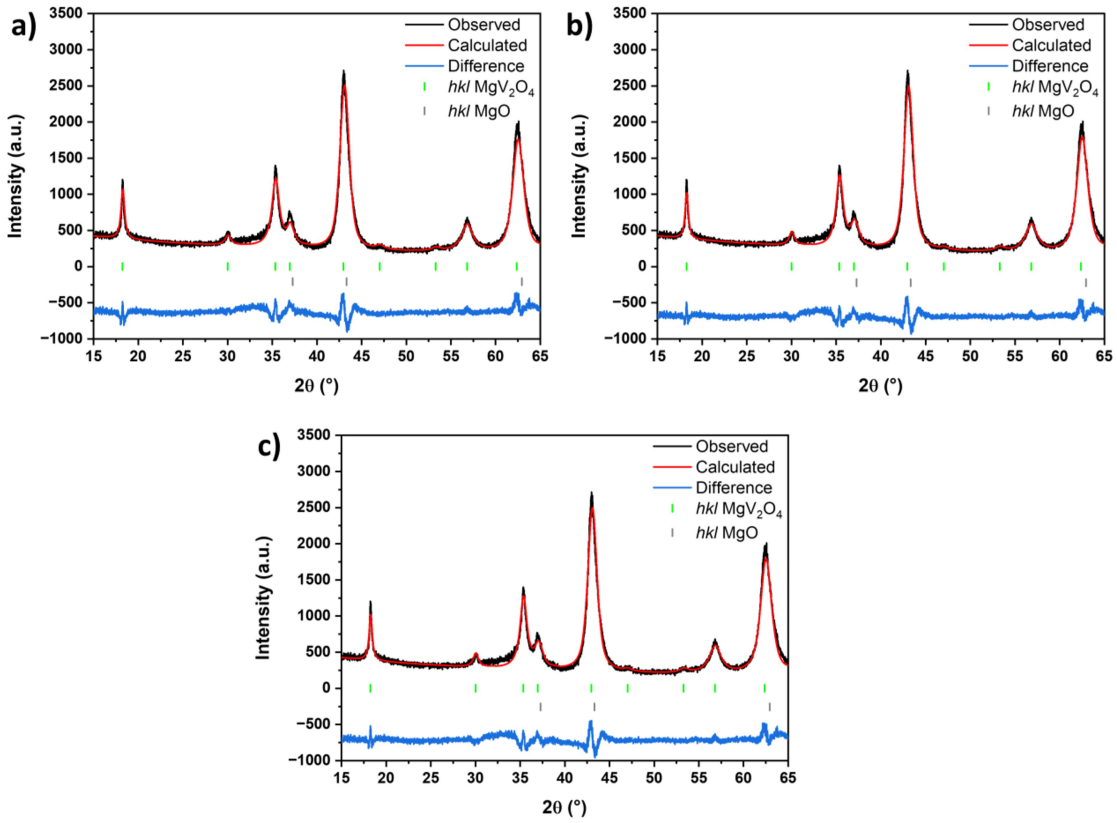

Figure S4: Different Rietveld refinements performed for MgV_2O_4 at 700 rpm, including (a) the use of stoichiometric MgV_2O_4 and MgO and using MgV_2O_4, while also allowing an insertion of (b) V(III) or (c) V(II) into MgO. In all figures, the experimental diffraction pattern is shown in black, the Rietveld refinement in red and the difference between both in blue. Green ticks indicate the Bragg positions of MgV_2O_4 ($Fd\bar{3}m$), gray ones of MgO ($Fm\bar{3}m$).

Table S3: Refinement parameters for the 700 rpm sample using both stoichiometric MgV_2O_4 and MgO, stoichiometric MgV_2O_4 and $Mg_{1-3x}V_{2x}O$ (V(III) insertion into MgO) and non-stoichiometric MgV_2O_4 and $Mg_{1-x}V_xO$ (V(II) insertion into MgO). The background polynomial is set to the 5th degree.

Phase	wt%	*a* (pm)	cry size (nm)	strain (%)	R_{wp}	GOF	composition
MgO	61	419.80(3)	13(2)	0.48(3)	8.36	1.62	$Mg_{8.25}V_2O_{11.25}$
MgV_2O_4	39	841.91(9)	16(1)	0.35(1)			
$Mg_{0.39}V_{0.40}O$	60	419.76(3)	13(2)	0.48(3)	8.14	1.58	$Mg_{1.52}V_2O_{4.56}$
MgV_2O_4	40	841.71(9)	24(2)	0.39(1)			
$Mg_{0.77}V_{0.23}O$	55	419.77(3)	14(2)	0.49(3)	8.07	1.57	$Mg_{3.81}V_2O_{6.64}$
$Mg_{1.51}V_{1.49}O_4$	45	841.69(9)	26(2)	0.40(1)			

3 Mechanochemical Stability of MgV_2O_4

To investigate the mechanochemical stability of MgV_2O_4, MgV_2O_4 prepared from V_2O_5 and Mg at 700 rpm in 20 min is further ball milled at 700 rpm. After only 30 min, reflections of MgV_2O_4 are barely visible anymore, showing its low mechanochemical stability. In addition to the decreasing MgV_2O_4 reflections, new reflections at ~31.5° and 48.3° 2θ are observable, which can be attributed to WC with space group ($P\bar{6}m2$) originating from abrasion of the WC milling material. The original sample prepared in 20 min of milling exhibits a low abrasion of WC with weight percentage of tungsten smaller than 0.3 wt%, as determined by ICP-MS measurements.

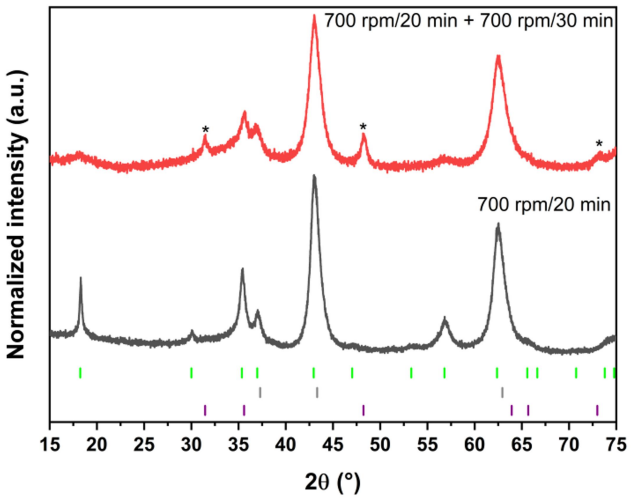

Figure S5: Normalized PXRD patterns of MgV_2O_4 prepared mechanochemically from V_2O_5 and Mg in 20 min at 500 (black) and 700 rpm (blue) and after subsequent ball milling at 700 rpm for 30 min (red, green). Green ticks indicate the Bragg positions of MgV_2O_4 ($Fd\bar{3}m$), gray ones of MgO ($Fm\bar{3}m$), and purple ones of WC ($P\bar{6}m2$). Asterisks mark the reflections of WC.

4 Simulation of Electron Paramagnetic Resonance Spectra

All spectra were recorded at a temperature of 5 K using a microwave power of 0.2 mW and magnetic field modulation amplitude set at 0.5 G with a frequency of 100 kHz.

For all optimizations, the Nelder-Mead simplex optimization algorithm was used together with the function *pepper* of EasySpin[3] with a convergence criterium of 10^{-5}.

Table S4: Simulation parameters for the 300 rpm sample using EasySpin (S = 1/2):

Simulation Parameter	Value
g-factor	$g_{\perp} = 1.940 \pm 0.003$, $g_{\parallel} = 1.989 \pm 0.001$
g-Strain	g-Strain$_{\perp} = 0.103 \pm 0.06$, g-Strain$_{\parallel} = 0.005 \pm 0.047$
Hyperfine tensor A	$A_{\perp} = 119.80 \pm 3.29$ MHz, $A_{\parallel} = 226.68 \pm 1.46$ MHz
A-Strain	A-Strain$_{\perp} = 0$ MHz, A-Strain$_{\parallel} = 2.34 \pm 3.46$ MHz
Gaussian linewidth	0.79 ± 0.46 mT

Table S5: Simulation parameters for the 700 rpm / 50 min sample EasySpin (S = 1/2):

Simulation Parameter	Value
g-factor	$g_{\perp} = 1.977 \pm 0.001$, $g_{\parallel} = 1.951 \pm 0.001$
g-Strain	g-Strain$_{\perp} = 0$, g-Strain$_{\parallel} = 0$
Hyperfine tensor A	$A_{\perp} = 158.03 \pm 1.34$ MHz, $A_{\parallel} = 490.03 \pm 2.51$ MHz
A-Strain	A-Strain$_{\perp} = 20.01 \pm 8.7$ MHz, A-Strain$_{\parallel} = 50.02 \pm 7.7$ MHz
Gaussian linewidth	4.24 ± 0.20 mT

5 Rietveld refinement after MgO removal

Table S6: Phase percentage obtained by Rietveld refinement depending on the washing procedure.

Sample	MgV_2O_4 (wt%)	MgO wt(%)
300 rpm - unwashed	81	19
300 rpm - washed	98	2
500 rpm - unwashed	62	38
500 rpm - washed	95	5
700 rpm - unwashed	45	55
700 rpm - washed	79	21

Table S7: Refinement parameters for the washed 700 rpm sample using both stoichiometric MgV_2O_4 and MgO, stoichiometric MgV_2O_4 and $Mg_{1-3x}V_{2x}O$ (V(III) insertion into MgO) and non-stoichiometric MgV_2O_4 and $Mg_{1-x}V_xO$ (V(II) insertion into MgO). The background is set to 5.

Phase	wt%	a (pm)	cry size (nm)	strain (%)	R_{wp}	GOF	composition
MgO	25	418.75(3)	13(1)	0.24(1)	7.95	1.52	$Mg_{2.6}V_2O_{5.7}$
MgV_2O_4	75	841.22(9)	58(3)	0.27(1)			
$Mg_{0.29}V_{0.47}O$	25	418.78(3)	11(1)	0.23(1)	7.89	1.51	$Mg_{1.06}V_2O_{4.06}$
MgV_2O_4	75	841.20(3)	61(4)	0.27(1)			
$Mg_{0.77}V_{0.23}O$	24	418.75(3)	12(1)	0.23(1)	7.83	1.50	$Mg_{1.78}V_2O_{4.70}$
$Mg_{1.18}V_{1.82}O_4$	76	841.19(6)	63(4)	0.27(1)			

6 EPR spectra after washing

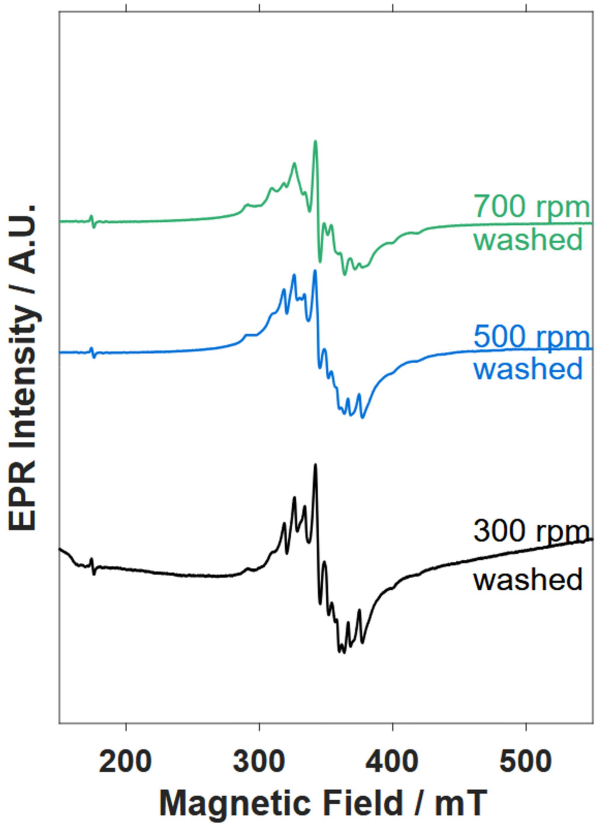

Figure S6: (a) Overview of continuous wave (CW) EPR spectra at 5 K of MgV_2O_4 prepared in 20 min at 300 (black), 500 (blue) and 700 rpm (red), followed by acid washing.

7 Determination of the Mg to V ratio by ICP-MS analysis

Table S8: Ratio of magnesium to vanadium determined by ICP-MS measurements of unwashed and washed samples prepared by milling V_2O_5 with 2 eq. Mg for 20 min for different rotational speeds.

Sample	Ratio Mg : V
300 rpm, unwashed	0.93 : 1
300 rpm, washed	0.66 : 1
500 rpm, unwashed	0.98 : 1
500 rpm, washed	0.59 : 1
700 rpm, unwashed	0.96 : 1
700 rpm, washed	0.68 : 1

8 Results of SEM measurements

While SEM images of the sample prepared at 300 pm reveal the presence of mainly micrometer-sized particles along with a few smaller ones, harsher milling conditions lead to a decrease of the particle size towards the nanometer range. In addition, the formation of agglomerates is observed.

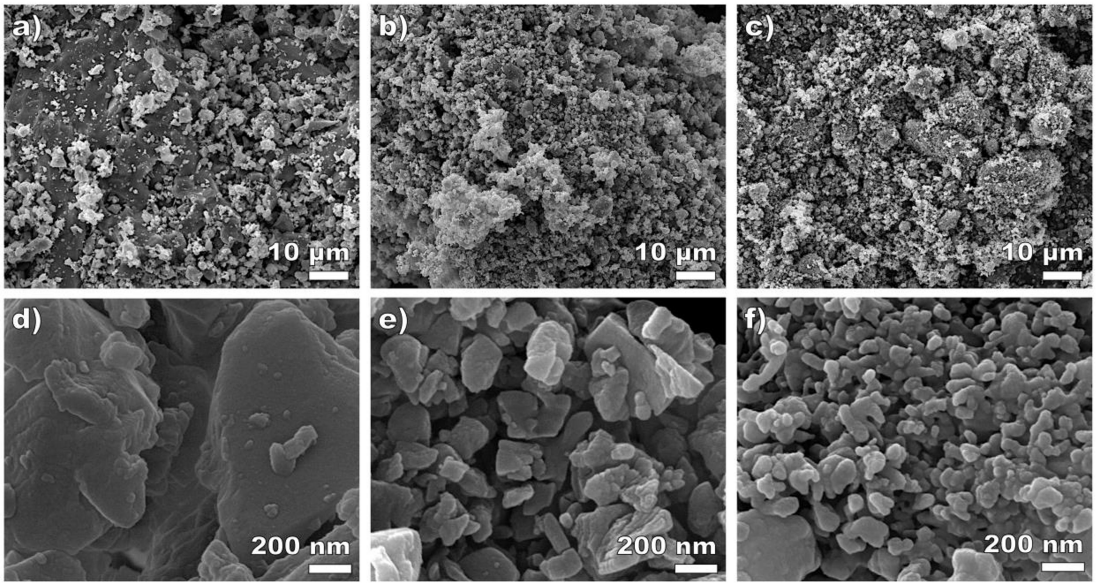

Figure S7: SEM photographs of samples prepared at (a) and (d) 300 rpm, (b) and (e) 500 rpm, as well as (c) and (f) 700 rpm. For better visualization, note the different magnification factors of the top and bottom rows for the same samples.

9 Electrochemical Impedance Spectroscopy

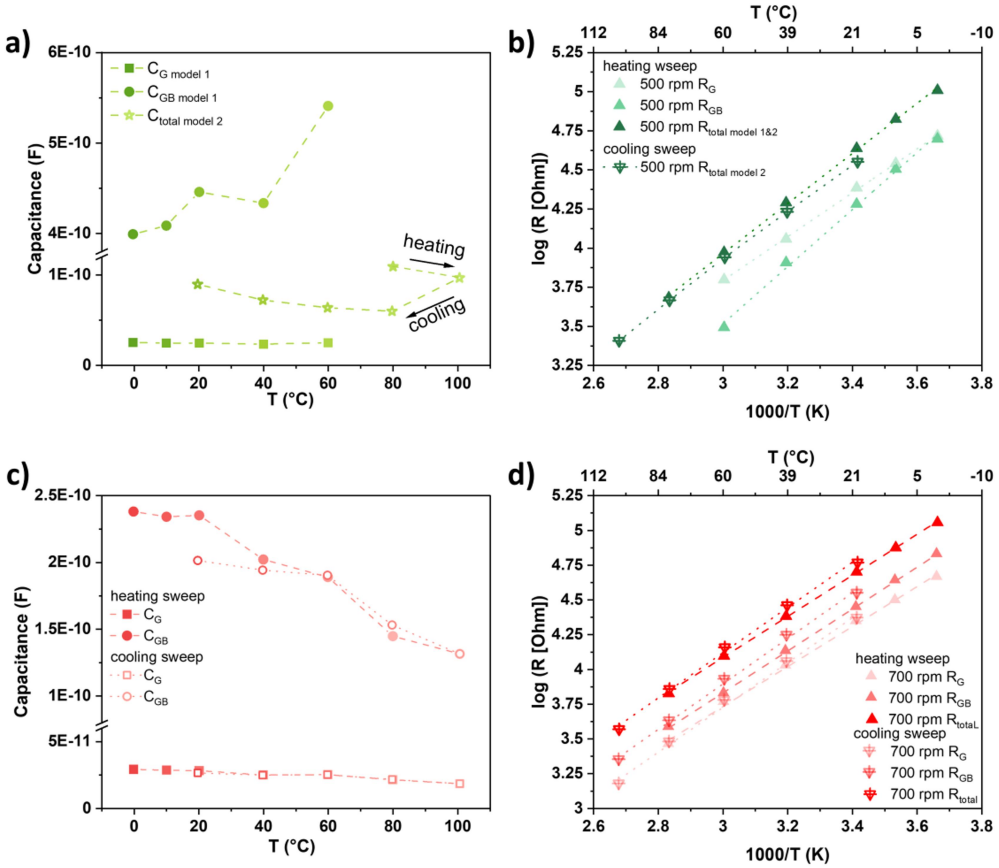

Figure S8: (a) Temperature-dependent bulk(grain) capacitance and grain boundary capacitance for 500 rpm-milled sample; (b) temperature-dependent bulk(grain), grain boundary and total resistance for 500 rpm-milled sample; (c) temperature-dependent bulk(grain) capacitance and grain boundary capacitance for 700 rpm-milled sample and (d) corresponding bulk(grain), grain boundary and total resistance.

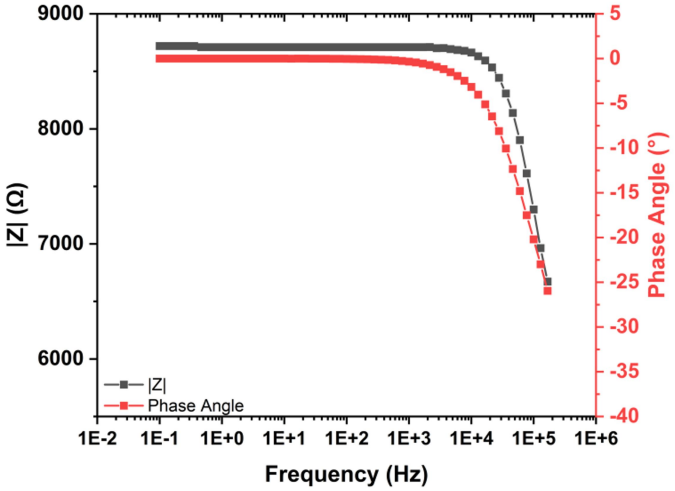

Figure S9: Bode plot of 500 rpm-milled sample at 60 °C on cooling sweep.

10 References

(1) Bruker AXS Inc.: *DIFFRAC.SUITE, Topas 5 User Manual*, Karlsruhe (Germany), **2014**.
(2) Scarlett, N. V. Y.; Madsen, I. C. Quantification of phases with partial or no known crystal structures. *Powder Diffr.* **2006**, *21*, 278-284.
(3) Stoll, S.; Schweiger, A. EasySpin, a comprehensive software package for spectral simulation and analysis in EPR. *J. Magn. Reson.* **2006**, *178*, 42-55.